STUDIES ON MODIFIED LANTHANUM NICKEL OXIDE PEROVSKITE CATALYSTS FOR DRY REFORMING OF METHANE

THESIS

SUBMITTED TO THE

NATIONAL INSTITUTE OF TECHNOLOGY WARANGAL

FOR THE AWARD OF THE DEGREE OF

DOCTOR OF PHILOSOPHY

IN CHEMISTRY

By

TATIPARTHI VIKRAM SAGAR

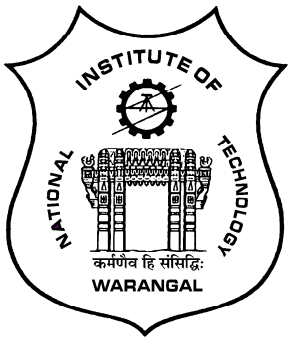

DEPARTMENT OF CHEMISTRY

NATIONAL INSTITUTE OF TECHNOLOGY WARANGAL

WARANGAL-506004

TELANGANA, INDIA

November, 2017

Dedicated to

My Beloved Parents, Brothers & Friends

National Institute of Technology
Warangal – 506 004, Telangana, India

Prof. I Ajit Kumar Reddy, ***Ph.D.***

Professor (Retd.)
Department of Chemistry

Phone : 0870 2462688
Mobile: 098664 40460
E-mail: iakreddy@nitw.ac.in

CERTIFICATE

This is to certify that **Mr. Tatiparthi Vikram Sagar,** a bonafide student of Ph.D. degree of National Institute of Technology, Warangal has carried out this research work under my guidance and supervision. It is to certify that the investigations, findings and the inferences reported by him in the form of the thesis titled **"Studies on Modified Lanthanum Nickel Oxide Perovskite Catalysts for Dry Reforming of Methane"**, for the award of Ph. D. degree in Chemistry, are original contributions to the Chemical Sciences. It is also certified that he has not submitted the same in part or in full to any other university for the award of a diploma or a degree.

Date : 23-11-2017
Place: Warangal

(I. AJIT KUMAR REDDY)
Professor of chemistry (Retd.)
Research Fellow (Emeritus), TLC

सीएसआईआर-भारतीय रासायनिक प्रौद्योगिकी संस्थान
CSIR-Indian Institute of Chemical Technology
तारनाका/Tarnaka, हैदराबाद/Hyderabad - 500 007. भारत/INDIA

Dr. P. S. Sai Prasad, M. Tech., Ph.D. MIIChE, FAPS
Emeritus Scientist
Inorganic & Physical Chemistry Division

डॉ. पी. एस. साई प्रसाद
अवकाश प्राप्त वैज्ञानिक
अकार्बनिक व भौतिक रसायनशास्त्र प्रभाग

CERTIFICATE

This is to certify that the research work presented in this thesis titled **"Studies on Modified Lanthanum Nickel Oxide Perovskite Catalysts for Dry Reforming of Methane"** submitted by **Mr. Tatiparthi Vikram Sagar** for the award of the degree of **Doctor of Philosophy in Chemistry,** to National Institute of Technology, Warangal (Telangana), is carried out under my guidance and supervision. This work has not been submitted earlier in part or full for any degree or diploma to this or any other university.

(P. S. SAI PRASAD)

Emeritus Scientist

Date:

Place: Hyderabad

CSIR – Indian Institute of Chemical Technology

Phone : (O)+91-40-27191497, (M) : 9177230595, Fax : +91-40-27160921
E-mail : saiprasad@iict.res.in pssaiprasad@gmail.com Website : www.iictindia.org

DECLARATION

I hereby declare that the research work presented in this thesis titled **"Studies on Modified Lanthanum Nickel Oxide Perovskite Catalysts for Dry Reforming of Methane"** is based on the results of the investigations and research work carried out by me under the supervision of Prof. I. Ajit Kumar Reddy, Department of Chemistry, National Institute of Technology, Warangal, India and Dr. P. S. Sai Prasad, Emeritus Scientist, I&PC Division, CSIR-IICT, Hyderabad, India. I declare that this work is original and has not been submitted in part or full, for any degree or diploma to this or any other university.

Date: 23-11-2017 **(TATIPARTHI VIKRAM SAGAR)**

Place: Warangal

ACKNOWLEDGMENTS

I wish to express my deep sense of gratitude and profound thanks to my research supervisors ***Prof. I. Ajit Kumar Reddy***, Department of Chemistry, National Institute of Technology, Warangal and ***Dr. P. S. Sai Prasad***, Emeritus Scientist, Inorganic & Physical Chemistry Division, CSIR–Indian Institute of Chemical Technology, Hyderabad, for their valuable guidance, unfailing attention, constant encouragement, inspiring and thought provoking discussions throughout the execution of research work embodied in this Ph.D. thesis. The research work in this thesis would not have seen the light of the day without their unrelenting support and cooperation. They have been a great source of motivation and inspiration. I have been able to learn a great deal from them and consider my association as a rewarding experience for me.

I express my sincere thanks and gratitude to ***Prof. N. V. Ramana Rao,*** Director, National Institute of Technology, Warangal for permitting me to utilize the facilities and allowing me to submit this research work in the form of a thesis. I whole-heartedly thank ***Dr. S. Chandrasekhar***, Director CSIR–Indian Institute of Chemical Technology, for providing me an opportunity to carry out my research work and for his kind support at every stage of this endeavor.

I express my sincere thanks to ***Dr. K. V. Gobi,*** Head, Department of Chemistry, National Institute of Technology, Warangal for his valuable help and support. My heartfelt thanks are due to ***Dr. K. S. Rama Rao***, Head, Inorganic & Physical Chemistry Division, for his constant encouragement during my stay in CSIR–Indian Institute of Chemical Technology.

I would like to express my gratitude to ***Prof. K. Laxma Reddy*** *and* ***Prof. P. Nageswara Rao,*** Doctoral Scrutiny Committee members, Department of Chemistry, National Institute of Technology, Warangal for their support and advice. I express my sincere thanks to ***Prof. M. K. Mohan,*** Head and Professor, Department of Metallurgical and Materials Engineering, National Institute of Technology Warangal and Doctoral Scrutiny Committee member for his unflinching moral support and inspiration.

I wish to express my thanks to ***Prof. A. Ramachandraiah, Prof. V. Rajeswara Rao, Dr. P. V. Srilaxmi, Dr. Vishnu Shanker and Dr. N. Venkatathri Narayanan,***

faculty members of the Department of Chemistry, NIT Warangal for their cooperation and encouragement. I express my sincere thanks to ***Dr. N. Lingaiah, Dr. B. David Raju***, ***Dr. K. V. R. Chary***, ***Dr. V. Durga kumari*** and ***B. Sreedhar*** Scientists, CSIR–Indian Institute of Chemical Technology, Hyderabad. I would like to express my deep sense of gratitude to ***Dr. C. V. V. Sathyanarayana,*** Senior principal Scientist, Catalysis Division, CSIR–NCL, Pune for allowing me to carry out a part of my research work in his laboratory.

I appreciate the cooperation rendered by my colleagues *Dr. K. Hari Prasad Reddy, Dr. A. Srihari Kumar, Dr. P. S. N. Rao, Dr. Ch. Ramesh, Dr. K. Upendar, Dr. C. V. Pramod, Dr. P. Sudarsanam, Dr. B. Mallesham, Dr. M. Surendar, Dr. B. Hari babu, Dr. V. Rekha, Dr. G. Raveendra, Dr. M. Suresh, Dr. M. Ravi Kumar, Dr. G. Saidhulu, Dr. V. Venkateswarlu, Dr. B. Rami Reddy, Dr. G. Parameswaram, Dr. M. Nookaraju, Dr. G. Srinivasarao, Mr. V. Phani Kumar, Mr. E. Hari Mohan, Mr. Ashathosh, Mr. Ch. Suman, Mr. D. Mallesh, Mr. A. Rajashekar, Mr. J. Md. Rafi, Mr. N. Raju, Mr. B. Srinivasa Rao, Mr. Ch. Manohar, Mr. Ismail, Mr. Thirupathi, and Mr. D. Padmakar* for their lively company, moral support, motivation, encouragement and help.

At this juncture today I dedicate my thesis to my parents and family members. My parents ***Sri. T. Koteswara Rao*****,** ***Smt. K. Saramma***, who with all their patience, prayers and faith in the almighty, waited all these long years to see me reaching this stage. Their blessings and care always gave me new zeal and enthusiasm to do something more with perfection. My sincere thanks goes to ***Mr. T. Vidya Sagar*** (brother)**,** ***Smt. P. Ramya*** (sister-in-law)**,** ***T. Rithwick Sagar*** (nephew), ***Mr. T. Vinod Sagar*** (brother)**,** ***Smt. G. Niveditha*** (sister-in-law)**,** and ***T. Ishitha Sagar*** (niece) who have been a source of relief while I am away from the work.

I thank ***Council of Scientific and Industrial Research*****,** New Delhi, India and ***Department of Science & Technology*****,** New Delhi, India for financial assistance in the form of a project and ***University Grants Commission,*** New Delhi, India in the form of Research fellowship.

(**Tatiparthi Vikram Sagar**)

Contents

List of Figures

P. No.

List of Tables

P. No.

Abbreviations

Å	Angstrom
θ	Theta
α	Alpha
β	Beta
γ	Gamma
δ	Delta
λ	Lambda
eV	Electron Volt
ml	Milli Litre
h	Hour
min	Minutes
ºC	Degree Centigrade
g	Grams
mg	Milli Grams
DRM	Dry Reforming of Methane
SRM	Steam Reforming of Methane
RWGS	Reverse Water Gas Shift
XRD	X-ray Diffraction
TPR	Temperature Programmed Reduction
FTIR	Fourier Transformed Infra Red
BET	Brunauer Emmett Teller
XPS	X-ray Photoelectron Spectroscopy

Abstract

The accumulation of greenhouse gases, particularly carbon dioxide and methane, in the Earth's atmosphere is making the survival of the mankind very difficult due to global warming. In the case of carbon dioxide, though its capture and sequestration (CCS) is one of the methods to decrease its effect, this methodology is highly energy consuming and technologically cumbersome. Instead, the utilization of CO_2 as a cheap C1 source for chemical production is found advantageous. Among the several methods suggested, dry reforming of methane (DRM) with CO_2 takes the lead, and has been exploited worldwide by many researchers.

DRM is a very difficult reaction due to its highly endothermic nature and it necessitates use of active catalysts that can withstand high reaction temperatures. Catalyst deactivation through coke formation and sintering is yet another serious problem hindering the deployment of DRM catalysts. Many side reactions such as reverse water gas shift (RWGS), methane decomposition and Boudouard reaction that may alter the syngas ratio also accompany DRM reaction. Noble metal catalysts containing Pt and Ru are good for the reaction, but they are expensive and their availability is limited. Supported Ni catalysts are better alternatives to the noble metal catalysts in terms of the above two factors. Even though, Ni/γ-Al_2O_3 shows high catalytic activity, the prevention of metal sintering is a major problem. Commercial scale development of this process suffers from several issues, such as high energy cost and ineffective catalysts which cannot resist sintering and coking. In place of normal supported catalysts, the structural oxides that can fix the Ni in their structure thereby preventing its sintering have shown good results. It has been observed that the redox and acidic properties of the catalysts should be thoroughly understood so as to identify the active and stable catalyst. Thermodynamic

considerations have promulgated the favorable operating parameters, such as pressure of 1 atmosphere, temperature around 900 °C and the CO_2/CH_4 ratio >1, to minimize carbon formation in the DRM reaction. However, from an industrial viewpoint, it is desirable to operate at lower temperatures and with a CO_2/CH_4 ratio near unity. Such an operation requires a catalyst that kinetically inhibits the carbon formation. Thus, new catalysts that can offer high reaction rates and also prevent net carbon deposition are necessary. A variety of Ni-based structural oxides such as spinels, perovskites and pyrochlores are prepared and studied for dry reforming of methane. A perovskite-type oxide ($ABB'O_3$) catalyst containing La, Ni and Al is shown to possess good activity and longer life. However, detailed studies explaining the nature of metals in the perovskite and its role in the catalyst activity and life are not available.

The main objective of the work presented in this thesis is to design and synthesize effective catalysts for dry reforming of methane. The most desirable catalyst for this reaction is the one with high dispersion (smaller particle size) and stability of active metal during high temperatures. It should also possess moderate acidity so as to resist coke formation. The scope of this study includes synthesis of the structural oxide $LaNiO_3$ (ABO_3) and its modification with Al, Ce and Zr in its B-site by two different methods; the sol-gel and the hydrothermal methods. The fresh catalysts are characterized by BET, XRD, TPR, FT-IR, XPS and H_2 chemisorption and NH_3-TPD analyses. The used catalysts are also characterized by the CHNS analysis for the estimation of coke formation. These catalysts were evaluated for dry reforming of methane at atmosphere and in the temperature range of 700-800 °C. The novelty of the study lies in fixing the active species in a predetermined structure, such as perovskite, solid solution and pyrochlore and study the suitability of the structure that provides the best performance of the catalyst.

Modification of $LaNiO_3$ with Al carried out by using two synthesis methods *viz.* sol-gel method and hydrothermal methods has shown the formation of trimetallic perovskite phase due to the incorporation of Al in the B-site of $LaNiO_3$. During the reduction of this phase, highly dispersed and low particle size of Ni has been achieved. It is also observed that the trimetallic phase enhances the thermal stability of the catalyst during the reaction at high temperature. Ce modification of $LaNiO_3$ has also been carried out by sol-gel and hydrothermal methods. This modification has changed the active metal environment in the catalysts. The formation of two forms of active phase has been observed; one $LaNiO_3$perovskite and the other, the Ce-Ni-O solid solution. Improved catalytic activity of the catalysts has been attributed to the predominance of the solid-solution phase due to increased mobile oxygen content and thereby increasing the resistance towards coke formation. In the case of Zr modified $LaNiO_3$ catalysts synthesized by sol-gel and hydrothermal methods, low Zr addition has led to the formation of bimetallic perovskite phase ($LaNiO_3$), whereas high Zr resulted in the formation of pyrochlore structure ($La_2Zr_2O_7$). The Ni incorporation into the bimetallic perovskite structure is highly dispersed and it displayed high catalytic activity. The deposition of Ni on the surface of pyrochlore has led to easy sintering and high coking, thereby decreasing the catalytic activity.

A thorough analysis of the results observed in this thesis has revealed that the structural and redox properties are highly dependent on Ni/M (M= Al, Ce, Zr) composition and the method of preparation. The formation of trimetallic perovskite phase in Al–modified $LaNiO_3$ catalysts offered higher conversions of CH_4 and CO_2 and syngas ratio than the pyrochlore and solid-solution containing catalysts for the DRM reaction.

*****

Chapter 1

Introduction

1.1. World energy utilization and its impact on the environment

The influence of industrial revolution of the past century has an immense impact on human civilization in terms of improved technology as well as transportation networks. However, there has been an undue exploitation of fossil fuels namely coal, oil, and natural gas [1]. The urge for the additional supply of energy has caused enormous damage to the environment. Tremendous rate of population growth also aided this destruction. A report by the International Energy Agency predicts 33% increase in the oil consumption by 2020, mainly used by automobiles in the world leading to high amount of pollutants released into the atmosphere. Also, there has been a doubt about the long term availability of the fossil fuels. At the same time there is an uncertainty about the cost of fossil fuels. A comparison of the world energy consumption in the form of various types of fuels over the period 1990 to 2038 (Figure 1.1) shows continuous increasing trend [2].

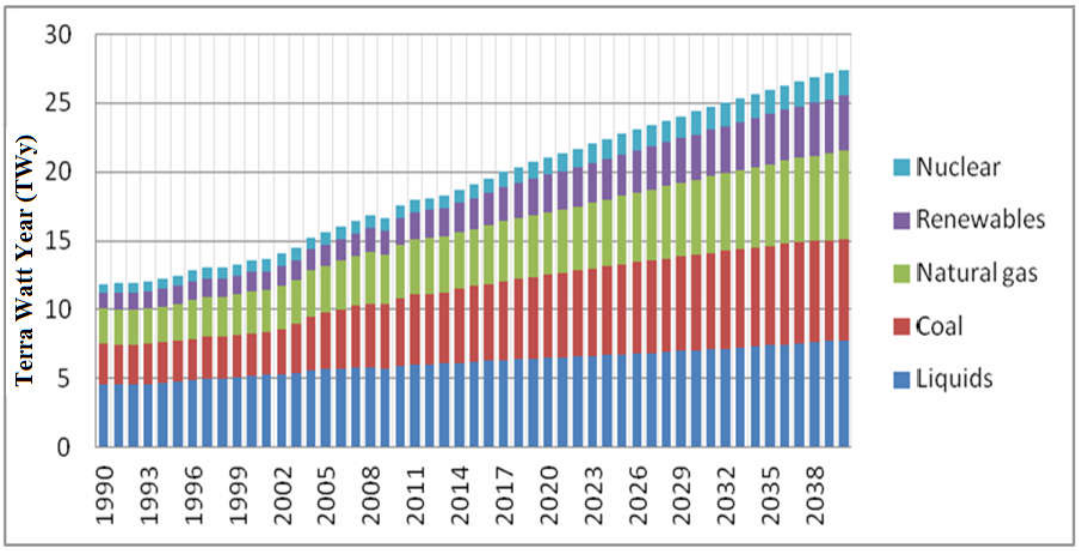

Figure 1.1: Trend in the world energy consumption during 1990–2038 [2].

Increasing demand for energy is driving the mankind to look for alternate resources. However, it is almost certain that the extent of availability of renewable fuels cannot match the demand for energy and the fossil fuels continue to be used at least for

the next few decades. Thus, the accumulation of the gaseous pollutants, especially the greenhouse gases in the atmosphere is going to continue.

1.2. Greenhouse gases

A gaseous compound that has the capability of absorbing radiation, trapping and holding heat in the atmosphere is called a greenhouse gas. A set of gases are found to be responsible for the increase in global warming and a consequential climate change. Important greenhouse gases are H_2O, CO_2, CH_4, N_2O, CFC–11, CFC–12, CFC–113, HCFC–22, HCFC–141b, HCFC–142b, CH_3CCl_3, CCl_4, HFC–125, HFC–134a, HFC–152a, HFC–23, SF_6, CF_4 (PFC–14) and C_2F_6 (PFC–116). Among these CO_2 and CH_4 have major influence on the environment.

Though the global warming potential of carbon dioxide (CO_2) is low, it is considered to be the most polluting gas because of its emissions in large quantities (about 35 billion tons per year). Figure 1.2 represents the extent of CO_2 emissions by different countries during the period 1990 and 2015 [3]. It can also be observed from the figure that major contributors for the emission of CO_2 into the atmosphere are China and USA.

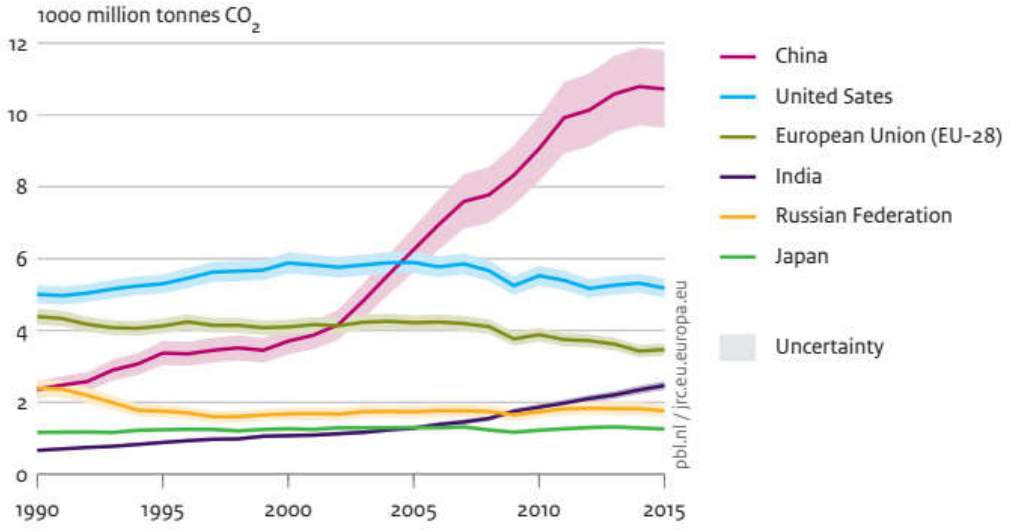

Figure 1.2: Emission of CO_2 by different countries during the period 1990–2015 [3].

Methane is also a major contributor to global warming. The extent of contribution of methane to global warming is 28 times as that of CO_2. Major sources of methane (CH_4) emission are both natural and anthropogenic. Bio–waste from living beings and emissions by oil and gas industry are considered as the major source [4]. Figure 1.3 shows the mean temperature rise of earth since 1880 due to global warming [5]. A close look at this figure reveals that the development of methods for controlling the accumulation of greenhouse gases, especially CO_2 and CH_4 are highly essential.

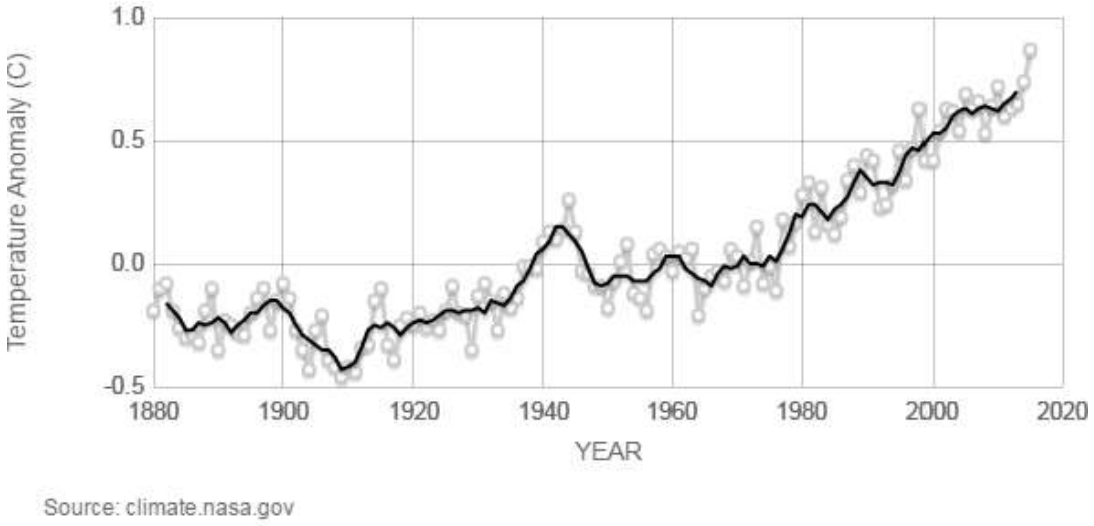

Figure 1.3: Mean temperature rise due to global warming since 1880 (circles represent the mean temperature rise by year and the dark line represents the 5 year mean temperature).

1.3. Processes to control CO_2 and CH_4 emissions

1.3.1. Applications of CO_2

CO_2 is being used in enhanced oil recovery, food industry, dry–cleaning equipment, refrigerators, air conditioners, fire–extinguishers and in processes such as separation techniques and water treatment. Application of CO_2 as a supercritical fluid has been in practice extensively because under supercritical conditions it has the advantages of gas–like diffusivities that improve reaction kinetics, and liquid–like densities that allow

for salvation of many compounds. This application is widely used in catalytic polymerization. However, CO_2 is a poor solvent for most of the high molar mass polymers. In nature, CO_2 is transformed into carbohydrate in enzymatic systems. CO_2 is used as a feedstock for chemical processes such as inorganic carbonates and pigments, additive to CO for the synthesis of methanol and production of urea. The extent of usage of CO_2 on account of all these applications is very small compared to the huge quantity of it being liberated [6].

1.3.2. CO_2 capture and sequestration

Carbon capture and sequestration (CCS) is an important philosophy that needs to be adopted on urgent basis. Among various methods for the separation of CO_2 from flue gases, absorption, adsorption, cryogenic separation are frequently mentioned. Absorption involves severe corrosion. Membrane separation is still in the laboratory investigation stage. Identification of an efficient, durable and cost–effective separation technique is necessary. So far, no suitable industrial technology is available in the world for the purpose of CCS.

For the sequestration of atmospheric CO_2, the following options are available (Figure 1.4): i) oceanic injection, ii) geological injection, and iii) scrubbing and mineral carbonation. The process of sequestration that involves long-term storage of the captured CO_2 gas has several technical difficulties, even though it is possible in theory. In order to inject CO_2 deep in the ocean, a pure stream of the gas is preferable. However, CO_2 injection has the disadvantage of harming the deep sea biota. Geological sequestration can consume industrial CO_2, but the cost is prohibitive and the arrest of leakages is a major issue. Transformation of CO_2 into geologically and thermodynamically stable mineral carbonates such as $CaCO_3$, $MgCO_3$ is a slow and expensive approach. Therefore,

utilization of CO_2 is a more attractive solution to solve CO_2 problems. Figure 1.4 illustrates various methods available for carbon sequestration [7].

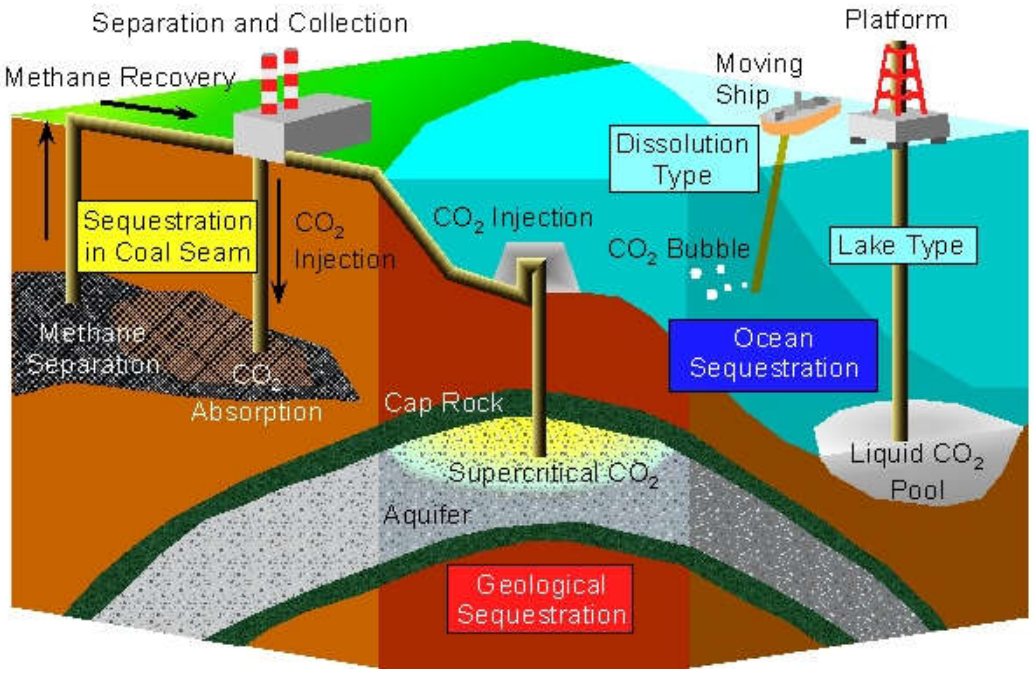

Figure 1.4: Methods available for carbon sequestration [7].

1.3.3. Strategies to control methane emissions

Some of the strategies of controlling methane emissions are as follows. Upgrading the equipment used to produce, store, and transport oil and gas can reduce many of the leaks that contribute to CH_4 emissions. Methane from coal mines can also be captured and used for energy production. In the agriculture front, methane can be reduced and also captured by altering manure management strategies at livestock operations or animal feeding practices. Capturing landfill CH_4 is an effective strategy to control its emissions. However, all these methods consume energy. Utilization of methane for producing value–added products is a better option.

1.4. Methane reforming to produce syngas

There are several methods for syngas production from methane. The following paragraphs briefly discuss the salient features of these methods.

1.4.1. Steam reforming of methane

Steam reforming of methane (SRM) is a commercial process (Eq. 1.1). It was first employed by Standard Oil of New Jersey in 1930. SRM suffers from severe limitations like high energy requirement, high H_2/CO product ratio and poor selectivity for carbon monoxide [8].

$$CH_4 + H_2O \rightarrow 3H_2 + CO \quad \Delta H° = 206.3\ kJ/mol \text{ --------- 1.1}$$

1.4.2. Partial oxidation of methane

Another method for syngas production is the partial oxidation of methane (POM) shown in equation 1.2. It is a better option compared to steam reforming, because of its greater selectivity to syngas production, exothermicity and more desirable H_2/CO ratio.

$$2CH_4 + O_2 \rightarrow 4H_2 + 2CO \quad \Delta H° = -35.6\ kJ/mol \text{ --------- 1.2}$$

Partial oxidation also has several disadvantages. The non-catalytic reaction must be operated at very high temperatures. The application of group VIII metal-based catalysts reduces the reaction temperature. However, a small decrease in CO selectivity results in a large increase in the reaction temperature. Under high methane conversions and at high space velocity, the reaction produces a large amount of heat in a small catalyst zone. This sort of hot-spot creation, particularly in a large reactor, is very hazardous and makes temperature control very difficult. Further, when Ni is used as a catalyst, it deactivates very fast because of carbon deposition.

1.4.3. Dry reforming of methane

A method of producing syngas by reacting carbon dioxide with methane is called dry reforming of methane (DRM). The reaction can be represented as.

$$CH_4 + CO_2 \rightarrow 2\,H_2 + 2\,CO \quad \Delta H° = 247.3\ kJ/mol \text{ --------- 1.3}$$

This reaction is highly endothermic and requires high reaction temperature for operation. The reaction utilizes two environmentally harmful gases, CO_2 and CH_4. The

reaction produces lower syngas ratio, which is very close to that required for Fisher–Tropsch synthesis. However, as DRM reaction is highly endothermic, the catalyst used for this reaction is susceptible to sintering and coking. On the other hand, the energy used for CO_2 reforming is same as that for steam reforming, but DRM utilizes CO_2 and SRM liberates CO_2. From the consideration of energy standpoint, this reaction is a good option for CO_2 utilization. Further, solar energy is also used for CO_2 reforming, which will continue to play an important role in syngas or hydrogen production and in energy storage [9,10].

1.4.4. Autothermal reforming of methane

This reforming reaction of methane utilizes two reformates, oxygen and carbon dioxide or steam to produce synthesis gas. The exothermicity of the partial oxidation is used to compensate the endothermicity of either dry reforming or steam reforming to produce desirable synthesis gas ratios.

The autothermal reforming of methane with CO_2 is represented as:

$$2CH_4 + {}^1/_2\, O_2 + CO_2 \rightarrow 4\, H_2 + 3\, CO \quad \text{--------- 1.4}$$

The autothermal reforming of methane with H_2O is represented as follows:

$$2CH_4 + {}^1/_2\, O_2 + H_2O \rightarrow 5\, H_2 + 2\, CO \quad \text{--------- 1.5}$$

In both the reactions syngas is the product but the ratio of the syngas is different. With steam, the produced syngas ratio is high. The hydrogen rich synthesis gas is further used for methanol production, ammonia synthesis, etc. In the CO_2 autothermal reaction the syngas ratio is ~1.33, which is a suitable feed ratio for higher hydrocarbon production by Fisher–Tropsch synthesis. Autothermal reforming requires less energy to start the reaction in the above reformates. By altering the space velocities of the feeds, the product ratio can be adjusted as necessary.

1.4.5. Tri reforming of methane

When the three reformates, CO_2, steam and O_2 are combinedly used with methane to produce synthesis gas, the reaction is called tri reforming of methane. In this reaction, the two endothermic reactions of methane can be combined together with the exothermic oxidation reaction to compensate the energy requirement. Product ratio can be altered by the ratio of reaction feeds. The tri reforming of methane can be expressed by the following equation:

$$3CH_4 + {}^{1}/_{2}\, O_2 + CO_2 + H_2O \rightarrow 7\, H_2 + 4\, CO \text{ --------- } 1.6$$

1.4.6. Applications of syngas

- Syngas is used in direct reduction of iron ore. The reduced iron or sponge iron is further used to produce wrought iron.
- Syngas is a major feed stock in the process of producing higher hydrocarbons like naphtha, petrol, diesel and wax by Fisher–Tropsch Synthesis which can be represented by the general equation:

$$(2n+1)\, H_2 + n\, CO \rightarrow C_nH_{(2n+2)} + n\, H_2O \text{ --------- } 1.7$$

  The ideal syngas ratio for this reaction to achieve higher hydrocarbon chain is ~1.8–2.1.

- Syngas is used in methanol synthesis plants across the world along with a purge of CO_2. The CO is more preferred to CO_2 during the methanol synthesis because, it requires less stoichiometry number of hydrogen, i.e. 2. Whereas, CO_2 requires stoichiometry number of hydrogen as 2.5–3.5. During the reaction, CO and CO_2 should be converted to the maximum extent to obtain the highest methanol yield [11]. Methanol synthesis is represented by the following equation:

$$CO + 2H_2 \leftrightarrow CH_3OH \quad \Delta H° = -90.8\, kJ/mol \text{ --------- } 1.8$$

- Methane production from syngas is another important process (Eq. 1.9). This process is possible with H_2 rich syngas. According to stoichiometry, three moles of H_2 and one mole of CO are required to produce one mole of methane. This reaction is an endothermic reaction [12].

$$CO + 3H_2 \leftrightarrow CH_4 + H_2O \quad \Delta H° = -206.2\ kJ/mol \text{ --------- 1.9}$$

1.5. The preference for dry reforming of methane

Dry reforming of methane is also referred to as "*CO_2 reforming of methane*". It was first carried out by Fischer and Tropsch in 1928 [13]. This reaction has several advantages. The low H_2/CO syngas ratio produced has higher energy efficiency in conversion to hydrocarbons. This highly endothermic reaction can be used in energy transfer from solar energy to chemical energy and energy storage in the form of H_2 and CO. When CO_2 is abundantly available, dry reforming becomes a promising industrial process.

Although the endothermicity of this process is very high, it produces synthesis gas with a lower H_2/ CO ratio than steam reforming. Low syngas ratios are suitable for the Fischer–Tropsch synthesis of long–chain hydrocarbons [14]. A major advantage of this process is that the reaction can be carried out with natural gas containing large amounts of CO_2, without the pre-separation. This process also acquires greater importance because it utilizes two global warming gases namely, CO_2 and CH_4 to produce value-added chemicals. Commercial scale development of this process suffers from several issues, such as high energy cost and ineffective catalysts which cannot resist sintering and coking.

The dry reforming reaction can be directly carried out using the following different sources: i) Flue gas released from power plants containing large amount of CO_2. ii) Landfill gas consisting of 50% CH_4 and 50% CO_2 iii) Natural gas containing a large

portion of CH_4 and iv) Industrial wastewater after digestion. The Calcor process is one such method developed to use CO_2–rich feedstock for the production of syngas [15]. But the nature of catalyst is a closely guarded secret. DRM reaction has not been commercialized yet mainly because of the disastrous nature of coking. Recently, there has been a renewed interest in this process because of the above mentioned potential industrial applications as well as protection of the environment. Focus on this reaction stems from the fact that the two–stage steam reforming–methanation cycle is being replaced by the one stage CO_2 reforming–methanation cycle [16,17], especially for the solar energy application.

1.5.1. Thermodynamic limitations of dry reforming of methane

The dry reforming of methane reaction is highly endothermic. It is carried out at atmospheric pressure and high temperatures. The reverse water–gas shift (RWGS) reaction always accompanies the main reaction. RWGS is represented by the following equation:

$$CO_2 + H_2 \rightarrow H_2O + CO \quad \Delta H^\circ = 41\ kJ/mol \text{ --------- } 1.10$$

DRM proceeds above 640 °C accompanied by the methane cracking reaction. Above 820 °C, RWGS reaction and the Boudouard reaction are favourable. Additionally, in the temperature range of 600–750 °C, at atmospheric pressure and when the CO_2/CH_4 feed ratio is 1:1, carbon formation is thermodynamically favourable by methane cracking or the Boudouard reaction. Therefore, excess CO_2 and lower temperatures are favourable for carrying out the dry reforming reaction efficiently. Water formation is possible in the dry reforming through RWGS reaction. RWGS reaction produces CO, thus making carbon formation highly feasible. Reaction temperature, pressure, initial reactant ratio and the content of inert gas influence the equilibrium conversion and the equilibrium product composition. For a given pressure, CO_2 conversion increases as the feed ratio decreases.

Supported Ru, Rh and Ni are found to be catalytically active for the DRM reaction. However, this process suffers from lower catalytic activity and high operating temperatures. Thus, there is a strong need for the development of efficient catalysts.

The dissociative adsorption of reactants is structure sensitive. Metal–support interactions and/or the participation of oxygen and –O–H species exist on the catalyst surface. A number of kinetic models have been proposed [18,19] to describe the DRM reaction: (1) reversible dissociation of CH_4 to CH_x and H_x species carried out on the metal, (2) dissociation of CO_2 on the support, (3) reaction of the CH_x species with adsorbed OH or mobile O created on the metal–support interfacial region to form CH_xO species and (4) breaking down of these species to form syngas [20].

1.5.2. The need for the development of new catalysts for dry reforming of methane

Thermodynamic considerations have promulgated the favourable operating parameters, such as pressure of 1 atmosphere, temperature around 900 °C and the CO_2/CH_4 ratio >1, to minimize carbon formation in the DRM reaction. However, from an industrial viewpoint, it is desirable to operate at lower temperatures and with a CO_2/CH_4 ratio near unity. Such an operation requires a catalyst that kinetically inhibits the carbon formation [7]. Thus, new catalysts that can offer high reaction rates and also prevent net carbon deposition are necessary.

1.6. Development of catalysts for dry reforming of methane

Three properties namely activity, selectivity, and stability of the catalysts are considered critical for the improvement of efficiency of dry reforming reaction. Supported noble metals (Ru, Rh, Ir, Pd, Pt) and non-noble metals (especially, Ni) have exhibited good catalytic performance (Table 1.1 in Page 17). In terms of stability, the noble metal catalysts are found to be much superior to non-noble metal catalysts by virtue of their higher carbon-free operation. Main drawbacks associated with noble metal

catalysts are their high cost and limited availability. The activity and selectivity of Ni catalysts are comparable to those of noble metals. Therefore, development of non-noble metal based catalysts particularly that of Ni which can inhibit carbon deposition during CO_2 reforming of methane, is very important.

Catalysts for high temperature processes of methane conversion should possess good thermal properties such as resistance to temperature shocks, long term stable activity, resistance to coke formation and high geometrical surface. Noble metal catalysts are less sensitive to carbon deposition. But their limited availability and high cost limit their utility in the reaction. Ni catalyst is commonly used because of its availability in large quantities and also in low price. Adaptability in a broad range of CO_2/CH_4 ratio, ease of loading, facile reduction, reasonable resistance to sulphur content in the feed and possibility for regeneration after coking are some more advantages of Ni catalyst. But the problems associated with Ni catalyst are: vulnerability for changes in the catalyst properties under heavy process conditions, i.e.: high temperature (800–900°C) and feed gas mixture. Further, there could be sintering of the active metal Ni in the catalysts. Some reactions taking place between catalyst components may lead to changes in the textural and mechanical strength. Small amount of additives, called promoters, introduced into the catalysts have significant influence on their textural properties, activity, selectivity and stability [21].

1.6.1. Influence of Ni particle size

It is observed that the catalytic activity during DRM reaction increases with decrease in Ni particle size. Combination of NiO with other metal oxides like MgO forms solid solutions which offer high activity and stability due to isolation effect. Reduction of NiO in such solid solutions and structural oxides delivers small Ni particles, which enhance the active metal surface area, thereby improving catalytic activity. Thus, it is

necessary to have detailed studies to exploit the advantages of solid solutions and structural oxides for catalytic purposes.

A reduction in energy consumption during DRM reaction can be achieved by identifying catalysts that operate at large volumetric hourly space velocity, while maintaining high conversions that yield larger syngas production per unit mass of catalyst. In DRM reaction, small particles of Ni can tend to resist the carbon deposition under severe reaction conditions, whereas in steam reforming of methane, excess steam is employed to limit carbon formation [22]. It has been reported that the nature of the support significantly influences the performance of the catalyst due to metal–support interactions, acid–base properties of the support materials, particle size of active metal and involvement of activation of CO_2. It is known that MgO, CeO_2, La_2O_3, and ZrO_2 interact favourably with nickel to inhibit carbon deposition on the catalyst [22,23].

1.6.2. Deactivation of Ni catalysts due to coke formation

Coke formation over Ni catalyst is a serious problem and it leads to rapid deactivation of the catalyst. Several efforts have been made to develop coke resistant catalysts with Ni supported on zeolites, perovskites, hexaaluminates, pyrochlores, montmorillonites, hydrotalcites and solid solution [23]. However, a catalyst which is effective and economical has not been discovered so far. Therefore, it is important to develop a coke resistant Ni–based catalyst.

Rare earth oxides, La_2O_3 and CeO_2, and transition metal oxides, ZrO_2 and Co_3O_4, have been used as promoters for suppression of carbon formation. Yang et al. used, CeO_2 to minimize carbon formation [24]. Although the mechanism of carbon suppression by the promoters is not known clearly, catalysts with smaller Ni particles and stronger adsorption of CO_2 can assist in decreasing the carbon formation. Xu et al. [25] reported that depending on Ni loading and calcination temperature, two kinds of Ni sites i.e., free

Ni sites and bound state Ni sites exist in supported Ni catalysts. The former is found to be responsible for carbon formation. Spinel catalysts, like $NiAl_2O_4$ result in bound state Ni sites which are highly active and resistant to coking and sintering. Promoters such as CeO_2 and ZrO_2 enhance the gasification of carbon formed on the catalyst surface due to their high oxygen storage capacity [26].

Zirconium oxide (ZrO_2) supported Ni catalyst was deactivated rapidly during DRM reaction due to carbon formation and the modification was pursued by adding support promoters for improved resistance to coking [27]. Dissociation of CH_4 and CO disproportion takes place on the Ni particles resulting in the production of H_2, CO_2, and carbon. The formed carbon then reacts with mobile oxygen, which is available in the support. The decomposition of CO_2 on the catalyst surface leads to regenerate the mobile oxygen.

Synthesizing coke resistant Ni catalysts for DRM reaction is a challenge even today. The mechanism of coke formation is fairly well understood. There are two principal coke formation pathways: (i) the methane decomposition (Eq. 1.11) and (ii) the disproportionation of CO or Boudouard reaction (Eq. 1.12).

$$CH_4 \rightarrow C + 2\,H_2 \quad \Delta H° = 74.9\,kJ/mol \qquad \text{--------- 1.11}$$

$$2\,CO \rightarrow CO_2 + C \quad \Delta H° = -172.2\,kJ/mol \qquad \text{--------- 1.12}$$

Although, the mechanism of the coke formation for DRM reaction is similar to steam reforming, the potential for the coke formation on Ni catalysts with CO_2 reforming is much higher. It is known that the decrease in Ni particle size has potential towards coke resistance in catalysts [28]. Small particles of Ni can be achieved by using a promoter, a change in the support, or the adjustments in the catalyst preparation. It is important to consider the synergy of size, morphology, structure and composition for the design and controlled preparation of Ni–based catalysts. The supporting materials with well defined

structures can be used as a source of small nickel particles. Additionally, a catalyst or support with basic properties promotes the reaction between CO_2 and carbon. This increases the coke resistance of the catalyst. A catalyst with redox promoters can enhance the coke resistance [29]. Moreover, strong interaction between nickel and the support significantly improves the coke resistance and also helps to reduce nickel sintering [28].

The coke resistance of the Ni based catalysts can be improved by enhancing the adsorption of CO_2 or by decreasing the rate and degree of methane activation and dissociation. Hu and Rukenstein observed that alkali or alkaline earth metal promoted catalysts enhance CO_2 adsorption over Ni catalysts [30]. The noble metal promoted catalysts possess high activity with excellent coke resistance [31]. Because of the high cost, noble metals are more suitable as promoters of the Ni–based catalysts. Addition of small amounts of noble metals to Ni catalysts can control the aggregation of Ni particles during the DRM reaction and hence lead to excellent coke resistance.

Researchers have explored the use of lanthanides as promoters for DRM reaction over Ni catalysts [32-35]. It is observed that, excellent redox properties and the oxygen storage capacity exhibited by ceria or ceria based materials significantly helps the oxidation of carbon formed on the surface. Ceria–based Ni catalyst shows strong metal–support interaction which helps the stabilization of the catalyst [32-35].

Method of preparation of catalyst has significant effect on its stability and activity. Most of the reported work on catalysts for DRM reaction is based on using catalysts prepared by conventional methods. Strong interaction between the metal and support created by suitable method of preparation makes the catalyst more resistant to sintering and coking, thereby enhancing its stability and activity.

1.6.3. Role of structured oxides

Materials with perovskite structure exhibit solid–state properties that make them useful as model catalysts. ABO_3 perovskite catalysts, in which the A–site cation is a rare earth and/or alkaline earth, and the B–site cation is a transition metal, are used as catalysts for CH_4 reforming. Perovskite oxide satisfies the stability requirement for the reforming reaction conditions [36]. Further, reduction of these perovskite oxide catalysts forms well dispersed and stable metallic particle. It is known that alkali earth or rare earth elements as promoters are effective in decreasing carbon deposition in DRM reaction [36]. Sintering of Ni in the metallic state can be prevented by dilution using a second metal such as Mn, Fe, Cu, or Al. Modification of $LaNiO_3$ perovskite oxide shows significant change in the Ni reducibility, stabilizes the structure under the reaction conditions and limits the migration of active Ni [37].

Literature reveals that solid solution supported Ni catalysts exhibit higher activity [9,38]. Solid solution catalysts also exhibit active metal particles of very small size, generated after the reduction of the catalyst. Compared to the bulk NiO, the reduction of NiO in the NiO–MgO solid solution is found to be more difficult, due to the isolation effect that restricts the formation of the metal–metal bond during the reduction [9]. It is observed that $Ce_xZr_{1-x}O_2$ solid solution supported Ni catalysts exhibit higher activity and coke resistance than ceria or zirconia supported Ni catalysts [38]. Corthals et al. have found that both CeO_2 and ZrO_2 promoted $Ni/MgAl_2O_4$ catalysts have good potential for catalyzing the DRM reaction [38].

Another commonly used structural oxide for dry reforming of methane is the pyrochlore type oxide. La–Zr pyrochlore structures are usually used for the DRM reaction with exchange of one or both cations. Ni substituted pyrochlore catalyst was synthesized by modified Pechini method [39]. This catalyst was tested for the bi–reforming reaction

with CO_2 and steam. The catalyst showed stable activity with time at temperatures ranging from 700–950 °C over a period of 170 h. It is found that smaller Ni particles contributing to high active surface area in Ni supported on pyrochlore have considerably improved the catalytic activity, stability and coke resistance under plasma treatment. However, exclusive research reports on the application of pyrochlore structures for the DRM reaction are scarce.

Thus, the design and preparation of coke resistant Ni catalysts is the key for further applications of CO_2 reforming of methane. The size, shape, structure, and surface composition of Ni particles have significant effect on the activity and coke resistance. Thus, the composition and the structure of the catalysts play a vital role in obtaining Ni particles of suitable size by means of reducing coke formation during the reforming reaction.

Table 1.1: Noble and Ni-based metal catalyst

Nobel Metal catalysts					
S.No.	Catalyst	CH_4 Conversion (%)	CO_2 Conversion (%)	H_2/CO Ratio	Reference
1	$Pt/\gamma\text{-}Al_2O_3$ Temp. 700 °C Pt-0.4%	66	76	0.68	40
2	$Ru/SrTiO_3$ Temp. 940 °C Ru-7%	99	94	0.9	41
3	Ru/ $Ce_{0.75}Zr_{0.25}O_2$ Temp. 900 °C Ru-3%	92	94	0.96	42
4	$Pt\text{-}CeO_2\text{-}ZrO_2/MgO$ Temp. 800 °C Pt-0.8%	79	87	n/a	43
5	$Ru/MgAlO_x$ Temp. 800 °C Ru- 2%	95	97	n/a	44
6	$Pt/MgAlO_x$ Temp. 800 °C Pt- 2%	76	84	n/a	44

Ni-Based catalysts					
S.No.	**Catalyst**	**CH_4 Conversion (%)**	**CO_2 Conversion (%)**	**H_2/CO Ratio**	**Reference**
1	Ni−1CeAl Ce/(Ce+Al)=1 Temp. 700 °C Ni-7%	68	70	1.04	45
2	Ni/ZrO_2 Temp. 600 °C Ru-5%	66	67	0.71	46
3	Ni/CeO_2 Temp. 600 °C Ni-5%	40	39	0.87	46
4	Ni/Mg/mesoporous Al Temp. 750 °C Ni-5%	60	73	1.25 (CO/H_2)	47
5	Ni/mesoporous Al Temp. 750 °C Ni-5%	78	88	1.25 (CO/H_2)	47
6	M-5Ni5Ca90Al Temp. 700 °C Ni-5mol%	78	81	0.8	48

1.7. Objectives of the thesis work

- To synthesize thermally stable and coke resistant catalysts, suitable for high temperature dry reforming of methane reaction.
- To study the performance of Ni based structured oxide catalysts for the dry reforming of methane.
- To synthesize the above type of catalysts by different methods in order to select the method that produces the most efficient catalyst.
- To carryout detailed characterization studies on the synthesized catalysts to determine their physico–chemical properties and understand their structure–activity relationships.
- To study the influence of incorporation of metals like Al, Ce and Zr in B–site of $LaNiO_3$ on phase transformations.

- To identify the changes associated with pre–reduction of catalyst in order to predict the nature of active species under reaction conditions.
- To understand the formation of bi or trimetallic perovskite oxide phases and their behavior in the dry reforming of methane reaction.
- To optimize the reaction conditions for the most promising catalyst for the dry reforming of methane.
- To carryout long term stability tests on the most efficient catalyst by estimating the coke formed on its surface.

1.8. Scope of the thesis work

Ni based catalysts were chosen for the dry reforming of methane. The B–site metal modification in $LaNiO_3$ perovskite was carried out by two methods, namely the sol-gel method and the hydrothermal method. In both the methods propionic acid was used as a solvent.

The physico–chemical characterization of calcined and used catalysts was carried out using the following techniques:

- Surface area was estimated with Brunauer–Emmett–Teller (BET) method using a Smart Sorb 92/93, India.
- Crystal structure properties were identified with Powder X–ray Diffraction using Rigaku Ultima IV, Japan.
- Reduction behavior of the catalysts was studied over homemade Temperature Programmed Reduction (TPR) unit.
- Identification of the oxidation states of the metals was carried out by X–ray Photoelectric Spectroscopy using KRATOS AXIS 165 instrument, UK.
- The dispersion of active metal (Ni) is estimated with H_2 chemisorption technique using homemade reactor setup.

- ✶ The amount of coke deposited on used catalysts was characterized by CHNS analyzer using Elementa V, Germany.

Evaluation of dry (CO_2) reforming of methane was carried out by using optimized reaction parameters by taking 0.5 g (SI units $5x10^{-4}$ Kg) catalyst diluted with the same amount of ceramic beads and a reaction mixture of CO_2, CH_4 and N_2 at a ratio of 80 ml flow of each, equalizing a total flow rate of 240 ml/min (SI units 14.4 l/h) with GHSV of 28,800 h^{-1} under atmospheric pressure.

1.9. Organization of the thesis

The thesis is divided into seven chapters.

Chapter 1: Introduction

This chapter narrates the circumstances leading to increased concentrations of greenhouse gases in the atmosphere, with particular reference to CO_2 and CH_4. The need for the conversion of these two gases into value–added products is stressed. The advantages of DRM over the other methodologies are discussed. The progress made in catalyst development is brought forward, particularly in Ni based structured oxide catalysts.

Chapter 2: Review of Literature

This chapter is initiated with a small introduction of different types of catalysts that are used for DRM reaction. A detailed review of literature on Ni–based structural oxide catalysts such as perovskite, pyrochlore and solid solution that are employed for DRM reaction is presented.

Chapter 3: Experimental

This chapter deals with the detailed procedures adopted for the synthesis of $LaNi_xM_{1-x}O_3$ (M = Al, Ce, Zr) catalysts. The general principles of various characterization techniques employed and the conditions under which the characterization data were acquired are discussed.

Chapters 4, 5 & 6: Results and Discussions

Chapter 4: Studies on Aluminium modified $LaNiO_3$ catalysts for CO_2 reforming of methane.

This chapter is divided into two sections namely Section 4.1 and Section 4.2.

Section 4.1 deals with Al modified $LaNiO_3$ catalysts synthesized by sol-gel method and Section 4.2 deals with Al modified $LaNiO_3$ catalysts synthesized by hydrothermal method.

Chapter 5: Studies on Cerium modified $LaNiO_3$ catalysts for CO_2 reforming of methane. This chapter is divided into three sections namely Section 5.1, Section 5.2 and Section 5.3.

Section 5.1 deals with Ce modified $LaNiO_3$ catalysts synthesized by sol-gel method, Section 5.2 deals with Ce modified $LaNiO_3$ catalysts synthesized by hydrothermal method and Section 5.3 is on Ni–Ce solid solution catalysts synthesized by sol-gel method.

Chapter 6: Studies on Zirconium modified $LaNiO_3$ catalysts for CO_2 reforming of methane. The influence of Zr modification of $LaNiO_3$ catalysts is discussed in two sections namely Section 6.1 and Section 6.2.

Section 6.1 deals with Zr modified $LaNiO_3$ catalysts synthesized by sol-gel method and Section 6.2 describes Zr modified $LaNiO_3$ catalysts synthesized by hydrothermal method.

Chapter 7: Summary and Conclusions

This chapter gives the summary of the entire thesis and the conclusions drawn from this work.

1.10. References

1. http://www.planetforlife.com/index.html
2. https://johnbrianshannon.com/2015/01/19/geopolitics-renewable-energy/
3. J. G. J. Olivier, G. Janssens-Maenhout, M. Muntean, J. A. H. W. Peters, Trends in Global CO_2 emissions: 2016 report, Editing PBL and EC-JRC, pp. 14
4. http://www.publicagendaarchives.org/charts/origins-greenhouse-gases
5. http://climate.nasa.gov/vital-signs/global-temperature/
6. Hu, Y. H. (2010). Advances in catalysts for CO_2 reforming of methane. In *Advances in CO_2 Conversion and Utilization* (pp. 155-174). American Chemical Society.
7. http://www.rite.or.jp/English/welcome/Project/sequestration/sequestration.html
8. Wang, S., Lu, G. Q., & Millar, G. J. (1996). *Energy & Fuels*, *10*, 896-904.
9. Liu, C. J., Ye, J., Jiang, J., & Pan, Y. (2011). *ChemCatChem*, *3*, 529-541.
10. Gokon, N., Yamawaki, Y., Nakazawa, D., & Kodama, T.(2010). *International journal of hydrogen energy*, *35*, 7441-7453.
11. http://www.supermethanol.eu/index.php%3Fid%3D21%26rid%3D12%26r%3Dmethanol_synthesis
12. Schaaf, T., Grünig, J., Schuster, M. R., Rothenfluh, T., & Orth, A. (2014). *Energy, Sustainability and Society*, *4*, 2.
13. Fisher, F., & Tropsch, H. (1928). *Brennst.-Chem.*, 3, 39.
14. Tsipouriari, V. A., Efstathiou, A. M., Zhang, Z. L., & Verykios, X. E. (1994). *Catalysis Today*, *21*, 579-587.
15. Corigliano, O., & Fragiacomo, P. (2015). *Fuel*, *158*, 538-548.

16. Fujimoto, K., Omata, K., Nozaki, T., Yamazaki, O., & Han, Y. (1992). *Energy Conversion and Management*, *33*, 529-536.

17. Wang, S., Lu, G. Q., & Millar, G. J. (1996). *Energy & Fuels*, *10*, 896-904.

18. Benguerba, Y., Dehimi, L., Virginie, M., Dumas, C., & Ernst, B. (2015). *Reaction Kinetics, Mechanisms and Catalysis*, *114*, 109-119.

19. Snoeck, J. W., Froment, G. F., & Fowles, M. (2002). *Industrial & Engineering Chemistry Research*, *41*, 4252-4265.

20. Valderrama, G., Goldwasser, M. R., de Navarro, C. U., Tatibouët, J. M., Barrault, J., Batiot-Dupeyrat, C., & Martínez, F. (2005). *Catalysis Today*, *107*, 785-791.

21. Borowiecki, T., & Ryczkowski, J. (2006). *Promoters of the catalysts for methane conversion into synthesis gases* (pp. 101-146). Nova Publishers (ISBN: 1-59454-810-2).

22. Roh, H. S., & Jun, K. W. (2008). *Catalysis Surveys from Asia*, *12*, 239-252.

23. Pakhare, D., & Spivey, J. (2014). *Chemical Society Reviews*, *43*, 7813-7837.

24. Yang, Y., Li, W., & Xu, H. (2002). *Reaction Kinetics and Catalysis Letters*, *77*, 155-162.

25. Xu, Z., Li, Y., Zhang, J., Chang, L., Zhou, R., & Duan, Z. (2001). *Applied Catalysis A: General*, *210*, 45-53.

26. Wang, H., & Zaidi, S., Suib, S. L. (Ed.). (2013). *New and future developments in catalysis: activation of carbon dioxide*. Newnes. (Chapter 15, http://dx.doi.org/10.1016/B978-0-444-53882-6.00016-4).

27. Li, X., Chang, J. S., Tian, M., & Park, S. E. (2001). *Applied Organometallic Chemistry*, *15*, 109-112.

28. Liu, C. J., Ye, J., Jiang, J., & Pan, Y. (2011). *ChemCatChem*, *3*, 529-541.

29. Huang, B., Li, X., Ji, S., Lang, B., Habimana, F., & Li, C. (2008). *Journal of Natural Gas Chemistry*, *17*, 225-231.

30. Hu, Y. H., & Ruckenstein, E. (2004). *Advances in Catalysis*, *48*, 297-345.

31. Yamaguchi, A., & Iglesia, E. (2010). *Journal of Catalysis*, *274*, 52-63.

32. Daza, C. E., Gallego, J., Mondragón, F., Moreno, S., & Molina, R. (2010). *Fuel*, *89*, 592-603.

33. Yang, R., Xing, C., Lv, C., Shi, L., & Tsubaki, N. (2010). *Applied Catalysis A: General*, *385*, 92-100.

34. Kambolis, A., Matralis, H., Trovarelli, A., & Papadopoulou, C. (2010). *Applied Catalysis A: General*, *377*, 16-26.

35. Gonzalez-Delacruz, V. M., Ternero, F., Pereñíguez, R., Caballero, A., & Holgado, J. P. (2010). *Applied Catalysis A: General*, *384*, 1-9.

36. Goldwasser, M. R., Rivas, M. E., Pietri, E., Pérez-Zurita, M. J., Cubeiro,M.L., Grivobal-Constant, A., & Leclercq, G. (2005). *Journal of Molecular Catalysis A: Chemical*, *228*, 325-331.

37. Khalesi, A., Arandiyan, H. R., & Parvari, M. (2008). *Chinese Journal of Catalysis*, *29*, 960-968.

38. Corthals, S., Van Nederkassel, J., Geboers, J., De Winne, H., Van Noyen, J., Moens, B., Sels, B., & Jacobs, P. (2008). *Catalysis Today*, *138*, 28-32.

39. Kumar, N., Roy, A., Wang, Z., L'Abbate, E. M., Haynes, D., Shekhawat, D., & Spivey, J. J. (2016). *Applied Catalysis A: General*, *517*, 211-216.

40. García-Diéguez, M., Pieta, I. S., Herrera, M. C., Larrubia, M. A., Malpartida, I., & Alemany, L. J. (2010). *Catalysis Today*, *149*, 380-387.

41. Gangurde, L. S., Sturm, G. S., Valero-Romero, M. J., Mallada, R., Santamaria, J., Stankiewicz, A. I., & Stefanidis, G. D. (2018). *Chemical Engineering and Processing-Process Intensification*, 127, 178-190

42. Chen, J., Yao, C., Zhao, Y., & Jia, P. (2010). *International Journal of Hydrogen Energy*, *35*, 1630-1642.

43. Yang, M., Guo, H., Li, Y., & Dang, Q. (2012). *Journal of Natural Gas Chemistry*, *21*, 76-82.

44. Tsyganok, A. I., Inaba, M., Tsunoda, T., Hamakawa, S., Suzuki, K., & Hayakawa, T. (2003). *Catalysis Communications*, *4*, 493-498.

45. Wang, N., Shen, K., Huang, L., Yu, X., Qian, W., & Chu, W. (2013). *ACS Catalysis*, *3*, 1638-1651.

46. Wolfbeisser, A., Sophiphun, O., Bernardi, J., Wittayakun, J., Föttinger, K., & Rupprechter, G. (2016). *Catalysis Today*, *277*, 234-245.

47. Arbag, H. (2018). *International Journal of Hydrogen Energy*, *43*, 6561-6574.

48. Xu, L., Song, H., & Chou, L. (2012). *ACS Catalysis*, *2*, 1331-1342.

Chapter 2

Review of Literature

Perovskite

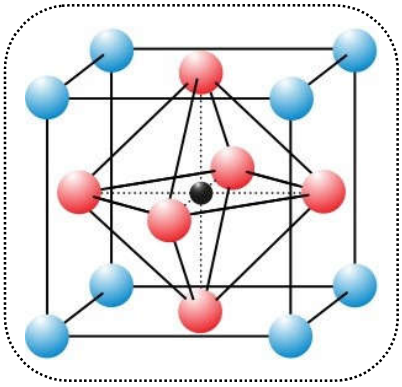

solid solution

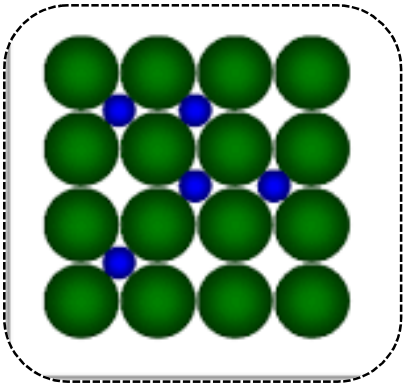

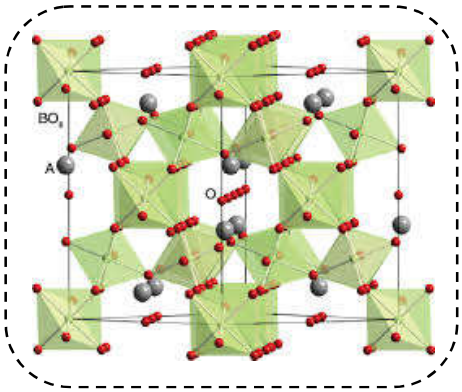

Pyrochlore

2.0. Introduction

In recent years, researchers have been attracted towards studies on dry reforming of methane (DRM) because it is a very important alternative to steam reforming for the production of syngas (H_2 and CO) and also it utilizes two potent greenhouse gases (CH_4 and CO_2). Stoichiometry of this reaction reveals that the product syngas is obtained at a ratio of unity (H_2/CO=1). This syngas ratio is more appropriate for obtaining valuable oxygenated chemicals and also as a major feed stock in Fischer–Tropsch synthesis. However, the endothermic nature of the reaction is a major drawback since it requires high operating temperature. Under typical conditions of dry reforming, the catalysts usually show deactivation due to coke formation and/or metal sintering. Thus, finding a catalyst that offers high stability and coke resistivity is a challenging task.

The activity of a catalyst depends on the nature of its support, the precursors used, the synthesis method adopted and the pretreatment methodology. Among a wide range of catalysts studied for DRM reaction, Ni based catalysts are found to yield excellent results under the non–noble metal catalyst category. Studies on Ni based catalysts have gained prominence because of the advantages associated with Ni, such as easy availability, high temperature resistivity and lower cost. Ni supported on simple oxides like Al_2O_3 [1-3], CeO_2 [4-6], ZrO_2 [7,8] and La_2O_3 [9] were studied initially. Mixed oxide supported Ni catalysts were also studied. They included Ni/Al_2O_3–ZrO_2 [10], CeO_2 and Fe_2O_3 doped Ni/Al_2O_3 [11, 12], Ni on CeO_2–ZrO_2 [13,14] and Ni/La_2O_3–ZrO_2 [15,16]. Spinel type oxides such as $NiAl_2O_4$ [17-20], Ni/$MgAl_2O_4$ [21,22] were tested for DRM reaction. Other structural oxides like perovskites, pyrochlores and solid solution type oxides were also investigated. A comparison of their performance is illustrated in Table 2.1 (Page 44). The following paragraphs bring forward the progress made in this direction.

2.1 Perovskite type oxides

$CaTiO_3$, a mineral discovered in 1839 by a Russian scientist Gustav Rose in the mountains of the Ural in Russia, was named after the Russian mineralogist Lev Perovski [23]. Its structure has a general formula ABO_3 (Figure 2.1). It is described in many ways with cubic close–packed layers of AO_3 surrounded by 'O' closely associated by the neighbors filled with the 'B' metal. The easiest way to understand the representation is by the corner shared BO_6 octahedral along with 12–coordinated site filled by A metal [24-26]. The perovskite oxide was found to possess not only versatile chemical composition but also enormous structural flexibility. The 'A' and 'B' metals can have various combinations and possibilities to ensure charge balance in the stoichiometric ABO_3 oxides. The commonly found formulations are $A^{1+}B^{5+}O_3$, $A^{2+}B^{4+}O_3$, and $A^{3+}B^{3+}O_3$. The ideal perovskite structure contains a larger 'A' cation having 12–fold coordination with oxygen and smaller 'B' cation occupying 6–fold coordination with oxygen. Structural defects or deviation in perovskite structure can be identified with the tolerance factor (**t**) defined as: $\mathbf{t = (r_A + r_O) / [\sqrt{2}\,(r_B + r_O)]}$. The tolerance factor for an ideal perovskite is 1. Solids with **t** lower than 1 change from cubic structure to distorted tetragonal, rhombohedral or lower symmetrical structures. On the other hand, $\mathbf{t} > 1$ leads to hexagonal structure due to higher ionic radii of A [27].

The regular perovskite oxides used for dry reforming contain lanthanides in A site and active metals in the B site. Promoters can be added in either A or B sites and also in both sites such that they can be expressed with general formulae: $ABB'O_3$, $AA'BO_3$ and $AA'BB'O_3$. Results of major studies carried out on these perovskite–type catalysts used for the DRM reaction are consolidated and presented below.

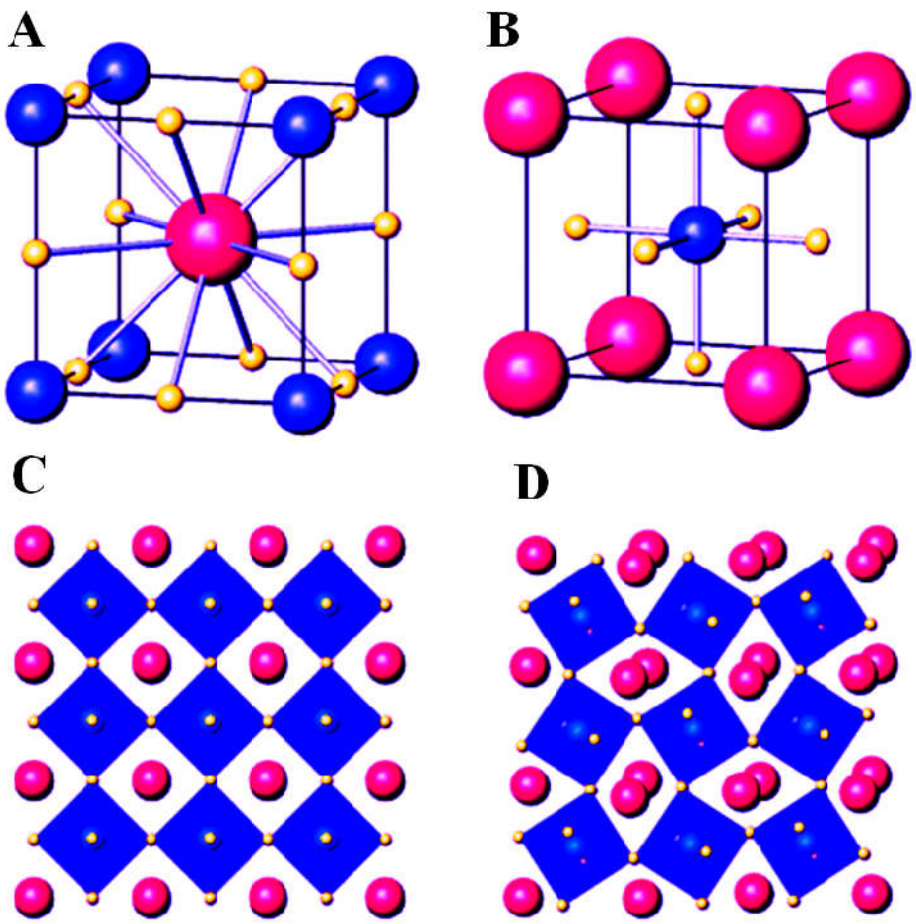

Figure 2.1: ABO_3 perovskite structures: A) cubic A unit cell, B) cubic B unit cell, C) polyhedral view of corner–shared BO_6 octahedral units for the highest symmetry cubic form and D) distorted polyhedral view of a perovskite (orthorhombic $GdFeO_3$ type) [24].

2.1.1. Perovskite type oxide catalysts used for DRM reaction

Pereniguez et al. [28,29] studied structural properties and catalytic performance of $LaNiO_3$ perovskite oxide synthesized by spray pyrolysis method. They confirmed the presence of perovskite phase through X–ray diffraction (XRD) studies. Although, XRD data did not show any sign of NiO phase, the coexistence of an amorphous NiO with crystallite $LaNiO_3$ phase was confirmed in the calcined sample with the X–ray absorption spectroscopy (XAS) and Temperature programmed reduction (TPR) studies. The perovskite phase was achieved partially by the re-oxidation of the reduced Ni/La_2O_3

catalyst, which indicated easy regeneration of the used catalyst. The catalyst was tested for different types of reforming reactions of methane with oxygen, water and CO_2. Results obtained were very promising with remarkable stability of the catalyst under DRM conditions. The performance of these catalysts was explained on the basis of high resistance of the nickel particles, as detected by *in situ* XAS analysis.

Parvary et al. [30] developed trimetallic $ABB'O_3$ type perovskite oxides prepared by sol-gel method. Formation of trimetallic perovskite phases $LaNi_xAl_{1-x}O_3$ ($0.1 \leq x \leq 0.9$) was clearly observed in their XRD patterns. Homogeneity of the prepared catalysts was identified by scanning electron microscopy and Energy dispersive X–ray spectroscopy studies (EDXS). These catalyst systems were found to be efficient for syngas production in the DRM reaction.

Gallego et al. [31] synthesized $LaNiO_3$, $LaNi_{1-x}Mg_xO_{3-\delta}$ and $LaNi_{1-x}Co_xO_{3-\delta}$ perovskite type oxide catalysts by auto–combustion method. TPR analysis revealed that Mg or Co containing catalysts were more difficult to reduce. In case of Co containing samples a decrease in catalytic activity was noticed. This was attributed to the Co–Ni alloy formation. Computational calculations showed that, degradation of C–H bond was active on Ni, while Co was not active for the methane cracking reaction.

Rivas et al. [32] synthesized several series of ternary metallic perovskite type oxides of $ABB'O_3$. It was observed that the method of preparation and the addition of dopant influence the catalytic performance. $LaNi_{1-x}Rh_xO_3$ perovskite type oxides were prepared by two different methods namely, sol-gel method using citric acid as solvent and co-precipitation method using K_2CO_3 as a precipitating agent. Reference sample, $LaNiO_3$, was prepared by the impregnation method using La_2O_3 with nickel nitrate solution. These catalysts were highly homogeneous. Crystal oxides with different particle sizes were observed depending on the synthesis method. Results obtained were interpreted in terms

of formation of variety of lanthanum phases like La_2O_3 and $LaNiO_3$ perovskite, during the reaction. It was further observed that the substitution of dopant Rh in small amounts in place of Ni improved the catalytic activity.

Vlach et al. [33] investigated $LaNi_xCu_{1-x}O_3$ (x = 0, 0.2, 0.5, 0.8, 1) catalysts by partially modifying Ni with active metal Cu. Perovskites were synthesized using NaOH and diethylenetriaminepentaacetic acid (DTPA). The catalytic activity increased with increase in Ni content. Characterization studies revealed that the improved activity for the reforming reaction was mainly due to the formation of Ni and Cu species with low particle size. The catalytic tests showed good conversions and selectivities.

Kapokova et al. [34] investigated the activity of $LnFe_{0.7}Ni_{0.3}O_{3-\delta}$ (Ln = La, Pr, Sm) perovskite catalysts synthesized by Pechini method. The catalyst performance was affected by the pretreatment method and the type of Ln cation used. Improved catalytic activity was attributed to the formation of Ni–Fe alloy particles formed in the perovskite lattice. $PrFe_{0.7}Ni_{0.3}O_{3-\delta}$ was observed as an active and stable catalyst due to the presence of non-segregated Ni–Fe alloy particles with efficient redox properties.

Lima et al. [35] prepared $ABB'O_3$ type $LaNi_{1-x}Fe_xO_3$ (x=0, 0.2, 0.4 and 0.7) perovskite type oxide catalysts to attain improved stability and resistance to carbon deposition during the DRM reaction. Appropriate combinations of preparation methods and calcination steps resulted in oxides with both structure and improved stability. Partially modified structural oxide catalysts were reported to be highly stable and $LaNi_{0.8}Fe_{0.2}O_3$ catalyst showed the highest catalytic activity.

Lima et al. [36] also studied La, Ce and Ni mixed oxides with molecular combinations of $La_{1-x}Ce_xNiO_3$ (exchanging A–site in ABO_3) prepared by sol–gel citrate method. XRD studies evidenced the formation of $LaNiO_3$ perovskite phase, which exhibited good activity and slow deactivation with time on stream in DRM reaction. The

A–site metal ion of the perovskite was modified with a tetravalent metal cation (Ce) resulting in increased catalytic activity as well as the stability of the catalysts. In high Ce containing catalysts, ceria appeared in a segregated CeO_2 phase inhibiting the perovskite phase formation. The insertion of Ce into the perovskite structure was possible at low Ce content. The incorporated cerium was not only responsible for the enhanced catalytic performance of the perovskite but also for the reduction of carbon deposition.

Lima et al. [37] also prepared $AA'BO_3$ perovskite–type ternary oxides with general formula $La_{1-x}Ca_xNiO_3$ by using citrate acid method. Addition of Ca in the perovskite not only stabilized the Ni particles but also improved the resistance towards coking. XRD patterns revealed the formation of spinel-type La_2NiO_4 and simple oxides (NiO and CaO) with perovskite phase were also observed. TPR and X–ray photoelectron spectroscopy studies revealed the segregation of NiO when x = 0. Results of activity tests of catalysts showed enhanced activity and stronger resistance to carbon deposition which was attributed to the replacement of La with Ca having lower ionic radius. However, resistance towards coking was found to be dependent on the Ca loading. The catalysts with x = 0.05 and 0.8 were found to be the most stable.

Gallego et al. [38] also prepared $AA'BO_3$ perovskite type oxide with $La_{1-x}A_xNiO_{3-\delta}$ (A = Pr, Ce) by auto–combustion method. Small particles of Ni were identified with the addition of promoters. Reduced catalysts showed improved results than the unreduced catalysts. Pr promoted $LaNiO_3$ perovskite showed the highest catalytic activity. Carbon deposition was not observed even after 100 h of reaction. The lower Ni^0 particle size and the redox property of praseodymium oxide (Pr_2O_3) were the main reasons for the highest catalytic activity. A simple mechanism was developed for Pr redox cycle: $Pr_2O_3 + CO_2 \rightarrow 2PrO_2 + CO$ and $2PrO_2 + C$ (CH_4 cracking) $\rightarrow Pr_2O_3 + CO$.

In Pr doped samples, increase in the doped metal content increased the resistivity towards carbon deposition.

Moradi et al. [39] studied the effect of the addition of alkali earth metals to the perovskite type oxides. XRD studies showed decrease in the active metal particle size by the addition of alkali metals in A–site. Promising results in catalytic activity and resistance to coke formation were observed with Ba having a composition of $La_{0.9}Ba_{0.1}NiO_3$ sample.

Valderrama et al. [40] used an auto– combustion method to prepare $La_{1-x}Sr_xNiO_3$ perovskite type oxides and evaluated them for DRM reaction at 700 °C and 1 atm. The reaction was studied by a pulse technique using CH_4/CO_2 ratio close to 1. XRD analysis of reduced perovskite catalysts showed the intermediate species, i.e., Ni^0, La_2O_3 and SrO. $LaNiO_3$ perovskite resulted in high activity among the catalysts prepared, while La_2NiO_4 phase was not active for the reforming. The results of catalytic activity over DRM reaction with Sr samples was found to be in the order $LaNiO_3$ > $La_{0.6}Sr_{0.4}NiO_3$ > Ni (5%)/La_2O_3 > $La_{0.9}Sr_{0.1}NiO_3$. In Sr doped catalysts, nickel remained as Ni^0 and the other two phases, $SrCO_3$ and $La_2O_2CO_3$ produced during the reaction facilitated the improvement of the regeneration of the La_2O_3 phase and decrease in carbon deposition.

The same group [41] conducted studies on $AA'BB'O_3$ perovskite type oxides having formulae $La_{1-x}Sr_xNi_{0.4}Co_{0.6}O_3$ and $La_{0.8}Sr_{0.2}Ni_{1-y}Co_yO_3$ prepared by sol-gel method. XRD patterns and cell parameter studies revealed the formation of La–Sr–Ni–Co–O solid solution with $La_{0.9}Sr_{0.1}CoO_3$ and/or $La_{0.9}Sr_{0.1}NiO_3$ phases in the catalysts. The catalysts showed improvement in the reducibility of Ni by the addition of Sr. Formation of Ni^0, Co^0 with small particle size over SrO and La_2O_3 phases were noticed. Formed metallic species were highly dispersed on the solid matrix, thereby

improving the activity. Addition of Sr also reduced carbon formation and promoted water-gas shift reaction to a small extent during the DRM reaction.

Pietri et al. [42] studied modified $LaA'Ru_{0.8}Ni_{0.2}O_3$ (A′= Sm, Nd, Ca) perovskite type catalysts prepared by polymerizable complex method using citric acid as solvent. Activity tests were conducted for the catalysts at 700 °C. Addition of promoter decreased the reduction temperature and increased the catalytic activity. Whereas, the small amount of addition of O_2 during the DRM reaction decreased its endothermic nature. Simultaneous oxidation and DRM reaction diminished coke formation on Ni and increased syngas production.

Khalesi et al. [43] studied the catalytic effect by modifying Ni with alkali metals like Li, Na and K in A–site of $LaNi_{0.3}Al_{0.7}O_3$ perovskite type oxide catalysts prepared by sol–gel method using propionic acid as a solvent. $M_xLa_{1-x}Ni_{0.3}Al_{0.7}O_{3-\delta}$ samples showed crystalline phase with well defined crystal structures. The addition of alkali metals to the catalysts increased the reduction temperature. These catalysts showed no deactivation even after 15 h of reaction. Catalysts promoted with low Li ($Li_{0.2}La_{0.8}Ni_{0.3}Al_{0.7}O_{2.8}$) showed better performance and less coke formation. In the Na series, $Na_{0.5}La_{0.5}Ni_{0.3}Al_{0.7}O_{2.5}$ catalyst showed high hydrogen yield, in the K series, $K_{0.5}La_{0.5}Ni_{0.3}Al_{0.7}O_{2.5}$ catalyst produced synthesis gas with H_2/CO ratio close to 1.

Khalesi et al. [44] studied the partial substitution of A–site by Ca and Sr. The mixed quaternary perovskite oxides with $Ca_xLa_{1-x}Ni_{0.3}Al_{0.7}O_{3-\delta}$ and $Sr_xLa_{1-x}Ni_{0.3}Al_{0.7}O_{3-\delta}$ (x = 0, 0.2, 0.5, 0.8, and 1.0; $\delta = 0.5x$) components were synthesized by sol-gel method. The characterization results revealed that fresh catalysts had the perovskite structure and exhibited small surface area in the range of 3.5 to 9.5 m^2/g. In Sr series samples, $Sr_{0.2}La_{0.8}Ni_{0.3}Al_{0.7}O_{2.9}$ catalyst showed excellent catalytic performance with syngas ratio

of 1, whereas in Ca series, $Ca_{0.8}La_{0.2}Ni_{0.3}Al_{0.7}O_{2.6}$ catalyst showed the lowest coke formation of nearly 0.71%.

Alvarez et al. [45] synthesized catalysts with perovskite–related mixed oxides of La–Ni–Nb and La–Sr–Ni–Nb by auto–combustion method. The XRD analysis confirmed the presence of $LaNiO_3$ perovskite phase and $LaNbO_4$ of Ruddlesden–Popper structure. It was shown that the structure alteration can be affected by Nb content. With the lower amounts of Nb ($x \leq 0.3$), Ni crystallized as $LaNiO_3$ perovskite–type oxide, while with the higher amounts of Nb ($x \geq 0.7$), mainly the orthoniobate phase of $LaNbO_4$ is formed. High temperature calcination showed Ruddlesden–Popper structure consisting of three perovskite type layers along the c–axis alternating with a layer of the rock salt phase. Transmission electron microscopy analysis revealed the presence of a cubic structure with particle sizes varying from 5 to 60 nm depending on the substitution of Nb. Reduction of the catalysts produced a series of $Ni^0/La_2O_3–NbO_x$ oxides, with the promoter having high active metal dispersion thereby improving the activity and stability of Ni. Another dopant Sr introduced into $LaNi_{0.8}Nb_{0.2}O_{3\pm\lambda}$ structure produced a mixture of oxides where Sr gets dissolved in the lanthanum orthoniobate ($LaNbO_4$) with Scheelite–type structure due to the similarity of ionic radii of La and Sr.

Sutthiumporn et al. [46] synthesized $La_{0.8}Sr_{0.2}Ni_{0.8}M_{0.2}O_3$ (where M = Bi, Co, Cr, Cu and Fe) perovskite catalysts by citrate sol-gel method. Among all the catalysts, the Cu doped Ni catalyst produced the highest initial catalytic activity. This was attributed to the highest amount of accessible Ni. C–H decomposition occurred preferentially on the mobile lattice oxygen species, thus resulting in significant improvement of catalytic activity. However, the Ni particles were agglomerated during the reaction and caused deactivation of catalysts. Fe substituted catalyst displayed low initial activities due to the lower reducibility of Ni–Fe phase and also less mobility of lattice oxygen species.

Fe substituted Ni catalyst showed highest stability due to strong metal–support interactions which completely resisted the sintering of Ni particles. The lattice oxygen species was highly active to react with CO_2 to form $La_2O_2CO_3$, hence the coking on the catalyst surface was removed to form CO.

2.2. Pyrochlore type oxides

Another commonly used structural oxide for dry reforming of methane is the pyrochlore oxide. The pyrochlore oxide has a general formula $A_2B_2O_7$, which can also be expressed as $A_2B_2O_6O'$ (Figure 2.2). The occurrence of this oxide was first described in 1826 in Stavern town in Larvik municipality, Norway. First discovered mineral pyrochlore contained Nb with other metals and has the general formula $(Na,Ca)_2Nb_2O_6(OH)$.

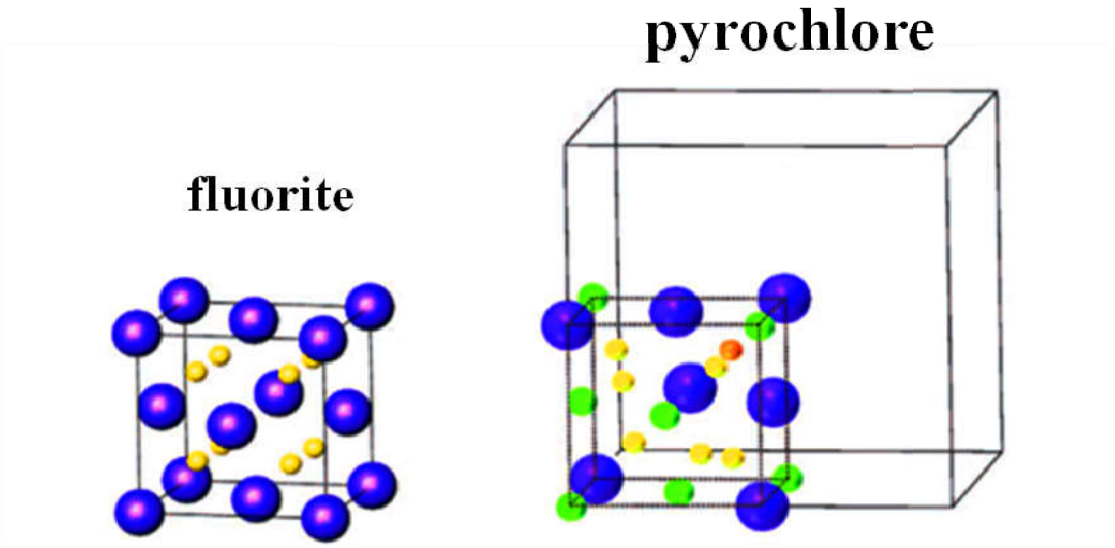

Figure 2.2: Structures depicting close relationship between fluorite and pyrochlore [24].

In a simple way, it can be understood by considering a defected fluorite structure with 1/8 of its anions removed in an ordered manner to create distorted 8 coordination number for one half of the cations and the regular octahedral model with 6 coordination number to other half of the cations. This ordering provides a distorted structure with new

dimensions which are about twice that of the regular fluorite structure. The ionic radius of A and B metals has significant effect on the structural properties of the ideal cubic pyrochlore (tolerance factor (**t**)) [47]. Most common oxidation states of A and B metal cations in the pyrochlore are $(A^{3+})_2(B^{4+})_2O_6O'$ and $(A^{2+})_2(B^{5+})_2O_6O'$. La–Zr pyrochlore structures are usually used for the DRM reaction with the exchange of one cation or both cations. The structures under this class are depicted below.

Ni substituted pyrochlore catalyst was synthesized by modified Pechini method [48]. 1 wt% Ni was doped into the pyrochlore structure ($La_2Zr_2O_7$). The catalyst was tested for the bi–reforming reaction with CO_2 and steam. The catalyst studied for two consecutive TPR/TPO spectra showed no change, indicating its stability at high temperatures and reversibility of the oxidation/reduction process of Ni. The catalyst showed stable activity with time at temperatures ranging from 700–950 °C over a period of 170 h. TPO of spent catalyst recorded after the reaction showed detectable but unquantifiable carbon deposition. The presence of steam in bi–reforming greatly limited the carbon deposition.

2.2.1. Pyrochlore type oxide catalysts used for DRM reaction

Peng et al. [49] studied $Ni/La_2Zr_2O_7$ pyrochlore catalysts synthesized by impregnation method and treated with plasma. The catalysts treated with plasma showed improved activity and coke resistance as compared to the untreated catalysts. The best performance was achieved on the H_2 plasma treatment before calcination. XRD and TEM studies showed decrease in Ni particle size after reduction. This treatment enhanced the metal dispersion and also interactions between Ni sites with support which were considered as main reasons for high catalytic activity.

Fang et al. [50] studied the dielectric barrier discharge plasma (DBD) treated catalysts ($Ni/Y_2Zr_2O_7$) prepared by impregnation method. The catalyst characterization

studies revealed that the plasma treatment enhanced the interaction between active phase (NiO/Ni) and the support pyrochlore ($Y_2Zr_2O_7$), thereby producing smaller NiO and Ni particles which contribute to high metallic Ni active surface area. This considerably improved the activity, stability and coke resistance of the catalysts. Atmosphere used during the plasma treatment played a vital role. H_2/Ar gas atmosphere was found to be the best condition to prepare Ni/$Y_2Zr_2O_7$. Smaller Ni particle size enhanced the metallic Ni active surface area during the plasma treatment accounting for the high performance of the Ni/$Y_2Zr_2O_7$ pyrochlore catalysts.

Fang et al. [51] later studied the $Y_2Zr_2O_7$ pyrochlore supports using a verity of synthesis methods: co–precipitation (CP), glycine–nitrate combustion (GNC) and hydrothermal (HT) methods with 10% Ni impregnation. These catalysts were tested for methane steam reforming using three supports consisting of pyrochlore phases with different morphologies, pore structures and surface area. The support prepared by hydrothermal method possessed the highest surface area (62.9 m^2/g). The reduction profiles suggested that, support prepared by GNC method had strong interaction with Ni active species and produced small Ni crystallites with enhanced metallic Ni active surface area. XPS results confirmed that this catalyst had Ni rich species. Catalysts prepared by GNC method exhibited high catalytic activity, stability and resistant to coke formation among other methods. They concluded that Ni rich surface played a vital role in activity and coke resistance during reforming reaction.

Gaur et al. [52] studied DRM reaction on multiple pyrochlore systems. Rh and Ni were partially substituted for B–site (Zr) in lanthanum zirconate ($La_2Zr_2O_7$) with 0.112, 2 wt% Rh and 0.112, 1 wt% Ni. All the pyrochlore catalysts showed cubic unit cell lattice in XRD. XPS studies predicted two oxide phases in Rh substituted (RhO_2 and Rh_2O_3) and Ni substituted (NiO and Ni_2O_3) catalysts. Two reducible species for Rh and

four reducible Ni species are observed in reduction studies. Activity results suggested that Rh substitution into the pyrochlore lead to more active and selective catalyst for syngas compared to Ni catalysts. The Ni based pyrochlore showed higher carbon deposition than Rh based pyrochlore. Further, Ca substitution on the A–site (La) along with Rh substitution on B–site in pyrochlore systems were also developed with empirical formula $La_{1.95}Ca_{0.05}Zr_{2-x}Rh_xO_{7-\delta}$ (x = 0.055, 1 wt% Rh). This resulted in increase in the surface area and pore volume. Addition of Ca showed lower carbon built–up. Characterization of used catalysts revealed that the pyrochlore structure was unchanged during the course of reaction. The lattice oxygen defects arose due to the replacement of Ca^{2+} for La^{3+}. This improved the oxygen mobility and also acted towards protection of active sites from carbonaceous deposits during the reaction. Substitution of these metals into pyrochlore decreased the bond energy of La–O and Zr–O, producing the mobile oxygen from the lattice.

Pakhare et al. [53] examined lanthanum zirconate ($La_2Zr_2O_7$) pyrochlores prepared by modified Pechini method. The B–site substitution was carried out with Ru (2.0 wt%) and Pt (3.78 wt%). Activation energies of Ru and Pt substitution on the B–site were determined (CH_4 = 14.5 ± 0.7, 36.5 ± 0.4 (Ru and Pt) and CO_2 = 11.5±0.8, 27.9±0.2 (Ru and Pt)). These results showed that both CH_4 and CO_2 reaction rates were much lower on Ru catalyst than Pt. The catalytic activity and stability was enhanced by Ru substitution. Further, they carried out kinetic modelling using 2 wt% Rh–substituted pyrochlore over DRM reaction [54]. This study suggested a dual–site mechanism, where CH_4 and CO_2 were activated on two different sites.

Recently, Weng et al. [55] prepared pyrochlore oxides of $La_2Ce_{2-x}Ni_xO_{7-\delta}$ and evaluated them for oxidative steam reforming of ethanol. Characterization studies revealed that Ni was incorporated into the pyrochlore structure. They also proposed that

the reduction behaviour and catalytic activity were directly related to the Ni content. The catalytic activity improved with the synergetic effect of cerium and nickel ions in the pyrochlore framework. The induced oxygen vacancies enhanced the carbon resistance.

2.3. Solid solution catalysts

A homogeneous mixture of two or more metals in solid state is known as a solid solution. The metal present in higher quantity is referred to as solvent and the metal present in lower quantity is called solute. Uniform distribution of these metals may be achieved by combining either metals in their molten state (at high temperature above their melting points) or dissolving the metals in a liquid followed by mixing and evaporation [56-58]. Solid solutions are of two types: i) Substitutional solid solution and ii) Interstitial solid solution.

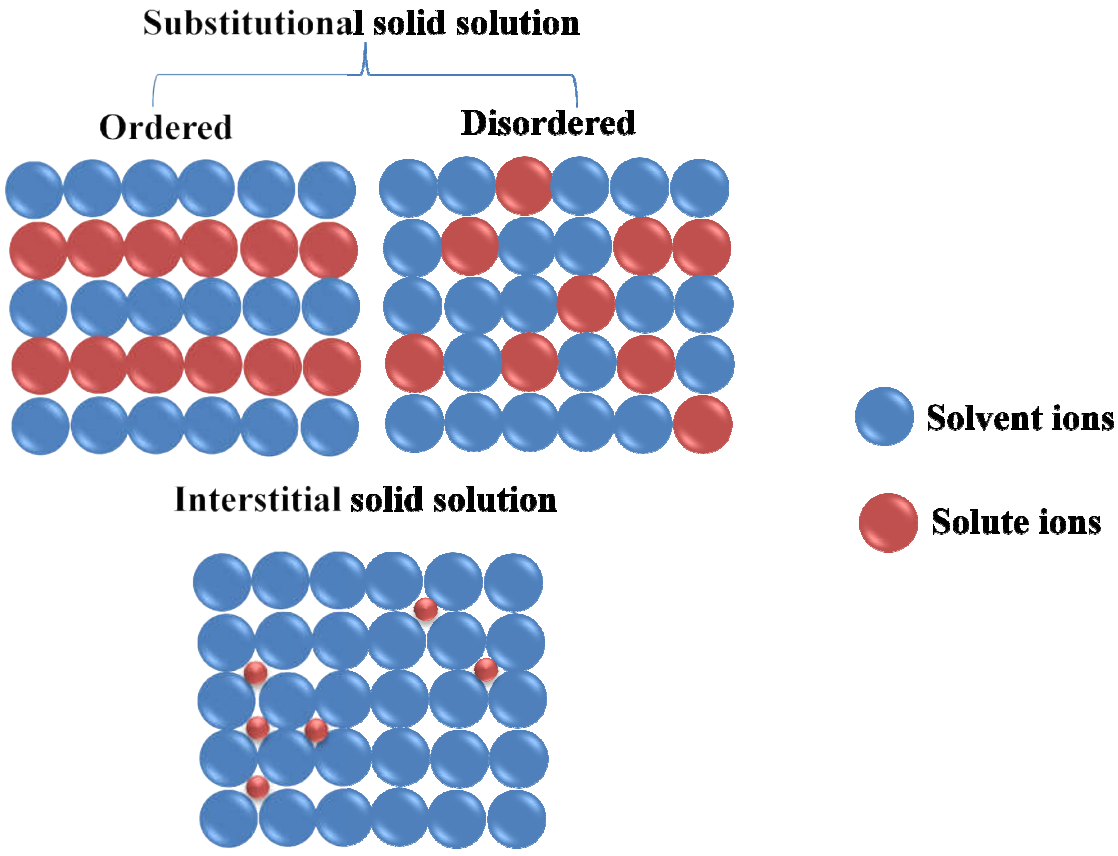

Figure 2.3: Schematic representation of different types of solid solutions.

In substitutional solid solution, solvent metal ions are replaced by the solute metal ions in their crystal lattice. Formation of these solid solutions without disturbing the parent crystal structure are termed as ordered substitutional solid solutions, whereas the substitution of solute ions with change in the crystal structure are called disordered substitutional solid solutions. In interstitial solid solution, the solute ions do not displace the solvent ions but they enter into the holes of interstitial spaces between the solvent ions. Schematic representation of different types of solid solutions is shown in Figure 2.3

The formation of solid solution leads to structural defects. Mobile oxygen generated during the solid solution formation enhances coke resistance during the reforming process. $Ce_{1-x}Zr_xO_2$ solid solutions have been studied extensively by researchers for dry reforming of methane. Natural mineral olivine group falls under this class [59]. Many researchers studied dry reforming of methane reaction using this mineral as catalyst [60-62]. Brief discussion on the use of metal oxide solid solution as catalysts for dry reforming of methane is presented below.

2.3.1. Solid solution catalysts used for DRM reaction

Kambolis et al. [63] investigated the catalytic performance of Ni catalysts supported on CeO_2–ZrO_2 (28–100% CeO_2 molar content, co_precipitation method) for the DRM reaction. The support exhibited improved textural properties that influenced the catalytic activity and thermal stability of the catalyst. X–ray diffraction analysis of the support confirmed the formation of $Ce_xZr_{1-x}O_2$ solid solution for all different ratios of Ce (28–100%). Considerable amount of lattice defects in the support were observed due to the modifications in the electronic environment around cations. CeO_2–ZrO_2 samples exhibited much higher catalytic activity as compared to lone ZrO_2 samples. This behavior was attributed to the increase in the active metal dispersion on the support. However, coke deposition was not directly related to the activity. Increase in ZrO_2 content in the

catalysts exhibited positive effect on the activity as well as resistance towards carbon deposition.

Montoya et al. [64] synthesized catalytic systems with Ni supported on ZrO_2 modified with CeO_2 (0, 1, 8 and 20 wt. %). The tetragonal phase of ZrO_2 was identified in XRD studies. The promoter CeO_2 avoids the low active monoclinic phase composition by the formation of solid solution with tetragonal ZrO_2. The Ni^{2+} ion competed with Ce^{4+} in the incorporation to ZrO_2 lattice. Sintering of Ni was minimized with the addition of ceria. Graphite carbon accumulation on active sites during the reaction did not play any role in the deactivation of the catalyst. Surface dispersion of Ni and the NiO reducibility improved with the addition of CeO_2.

Wolfbeisser et al.[65] studied the CeO_2–ZrO_2 mixed oxide catalysts prepared by different methods for DRM reaction. They concluded that the usage of surfactant results in the formation of Ce_Zr solid solution phase. The surfactant used in the synthesis process did not yield good results due to the encapsulation of active sites by the support species, whereas, solids prepared by co–precipitation method showed promising results in the DRM reaction.

Sadykov et al. [66] synthesized nano–crystalline CeO_2–ZrO_2 support doped with rare–earth (Gd, Pr, La) cations via adopted Pechini route and promoted with Pt metal by wet impregnation method. Synthesized catalysts were tested for oxygen mobility. Reactions of partial oxidation and DRM were carried out in diluted feeds. Catalytic activity was correlated with Pt dispersion and mobile oxygen phase suppressed coke formation.

Wang et al. [67] studied dry reforming reaction over Ir catalysts supported on ceria–based solid solutions. The doping of Pr or Zr oxide into ceria matrix produced more oxygen defects. This further improved the redox property and showed enhanced

metal–support interaction in $Ir/Ce_{0.9}M_{0.1}O_2$ (M = Pr, Zr) catalysts. These catalysts showed higher catalytic performance and better stability than the un–promoted (Ir/CeO_2) catalyst. Doping of Pr or Zr had shown positive effect on reducing Ir particles size, stabilizing the structure of catalyst and improving metal–support interaction.

Laosiripojana et al. [68] studied the effect of CeO_2 on Ni/Al_2O_3 catalysts for the DRM reaction. The catalyst showed enhanced catalytic activity and resistance towards coke deposition than the conventional Ni/Al_2O_3. These improvements were achieved due to the redox property of ceria. A combination of reactions, namely methane cracking on Ni sites and the CO formation with lattice oxygen (O_x) took place in DRM reaction on ceria surface. The reaction associated with the lattice oxygen played a vital role in suppressing the carbon deposition on active phase of the catalysts by methane decomposition reaction and Boudard reaction. The amount of addition of CeO_2 to Ni/Al_2O_3 was inversely proportional to the coke formation on the catalysts during the reaction. However, higher amounts of dopant addition resulted in oxidation of active phase, NiO. Spent catalyst studies revealed the existence of small amount of Ce_2O_3. The reaction rate increased with increasing methane partial pressure and the operating temperature.

Sahli et al. [17] prepared a spinel of Ni and Al by sol-gel method using propionic acid. Characterization of catalysts showed that the spinel phase is formed when stoichiometric ratio of Ni to Al is 0.5, whereas a solid solution is formed when the ratio is < 0.5. The spinel structure was achieved by change of Ni to Al ratio > 0.5. Addition of excess Ni provided bigger particles of NiO on the spinel phase. Under suitable reduction and reaction conditions Ni sintering was reduced during the course of reaction.

Torres et al. [69] studied the DRM reaction over $Ni_xMg_{1-x}O$ solid solution catalysts and achieved promising activity and stability of catalysts. Carbon accumulation

was suppressed by the Ni nanoparticles supported on MgO. These Ni particles were derived after the reduction of Ni–Mg solid solution. Resistance to carbon deposition and catalytic activity strongly depended on the morphology of the catalysts. Added metal particles generated oxygen vacancies. The active species inside the MgO matrix created Ni–O vacancy pair. By altering the active metal loading, the Ni–O vacancy pair segregation could be deferred. This was driven by the strong interaction between oxygen vacancies and Ni ions.

Zanganeh et al. [70] conducted a comparative study on different $Ni_xMg_{1-x}O$ solid solution catalysts. Inclusion of MgO improved the catalytic activity and coke resistance during the reaction. These catalysts had excellent anti–coking property. Authors also concluded that the catalysts with low Ni content had high dispersion of Ni species and nickel–support interaction. Synergistic effect developed between Ni and basic support is vital for improving the resistance to carbon formation.

Valderrama et al. [71] studied the effect of promoter addition to the B_site by Co in $LaNiO_3$ perovskite system synthesized by sol-gel method. XRD analysis confirmed the formation of $LaNiO_3$ and/or $LaCoO_3$ as main phases in the catalysts, depending on the degree of substitution. Detailed study on the intensity of the peaks and change in cell parameters from XRD revealed the formation of Ni–Co solid solutions. The catalysts were reduced before the start of the catalytic tests to obtain Ni^0, Co^0 and $La_2O_2CO_3$ active phases. These phases which remained during the reforming reaction were found to be responsible for the higher activity as well as inhibition of carbon deposition.

Bellido et al. [72] studied Ni supported ZrO_2 and Ca promoted ZrO_2 catalysts prepared by polymerization method with different loadings of promoter. The presence of the oxide precursor (NiO) and tetragonal phase of CaO–ZrO_2 solid solution were confirmed by the XRD studies. Different reduction patterns of NiO species were

identified by the TPR technique. They pointed out that these differences are mainly due to the change in the strength of interaction between active metal and supports of varying composition. The catalytic activity depended on the nature of $CaO–ZrO_2$ solid solution formed and its interaction with Ni metal.

Table 2.1: Structured catalysts used for DRM reaction.

Perovskite Catalysts					
S.No.	Catalyst	CH_4 Conversion (%)	CO_2 Conversion (%)	H_2/CO Ratio	Reference
1	$LaNiO_3$ Temp. 800 °C	30	41	0.39	36
2	$LaNi_{0.9}Mg_{0.1}O_{3-\delta}$ Temp. 700 °C	56	67	0.47	31
3	$LaNi_{0.9}Co_{0.1}O_{3-\delta}$ Temp. 700 °C	44	62	0.47	31
4	$LaNi_{0.8}Cu_{0.2}O_3$ Temp. 750 °C	74	90	0.83	33
5	$La_{0.95}Ce_{0.05}NiO_3$ Temp. 800 °C	46	59	0.39	36
6	$La_{0.7}Ca_{0.3}NiO_3$ Temp. 750 °C	78	81	0.64	37
7	$La_{0.8}Sr_{0.2}Ni_{0.8}Cu_{0.2}O_3$ Temp. 700 °C	88	86	n/a	46
8	$La_{0.8}Sr_{0.2}Ni_{0.8}Fe_{0.2}O_3$ Temp. 700 °C	85	86	n/a	46
Pyrochlore Catalysts					
S.No.	Catalyst	CH_4 Conversion (%)	CO_2 Conversion (%)	H_2/CO Ratio	Reference
1	Ni/La_2 Zr_2 O_7 -H_2P-C (Plasma treatment with H_2 presence before and after calcination) Temp. 700 °C Ni-6%	83	87	0.98	49
2	Ni/$La_2Zr_2O_7$-C –ArP (Plasma treatment with Argon after calcination) Temp. 700 °C	80	85	0.97	49

3	Ni-6% $Ni/Y_2Zr_2O_7$-H2/Ar-P (Plasma treatment with Hydrogen-Argon before calcination) Temp. 800 °C	90	91	n/a	50
4	Ni-10% La-Pt-Zr Temp. 625 °C Pt-3.78%	45 (10h)	60 (10h)	0.35 (10h)	53
5	La-Ru-Zr Temp. 625 °C Ru-2%	79 (10h)	82 (10h)	0.69 (10h)	53

Solid-solution Catalysts

S.No.	Catalyst	CH_4 Conversion (%)	CO_2 Conversion (%)	H_2/CO Ratio	Reference
1	Ni/CeO_2-ZrO_2 Temp. 600 °C Ni-5%	52	72	0.63	65
2	$Ni_{0.10}Mg_{0.90}O$ Temp. 700 °C	67	77	0.87	70
3	Ni/ ZrO_2- 8CaO Temp. 800 °C Ru-5%	90	89	0.79	71
4	Ni/28Ce-Zr Temp. 700 °C Ni-5%	39	52	n/a	63

2.4. Observations from review of literature on catalysts for DRM reaction

- Ni rich surfaces play a vital role in the activity and coke resistance of catalysts.
- CH_4 and CO_2 are activated on two different sites.
- Resistance to carbon deposition and catalytic activity strongly depends on the morphology of the catalysts.
- Decrease in the reduction temperature of the active metal oxide increases the catalytic activity.
- The structured oxides (Perovskites, pyrochlores, and solid–solutions) are mainly used either as precursors or catalysts because of their thermal resistance.

However, these oxides after pre–reduction, transform into metallic active phase (in this case Ni) supported on the non–reducible oxides.

- Trimetallic perovskites like $LaNi_xCu_{1-x}O_3$ led to the formation of small particles of Ni and in some cases the formation of Ni–Cu alloy also enhanced the activity. In the case of Ce inserted perovskites, the insertion of Ce is limited to low concentrations. Promoters like praseodymium oxide impart lower Ni^0 particle size and also increase in the redox property offering the highest catalytic activity. In the case of multiple substitutions, the cell parameter studies on the perovskites such as $La_{1-x}Sr_xNi_{0.4}Co_{0.6}O_3$ revealed the formation of La–Sr–Ni–Co–O solid solution with $La_{0.9}Sr_{0.1}CoO_3$ and/or $La_{0.9}Sr_{0.1}NiO_3$ phases in the catalysts. The catalysts show improvement in the reducibility and the formation of Ni^0 with small particle sizes over SrO and La_2O_3 phases. The formed metallic species are highly dispersed on the solid matrix, thus improving the activity.
- The nature of perovskite formed varies with the composition. For example, with the lowest amounts of Nb ($x \leq 0.3$), Ni crystallized as $LaNiO_3$ perovskite–type oxide, while for the high amount of Nb ($x \geq 0.7$) it forms mainly the orthoniobate phase of $LaNbO_4$. C–H decomposition undergoes preferentially on the mobile lattice oxygen species, formed after substitution.
- In the case of La based perovskites, the highest stability is achieved due to strong metal–support interactions which completely resist the sintering of Ni particles. The lattice oxygen species reacts with CO_2 to form $La_2O_2CO_3$, hence the coking on the catalyst surface is minimized by the formation of CO.
- The ionic radius of A and B metals show significant effect on the structural properties of the pyrochlore. In the case of Ni containing $La_2Zr_2O_7$ pyrochlore, stability at high temperatures and the oxidation/reduction process of Ni is found to

be reversible. The catalyst shows stable activity at 700–950 °C over a time period of 170 h with unquantifiable carbon deposition. The pyrochlore structure is unchanged during the course of reaction. Lattice oxygen defects arise due to the replacement of La^{3+} by other metal ions. These defects improve the oxygen mobility. Mobile oxygen acts as a protection for active sites from carbonaceous deposits during the DRM reaction.

- Formation of solid solution leads to structural defects of catalysts. Mobile oxygen generated during the solid solution formation enhances coke resistance during the reforming process. The support exhibits improved textural properties that influence the catalytic activity and thermal stability of the catalyst. The reaction associated with lattice oxygen plays a vital role in suppressing the carbon deposition on active phase of the catalysts.

This review of literature reveals the continued exploration to find suitable catalysts for the DRM reaction with enhanced anti–coking and resistance to sintering of active metal particles. Work presented in the following chapters is a step towards resolving these issues.

2.5. References

1. Juan-Juan, J., Roman-Martinez, M. C., & Illan-Gomez, M. J. (2009). *Applied Catalysis A: General*, *355*, 27-32.
2. Osaki, Toshihiko, and Toshiaki Mori. "The Catalysis of NiO-Al_2O_3 Aerogels for the Methane Reforming by Carbon Dioxide." *Advances in Science and Technology*. Vol. 45. Trans Tech Publications, 2006.
3. Newnham, J., Mantri, K., Amin, M. H., Tardio, J., & Bhargava, S. K. (2012). *International journal of hydrogen energy*, *37*, 1454-1464.
4. Odedairo, T., Chen, J., & Zhu, Z. (2013). *Catalysis Communications*, *31*, 25-31.
5. Laosiripojana, N., & Assabumrungrat, S. (2005). *Applied Catalysis B: Environmental*, *60*, 107-116.
6. Gonzalez-DelaCruz, V. M., Holgado, J. P., Pereñíguez, R., & Caballero, A. (2008). *Journal of Catalysis*, *257*, 307-314.
7. Rezaei, M., Alavi, S. M., Sahebdelfar, S., & Yan, Z. F. (2006). *Energy & Fuels*, *20*, 923-929.
8. Yajun Zhao, Xinmei Liu and Zifeng Yan (2004) *Preprints of Papers- American Chemical Society, Division of Fuel Chemistry*, *49*, 135-136
9. Verykios, X. E. (2003). *International Journal of Hydrogen Energy*, *28*, 1045-1063.
10. Therdthianwong, S., Therdthianwong, A., Siangchin, C., & Yongprapat, S. (2008). *International Journal of Hydrogen Energy*, *33*, 991-999.
11. Laosiripojana, N., Sutthisripok, W., & Assabumrungrat, S. (2005). *Chemical Engineering Journal*, *112*, 13-22.
12. Sivasangar, S., & Taufiq-Yap, Y. H. (2012). In *Advanced Materials Research* 364, 519-523.

13. Roh, H. S., Potdar, H. S., & Jun, K. W. (2004). *Catalysis Today*, *93*, 39-44.
14. Laosiripojana, N., & Assabumrungrat, S. (2005). *Applied Catalysis A: General*, *290*, 200-211.
15. Sokolov, S., Kondratenko, E. V., Pohl, M. M., Barkschat, A., & Rodemerck, U. (2012). *Applied Catalysis B: Environmental*, *113*, 19-30.
16. Bachiller-Baeza, B., Mateos-Pedrero, C., Soria, M. A., Guerrero-Ruiz, A., Rodemerck, U., & Rodríguez-Ramos, I. (2013). *Applied Catalysis B: Environmental*, *129*, 450-459.
17. Sahli, N., Petit, C., Roger, A. C., Kiennemann, A., Libs, S., & Bettahar, M. M. (2006). *Catalysis Today*, *113*, 187-193.
18. Pinheiro, A. L., Pinheiro, A. N., Valentini, A., Mendes Filho, J., de Sousa, F. F., de Sousa, J. R., da Graça C. R. M., Pascal B. & Oliveira, A. C. (2009). *Catalysis Communications*, *11*, 11-14.
19. de Sousa, F. F., de Sousa, H. S., Oliveira, A. C., Junior, M. C., Ayala, A. P., Barros, E. B., Bartolomeu C. V., Filho J. M. & Oliveira, A. C. (2012). *International journal of hydrogen energy*, *37*, 3201-3212.
20. de Sousa, H. S. A., da Silva, A. N., Castro, A. J., Campos, A., Josue Filho, M., & Oliveira, A. C. (2012). *International journal of hydrogen energy*, *37*, 12281-12291.
21. Guo, J., Lou, H., Zhao, H., Chai, D., & Zheng, X. (2004). *Applied Catalysis A: General*, *273*, 75-82.
22. Daza, C. E., Gallego, J., Mondragón, F., Moreno, S., & Molina, R. (2010). *Fuel*, *89*, 592-603.
23. https://en.wikipedia.org/wiki/Perovskite.

24. Modeshia, D. R., & Walton, R. I. (2010). *Chemical Society Reviews*, *39*, 4303-4325.

25. Bhalla, A. S., Guo, R., & Roy, R. (2000). *Materials Research Innovations*, *4*, 3-26.

26. Mitchell, R. H., (2002) *Perovskites Modern and Ancient*, Almaz Press, Thunder Bay, Ontario, (ISBN: 0968941109, 9780968941102).

27. Labhasetwar, N., Saravanan, G., Megarajan, S. K., Manwar, N., Khobragade, R., Doggali, P., & Grasset, F. (2015). *Science and Technology of Advanced Materials*, *16*, 036002.

28. Pereñíguez, R., González-DelaCruz, V. M., Holgado, J. P., & Caballero, A. (2010). *Applied Catalysis B: Environmental*, *93*, 346-353.

29. Pereñiguez, R., Gonzalez-delaCruz, V. M., Caballero, A., & Holgado, J. P. (2012). *Applied Catalysis B: Environmental*, *123*, 324-332.

30. Parvary, M., Jazayeri, S. H., Taeb, A., Petit, C., & Kiennemann, A. (2001). *Catalysis Communications*, *2*, 357-362.

31. Gallego, G. S., Batiot-Dupeyrat, C., Barrault, J., Florez, E., & Mondragón, F. (2008). *Applied Catalysis A: General*, *334*, 251-258.

32. Rivas, M. E., Fierro, J. L. G., Goldwasser, M. R., Pietri, E., Perez-Zurita, M. J., Griboval-Constant, A., & Leclercq, G. (2008). *Applied Catalysis A: General*, *344*, 10-19.

33. K. Vlach, D.-L. Hoang, M. Schneider, M.-M. Pohl, U. Armbruster, A. Martin, Physico-chemical characterisations and catalytic performance of Ni-based catalyst systems for dry reforming of methane DGMK Tagungsbericht (2012), 3(Preprints of the DGMK-Conference "Reducing the Carbon Footprint of Fuels and Petrochemicals", 2012), 195-201.

34. Kapokova, L., Pavlova, S., Bunina, R., Alikina, G., Krieger, T., Ishchenko, A., Rogov, V., & Sadykov, V. (2011). *Catalysis Today*, *164*, 227-233.

35. Lima, S. M., & Assaf, J. M. (2006). *Catalysis letters*, *108*, 63-70.

36. Lima, S. M., Assaf, J. M., Pena, M. A., & Fierro, J. L. G. (2006). *Applied Catalysis A: General*, *311*, 94-104.

37. Lima, S. M., Pena, M. A., Fierro, J. L. G., & Assaf, J. M. (2008). *Catalysis Letters*, *124*, 195, https://doi.org/10.1007/s10562-008-9484-7.

38. Gallego, G. S., Marín, J. G., Batiot-Dupeyrat, C., Barrault, J., & Mondragón, F. (2009). *Applied Catalysis A: General*, *369*, 97-103.

39. Moradi, G. R., & Rahmanzadeh, M. (2012). *Catalysis Communications*, *26*, 169-172.

40. Valderrama, G., Goldwasser, M. R., de Navarro, C. U., Tatibouët, J. M., Barrault, J., Batiot-Dupeyrat, C., & Martínez, F. (2005). *Catalysis Today*, *107*, 785-791.

41. Valderrama, G., Kiennemann, A., & Goldwasser, M. R. (2010). *Journal of Power Sources*, *195*, 1765-1771.

42. Pietri, E., Rivas, M. E., Goldwasser, M. R., Pérez-Zurita, M. J., Cubeiro, M. L., Leclercq, L., & Leclercq, G. (2004). *Preprints of Symposia - American Chemical Society, Division of Fuel Chemistry*, 49, 134.

43. Khalesi, A., Arandiyan, H. R., & Parvari, M. (2008). *Industrial & Engineering Chemistry Research*, *47*, 5892-5898.

44. Khalesi, A., Arandiyan, H. R., & Parvari, M. (2008). *Chinese Journal of Catalysis*, *29*, 960-968.

45. Alvarez, J., Valderrama, G., Pietri, E., Pérez-Zurita, M. J., de Navarro, C. U., Sousa-Aguiar, E. F., & Goldwasser, M. R. (2011). *Topics in Catalysis*, *54*, 170-178.

46. Sutthiumporn, K., Maneerung, T., Kathiraser, Y., & Kawi, S. (2012). *International journal of hydrogen energy*, *37*, 11195-11207.

47. Subramanian, M. A., Aravamudan, G., & Rao, G. S. (1983). *Progress in Solid State Chemistry*, *15*, 55-143.

48. Kumar, N., Roy, A., Wang, Z., L'Abbate, E. M., Haynes, D., Shekhawat, D., & Spivey, J. J. (2016). *Applied Catalysis A: General*, *517*, 211-216.

49. Peng, H., Ma, Y., Liu, W., Xu, X., Fang, X., Lian, J., Wang, X., Li, C., Zhou, W., & Yuan, P. (2015). *Journal of Energy Chemistry*, *24*, 416-424.

50. Fang, X., Lian, J., Nie, K., Zhang, X., Dai, Y., Xu, X., Wang, X., Liu, W., Li, C., & Zhou, W. (2016). *Journal of Energy Chemistry*, *25*, 825-831.

51. Fang, X., Zhang, X., Guo, Y., Chen, M., Liu, W., Xu, X., Peng, H., Gao, Z., Wang, X., & Li, C. (2016). *International Journal of Hydrogen Energy*, *41*, 11141-11153.

52. Gaur, S., Haynes, D. J., & Spivey, J. J. (2011). *Applied Catalysis A: General*, *403*, 142-151.

53. Pakhare, D., Shaw, C., Haynes, D., Shekhawat, D., & Spivey, J. (2013). *Journal of CO_2 Utilization*, *1*, 37-42.

54. Pakhare, D., Schwartz, V., Abdelsayed, V., Haynes, D., Shekhawat, D., Poston, J., & Spivey, J. (2014). *Journal of Catalysis*, *316*, 78-92.

55. Weng, S. F., Hsieh, H. C., & Lee, C. S. (2017). *International Journal of Hydrogen Energy*, *42*, 2849-2860.

56. https://www.britannica.com/science/solid-solution.

57. http://www.newagepublishers.com/samplechapter/000627.pdf.

58. Yonggang, W., Hua, W., Kongzhai, L., Xing, Z., & Yunpeng, D. (2010). *Journal of Rare Earths*, 28(spl. Issue), 357-361.

59. https://www.britannica.com/science/solid-solution.

60. Courson, C., Udron, L., Świerczyński, D., Petit, C., & Kiennemann, A. (2002). *Catalysis Today*, *76*, 75-86.

61. Courson, C., Udron, L., Petit, C., & Kiennemann, A. (2002). *Science and technology of Advanced Materials*, *3*, 271-282.

62. Courson, C., Makaga, E., Petit, C., & Kiennemann, A. (2000). *Catalysis Today*, *63*, 427-437.

63. Kambolis, A., Matralis, H., Trovarelli, A., & Papadopoulou, C. (2010). *Applied Catalysis A: General*, *377*, 16-26.

64. Montoya, J. A., Romero-Pascual, E., Gimon, C., Del Angel, P., & Monzon, A. (2000). *Catalysis Today*, *63*, 71-85.

65. Wolfbeisser, A., Sophiphun, O., Bernardi, J., Wittayakun, J., Föttinger, K., & Rupprechter, G. (2016). *Catalysis Today*, *277*, 234-245.

66. Sadykov, V., Muzykantov, V., Bobin, A., Mezentseva, N., Alikina, G., Sazonova, N., Sadovskaya, E., Gubanova, L., Lukashevich, A., & Mirodatos, C. (2010). *Catalysis Today*, *157*, 55-60.

67. Wang, F., Xu, L., Yang, J., Zhang, J., Zhang, L., Li, H., Zhao, Y., Li, H. X., Wu, K., Xu, G. Q., & Chen, W. (2017). *Catalysis Today*, *281*, 295-303.

68. Laosiripojana, N., Sutthisripok, W., & Assabumrungrat, S. (2005). *Chemical Engineering Journal*, *112*, 13-22.

69. Torres, D., & Liu, P. (2012). *Catalysis letters*, *142*, 1211-1217.

70. Zanganeh, R., Rezaei, M., & Zamaniyan, A. (2013). *International Journal of Hydrogen Energy*, *38*, 3012-3018.

71. Valderrama, G., Kiennemann, A., & Goldwasser, M. R. (2008). *Catalysis Today*, *133*, 142-148.

72. Bellido, J. D., De Souza, J. E., M'Peko, J. C., & Assaf, E. M. (2009). *Applied Catalysis A: General*, *358*, 215-223.

Chapter 3

Experimental

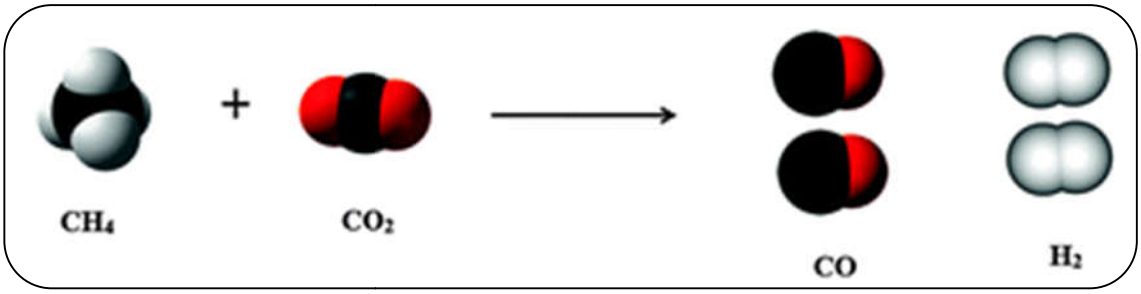

3.0. Introduction

This chapter describes the methods of synthesis, characterization and catalytic evaluation of $LaNi_xM_{1-x}O_3$ catalysts used in this thesis work. Details of procedure adopted for the synthesis of catalysts by sol-gel method and hydrothermal method are also discussed. Since characterization of catalysts is an essential part of catalysis research, basic principles and experimental procedures of characterization techniques are presented in this chapter.

The experimental details on Thermogravimetric Analysis (TGA), Determination of Specific Surface Area (N_2 adsorption–desorption by BET method), Powder X–ray Diffraction (XRD), H_2–Temperature Programmed Reduction (H_2–TPR), Fourier Transform Infrared Spectroscopy (FT–IR), Temperature Programmed Desorption of Ammonia (NH_3–TPD), X–ray Photoelectron Spectroscopy (XPS), Raman Spectroscopy, Carbon Analysis and H_2–Pulse Chemisorption are discussed. The details of actual equipment used and the conditions under which the data were collected are narrated. Further, the detailed procedure adopted for evaluation of catalysts in DRM reaction and the methodology followed in obtaining the product composition is also presented.

3.1. Materials and methods

3.1.1. Reagents

The metal nitrate precursors and solvent used in the synthesis of catalysts were Lanthanum nitrate hexahydrate, $La(NO_3)_3 \cdot 6H_2O$ (SD fine, India, 99.99%); Nickel nitrate hexahydrate, $Ni(NO_3)_2 \cdot 6H_2O$ (SD fine, India, 99.99%); Cerium nitrate hexahydrate, $Ce(NO_3)_3 \cdot 6H_2O$ (SD fine, India, 99.99%); Aluminium nitrate nonahydrate, $Al(NO_3)_3 \cdot 9H_2O$ (SD fine, India, 99.99%); Zirchonyl nitrate hydrate, $ZrO(NO_3)_2 \cdot xH_2O$ (SD fine, India, 99.99%) and solvent Propionic acid, $C_3H_6O_2$ (SD fine, India, 99.98%).

3.1.2. Synthesis of catalysts

The following series of catalysts are synthesized by sol-gel and hydrothermal methods

Series 1: ***$LaNi_xAl_{1-x}O_3$ (Sol-gel method)***

Series 2: ***$LaNi_xAl_{1-x}O_3$ (Hydrothermal method)***

Series 3: ***$LaNi_xCe_{1-x}O_3$ (Sol-gel method)***

Series 4: ***$LaNi_xCe_{1-x}O_3$ (Hydrothermal method)***

Series 5: ***$Ni_xCe_{1-x}O_2$ (Sol-gel method)***

Series 6: ***$LaNi_xZr_{1-x}O_3$ (Sol-gel method)***

Series 7: ***$LaNi_xZr_{1-x}O_3$ (Hydrothermal method)***

(where, x = 0 to 1 with an increment of 0.2)

3.1.2a. Synthesis of catalysts by sol-gel method

The perovskite–type oxides with general formula $LaNi_xM_{1-x}O_3$ (M= Ce, Al and Zr) are synthesized by sol-gel method with x values varying from 0 to 1 with a 0.2 step-wise increment. The amounts of the respective nitrate salts (Lanthanum nitrate, Nickel nitrate and Cerium nitrate or Aluminium nitrate or Zirconyl nitrate) necessary for each x value ($0 \leq x \leq 1$) were calculated and these metal nitrates were dissolved separately in hot propionic acid. The resulting nickel propionate solution and cerium propionate or aluminium propionate or zirconium propionate solutions were mixed together and each of these mixtures was instantly added to the lanthanum propionate solution. After 30 min of vigorous stirring the resulting solutions were subjected to reflux for 24 h and then the paste obtained in each case was dried under reduced pressure until the formation of the corresponding resin. In some cases, the concentration of the solution led to nitrate decomposition, producing nitrogenous vapours followed by the gel formation. The resulting solids were oven dried and calcined at 800 °C, with a temperature ramp of

2 °C/min, and maintained at the same temperature for 4 h. Figure 3.1 shows a pictorial representation of sol-gel method employed for synthesizing $LaNi_xM_{1-x}O_3$ catalysts.

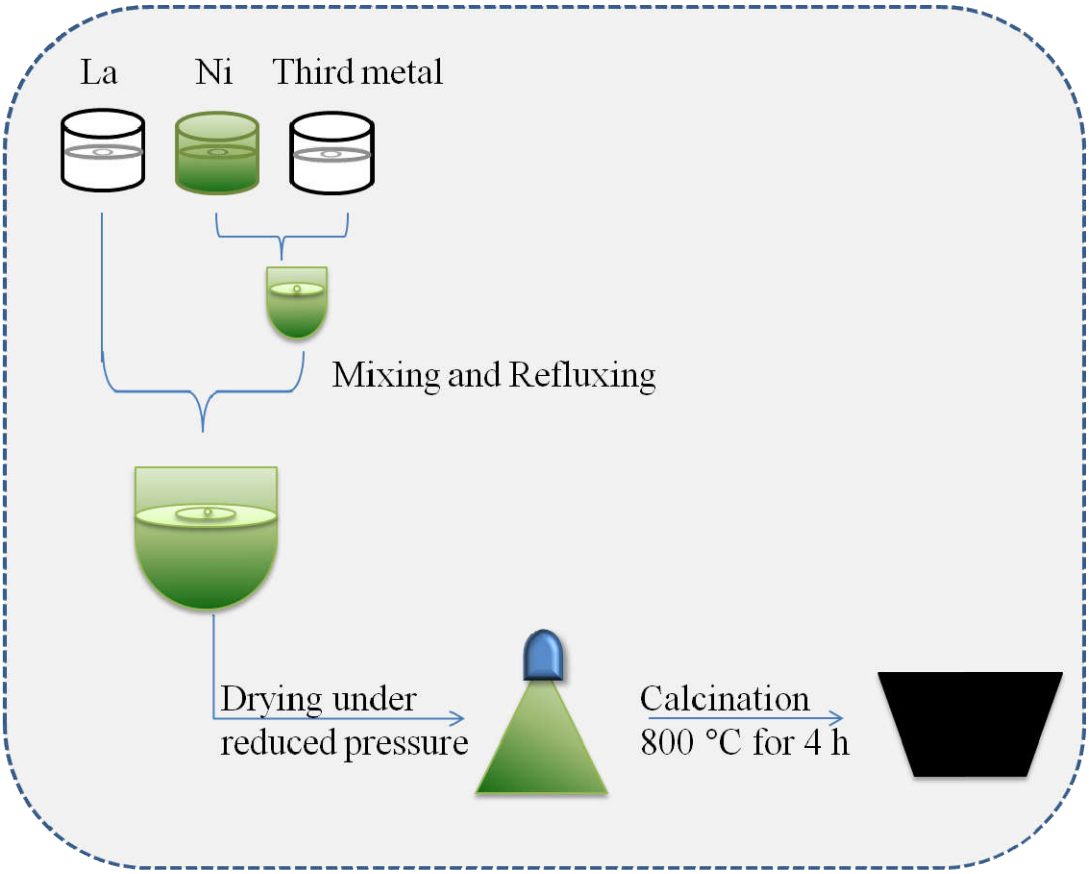

Figure 3.1: Pictorial representation of synthesis of $LaNi_xM_{1-x}O_3$ (M= Ce, Al, Zr) catalysts by sol-gel method.

3.1.2b. Synthesis of catalysts by hydrothermal method

$LaNi_xM_{1-x}O_3$ (M=Ce, Al, Zr) perovskite type oxide systems were also synthesized by hydrothermal method with x values varying from 0 to 1 with 0.2 step-wise increment. Calculated amounts of Lanthanum nitrate, nickel nitrate and cerium or aluminium or zirconyl nitrate salts corresponding to each x value were separately dissolved in hot propionic acid. The nickel propionate and cerium propionate or aluminium propionate or zirconium propionate solutions were first mixed and then to each of these mixed solutions lanthanum propionate solution was added. After vigorous stirring for 30 min, the resulting

solutions were placed under reflux for 24 h and then each of these solutions was transferred to separate autoclaves for hydrothermal treatment. The resulting masses were dried under reducing pressure and finally calcined at 800 °C for 4 h, with ramping of 2°C/min. Figure 3.2 depicts a pictorial representation of hydrothermal method employed for the synthesis of $LaNi_xM_{1-x}O_3$ catalysts

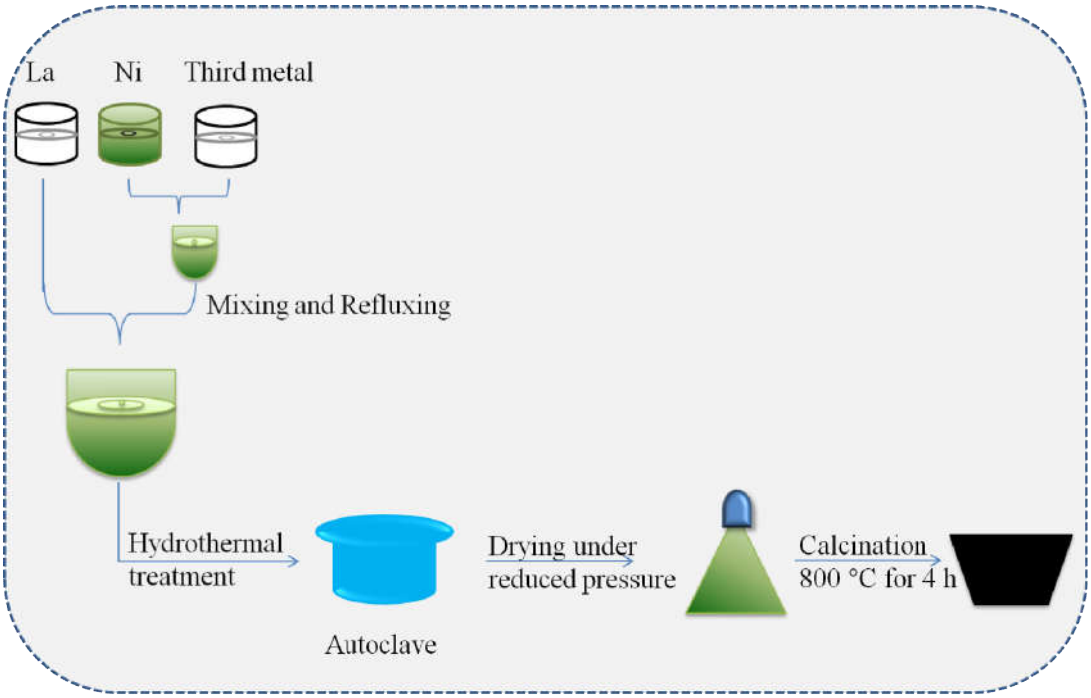

Figure 3.2: Pictorial representation of synthesis of $LaNi_xM_{1-x}O_3$ catalysts by hydrothermal method.

3.2. Characterization of catalysts

3.2.1. Thermogravimetric analysis

Thermogravimetric analysis (TGA) reveals changes in the mass of a sample as a function of temperature under controlled atmosphere. This measurement primarily confirms the details about the stability of the compound. Further, TGA measurements provide vital information about the physical changes occurring during vaporization, sublimation, absorption, adsorption, desorption, as the case may be. Also, TGA curves represent the chemical changes like decomposition, oxidation, and reduction. The thermal

analysis involves a continuous temperature programming or keeping under isothermal conditions first, followed by continuous heating [1]. TGA provides information on the optimum temperatures for drying and/or calcination of freshly synthesized catalysts. The typical curves observed in a TGA experiment are shown in Figure 3.3.

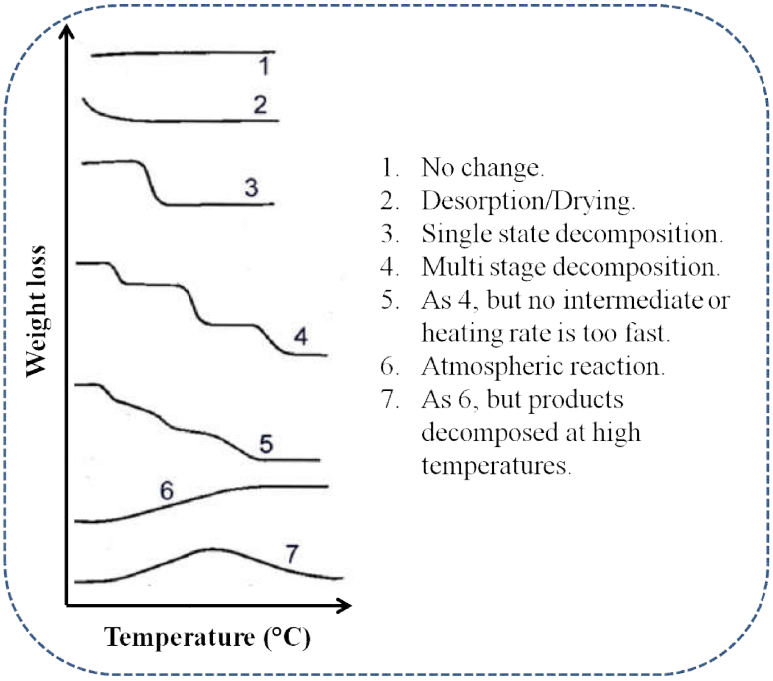

Figure 3.3: Typical curves observed during Thermogravimetric analysis studies [2].

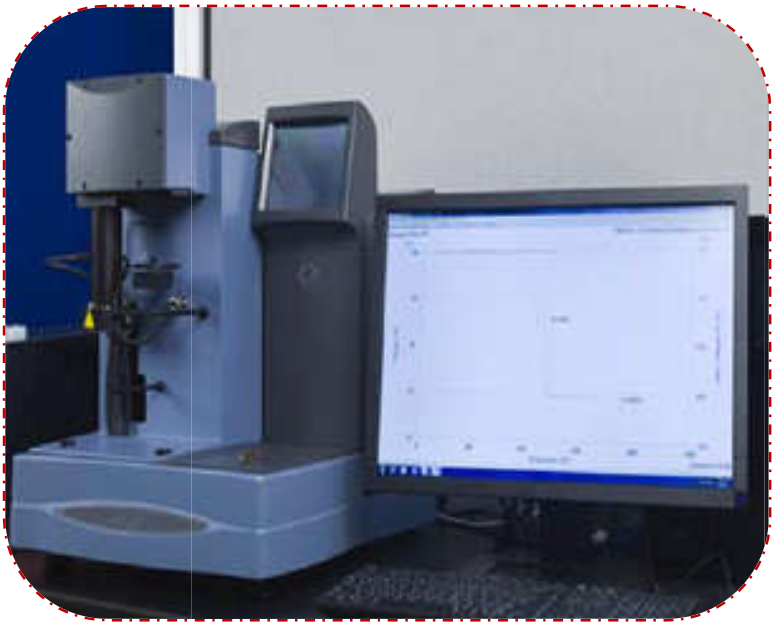

Figure 3.4: TGA Q500 Instrument employed in the studies.

TGAQ500, USA instrument was employed to obtain the TGA curves in the present investigations (Figure 3.4). The TGA instrument comprises of an ultra sensitive weighing balance. The change in weight of a substance reveals loss or gain of matter by the substance. In the present study, the catalyst samples were heated from ambient temperature to 800 °C under N_2 flow with a heating rate of 10 °C/min during the TGA study.

3.2.2. Specific surface area determination

The Brunauer–Emmett–Teller (BET) method is an indispensible technique in catalysis for estimating the specific surface areas of solid materials. This method involves continuous adsorption and desorption of N_2 gas at its boiling point. The quantity of adsorbed gas required to form a monolayer of molecules over the surface of a catalyst can be estimated by the following BET equation [3].

$$\frac{P}{V\,(P_0-P)} = \frac{1}{V_m C} + \frac{C-1}{V_m C}\left(\frac{P}{P_0}\right) \text{ --------- 3.1}$$

Where,

P and P_0 are the equilibrium pressure and the saturation pressure of N_2 at its boiling point,

V is the volume of the gas adsorbed at STP,

V_m is the amount of monolayer of N_2 adsorbed, and

C is BET constant.

Using the above equation one can calculate the volume of N_2 adsorbed at STP. A plot drawn between $P/V\,(P_0-P)$ against P/P_0 gives a straight line. The monolayer adsorption capacity and the BET constant are measured from the intercept and slope of that line, respectively.

The specific surface area of a sample can be found by the following equation:

$$Specific\ surface\ area\ (m^2/g) = \frac{V_m A_m N}{22414 \times W} \text{ --------- 3.2}$$

Where,

A_m is the cross sectional area of N_2 (16.2×10^{-20} m^2 for N_2)

N is the Avogadro number

W is the weight of the catalyst sample

In the present study, the specific surface area of the calcined catalysts was estimated using a Smart Sorb 92/93, India. Prior to the analysis, degasification was carried out for each catalyst at 150 °C for 12 h under vacuum. The BET surface area values were measured within the error margin of ± 3%.

3.2.3. X–ray diffraction (XRD) studies

X–ray diffraction (XRD) is a versatile characterization technique used for the identification of crystalline phases in solid materials. Further, this technique gives information about the lattice parameter calculated by lattice index method and the average crystallite size using Scherrer equation.

Figure 3.5: Instrument employed for powder XRD analysis of the samples.

The XRD spectrum arises due to the interaction of the high energy X–ray beam with the periodic structure of polycrystalline material. A fixed wave length of X–rays is selected as incident radiation. The X–rays are diffracted by the crystalline planes in a sample according to Bragg's Law [4]. The Bragg's equation helps to determine inter planar distances or d–spacing values as a function of scattering angle, 2θ.

The mathematical expression of Bragg's equation is as follows.

$$n\lambda = 2d\ sin\ \theta \text{ --------- 3.3}$$

Where,

n is the order of the diffraction (n =1,2,3 etc),

λ is the wavelength of the X–rays (depends on the source),

d is the interplanar distance, and

θ is the incident or diffracted angle of X–ray.

The universal database to identify the crystal phases is supplied by the International Centre for Diffraction Data (ICDD) and it is popularly known as Joint Committee on Powder Diffraction Standards (JCPDS) [5]. JCPDS is a compilation of crystal phases related to powder XRD patterns owing to interplanar distances matching with their relative intensities corresponding to crystallographic properties. In the work presented in this thesis XRD patterns were recorded on Rigaku ultima IV, Japan instrument equipped with Cu Kα (1.5418 Å) radiation source and the data collected in the 2θ range of 2−80° with a 0.02° step size per sec (Figure 3.5).

Lattice parameter determination: In a cubic cell (a=b=c), the lattice parameter can be estimated by a standard indexation method using the high intensity diffraction line (for example 111 plane of CeO_2). The following mathematical expression has been used to estimate the cell parameter in cubic lattice [6].

$$\frac{1}{d^2} = \frac{h^2+k^2+l^2}{a^2} \quad \text{--------- 3.4}$$

Where,

d is the interplanar distance,

h, k, l are the miller indices (cubic: 111), and

a is the lattice parameter.

3.2.4. Temperature programmed analysis

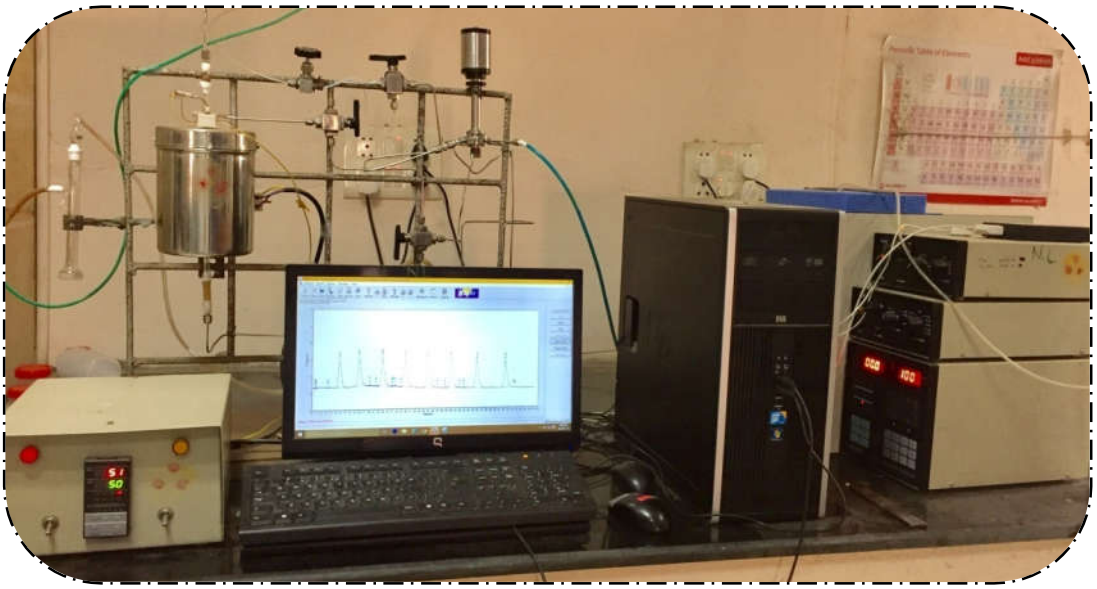

Figure 3.6: Home-made instrument for Temperature programmed reactions.

The reducibility and acidic/basic properties of the catalysts play a vital role in the catalytic activity. These fundamental properties of the catalysts can be identified qualitatively and quantitatively by temperature programmed experiments. The reducing property of a catalyst is revealed by the temperature programmed reduction using H_2. The acidity and basicity of the catalysts can be known from the temperature programmed desorption of the probe molecule with NH_3 and CO_2, respectively. Figure 3.6 shows the home-made apparatus for Temperature programmed analysis.

3.2.4a.Temperature programmed reduction studies

Temperature programmed reduction (TPR) with hydrogen is a sophisticated technique to study the reducible nature of the oxide materials. The main feature of this technique is the continuous monitoring of the reducible species with increasing temperatures. This technique provides precious information about the oxidation states of the metallic component, metal–support and metal–metal interactions, in the catalysts. However, the reduction profiles are sometimes complicated and it is not easy to distinguish these reduction peaks. In a typical TPR experiment, the catalyst is exposed to a mixture of H_2 balanced by an inert gas like N_2 or Ar. The rate of reduction is estimated by the composition of the reducing gas analysed at the reactor outlet. From the graph of Temperature Vs H_2 consumption, the amount of H_2 consumed is calculated. This helps the identification of the average oxidation state of the reduced metal. Schematic diagram of H_2–TPR setup is given in Figure 3.7.

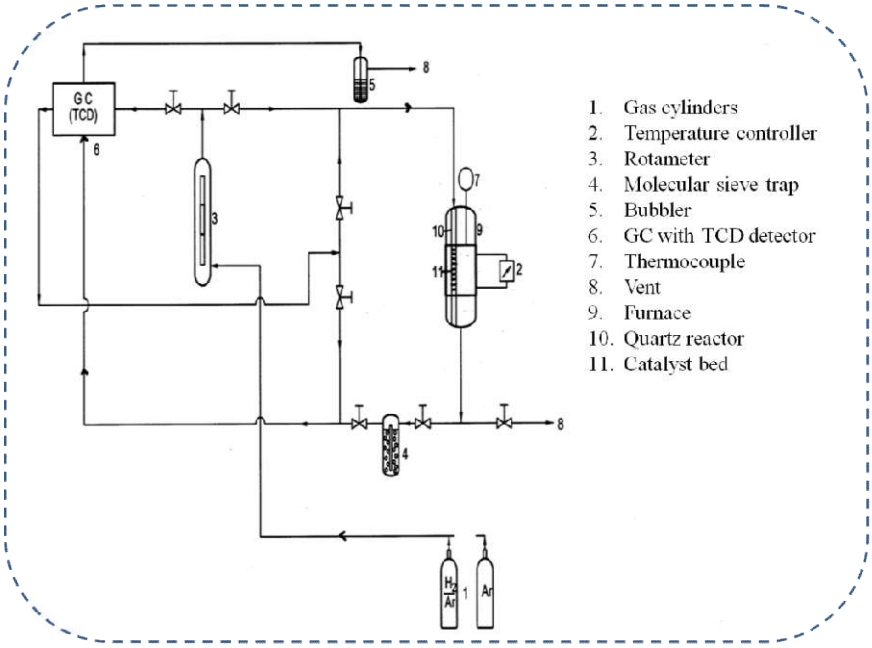

Figure 3.7: Schematic diagram of H_2–TPR analysis.

In the present study the TPR experiments were performed using the home-made apparatus (Figure 3.6). Samples of catalyst (50 mg) loaded in a quartz reactor were

reduced under 10% H_2/Ar gas mixture at a flow rate of 30 ml/min and with heating rate of 5 °C/min from ambient to 800 °C. Then the isothermal condition was maintained for 1h. Before the TPR run, the catalysts were pre–treated in Ar flow at 300 °C for 2 h. The hydrogen consumption was monitored using a gas chromatograph (Varian, 8301) connected with online thermal conductivity detector (TCD) with Ar as a carrier gas.

3.2.4b. NH_3–Temperature programmed desorption studies

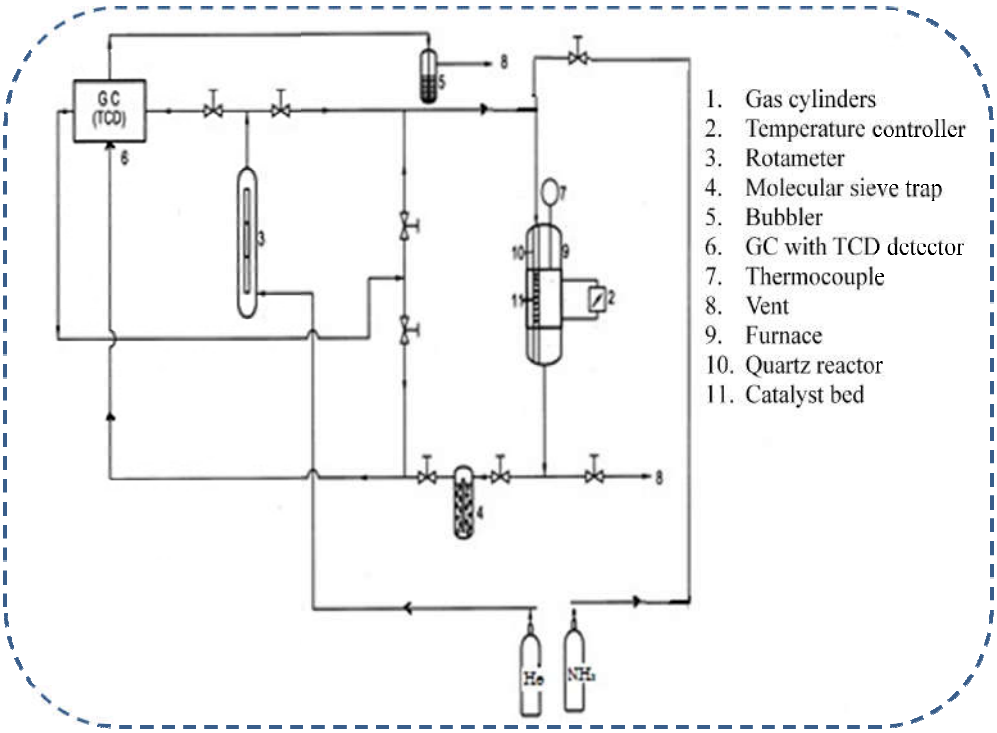

Figure 3.8: Schematic diagram of the equipment used for NH_3–TPD analysis.

Studies on surface acidity of catalysts were carried out by NH_3–Temperature programmed desorption (NH_3–TPD). The acid catalysis has its own importance in reactions like catalytic reforming, naphtha cracking, hydrocracking, hydro–dewaxing, isomerization, alkylation, and dealkylation. NH_3–TPD describes more specifically the surface acidity of the catalysts. However, the prepared solid materials may not have a single class of acidic sites. They may contain a large distribution of acid sites of varying strength. Lewis or Bronsted sites and sometimes mixture of both may be present in the same solid depending on the dopant and the synthesis method used. These acid sites can

be quantified with NH_3–TPD method. The flow chart of NH_3–TPD method is given in Figure 3.8.

NH_3–TPD experiments were conducted in a quartz reactor. In a typical experiment, 50 mg of catalyst was first pre–treated with He flow at 300 °C for 2 h. The reactor temperature was then brought to 100 °C. The ammonia adsorption was conducted with 10% NH_3 balanced He. The adsorption of probe molecule was carried out at 100 °C for 1 h. The solid was then subjected to temperature ramping from 100–800 °C with a rate of 10 °C/min. Desorption of NH_3 was estimated with gas chromatograph (Varian, 8301) equipped with thermal conductivity detector using He as a carrier gas.

3.2.5. H_2–Pulse chemisorption technique

This technique is used to determine the dispersion, particle size of metal and the active metal surface area of the catalysts. This technique is used more often in the metal active reactions such as reforming, dehydrogenation, hydrogenation etc. The metal dispersion plays a major role in these reactions as the small metal particles increase the active metal surface area.

In the present thesis work, this study was conducted in a home-made reactor setup (Figure 3.6). 100 mg of catalyst was loaded in a quartz reactor and then reduced in 5% H_2 balanced Ar with 30 ml/min flow rate at 600 °C for 2 h. The reactor temperature was brought down to 60 °C after reduction in inert flow. Then a series of H_2 pulses were given using a 6–port value until it reached saturation point. The uptake of H_2 was estimated with gas chromatograph (Varian, 8301) equipped with thermal conductivity detector using Ar as a carrier gas.

The following formulae were used to calculate dispersion, active metal surface area, and mean particle size of a metal.

$$Metal\ dispersion = \frac{V_{Chem} \times SF \times MW}{c/100} \times 100 \text{ ---------- 3.5}$$

$$Active\ metal\ surface\ area, A_m \left(\frac{m^2}{g}\right) = V_{Chem} \times 6.023 \times 10^{23} \times SF \times \sigma_m \times 10^{-8} \text{ ---- 3.6}$$

$$Mean\ particle\ size, S_m\ (nm) = \frac{6c}{A_m \times 100 \times \rho \times 10^6} \times 10^9 \text{ --------- 3.7}$$

Where,

V_{chem} / mol·g^{-1} is the volume uptake of H_2

MW is the atomic weight of the metal (Ni–58.69)

σ_m / nm^2 is the metal cross section area (Ni–0.0642)

SF is the Stoichiometry factor (2 for H_2)

c / wt% is the metal weight %

ρ / g·cm^{-3} is the metal density (Ni–8.908)

3.2.6. Fourier transform infrared spectroscopy studies

Fourier transform infrared spectroscopy (FT–IR) deals with the vibration of covalent bonds in a molecule at different frequencies depending on elements and types of bonds. It is noted as a first modern spectroscopic technique with significant impact in the characterization of catalysts. IR spectroscopy analysis is regularly used in the absorption range of infrared frequency, i.e., 4000–400 cm^{-1}. The wavelengths of absorption bands are characteristic to particular types of chemical bonds having permanent dipole moment. Hence it is most commonly used to identify the functional groups of molecules. In a typical FT–IR instrument, the source is modulated into an interferometer that controls the entire frequency region and hence all frequencies are measured simultaneously. FT–IR spectrum is generally divided into two regions namely functional group region and finger print region. The spectrum from 4000 to 1400 cm^{-1} is considered as functional group region and 1400 to 400 cm^{-1} range is known as fingerprint region. The finger print region provides the unique characteristic peaks for a given molecule [7]. FT–IR absorption

information is presented in the form of a spectrum with wave number on x–axis and % absorption or transmittance on y–axis. The recorded spectrum is analyzed and matched with known spectral data.

In the present thesis work, the FT–IR spectra were recorded on DIGILAB (USA) IR spectrometer adopting the KBr pellet method. A thin pellet is prepared by grinding of about 2 mg of powdered catalyst with 200 mg of KBr and then subjected to high pressure in order to obtain thin pellet.

3.2.7. X–ray photoelectron spectroscopy studies

X–ray photoelectron spectroscopy (XPS) is also called as electron spectroscopy for chemical analysis (ESCA). It is an outstanding surface analytical technique to understand the chemical environment on the catalyst surface. It is a vital technique to determine the oxidation states of the elements present in the catalysts as well as to estimate their surface chemical composition [8,9]. The attractiveness of this study is that each element exhibits a unique elemental spectrum. The continuous ejection of the electrons from the top of atomic layers is monitored by the instrument. Quantitative data can be estimated from the full width half maxima (FWHM) of peak. The oxidation state of an element is determined from the peak position and separation from certain spectral lines.

XPS technique usually involves irradiation of the sample with high energy beam in a closed container attached to a vacuum generator and analysis of the emitted electrons. Mg Kα (1253.6 eV) or Al Kα (1486.6 eV) are generally used sources for X–rays in XPS analysis. These photons have limited penetrating power into a solid, normally in the order of 1–10 μm, which interact with atoms in the surface region. This irradiation ultimately leads to ejection of electrons from the solid surface and the kinetic energy (KE) of emitted electrons is calculated by the equation for the photoelectric effect (Eq. 3.8).

$$KE = h\upsilon - BE - \varphi_s \text{ --------- 3.8}$$

Where,

$h\upsilon$ is the energy of photon (depends on the source used),

BE is the binding energy of electron, and

φ_s is the work function.

Binding energy is the ionization energy of the element for a particular shell involved. Different kinetic energies of the ejected electrons are attributed to a variety of possible ions from each type of elements. Studies presented in this thesis were carried out on a KRATOS AXIS 165 instrument. The non–monochromatized Al–Kα X–ray source ($h\upsilon = 1486.6$ eV) was operated at 12.5 kV and 16 mA. The analysis was performed at room temperature with extreme vacuum pressure < 10^{-8} Pa. Prior to this experiment, the sample was out gassed at 100 °C for 12 h. The energy calibration was carried out by setting the binding energy of carbon (C 1s) peak at 284.6 eV. Multiple scans of the specified spectral region of interest can increase the signal-to-noise ratios. All binding energies presented in this thesis were measured within the error maximum of ± 0.1 eV.

3.2.8. Raman spectroscopy studies

Raman spectroscopy is a very useful technique to obtain information about metal oxygen interaction in a variety of metal oxide materials [10]. The Raman scattering occurs when the incident light interacts with the electron cloud of an atom or molecule. If both incident and scattered photons contain the same energy, it is called Rayleigh scattering, [11,12]. If the scattered photon has lower energy than the incident photon, it is known as Stokes Raman scattering. Conversely, if the scattered photon contains a higher energy than the incident photon, it is called anti–Stokes Raman scattering.

The Raman shift is calculated from the following equation:

$$Raman\ Shift\ (\Delta_\omega) = \left(\frac{1}{\lambda_0} - \frac{1}{\lambda_1}\right) \text{ ---------- 3.9}$$

Where,

λ_0 is the excitation wavelength,

λ_1 is the Raman spectrum wavelength.

Raman spectroscopy is a widely used technique for chemical and structural properties of solid mixed oxides which are highly sensitive to M–O bond arrangement and lattice defects. In this thesis, Raman spectroscopy analysis was performed using a LabRam HR spectrometer (Horiba Jobin–Yvon, Japan) equipped with a charge coupled device (CCD) detector (Figure 3.9). The Ar^+ (emission line 638.2 nm) laser is focused on the sample with the diameter ~1μm. The incident beam power on the solids was typically 0.5 mW. In order to establish the homogeneity of the solids, the spectra were recorded at different points and compared.

Figure 3.9: Raman spectroscopy instrument LabRam HR spectrometer used in the present studies.

3.2.9. Carbon analysis of used catalysts

In reforming reactions, the carbon formation plays a major role on the catalyst stability. The formation of carbon during the reaction reduces the active sites thereby deactivating the catalyst. Carbon analysis is commonly carried out in a CHNS analyzer along with hydrogen, nitrogen and sulphur. This technique determines the amount of elements contained in organic and inorganic forms (liquid or solid state). In this thesis work, the carbon analysis was carried out using the instrument, Elementar V made in Germany (Figure 3.10) which is equipped with dynamic flash combustion facility.

Figure 3.10: Elementar V cube instrument used in the present studies.

The sample was loaded into a tin capsule and then placed in a quartz tube. The temperature of the tube was raised till 950–1200 °C with a carrier gas like helium. Prior to the analysis, the stream was filled with sufficient amount of high purity oxygen to achieve strong oxidation/combustion to highly thermal resistant substance. The outlet gas was passed through an oxidation catalyst zone. The formed nitrogen oxide and sulphuric anhydride (SO_3) are passed through a copper zone in order to reduce them into elemental

nitrogen and sulphurous anhydride (SO_2). The four components of combustion mixture are detected by thermal conductivity detector in the order of sequence N_2, CO_2, H_2O and SO_2. O_2 is analyzed separately by quantifying the carbon monoxide liberated from the organic oxygen using GC column packed with molecular sieves.

3.3. CH_4 reforming reactor setup

Figure 3.11 shows the schematic diagram of reactor system used in the studies presented in this thesis. Gas flow rates are adjusted with mass flow controllers (MFC). The reaction mixture is then pumped into reactor through preheating zone which is maintained at 100 °C. The reactor is covered with high temperature furnace consisting of two thermocouples. One estimates the skin temperature of the reactor and the other estimates the catalyst bed temperature of the reactor. MFC flow rate and furnace temperatures are adjusted using the system controller. Methane reforming reaction is carried out in a fixed bed reactor system. The fixed bed reactor was made up of Inconel material having 44 cm of length with 1.2 cm of inner diameter. 0.5 g of catalyst mixed with 0.5 g of ceramic beads was suspended in the centre of the reactor between two quartz plugs. The outlet gas mixture is directly connected to gas chromatograph through a moister trap.

3.4. Catalytic activity tests

The evaluation of activity of catalysts was performed in a fixed bed inconel reactor (Figure 3.11) under atmospheric pressure by passing a mixture of CO_2, CH_4 and N_2 at a ratio of 80/80/80 (total flow rate= 240 ml/min and GHSV of 28,800 h^{-1}). Prior to the activity measurements, the samples were reduced *in situ* under 60% H_2 balanced N_2 gas mixture at 600 °C for 6 h. After attaining the required temperature, the reaction was allowed to attain steady state for a period of 1 h. For each analysis the gas products were analysed two times with an interval of 30 min. The activity results provided in this thesis

work are the average values of the two consecutive analyses. The product analysis was carried out, online on a Nucon 5765 gas chromatograph equipped with a carbosphere column using Argon gas as carrier with TCD detector. The accuracy of the catalytic activity results in this thesis work is within the error margin of ± 3%.

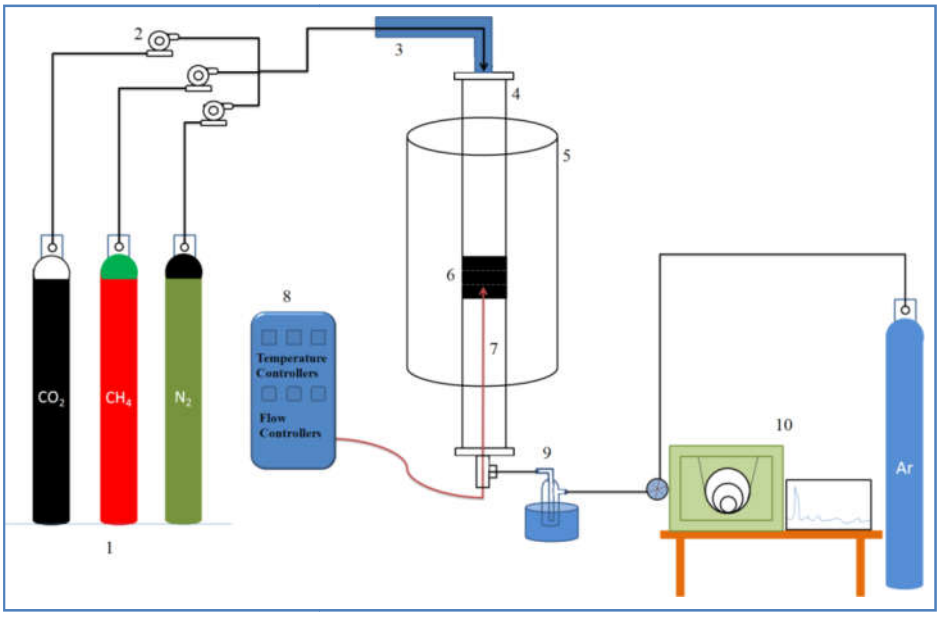

Figure 3.11: Experimental setup for studying the dry reforming of methane reaction. 1. Gas cylinders, 2. Mass flow controllers, 3. Pre–heater, 4. Reactor, 5. Furnace, 6. Catalysts bed, 7. Thermocouple, 8. System controllers, 9. Moister trap, 10. Gas chromatography.

3.5. Calculation of response factors

Standard gas mixtures containing the reactants and products of specified compositions (prepared by using individual mass flow controllers) were injected into the gas chromatograph and their peak areas measured. The response factor (RF) of each gas was obtained by drawing plots with sample concentration on x-axis and peak area on y-axis. The obtained linear graph was again fitted with linear trending line. The slope of the line was taken as the response factor of that particular gas. A sample RF calibration

curve for CO_2 is provided below as Figure 3.12. The unknown concentration of gas in the product was obtained from the peak area and the response factor of the individual gas.

$$\text{Unknown concentration of oulet gas} = \frac{\text{Peak Area of Sample}}{\text{Response Factor}} \text{ ---------- } 3.10$$

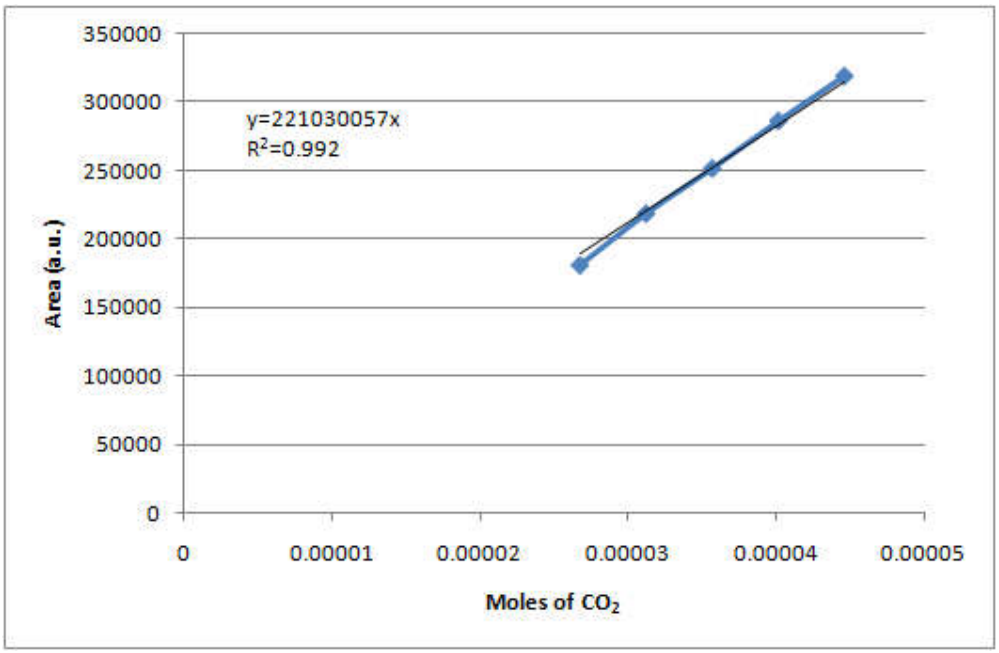

Figure 3.12: Calibration curve of CO_2 gas.

Figure 3.13 shows the original GC chromatograph obtained during the dry reforming of methane carried out over $LaNi_{0.3}Al_{0.7}O_3$ catalyst synthesized by sol-gel method. The first peak at retention time (RT) 1.162 sec corresponds to H_2 gas, the second peak RT 4.652 sec relates to CO, the third peak with RT of 9.037 sec is due to CH_4 and the fourth one appearing at 14.450 sec corresponds to CO_2.

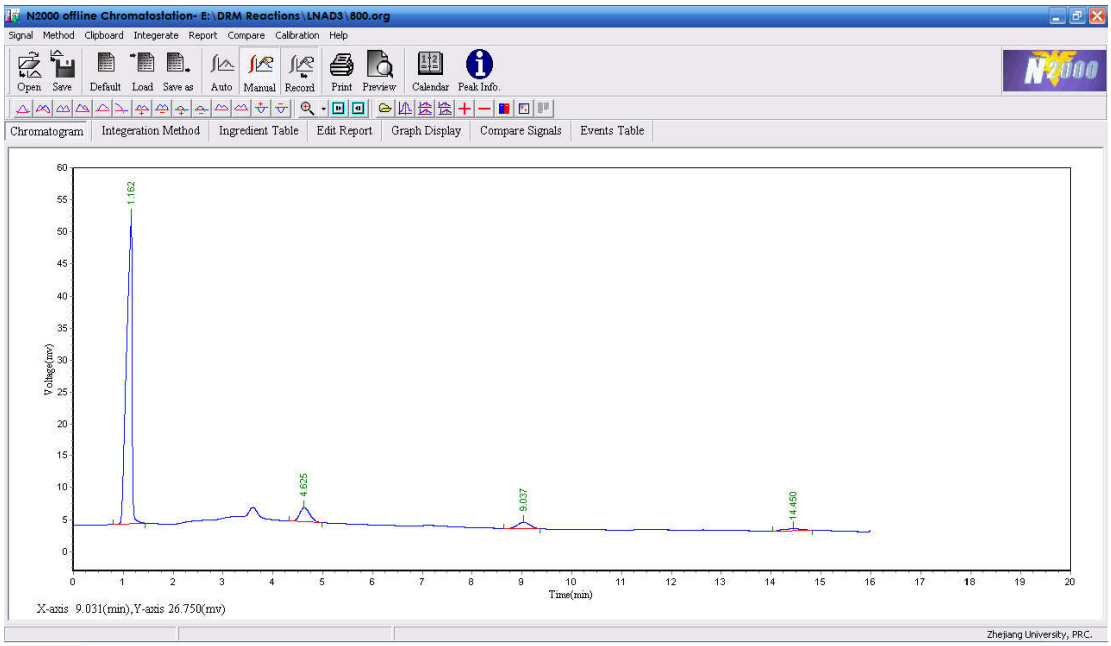

Results Data File - E:\DRM Reactions\LNAD3\800.org

Peak No.	Peak ID	Ret. Time	Peak Height	Peak Area	Peak Conc.
1	H_2	1.162	48154.098	3804058.101	86.8049
2	CO	4.652	2202.000	308509.893	7.3131
3	CH_4	9.037	998.780	93432.802	4.0504
4	CO_2	14.450	298.331	47334.225	1.8317
Total			51653.209	4253335.655	100.0000

Figure 3.13: GC chromatograph during reforming of methane.

3.6. References

1. Kenkel, J. (1994). *Analytical Chemistry for Technicians*, 2nd edition, CRC-Press/Lewis Publishers.
2. https://www.slideshare.net/KalsoomMohammed/thermogravimetry-analysis-tga.
3. Brunauer, S., Emmett, P. H., & Teller, E. (1938). *J. Am. Chem. Soc*, *60*(2), 309-319.
4. Gallezot, P. eds Anderson, J. R., & Boudart, M. (1984). *Catalysis: science and technology (Vol. 5). Springer Science & Business Media.*
5. Jenkins, R., & Snyder, R. L., (1996) *Introduction to X-ray Powder Diffractometry*, John Wiley & Sons Inc., New York, pp. 89–91.
6. Pijolat, M., Valdivieso, F., Vidal, H., Kašpar, J., Finocchio, E., Daturi, Binet M. C., Lavalley J. C., Baker, R. T., & Baker, R. (1998). *Journal of the Chemical Society, Faraday Transactions*, *94*, 3717-3726.
7. Niemantsverdriet, J. W., (2007). in: *Spectroscopy in Catalysis: An Introduction*, WILEY-VCH Publisher, New York, p. 224.
8. Watts, J. F., & Wolstenholme, J., (2003). in: *An Introduction to Surface Analysis by XPS and AES*, Wiley & Sons, Chichester, UK.
9. Moulder, J. F., Stickle, W. F., Sobol, P. E., & Bomben, K. D. (1992). in: *Handbook of X-ray Photoelectron Spectroscopy*, Perkin-Elmer Corp., Eden Prairie, USA.
10. Raman, C. V. (1928). *Indian J. Phys.,* 2, 387–398.
11. Benwell, C. N., & McCash, E. M. (1999). In: *Fundamentals of Molecular Spectroscopy*, ed. Hill, T. Mc., International Ltd., UK, 4th edition, 1999.
12. https://en.wikipedia.org/wiki/Raman_spectroscopy.

Chapter 4

Studies on Aluminium modified $LaNiO_3$ catalysts for CO_2 reforming of methane

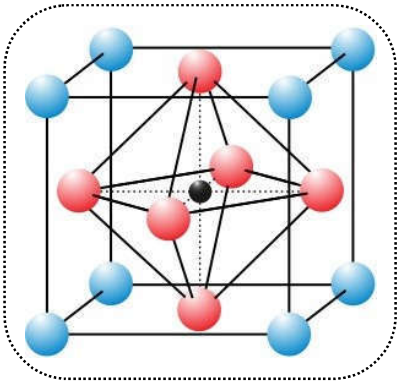

4.0. Introduction

CO_2 level in the atmosphere reached 406.07 ppm in January 2017 as reported by Mauna Loa Observatory, Hawaii [1]. These high levels of CO_2 in the atmosphere cause climate change and global warming [2,3]. CO_2 release into the atmosphere occurs by burning of carbon materials like coal, natural gas and oil. Researchers have been showing keen interest in developing new routes to contain the carbon dioxide levels in the atmosphere. These include separation by CO_2 capture, transportation and sequestration [4]. Carbon dioxide is known to be a cheap and nontoxic raw material of single carbon source chemistry [5]. Applications of CO_2 include transformation to hydrocarbon fuels [6]. Urea production is one of the largest industrial applications [7]. The chemical transformations of low grade oils like glycerol crude [8] and natural gas (mainly CH_4 using CO_2) yields promising results for the CO_2 related problems [5]. Reforming reaction with carbon dioxide to produce synthesis gas (H_2+CO) is a very promising route to produce energy and chemicals. These reforming reactions are of enormous importance, because they fall in the area of CO_2 utilization [9].

The CH_4 reforming reactions are of three types:

i) Dry reforming $(CH_4 + CO_2 \rightarrow H_2 + 2\,CO \quad [\Delta H° = 247.3\ \mathrm{kJ/mol}])$ --- 4.1

ii) Partial oxidation $(CH_4 + {}^{1}/_{2}\,O_2 \rightarrow 2\,H_2 + CO \quad [\Delta H° = -35.9\ \mathrm{kJ/mol}])$ --- 4.2

iii) Steam reforming $(CH_4 + H_2O \rightarrow 3\,H_2 + CO \quad [\Delta H° = 205.9\ \mathrm{kJ/mol}])$ --- 4.3

Partial oxidation and steam reforming of methane are usually operated at high temperature (1300 °C) and high pressure (up to 150 atm), respectively. Due to these difficulties, CO_2 reforming of methane has attracted the attention of researchers [10]. Dry reforming process utilizes two potent greenhouse gases and hence is a very useful method for controlling the global warming [11]. All of the above reactions produce syngas with different ratios. As mentioned in Chapter 1, the dry reforming reaction produces low ratio

syngas, which is a suitable feed stack for the Fischer–Tropsch synthesis [12,13]. But, it is an endothermic reaction and has a major concern about rapid catalytic deactivation by thermal sintering of active metal and coke formation. Carbon deposition on active sites of catalyst is mainly due to Boudouard reaction ($2CO \rightarrow CO_2 + C$) and methane decomposition ($CH_4 \rightarrow 2H_2 + C$) [14,15].

According to the literature reports, noble metals like Pd, Ru, Rh, Pt, and Ir show good results when used as catalysts for the DRM reaction. However, due to their less availability and high cost, their use as catalysts for industrial purposes has become a big question [16]. So, the development of non–noble metal catalysts for this reaction has drawn the attention for several researchers. Most of the group VIII metals are catalytically active for CH_4 reforming [9,17]. Ni catalysts exhibited good activity similar to that of noble metal catalysts. As compared to the noble metals, nickel is a very viable alternative as catalyst for the DRM reaction due to its availability, lower cost and remarkable long term stability [18]. Studies revealed that, Ni catalysts are not only active for the reforming reactions but also increase the carbon deposition [19,20]. As the methane reforming with CO_2 is a highly endothermic reaction, the catalysts should possess thermal stability to withstand high temperatures. Most of the metals have a tendency of sintering at high temperatures. Therefore, structural oxides have been used as catalysts for this reaction. The structural complexes like perovskite type oxides (ABO_3) are found to be effective for catalytic reforming of methane [11,21]. In ABO_3, the A–site offers thermal stability and the B–site is responsible for catalytic activity. Lanthanum is found to possess excellent thermal stability compared with other rare earth elements and nickel is identified as the active phase for chemical transformation [22]. Literature reports on perovskite type oxides $LaNi_{1-x}M_xO_3$ (where M = Cu, Co, Fe, etc.) [23], $La_{1-x}M_xNiO_3$ (where M= Ce) [24] and $LaNi_xM_{1-x}O_3$ (M= Al and Fe) [25,26] revealed that, Ni particles

exist in well dispersed state in the lattice. The size of Ni particles plays a major role in the stability of the catalysts during dry reforming process. In $La_{0.8}A_{0.2}NiAl_{11}O_{19}$, (A = Ca, Mg and Sr) the hexaaluminate crystalline structure is found to stabilize Ni crystallites and thereby increase the catalyst's lifetime as well as decrease the carbon deposition on the active sites [27]. Reports on these types of materials suggested that, further detailed studies are necessary to develop catalysts with suitable composition and also to optimize the reaction conditions for dry reforming of methane [28].

In this chapter, studies on synthesis, characterization and catalytic activity of $LaNi_xAl_{1-x}O_3$ catalysts are discussed. The catalysts have been synthesized by both sol-gel method as well as hydrothermal method in order to arrive at preferred method and also ideal composition.

Section 4.1: Al modified $LaNiO_3$ catalysts synthesized by sol–gel method

4.1.1. Introduction

Al modified $LaNiO_3$ catalysts were synthesized by the sol-gel method varying the Ni ratio between 0 and 1. Details of procedure followed for their synthesis are already discussed in Chapter 3, Section 3.1.2a. The catalysts thus prepared are given the general formula $LaNi_xAl_{1-x}O_3$ (x=0, 0.2, 0.3, 0.4, 0.6, 0.8 and 1). These catalysts are characterized and tested for their catalytic activity for the DRM reaction. The following paragraphs illustrate the results on characterization and catalytic activity studies. Conclusions are drawn by correlating the activity with the physico–chemical parameters.

4.1.2. Results and Discussion

4.1.2a. Specific surface area measurements

Table 4.1.1 shows the specific surface areas of $LaNi_xAl_{1-x}O_3$ catalysts synthesized by sol-gel method and calcined at 800 °C. This high temperature calcination resulted in decrease in the surface area of the catalysts [29]. Formation of highly crystalline compounds might have also led to low surface areas, as observed by Lima et al. [30]. Continuous decrease in the surface area with increase in Ni content in the catalysts is observed. This may be due to the involvement of third metal into the crystalline bimetallic perovskite, in order to form trimetallic perovskite.

Table 4.1.1: Specific surface area of $LaNi_xAl_{1-x}O_3$ catalysts synthesized by sol-gel method.

S. No.	Catalyst	Specific surface area (m^2/g)
1	$LaNi_{0.2}Al_{0.8}O_3$	11.2
2	$LaNi_{0.3}Al_{0.7}O_3$	17.7
3	$LaNi_{0.4}Al_{0.6}O_3$	18.6
4	$LaNi_{0.6}Al_{0.4}O_3$	9.6
5	$LaNi_{0.8}Al_{0.2}O_3$	1.9

4.1.2b. X–ray diffraction studies

The XRD patterns of the $LaNi_xAl_{1-x}O_3$ catalysts synthesized by sol-gel method are shown in Figure 4.1.1. The catalysts synthesized by this method comprised perovskite phases. All the synthesized catalysts showed bi and trimetallic perovskite phases. From Figure 4.1.2, it can be observed that by changing the active metal (Ni) ratio from x= 1 to 0, the peak at 2θ = 32.92° ($LaNiO_3$) gets shifted to 33.34° ($LaAlO_3$). Similar shift was also noticed by Moradi et al. [25].

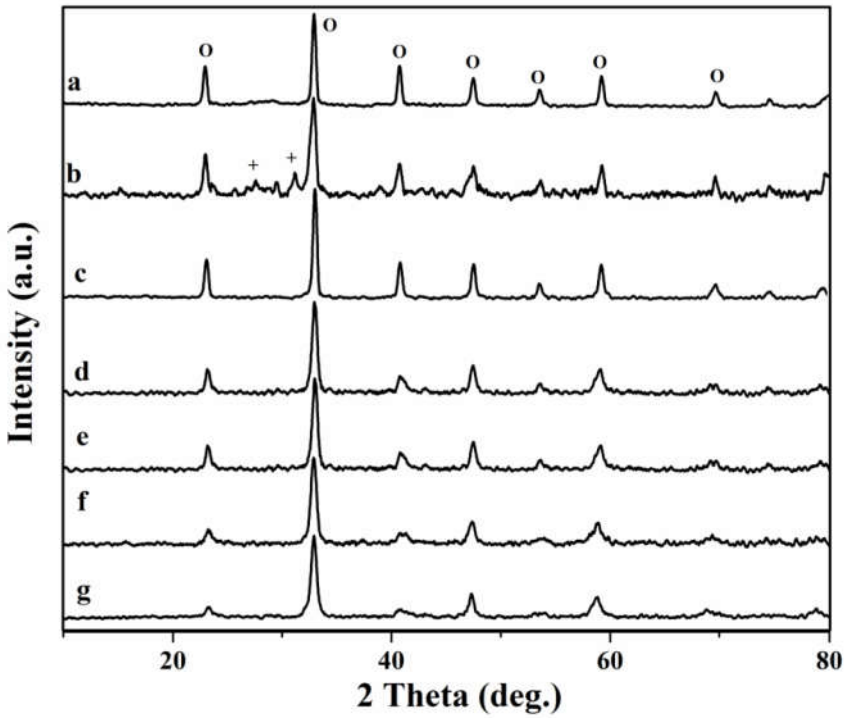

Figure 4.1.1: XRD patterns of $LaNi_xAl_{1-x}O_3$ catalysts synthesized by sol-gel method. a) x = 1; b) x = 0.8; c) x = 0.6; d) x = 0.4; e) x = 0.3; f) x = 0.2 and g) x=0, (+) cubic La_2O_3, (O) perovskite (a= $LaNiO_3$, g= $LaAlO_3$).

This gradual shift which is noticed in all the cases indicates the incorporation of Al into the perovskite lattice of $LaNiO_3$. Sharp and high intense peak indicates the formation of trimetallic oxides with high crystallinity. More number of diffraction peaks observed for the catalyst with x=0.8 can be attributed to the presence of La_2O_3 phase.

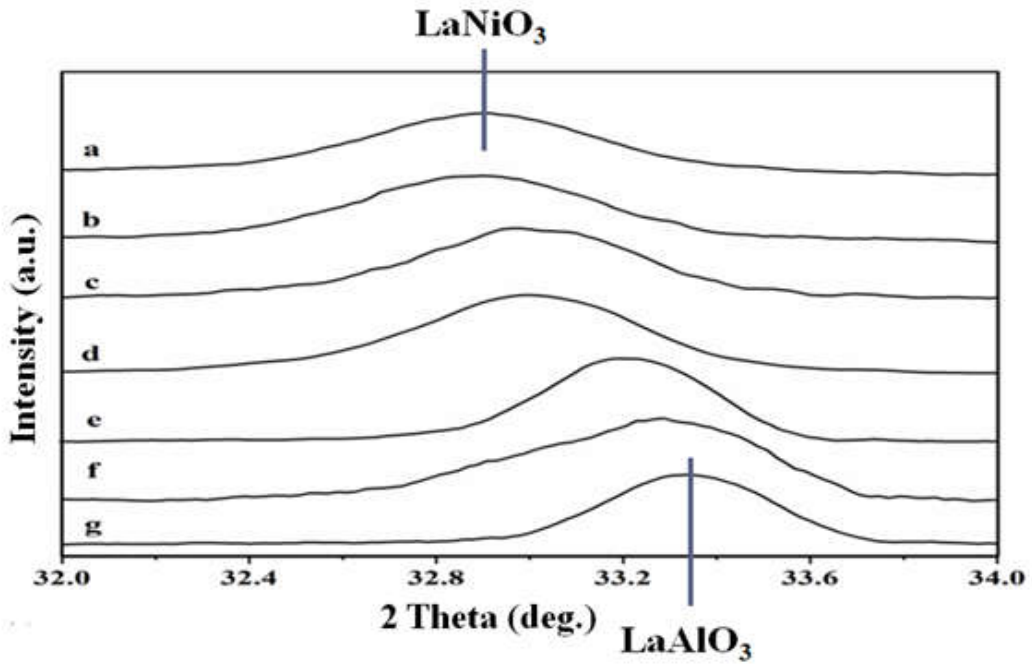

Figure 4.1.2: Zoomed XRD patterns of $LaNi_xAl_{1-x}O_3$ catalysts synthesized by sol-gel method. a) x = 1; b) x = 0.8; c) x = 0.6; d) x = 0.4; e) x = 0.3; f) x = 0.2 and g) x=0.

Table 4.1.2: Lattice parameter and crystallite size of $LaNi_xAl_{1-x}O_3$ catalysts synthesized by sol-gel method.

S. No:	Catalyst	Lattice parameter (Å)	Crystallite Size (nm)
1	$LaNi_{0.2}Al_{0.8}O_3$	3.802	13.91
2	$LaNi_{0.3}Al_{0.7}O_3$	3.812	12.90
3	$LaNi_{0.4}Al_{0.6}O_3$	3.820	13.63
4	$LaNi_{0.6}Al_{0.4}O_3$	3.831	20.67
5	$LaNi_{0.8}Al_{0.2}O_3$	3.840	20.86

The perovskite peaks are well correlated with JCPDS 34-1028. Moradi et al., calculated the lattice parameter values of the catalysts for the (110) plane considering the crystal phase as pseudo-cubic [25]. The crystallite size of perovskite catalysts calculated using Scherrer equation are presented in Table 4.1.2. A continuous shift in the lattice

parameter was observed displaying a continuous decrease in the crystallite size upto x=0.3 and an increase with further increase in Ni content.

4.1.2c. Temperature programmed reduction studies

The reduction behaviour of the $LaNi_xAl_{1-x}O_3$ catalysts is studied by H_2–TPR and the profiles obtained are presented in Figure 4.1.3. Reduction behaviour of $LaNiO_3$ (inset) shows two bands which can be attributed to the stepwise reduction of Ni^{3+} to Ni^{2+} and Ni^{2+} to Ni^0. The area ratio of the first and the second reduction peak, found as 1:2, is an indirect confirmation for the existence of bimetallic perovskite [23,30-33]. Any variation in this ratio implies the formation of a trimetallic perovskite or the individual oxide.

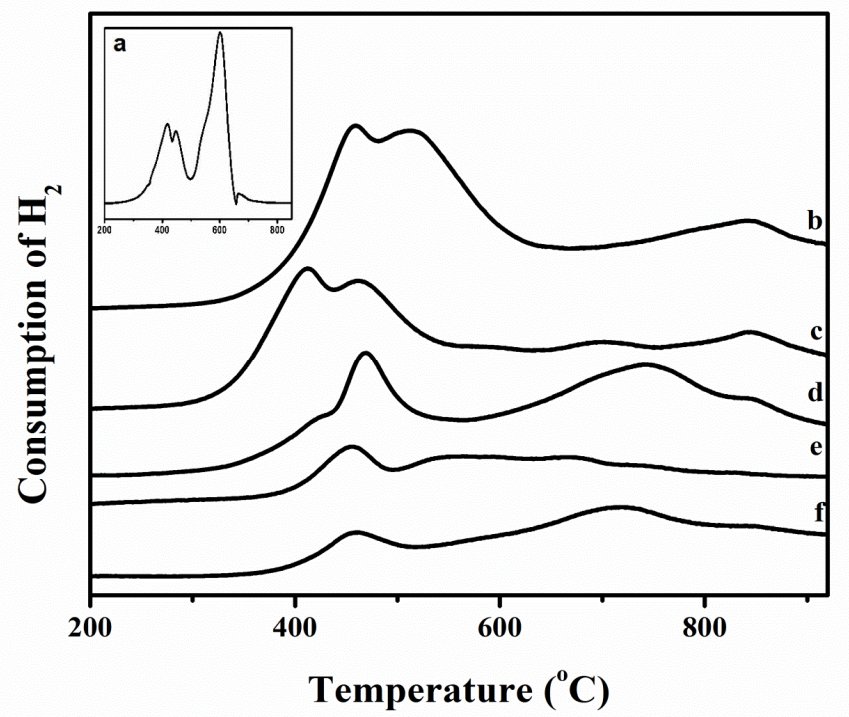

Figure 4.1.3: H_2–TPR Profiles of $LaNi_xAl_{1-x}O_3$ catalysts synthesized by sol-gel method. a) x = 1; b) x = 0.8; c) x = 0.6; d) x = 0.4; e) x = 0.3 and f) x = 0.2.

The reduction patterns can be explained by occurrence of the following reactions:

$$2LaNiO_3 + H_2 \rightarrow La_2Ni_2O_5 + H_2O \qquad \text{--- 4.4}$$

$$La_2Ni_2O_5 + 2H_2 \rightarrow La_2O_3 + 2Ni + 2H_2O \qquad \text{--- 4.5}$$

These Al modified catalysts showed two zones of reduction: the first zone falling in the 400–500 °C with one or two peaks and the second zone falling in the temperature region ~650–750 °C. The high temperature reduction peak i.e., < 600 °C indicates the stability of the perovskite phase as suggested by the previous researchers [25,34,35]. The position of high temperature reduction band after the addition of Al is shifted to right, when compared to the $LaNiO_3$ peak. This high temperature shift indicates the formation of trimetallic perovskite phase ($LaNi_xAl_{1-x}O_3$). These H_2–TPR results are in good agreement with the XRD results confirming the formation of trimetallic perovskite.

The reduction bands observed by Moradi et al. for the $LaNi_xAl_{1-x}O_3$ oxide showed the doublet bands in low Ni containing catalysts [25]. In contrary to the results obtained by Moradi et al., catalysts with high Ni content showed doublet reduction bands in this study. The catalysts with low Ni content showed only one single reduction peak in the first zone. Facile formation of bimetallic perovskite phase in catalysts with low Ni content is due to the free availability of NiO. The XRD pattern of catalyst with x= 0.2 is found to be similar to that of $LaAlO_3$ catalyst (Figure 4.1.2). On the other hand, the high temperature peak appearing with peak maximum greater than 700 °C indicates the trimetallic phase formation in the catalysts.

4.1.2d. Fourier transform infrared spectroscopy studies

FT–IR spectra of $LaNi_xAl_{1-x}O_3$ catalysts synthesized by sol-gel method are shown in Figure 4.1.4. The peak related to –O–H stretching band of inter layer molecular water is seen at 3400 cm^{-1} only in the case of catalysts with x=0.1. Strong and sharp absorption bands at ~1680, 1484 and 1382 cm^{-1}, can be ascribed to the asymmetric and symmetric COO^- stretching modes of the coordinated carboxylate groups [36]. These bands disappeared gradually with the increase of Ni content.

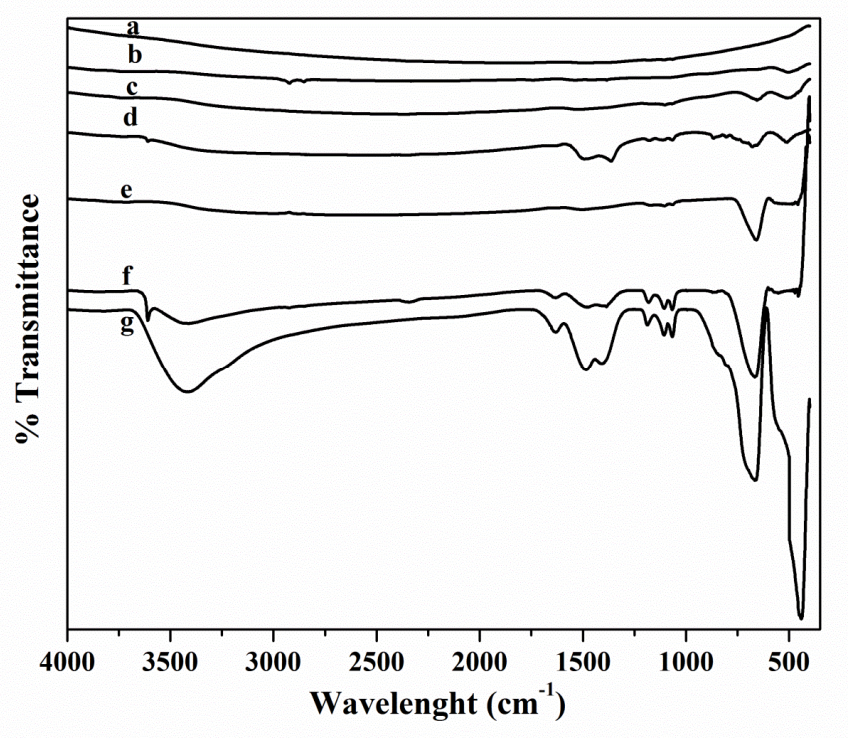

Figure 4.1.4: FT–IR patterns of $LaNi_xAl_{1-x}O_3$ catalysts synthesized by sol-gel method a) x = 1; b) x = 0.8; c) x = 0.6; d) x = 0.4; e) x = 0.3; f) x = 0.2 and g) x=0.

Absorption bands at ~1187, 1103 and 1063 cm^{-1} correspond to the Al–OH bending mode [37]. These bands have also vanished with increasing Ni content beyond x=0.2. On addition of Ni metal to $LaAlO_3$ perovskite phase, incorporation of Ni into the lattice takes place. This reduces the formation of inter layer water molecules and also the intensities of the Al–OH bands. Two absorption bands at ~678 and 436 cm^{-1} are attributed to the formation of AlO_6 octahedra in $LaAlO_3$ [36,38]. These peaks also disappeared with the increase in Ni content. These evidences are well corroborated with XRD and TPR results which also confirm the formation of trimetallic perovskite catalysts.

4.1.2e. X–ray Photoelectron spectroscopic studies

La 3d core level XP spectra of $LaNi_xAl_{1-x}O_3$ catalysts synthesized by sol-gel method are provided in Figure 4.1.5. The peaks with binding energies of 832, 834, 838 and 851–852 eV corresponds to La $3d_{5/2}$ and La $3d_{3/2}$, respectively [39].

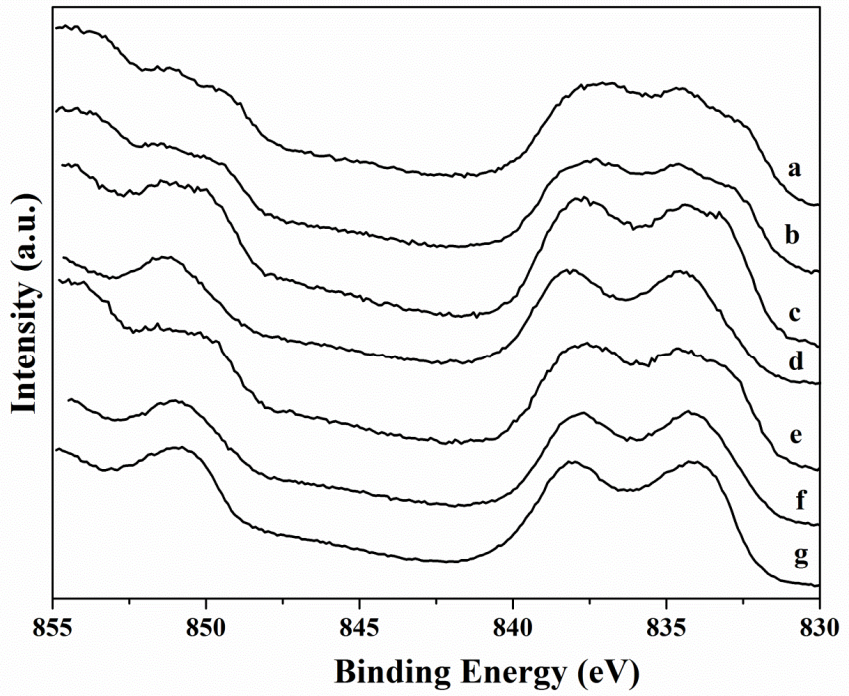

Figure 4.1.5: La 3d XPS patterns of $LaNi_xAl_{1-x}O_3$ catalysts synthesized by sol-gel method. a) x = 1; b) x = 0.8; c) x = 0.6; d) x = 0.4; e) x = 0.3; f) x = 0.2 and g) x=0.

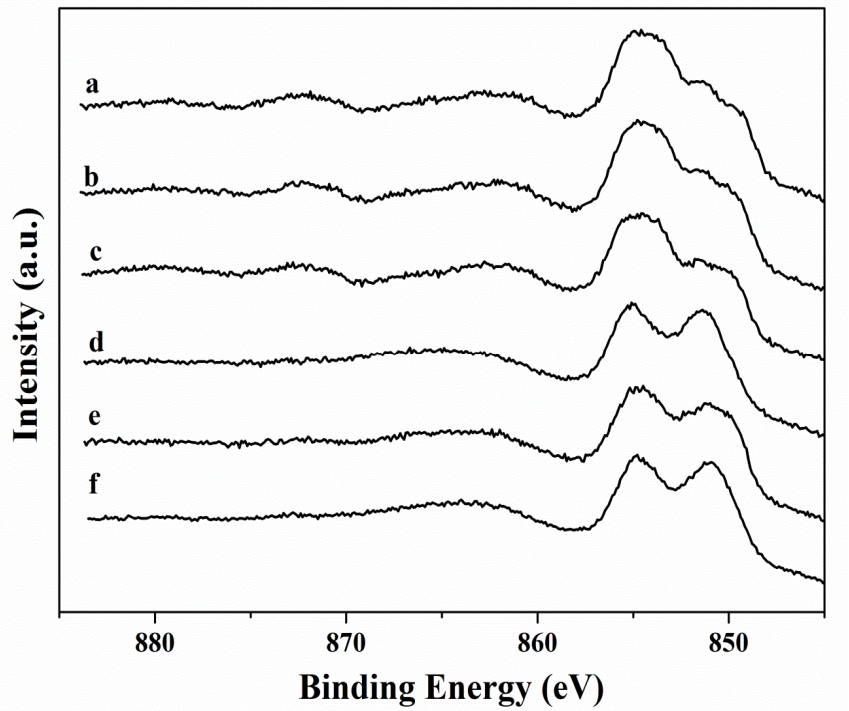

Figure 4.1.6: Ni 2p XPS patterns of $LaNi_xAl_{1-x}O_3$ catalysts synthesized by sol-gel method. a) x = 1; b) x = 0.8; c) x = 0.6; d) x = 0.4; e) x = 0.3 and f) x = 0.2.

Binding energy value for simple lanthanum oxide is found to be ~833 eV. In the present study, higher binding energies for La 3d spectra have been observed as compared to lanthanum oxide and lanthanum aluminate (833 and 837 eV). This indicates that the material is not a simple lanthanum oxide. The shift in binding energy peak of La 3d spectra towards high energy is due to the strong interactions of La with other metals [41].

Ni $2p_{3/2}$ and Ni $2p_{1/2}$ bands were clearly observed along with satellite peaks related to Ni $2p_{3/2}$ (Figure 4.1.6). Binding energies of peaks appearing at 851 and 855 eV can be assigned to Ni $2p_{3/2}$. The band at 872 eV corresponds to the Ni $2p_{1/2}$. A satellite peak of Ni was observed at 862 eV. The Ni $2p_{1/2}$ band related to the Ni^{2+} ion appeared only in the case of catalysts with high Ni content. This observation correlates well with the XRD results where the NiO peaks are clearly seen. The peak shift towards high binding energy confirms that the Ni exists in higher oxidation state. The bands corresponding to Ni $2p_{1/2}$, indicate the presence of Ni^{2+}. From the above observations, it can be concluded that Ni^{2+} and Ni^{3+} co–exist on the surface of catalysts, as observed by Rida et al. [32].

Figure 4.1.7 shows the combined binding energy peaks of Al 2p and Ni 3p. The peak observed at 72–73 eV is due to the Al 2p, whereas the peak at 67 eV corresponds to the Ni 3p. The Al 2p peak shift towards right is mainly due to the strong interactions with other metals. The high binding energy values of Ni $2p_{3/2}$ indicate strong interactions of nickel with other metals [42]. These Al 2p peaks showed higher binding energy values with the increase in nickel loading, indicating the change in electron environment of Al.

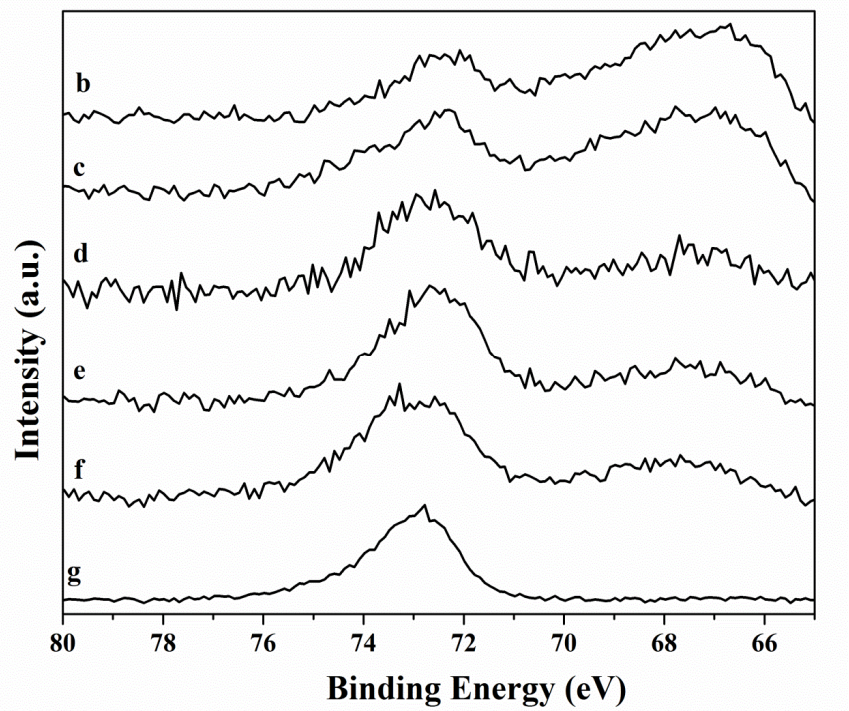

Figure 4.1.7: Al 2p XPS patterns of $LaNi_xAl_{1-x}O_3$ catalysts synthesized by sol-gel method. b) x = 0.8; c) x = 0.6; d) x = 0.4; e) x = 0.3; f) x = 0.2 and g) x=0.

These observations derived from XP spectra confirm the formation of trimetallic perovskite catalysts when they are synthesized by the sol-gel method. Results of XRD, FT–IR and TPR studies also confirm this conclusion.

4.1.3. Catalytic activity tests

DRM reaction was carried out using $LaNi_xAl_{1-x}O_3$ catalysts synthesized by sol-gel method, using a feed molar ratio of $CH_4/CO_2/N_2$ =1/1/1. Prior to activity test, the catalysts were reduced *in situ* at 600 °C for 6h in 60% H_2 balanced N_2 stream. The evaluation study was carried out at 800 °C for all the catalysts. Activity profiles of all the catalysts expressed as CH_4 and CO_2 conversion during the DRM reaction are displayed in Figure 4.1.8. The conversions increased with Ni content till x=0.3 and then started decreasing. The performance of catalyst with x=0.4 was found to be close to that of catalyst with x=0.3. Conversions of CH_4 and CO_2 reached values of 93 and 96%

respectively for catalyst with x=0.3 and syngas ratio reached 0.97, a value close to the theoretical value of 1 for synthesis gas produced in this reaction.

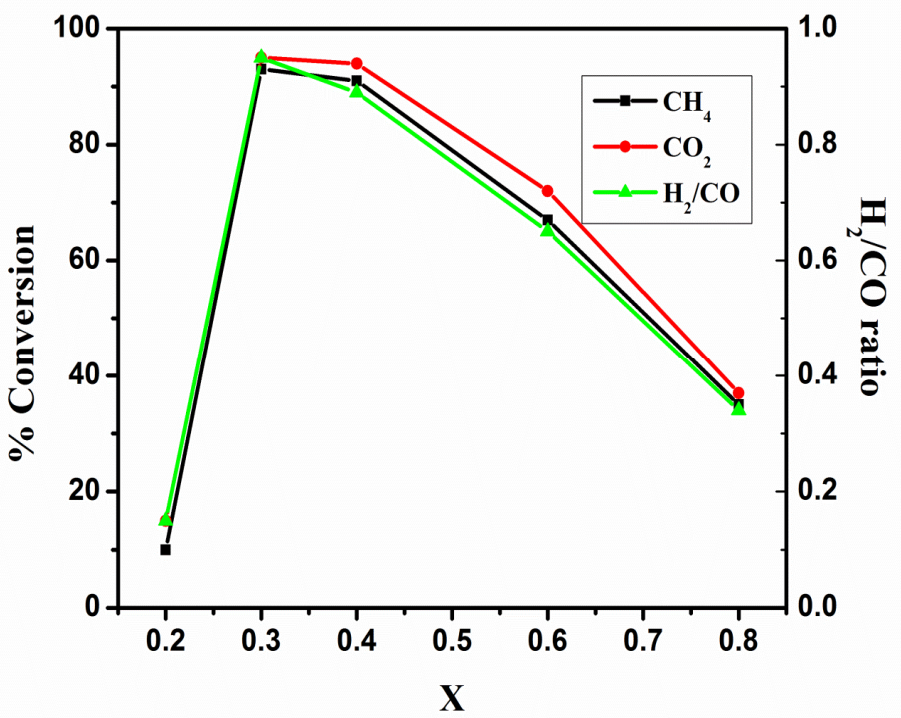

Figure 4.1.8: Catalytic activity study on DRM reaction over $LaNi_xAl_{1-x}O_3$ catalysts synthesized by sol-gel method. (Temperature = 800 °C).

Characterization studies on these catalysts revealed the formation of trimetallic perovskite phase at low Ni ratios. In the XRD studies, the characteristic peak related to the $LaNiO_3$ shifted continuously with the increase of Al indicating the formation of trimetallic perovskite phase. This changed the reduction behaviour of the catalysts. Formation of such trimetallic spices delivered highly dispersed Ni, which causes increase in the catalytic activity.

Table 4.1.3 describes the H_2 pulse chemisorption data, the dispersion of the active metal Ni along with the particle size of the active metal. From these values it is clearly observed that the decrease in metal particle size not only increases the dispersion of metal but also enhances the catalytic activity.

Table 4.1.3: Dispersion and particle size of $LaNi_xAl_{1-x}O_3$ catalysts of catalysts synthesized by sol-gel method.

S. No.	Catalyst	Dispersion (%)	Particle size (Å)
1	$LaNi_{0.2}Al_{0.8}O_3$	18.6	55.2
2	$LaNi_{0.3}Al_{0.7}O_3$	35.6	28.9
3	$LaNi_{0.4}Al_{0.6}O_3$	32.0	32.2
4	$LaNi_{0.6}Al_{0.4}O_3$	22.4	45.9
5	$LaNi_{0.8}Al_{0.2}O_3$	20.1	51.1

4.1.4. Carbon analysis of used $LaNi_xAl_{1-x}O_3$ catalysts

Table 4.1.4: Carbon deposition on the $LaNi_xAl_{1-x}O_3$ catalysts synthesized by sol-gel method after DRM reaction.

S. No.	Catalyst	Carbon (%)
1	$LaNi_{0.2}Al_{0.8}O_3$	3.14
2	$LaNi_{0.3}Al_{0.7}O_3$	2.89
3	$LaNi_{0.4}Al_{0.6}O_3$	2.93
4	$LaNi_{0.6}Al_{0.4}O_3$	2.56
5	$LaNi_{0.8}Al_{0.2}O_3$	3.50

The coke formed during the DRM reaction (over a period of 5h) was estimated with CHNS analyzer and the data is presented in Table 4.1.4. All the catalysts showed lower values of carbon deposition due to the enhanced dispersion of Ni particles which are produced by the formed trimetallic perovskite catalysts.

4.1.5. Conclusions

$LaNi_xAl_{1-x}O_3$ catalysts ($0 \leq x \leq 1$) synthesized by sol-gel method are studied for the DRM reaction. The formation of trimetallic perovskite type oxide phase when $0.2 < x < 0.8$ is confirmed by XRD, TPR, FT–IR and XPS techniques. These catalysts

produced well dispersed Ni metallic species upon reduction. Small metal particles appeared to enhance the catalytic activity for the reforming reaction. Among the series of catalysts studied, $LaNi_{0.3}Al_{0.7}O_3$ (GC chromatograph has been provided in Appendix section Figure 1) showed the highest activity in terms of CH_4 and CO_2 conversions as well as the production of synthesis gas. It is also found that the Al modified $LaNiO_3$ trimetallic perovskite increased the stability of the catalyst. These catalysts have also shown increased resistivity towards coke formation during the DRM reaction.

Section 4.2: Al modified $LaNiO_3$ catalysts synthesized by hydrothermal method

4.2.1. Introduction

Previous literature on the dry reforming of methane suggested that the deactivation of catalysts is mainly due to sintering and coking [43]. It is observed that these problems can be minimized by increasing the active metal dispersion.

In this section, characterization and activity studies on Al modified $LaNiO_3$ perovskite catalysts synthesized by hydrothermal method are presented, procedure followed for the synthesis is discussed in Chapter 3, Section 3.1.2b.

4.2.2. Results and Discussion

4.2.2a. Specific surface area measurements

Table 4.2.1 shows the specific surface areas of $LaNi_xAl_{1-x}O_3$ catalysts synthesized by hydrothermal method. The catalysts exhibited low values of specific surface area. The catalyst with x=0.2 showed 13.6 m^2/g surface area. With the increase in Ni ratio, the surface area decreased gradually reaching a value of 1.9 m^2/g for x=0.8. Khalesi et al., also observed low surface areas in their perovskite systems [29]. It is known that the surface area of catalysts is dependent on the calcination temperature. This was experimentally proved by the Valderrama et al., in their study on Sr doped $LaNiO_3$ perovskite [44].

Table 4.2.1: Specific surface area of hydrothermally synthesized $LaNi_xAl_{1-x}O_3$ catalysts determined by BET method.

S. No.	Catalyst	Specific surface area (m^2/g)
1	$LaNi_{0.2}Al_{0.8}O_3$	13.6
2	$LaNi_{0.3}Al_{0.7}O_3$	11.2
3	$LaNi_{0.4}Al_{0.6}O_3$	10.2
4	$LaNi_{0.6}Al_{0.4}O_3$	9.6
5	$LaNi_{0.8}Al_{0.2}O_3$	1.9

In the studies presented in this thesis, the catalysts were calcined at high temperature (800 °C). The observed low surface areas may be attributed to this reason. According to Khalesi et al., the low surface area materials are more suitable as catalysts, as they suppress the side reactions during the dry reforming reaction (DRM) [45]. The decrease in surface area with increasing Ni ratio suggests the formation of particles of larger size or decreased porous nature of the material.

4.2.2b. X–ray diffraction studies

The XRD patterns of the $LaNi_xAl_{1-x}O_3$ catalysts synthesized by hydrothermal method are shown in Figure 4.2.1.

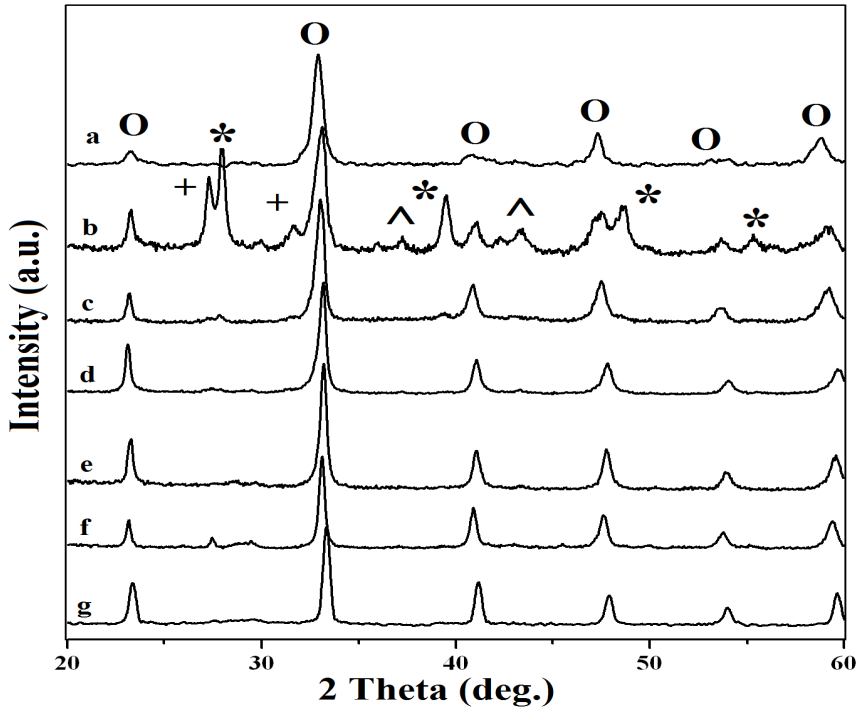

Figure 4.2.1: XRD patterns of $LaNi_xAl_{1-x}O_3$ catalysts synthesized by hydrothermal method. a) x = 1; b) x = 0.8; c) x = 0.6; d) x= 0.4; e) x = 0.3; f) x = 0.2; and g) x = 0. (*) monoclinic La_2O_3, (+) cubic La_2O_3, (O) perovskite (a= $LaNiO_3$,g= $LaAlO_3$), (^)NiO.

In the catalysts with x=1, the diffraction peaks appearing at 2θ = 23.6, 32.92, 41.2, 47.3 and 58.9° could be ascribed to the formation of $LaNiO_3$ (JCPDS 34–1028). For the catalyst with x=0, the peaks appearing at 2θ = 24.1, 33.55, 42.3, 48.0 and 59.5° confirm

the formation of another bimetallic perovskite, $LaAlO_3$ [25]. Intense peak observed in all the patterns showed a progressive shift from 32.92 to 33.34° with decrease in active metal (Ni) ratio (Figure 4.2.2). This type of shift towards high angle was also identified by Moradi et al. [25].

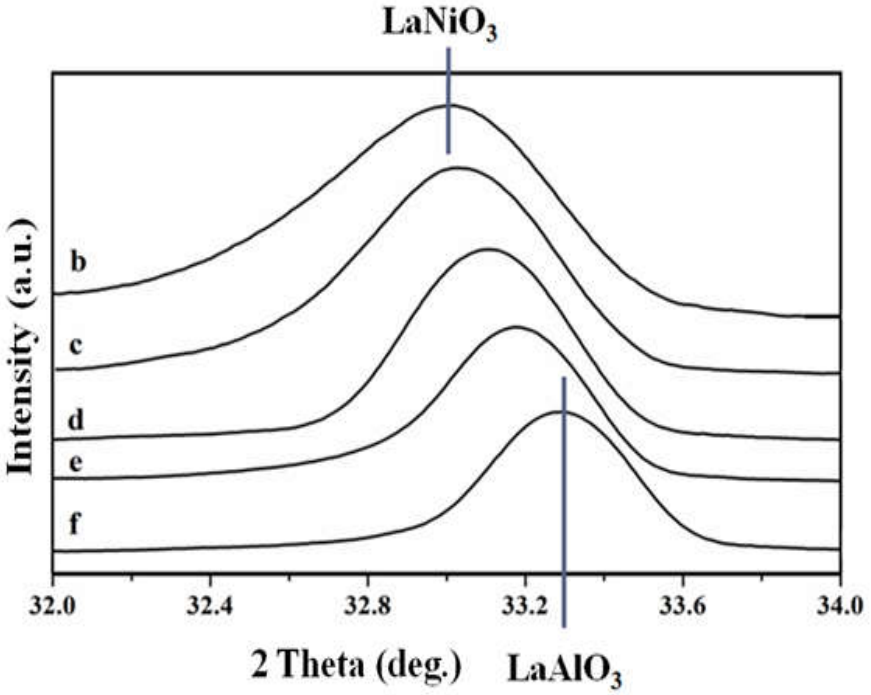

Figure 4.2.2: Zoomed XRD patterns of $LaNi_xAl_{1-x}O_3$ catalysts synthesized by hydrothermal method. b) x = 0.8; c) x = 0.6; d) x= 0.4; e) x = 0.3 and f) x = 0.2.

This shift indicates that the material acquires $LaAlO_3$ form from $LaNiO_3$ form through the formation of the trimetallic $LaNi_xAl_{1-x}O_3$, as the Ni content decreases. This type of trimetallic perovskite phase formation was not only identified in the case of Al modified Ni catalysts by Moradi et al. but also in case of Fe modified Ni catalysts studied by Provendier et al. [46]. With increase in active metal ratio, apart from the peaks due to perovskite, the diffraction patterns related to the individual metal oxides were also observed. Especially, when x=0.8 (Fig.4.1.1b), the catalyst exhibited peaks at 2θ = 27.92, 39.54, 48.77, 55.31 and 59.31°. These crystalline phases can be ascribed to the monoclinic La_2O_3 (JCPDS 220641), whereas peaks at 2θ = 27.28 and 31.7° can be

assigned to the cubic La_2O_3 (JCPDS 220369) and the peaks at 2θ = 43.21 and 37.27° to the presence of NiO phase (JCPDS 780643 file).

The crystallite size of perovskite catalysts was calculated using Scherrer equation and the values are presented in Table 4.2.2. A continuous shift in the lattice parameter was observed displaying a continuous decrease in the crystallite size upto x=0.6 and an increase with further increase in Ni content.

Table 4.2.2: Lattice parameter and crystallite size of $LaNi_xAl_{1-x}O_3$ catalysts synthesized by hydrothermal method.

S. No.	Catalyst	Lattice parameter (Å)	Crystallite Size (nm)
1	$LaNi_{0.2}Al_{0.8}O_3$	3.793	23.89
2	$LaNi_{0.3}Al_{0.7}O_3$	3.802	21.26
3	$LaNi_{0.4}Al_{0.6}O_3$	3.811	16.86
4	$LaNi_{0.6}Al_{0.4}O_3$	3.821	12.66
5	$LaNi_{0.8}Al_{0.2}O_3$	3.827	28.13

4.2.2c. Temperature programmed reduction studies

Particles in metallic state are considered to be the active species for the DRM reaction [29,34]. It is interesting to focus attention on the reduction behaviour of the catalysts. Figure 4.2.3 shows the H_2–TPR patterns of $LaNi_xAl_{1-x}O_3$ catalysts synthesized by hydrothermal method. The inset figure corresponds to the TPR of $LaNiO_3$ (x=1). It shows two major reduction zones: the first zone with peak maximum at ~450 °C and the second zone with peak maximum falling at ~600 °C.

Batiot–Dupeyrat et al. [47] and Gallego et al. [31] studied the reduction behaviour of $LaNiO_3$ perovskite and proposed a mechanism. According to them, the perovskite phase gets reduced in three steps $LaNiO_3 \rightarrow La_4Ni_3O_{10} \rightarrow La_2NiO_4 \rightarrow Ni^0$. Whereas in

the studies conducted by Rida et al. [32], and Lima et al. [30], the reduction of perovskite proceeded in two stages N^{3+} ($LaNiO_3$) → Ni^{2+} ($La_2Ni_2O_5$) → Ni^0.

From the above observations, first zone can be attributed to the reduction of Ni^{3+} to Ni^{2+}. The doublet peak observed in this zone may be due to the reduction of segregated NiO along with Ni^{3+} to Ni^{2+} reduction of the perovskite. Second zone is due to the reduction of Ni^{2+} species (in the brownmillerite phase) to Ni^0. Two–stage reduction of NiO in perovskite system was also reported earlier by Moradi et al., Rida et al., and Lima et al., [25,32,30]. An indirect confirmation of reduction of bimetallic perovskite phase is the agreement between expected and observed value of intensity ratio of the second peak to first peak which is 2 [33].

The two-stage reduction pattern can be formulated as follows.

$$2LaNiO_3 + H_2 \rightarrow La_2Ni_2O_5 + H_2O \qquad \text{--- 4.6}$$

$$La_2Ni_2O_5 + 2H_2 \rightarrow La_2O_3 + 2Ni + 2H_2O \qquad \text{--- 4.7}$$

Non–adherence to the intensity ratio of 2 implies that the materials are not true bimetallic perovskite oxide. With the addition of 3rd metal, a clear shift appeared in the high temperature peak maximum (600 °C of $LaNiO_3$). Similar observations in the shift of the peak position (650–750 °C) were made by previous researchers [25,35]. The high temperature shift signifies strong interaction of Ni with the other metals and the eventual formation of trimetallic (La–Ni–Al) perovskite phase. The changes associated with second zone reduction illustrate the stability of perovskite system, as suggested by Rodriguez et al., [48]. Thus, it can be expected that, there is formation of the trimetallic perovskite oxide of various proportions in the $LaNi_xAl_{1-x}O_3$ catalysts with intermediate x values.

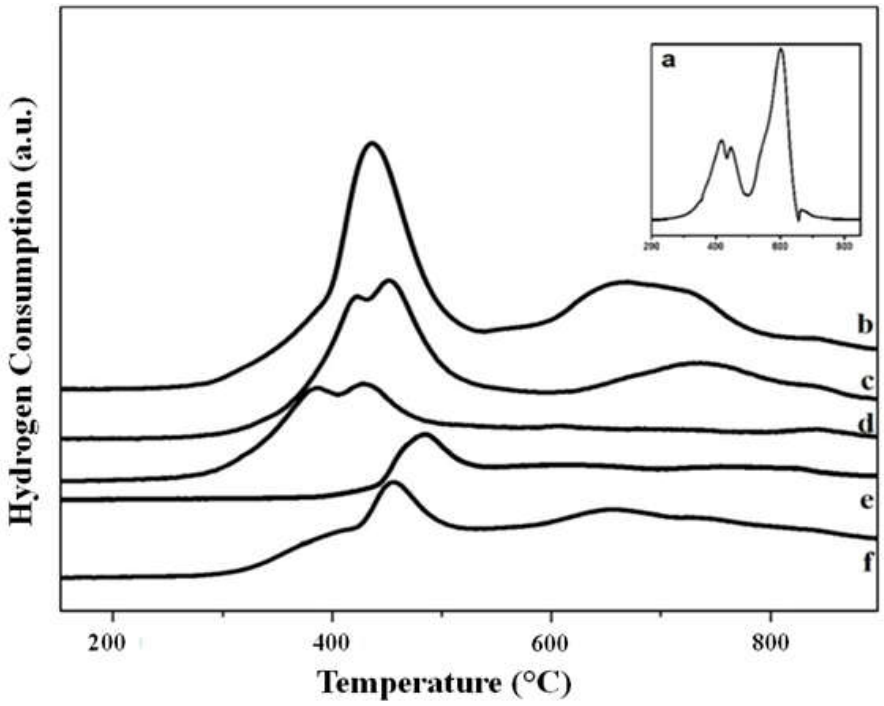

Figure 4.2.3: TPR profiles of $LaNi_xAl_{1-x}O_3$ catalysts synthesized by hydrothermal method. a) x = 1; b) x = 0.8; c) x = 0.6; d) x= 0.4; e) x = 0.3; and f) x = 0.2.

For catalysts with x=0.8 and x=0.2, only one single reduction peak in the first zone was observed. This may be due to the formation of bimetallic perovskite phases in both high and low Ni ratio catalysts. As described in the previous paragraphs, the XRD patterns of these two catalysts were identified as the bimetallic $LaNiO_3$ and $LaAlO_3$ perovskites, respectively. On the other hand, the trimetallic perovskite phase was observed in all the other catalysts.

4.2.2d. X–ray photoelectron spectroscopic studies

Figure 4.2.4 shows La 3d XP spectra of $LaNi_xAl_{1-x}O_3$ catalysts synthesized by hydrothermal method. Binding energies at ~835–839 eV and ~850–851 eV correspond to La $3d_{5/2}$ and La $3d_{3/2}$, respectively [39]. Sutthiumporn et al. [49], mentioned that the low electron density around metal leads to increase in the binding energy. Thus, the high binding energy values observed might have been the result of electron deficiency around

La due to its interactions with other metals [50,51]. Among the three metals La, Ni and Al, La (EN=1.1) has the lowest electronegativity (EN). So the transfer of electron from La to Ni (EN=1.9) or Al (EN=1.5) is favourable. Thus, it could be expected that this phase corresponds to lanthanum aluminate. The La $3d_{5/2}$ binding energy value for lanthanum aluminate is 834 eV, which is smaller than the present value. Sanchez–Sanchez et al., also observed higher values in the La 3d XP spectra of their perovskite samples [40].

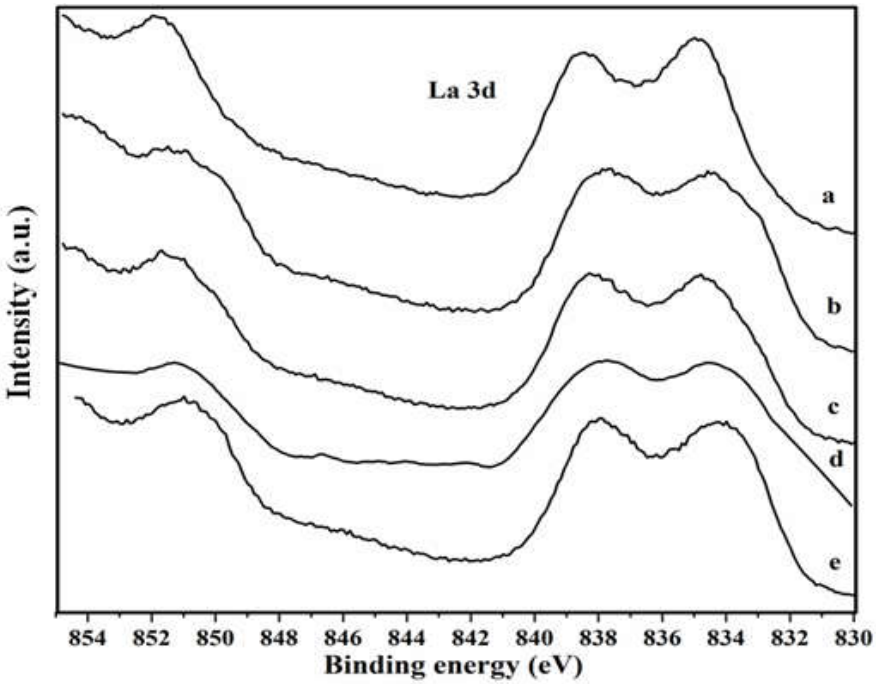

Figure 4.2.4: La 3d XP spectra of $LaNi_xAl_{1-x}O_3$ catalysts synthesized by hydrothermal method. a) x = 0.8; b) x = 0.6; c) x= 0.4; d) x = 0.3 and e) x = 0.2.

The Ni 2p XPS spectra of $LaNi_xAl_{1-x}O_3$ mixed oxide samples are depicted in Figure 4.2.5. Literature suggests that Ni is highly stable in its 2+ oxidation state i.e., NiO. The Ni $2p_{3/2}$ peak in NiO core level binding energy appears at 854 eV [52].

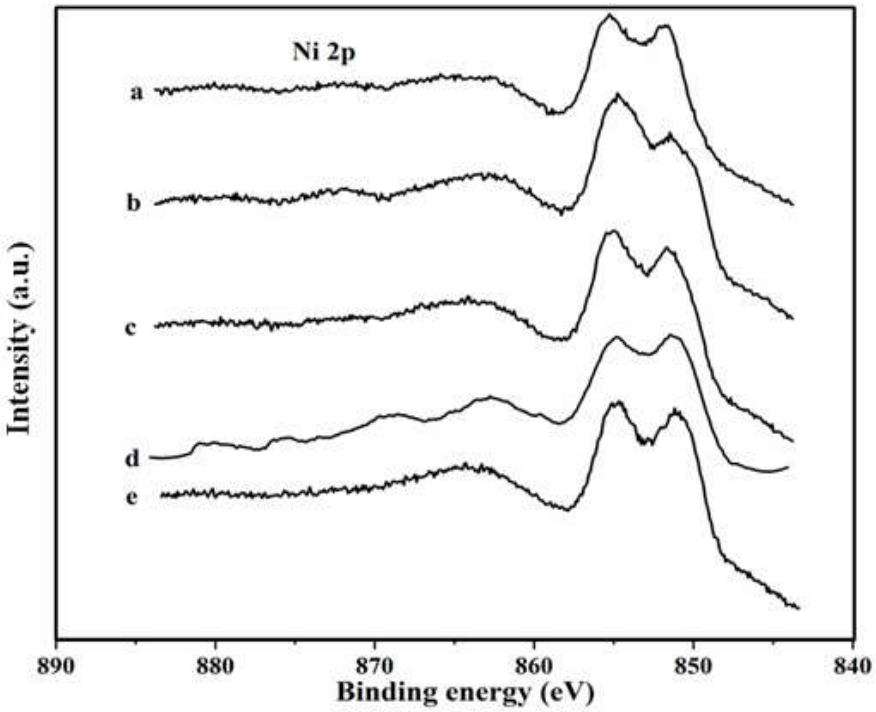

Figure 4.2.5: Ni 2p XP spectra of $LaNi_xAl_{1-x}O_3$ catalysts synthesized by hydrothermal method. a) x = 0.8; b) x = 0.6; c) x= 0.4; d) x = 0.3 and e) x = 0.2.

According to Khalesi et al. [29], La–Ni–Al trimetallic perovskite type oxide catalysts exhibit Ni in its Ni^{3+} oxidation state. In this work, the high intense doublet with binding energies at ~851 and 855 eV can be assigned to Ni $2p_{3/2}$ and the broad band appearing at the binding energy value of 872 eV at high x values (x=0.6 and x=0.8) can be assigned to $Ni2p_{1/2}$ core level. Since these values did not correspond to that of Ni in its 2+ state, it can be expected that Ni exists in higher oxidation state. With increase in Ni content there is a continuous shift in the Ni $2p_{3/2}$ binding energy towards right, further indicating the stabilization of Ni in higher oxidation state (3+). The 2 eV increment of binding energy in Ni 2p spectra in the present study indicates the presence of Ni^{3+} or/and Ni^{2+} on the surface of the catalysts [32].

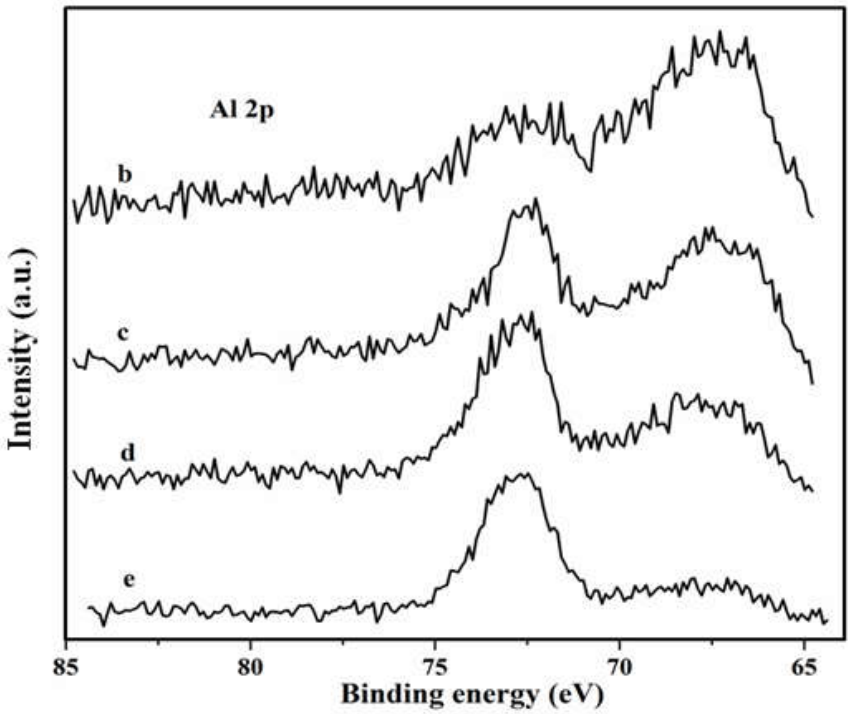

Figure 4.2.6: Al 2p XP spectra of $LaNi_xAl_{1-x}O_3$ catalysts synthesized by hydrothermal method. b) x = 0.8; c) x = 0.6; d) x= 0.4; and e) x = 0.2.

Figure 4.2.6 shows XP spectra of Al 2p along with Ni 3p of the catalysts. Djebaili et al. [53] made an in–depth analysis of the Al_2O_3 XP spectra and revealed that the binding energy at 74.83 eV was due to the Al–O state. Al–M state (M=La or Ni) yielded binding energy at 72.30 eV. The high electronegative oxygen adjacent to Al causes high electron deficiency around Al and makes the binding energy shift to high binding energy in the case of Al–O state. On the other hand in Al–M state, the metal interactions may not affect much on the Al electron environment. In the present study, the bands observed at 72.6 eV for Al 2p XP spectra indicates that Al is surrounded by other metal. The peak corresponding to Al shifted to its right with the increase in Al content. This shift is due to the increase in electron density on Al i.e., abstracting the electrons from neighbouring La (a low electronegative element than Al). The other binding energy peak at ~67 eV can be ascribed to Ni 3p core level electrons. The intensity of this peak

increased continuously with the addition of Ni. The increase in Ni 3p binding energy was also observed by Bulusu et al [42]. They concluded that the incorporation of Al into perovskite may lead to the increase in the oxidation state of Ni [42]. This observation is in good agreement with the XRD results of these samples where the formation of trimetallic phase is clearly identified.

Figure 4.2.7 displays O 1s core level XP spectra of the calcined catalysts. Two bands were observed at binding energies 528 and 531 eV; the lower one corresponding to oxygen in crystalline framework and the higher one due to defect oxygen sites or hydroxyl groups around metals [42,54]. The catalysts with x = 0.3, 0.4 and 0.6 showed both types of oxygen species. Whereas the catalysts with x = 0.2 and 0.8 showed only one peak related to crystalline oxygen. The defective oxygen sites appear due to the incorporation of metal into perovskite phase. A close observation on the lower binding energy band reveals that there is a small shift towards right i.e., decrease in binding energy with increase in Ni content.

From the above studies it can be inferred that the La 3d and Ni 2p XP spectra showed high binding energy values due to electron deficiency around the metals, whereas in Al 2p and O 1s spectra with low binding energy indicate the existence of electron rich species. The increase in electron density in catalysts with Ni content from x = 0.3 to 0.6 is mainly due to the oxygen in crystalline frame work. These results correlate well with the results of the diffraction studies, where the bimetallic perovskite phases were observed in low and high Ni content catalysts (x=0.2 and 0.8). On the other hand, catalysts with x=0.3 to 0.6 Ni contents form trimetallic perovskite phase.

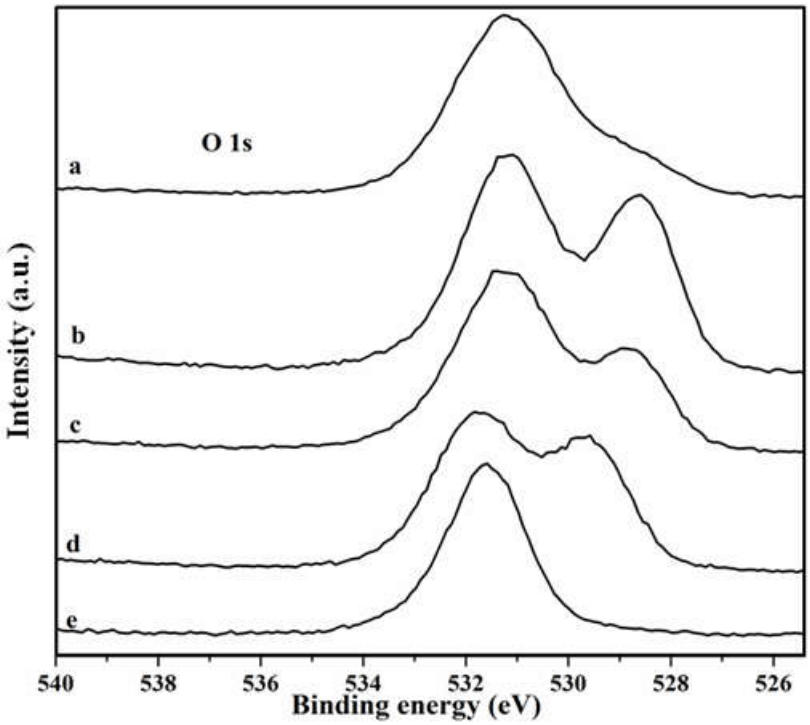

Figure 4.2.7: O 1s XP spectra of $LaNi_xAl_{1-x}O_3$ catalysts synthesized by hydrothermal method. a) x = 0.8; b) x = 0.6; c) x= 0.4; d) x = 0.3 and e) x = 0.2.

The carbon related binding energy peaks were observed at 284 and 288 eV in the literature. These peaks arise due to the C–H and C–O species, respectively. According to Cruz et al., basic materials like La readily adsorb the atmospheric CO_2 (when exposed to air) and form the carbonate species thereby giving rise to a high binding energy peak at 289 eV [55]. In this study, all the synthesized catalysts exhibited two peaks with binding energies 284 and 289 eV due to the hydrocarbon contamination and carbonate species formation, respectively. The adsorption of atmospheric CO_2 on freely available lanthana is possible [55]. In the spectra shown in Figure 4.2.8, the peak corresponding to carbonate ion decreased in its intensity with the increase in Ni, indicating that the availability of free lanthana was reduced by the formation of perovskite phase.

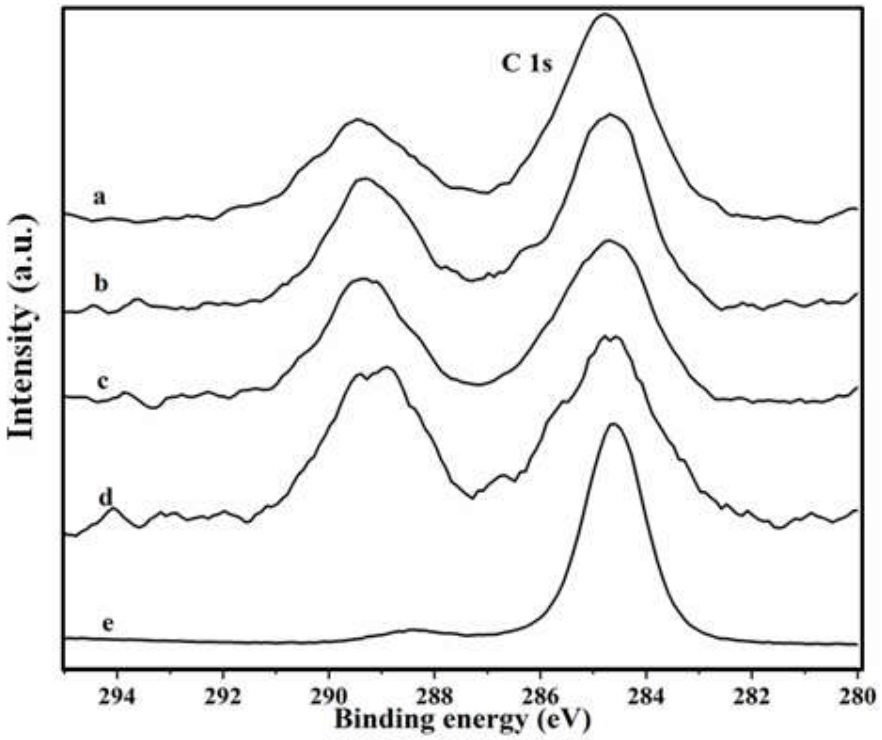

Figure 4.2.8: C 1s XP spectra of $LaNi_xAl_{1-x}O_3$ catalysts synthesized by hydrothermal method. a) x = 0.8; b) x = 0.6; c) x= 0.4; d) x = 0.3 and e) x = 0.2.

On the basis of the results of XPS study, a hypothetical chain link of metals and oxygen can be deduced as Ni–O–La–Al. The electron deficiency on La is mainly due to the direct contact with high electronegative elements O and Al, and the electron deficiency on Ni is due to the direct contact with O. It is clearly seen in the La and Ni XP spectra in terms of high binding energies. The electron richness of Al is due to the direct contact with low electronegative element La. The O XP spectra gave a clear indication of electron richness. This confirms the trimetallic perovskite formation as also evidenced from the XRD data.

4.2.2e. NH_3–Temperature programmed desorption (NH_3–TPD) studies

Figure 4.2.9 illustrates NH_3–TPD curves of $LaNi_xAl_{1-x}O_3$ catalysts synthesized by hydrothermal method. The patterns essentially exhibited two peaks; the low temperature and high temperature peaks due to weak and strong acid sites, respectively. It can be seen

from the figure that the two bimetallic perovskites (x=0 and 1) had their peaks falling in the temperature regions of 200–400 and 700–800 ºC. An important observation is that the catalysts with x=0.2 to 0.8 displayed their two peaks in between these two regions indicating changes in surface acidity. This implies that they were not in the bimetallic form, but probably in the trimetallic oxide phase. Both peak positions are shifted progressively towards the higher regions.

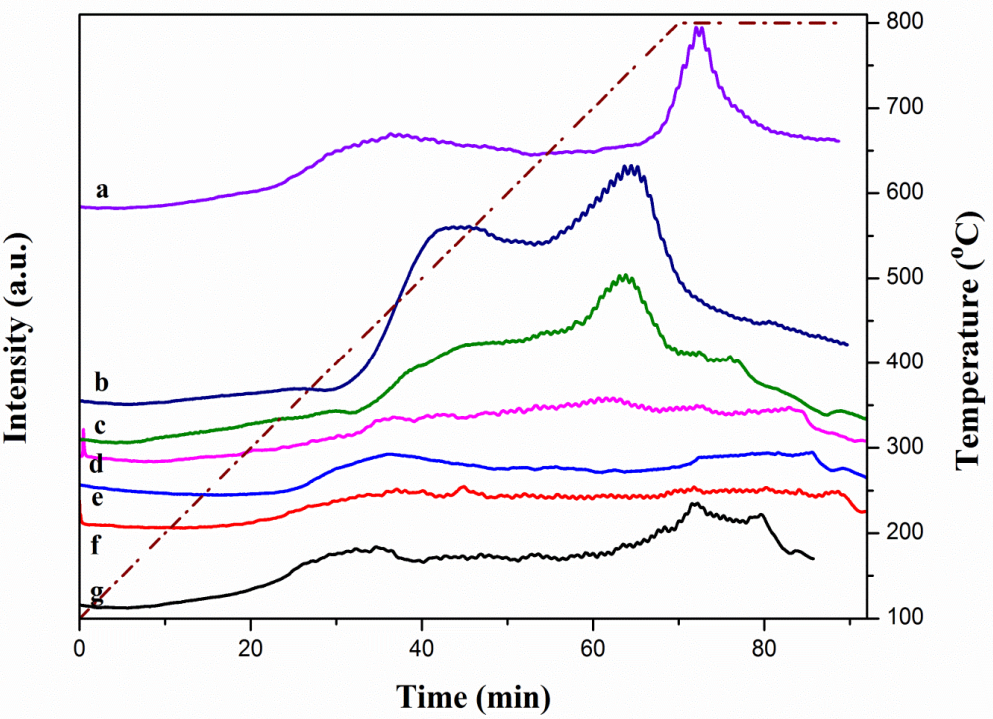

Figure 4.2.9: NH_3–TPD patterns of $LaNi_xAl_{1-x}O_3$ catalysts synthesized by hydrothermal method. a) x = 1; b) x = 0.8; c) x = 0.6; d) x= 0.4; e) x = 0.3; f) x = 0.2; and g) x = 0.

The presence of Lewis acid sites in the low temperature region and the Brønsted sites in the high temperature region was suggested by Cheng et al. [41,42] in their work on Co–Ni/Al_2O_3 catalysts. Cheng et al. also explained that the changes in the acidic sites were due to the metal–metal and/or metal oxide–aluminium interactions. Table 4.2.3 shows the total acidity of the catalysts. The variation in acidity may be due to the change in the nature of interactions among metals. These observations are in corroboration with

the results obtained from XPS and XRD analysis, where the formation of trimetallic perovskites was proposed.

Table 4.2.3: Total acidity of $LaNi_xAl_{1-x}O_3$ catalysts synthesized by hydrothermal method.

S. No.	Catalyst	Total acidity (mmol/g)
1	$LaNi_{0.2}Al_{0.8}O_3$	0.49917
2	$LaNi_{0.3}Al_{0.7}O_3$	0.44735
3	$LaNi_{0.4}Al_{0.6}O_3$	0.42226
4	$LaNi_{0.6}Al_{0.4}O_3$	0.41073
5	$LaNi_{0.8}Al_{0.2}O_3$	0.62117

4.2.2f. Fourier transform infrared spectroscopy studies

FT–IR spectra of $LaNi_xAl_{1-x}O_3$ catalysts synthesized by hydrothermal method are presented in Figure 4.2.10. These bands can be divided into four zones, with 2–3 peaks in each zone. In the first zone, the band at ~3500 cm^{-1} is associated with the O–H stretch of intermolecular hydrogen bonds or molecular water.

In the second zone, strong and sharp absorption bands appeared at ~1484 and ~1382 cm^{-1} which can be ascribed to the asymmetric and symmetric COO^- stretching modes of the coordinated carboxylate groups existing even after calcination at high temperature. Similar results are observed by Moradi et al. in their studies on La–Ni–Al perovskite catalysts prepared by sol-gel method [25,36]. The third zone, comprises three absorption bands at ~1187, 1103 and 1063 cm^{-1} corresponding to the Al–OH bending mode [37]. With increase in the Ni ratio, the bands related to Al–OH decreased in their intensity. In the fourth zone, the two absorption peaks appearing at ~678 and 436 cm^{-1} can be assigned to AlO_6 octahedral in $LaAlO_3$ [36,38]. Zhou et al. [36], in their studies on $LaAlO_3$ prepared by EDTA method, observed bands related to $LaAlO_3$ at 440 and 656 cm^{-1}. In the present study, these peaks decreased in their intensity considerably with

increase in Ni ratio. Small traces of nitrates were also observed in low Ni containing catalysts with peaks at ~870 and 807 cm^{-1}. These results are in agreement with the studies carried out by other researchers.

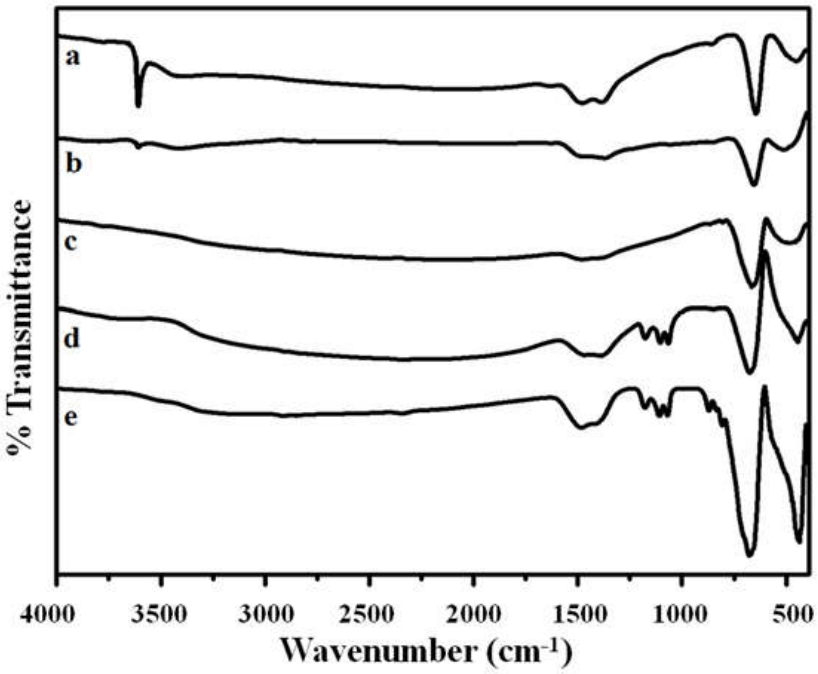

Figure 4.2.10: FT–IR profiles of $LaNi_xAl_{1-x}O_3$ catalysts synthesized by hydrothermal method. a) x = 0.8; b) x = 0.6; c) x= 0.4; d) x = 0.3; and e) x = 0.2.

4.2.2g. Scanning electron microscopy studies

The morphology changes in $LaNi_xAl_{1-x}O_3$ catalysts synthesized by hydrothermal method were studied by SEM technique (Figure 4.2.11). The catalysts showed porous structure, as also reported earlier by Khalesi et al [45]. Normally, when metal nitrates are used as precursor agents, pores are formed during the decomposition of nitrates when subjected to high temperature calcination [29,45]. The bright spots observed in the images are attributed to active metal oxide species. As the amount of Ni is increased, the bright spots related to NiO spices grew bigger in size signifying the formation of bulk NiO. This observation correlates well with the XRD studies where increase in Ni ratio resulted in the appearance of individual oxide phases along with the perovskites.

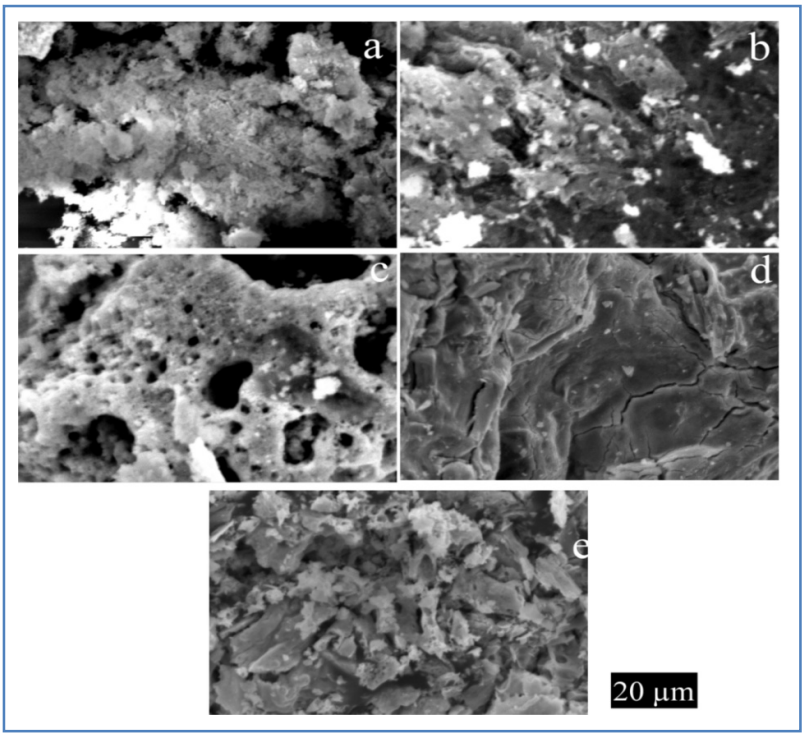

Figure 4.2.11: SEM images of $LaNi_xAl_{1-x}O_3$ catalysts synthesized by hydrothermal method. a) x = 0.8; b) x = 0.6; c) x= 0.4; d) x = 0.3 and e) x =0.2.

4.2.3. Catalytic activity studies of $LaNi_xAl_{1-x}O_3$ on DRM reaction

Methane reforming reaction with carbon dioxide is studied over the $LaNi_xAl_{1-x}O_3$ catalysts synthesized by hydrothermal method, with a feed molar ratio of CH_4/CO_2=1. The diluent nitrogen is also used with the same flow rate as CH_4. Before the start of the reaction, the catalyst was reduced *in situ* in a mixer of 60% H_2 balanced N_2 stream at 600 °C for 6 h. The activity studies of the catalysts were carried out at 800 °C. Figure 4.2.12 illustrates the variation of catalytic activity during DRM reaction with respect to Ni content in $LaNi_xAl_{1-x}O_3$. The conversion of CH_4 and CO_2 increased with the increase of Ni content from 0.2 to 0.6. Increase in the Ni content enhanced the reactant conversion as well as syngas ratio reaching the optimum values with catalyst having x value of 0.6. The conversion of CH_4 and CO_2 are found to be 94 and 97%, respectively.

The syngas ratio reached a maximum value of 0.98, which is close to the theoretical value of unity.

Strong metal–support interactions established by trimetallic perovskite phase seem to decrease the Ni particle size thereby increasing its dispersion [7]. Sutthiumporn et al., [56] studied the effect of substitution of Cu and Fe in the perovskite system and found enhanced mobility of lattice oxygen. This oxygen species is responsible for the removal of coke formed during the reforming and also improved stability of these catalysts. According to Lima et al. [30], the formed perovskite phase decomposed during reduction thereby transforming the catalyst to Ni supported on La_2O_3 form. The metallic Ni then activates the C–H bond leading to dissociation of CH_4 into CH_x and H_x species. The La based support enhances the CO_2 adsorption and its dissociation to CO with intermediate formation of $La_2O_2CO_3$. The formed CH_x species interacts with the mobile lattice oxygen produced at the metal–support interfacial region to form CH_xO adsorbed species. Finally all these species break down to form syngas [44].

In this study, the presence of trimetallic oxides in the form of crystalline $LaNi_xAl_{1-x}O_3$ perovskite was confirmed by the results on characterization of the catalysts. Upon reduction, the trimetallic perovskite phase decomposed into $Ni/LaAlO_3$ or Ni/La_2O_3. From the above mechanism, it can be concluded that higher amounts of dispersed metallic Ni and the mobile lattice oxygen species are necessary to achieve higher conversions and higher syngas ratio. The mobile oxygen is generated due to the incorporation of metal into perovskite lattice. The dissolution of nickel into the $LaAlO_3$ phase increased up to x value of 0.6 in $LaNi_xAl_{1-x}O_3$. Smaller sized particles of Ni formed during reduction of $LaNi_xAl_{1-x}O_3$ increases the dispersion of Ni.

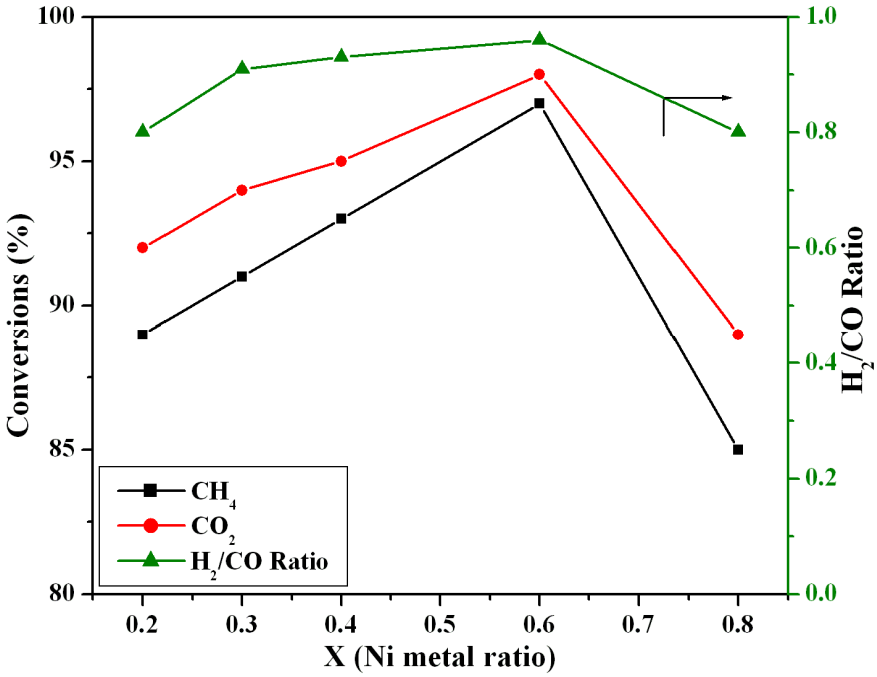

Figure 4.2.12: Catalytic activity study on DRM reaction over $LaNi_xAl_{1-x}O_3$ catalysts synthesized by hydrothermal method (Temperature = 800 °C).

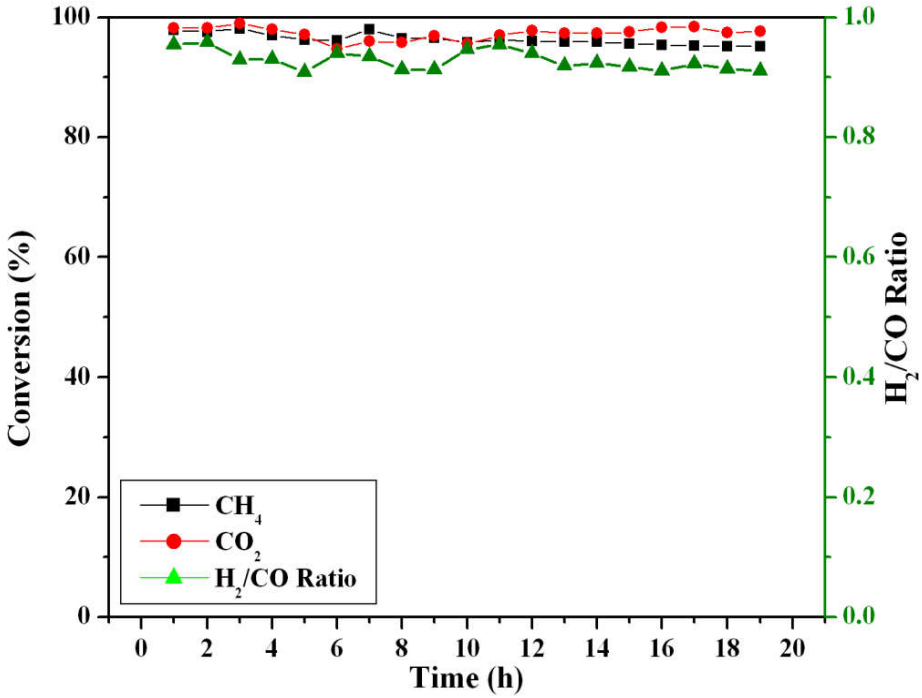

Figure 4.2.13: Time on stream study of DRM reaction over $LaNi_{0.6}Al_{0.4}O_3$ catalyst synthesized by hydrothermal method (Temperature = 800 °C).

Higher CO_2 conversion than that of CH_4 was observed in this study. This suggests that the reforming reaction is accompanied by the reverse water–gas shift (RWGS) reaction. The H_2/CO ratio, which is little lower than 1 also indicates the occurrence of RWGS reaction. The reaction of H_2 with CO_2 produces CO and H_2O. On the other hand, CO_2 molecules strongly interact with La–based materials to form $La_2O_2CO_3$ type species. This phase is highly active to react with carbon deposited on the surface of nickel particles leading to its further decomposition to form CO. Higher CO_2 conversion is influenced by its interaction with La–support, which increases the CO formation and decrease in the syngas ratio. Therefore, higher percentage of CO_2 conversion as well as H_2/CO ratio closer to unity is due to RWGS reaction.

Availability of sufficient mobile lattice oxygen species increases the catalyst stability, as also observed by Sutthiumporn et al. [56]. The best catalyst among the series was considered for the time on stream study. $LaNi_{0.6}Al_{0.4}O_3$ (GC chromatograph has been given in Appendix section Figure 2) catalyst showed remarkable stability for the dry reforming reaction up to the studied period of 20 h (Figure 4.2.13). Crystalline trimetallic phase delivers the formation of small Ni particles and their high dispersion. This prevented ensemble formation leading to increase in the resistance towards coking and sintering.

4.2.4. Characterization of used $LaNi_xAl_{1-x}O_3$ catalysts

4.2.4a. Carbon analysis

Figure 4.2.14 depicts variation in the carbon formation with Ni mole ratio and the corresponding % of dispersion in used $LaNi_xAl_{1-x}O_3$ catalysts. It is found that the carbon formation was dependent on Ni dispersion. Increase in active metal content increased the dispersion up to x=0.6, whereas the amount of carbon formed showed reverse behaviour i.e., decrease with increase in Ni ratio up to x=0.6.

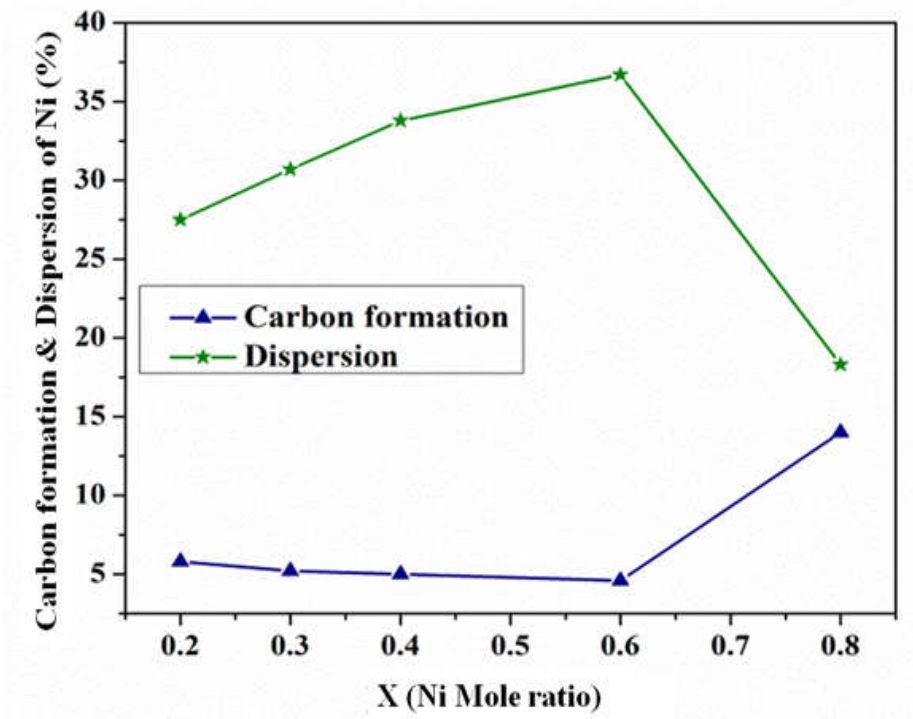

Figure 4.2.14: Variation of carbon formed with change in Ni metal ratio in used $LaNi_xAl_{1-x}O_3$ catalysts.

Beyond the value of x=0.6, the dispersion of Ni decreased drastically. This decreased the resistance to carbon formation. Carbon formation during CH_4 reforming (with CO_2/CH_4 ratios far above unity) is unfavourable at high temperature (730 °C). However, from an industrial perspective, it may be desirable to operate at lower temperatures with CO_2/CH_4 ratios near unity. This condition leads to the conclusion that a reforming catalyst that inhibits carbon formation is essential.

In NH_3 TPD studies two peaks appeared in the low and high temperature region indicating the Lewis sites and the mixture of both Lewis and Brønsted acid sites. According to literature reports, acidic nature of the catalyst results in coke formation [57]. Decrease in acidity is observed till x=0.6. The coke resistance is in good correlation with the acidity.

4.2.4b. X–ray diffraction studies

Figure 4.2.15 illustrates the XRD patterns of the used catalysts. The results obtained revealed that perovskite phase gets regenerated even after the reforming reaction. Studies carried out earlier also reported similar regeneration of perovskite phase after the reforming reaction [23,25]. Along with this, metallic Ni was also observed in the spent catalysts.

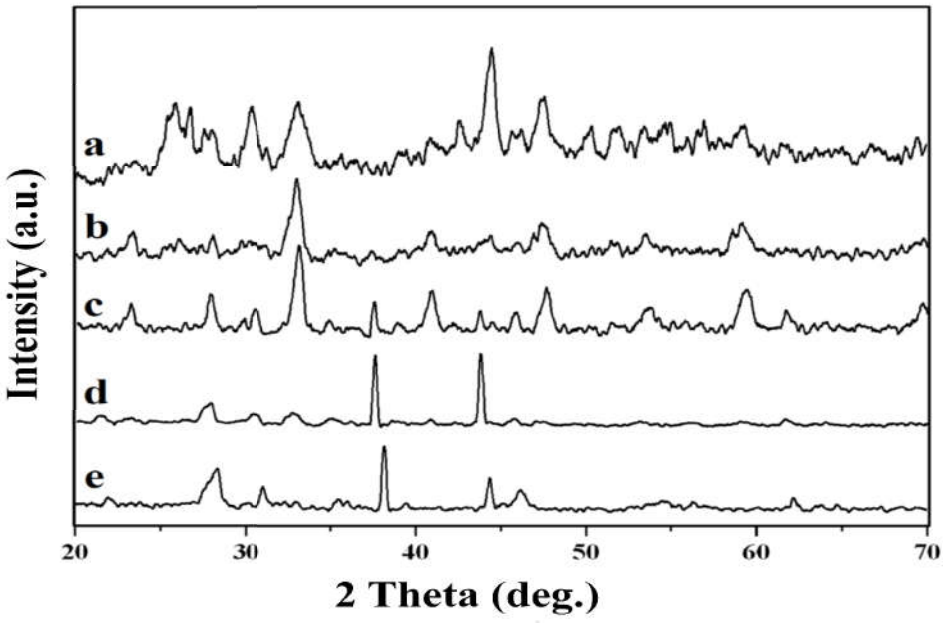

Figure 4.2.15: XRD patterns of $LaNi_xAl_{1-x}O_3$ catalysts after DRM reaction at 800 °C. a) x = 0.8; b) x = 0.6; c) x= 0.4; d) x = 0.3; and e) x = 0.2.

4.2.4c. Scanning electron microscopy studies

Figure 4.2.16 demonstrates the SEM images of the spent catalysts. This analysis clearly reveals the carbon formation on the catalyst surface. Different types of carbon species are observed depending on the composition of the catalyst. $LaNi_{0.2}Al_{0.8}O_3$ gave rise to whisker carbon/carbon nanotubes. Graphene oxide type carbon was noticed in $LaNi_{0.3}Al_{0.7}O_3$ and $LaNi_{0.4}Al_{0.6}O_3$. Amorphous carbon was observed in x= 0.6 and 0.8

catalysts. As suggested by Kang et al. and Kim et al. [58,59], filamentous carbon fibers and amorphous carbon accumulated on the catalyst surface during the reaction. These type of carbon species doesn't show any adverse effect on the catalytic activity.

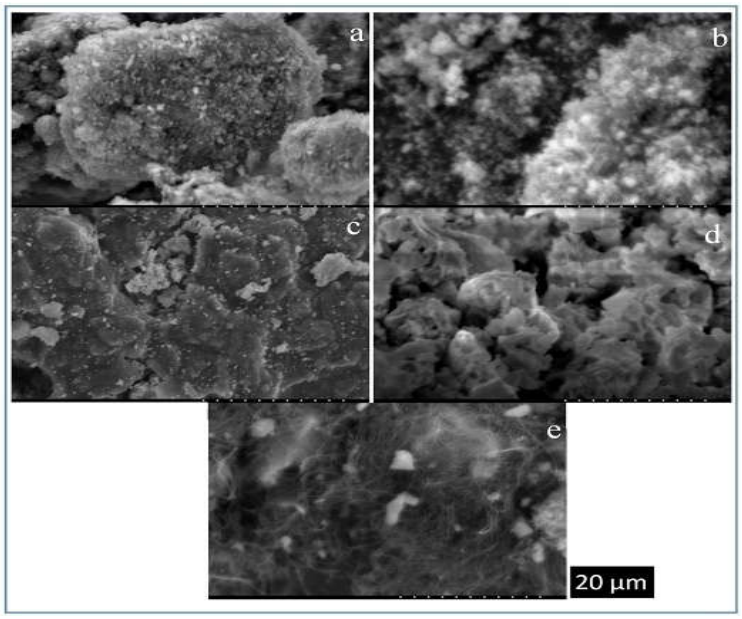

Figure 4.2.16: SEM images of $LaNi_xAl_{1-x}O_3$ catalysts after DRM reaction. a) x = 0.8; b) x = 0.6; c) x= 0.4; d) x = 0.3; and e) x = 0.2.

4.2.4d. Raman spectroscopy studies

Figure 4.2.17 shows the Raman spectra of used $LaNi_xAl_{1-x}O_3$ catalysts after performing the DRM reaction. By comparing the Raman spectra of fresh and used catalysts it is clear that the peaks appearing before 1100 cm^{-1} correspond to the $LaAlO_3$ perovskite, Figure 4.2.18 shows Raman spectra of fresh $LaAlO_3$ samples. The peaks observed after 1100 cm^{-1} could be attributed to carbon formation. As explained by Sadanandam et al. [60], in their study over $Ni/\gamma–Al_2O_3$ catalysts, the carbon peaks formed after the reaction were of two types; one appearing at lower wave length of 1335 cm^{-1} due to the disordered graphite (D band) and the other appearing at higher wave length of 1591 cm^{-1} corresponding to graphitic phase (G band). Further, the graphitic nature of the

formed carbon can be identified by the intensity ratio of the peaks I_D/I_G. Low ratio indicates the existence of disordered carbon formed and vice versa [36].

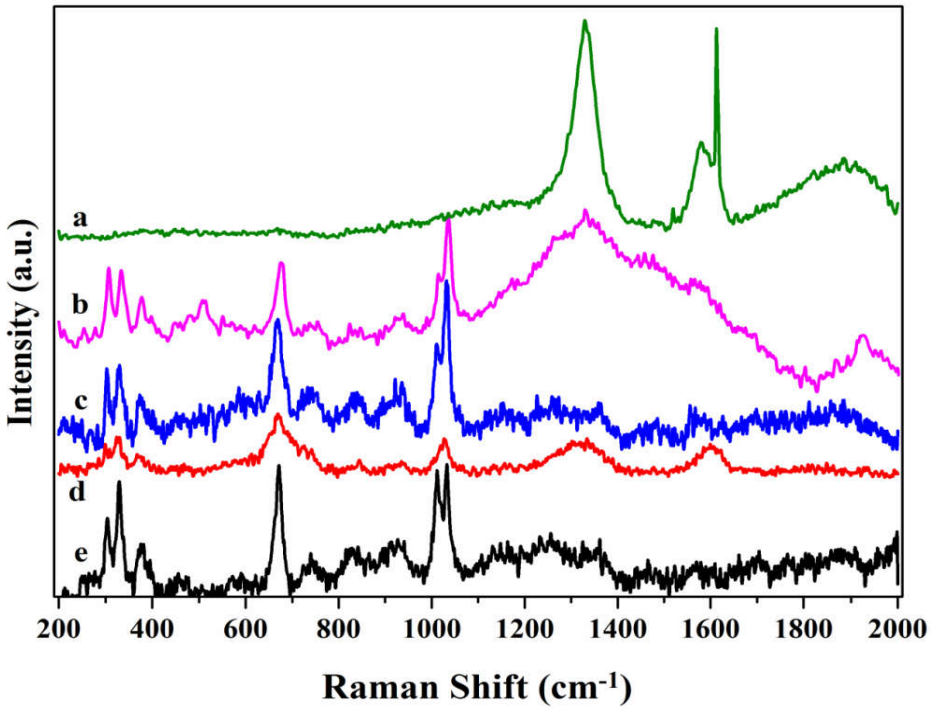

Figure 4.2.17: Raman spectral studies of used $LaNi_xAl_{1-x}O_3$ catalysts after DRM reaction. a) x = 0.8; b) x = 0.6; c) x= 0.4; d) x = 0.3; and e) x = 0.2.

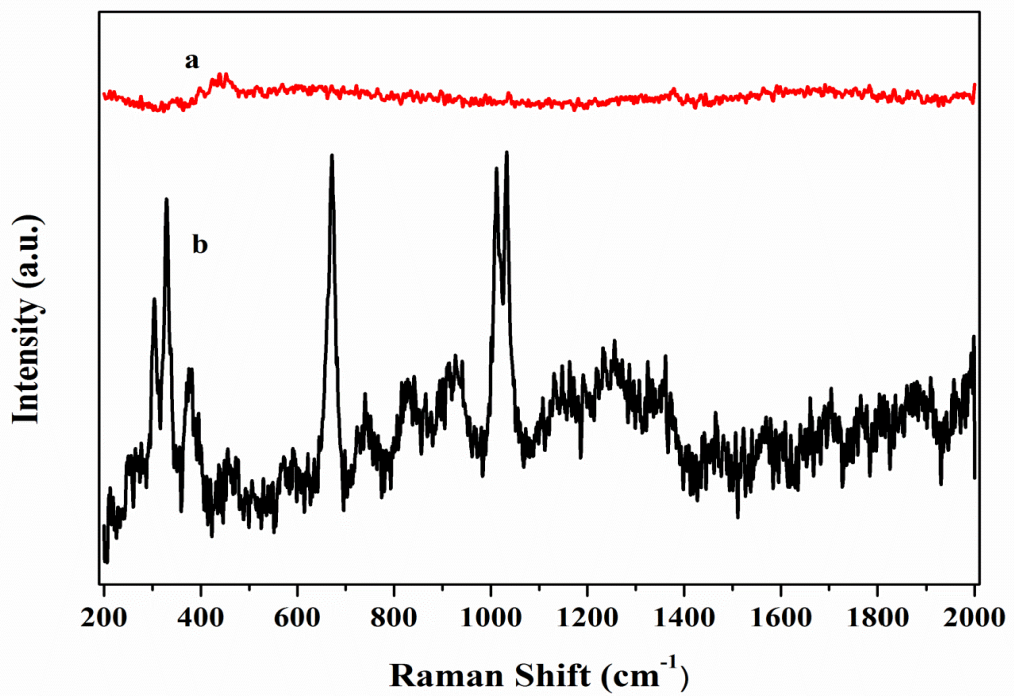

Figure 4.2.18: Raman spectral studies of fresh $LaNi_xAl_{1-x}O_3$ catalysts. a) x = 1 and b) x=0.

The two high intense bands observed at ~1330 and 1580 cm^{-1} can be assigned to the disordered graphite (D) and graphite phases (G), respectively. In the case of catalyst with x = 0.6, D and G bands are merged together indicating low graphitic carbon formation. Further, increase in the Ni content to x=0.8 gave rise to two major intense peaks of D and G bands indicating the graphitic carbon formation.

4.2.5. Conclusions

Catalysts with general formula $LaNi_xAl_{1-x}O_3$ ($0 \leq x \leq 1$) have been synthesized by hydrothermal method and characterized by different techniques. The synthesized catalysts have been evaluated for their efficacy towards the dry reforming of methane reaction. The formation of trimetallic perovskite type oxide phase is confirmed in catalyst samples with $0.2 < x < 0.8$. These catalysts produced well dispersed metal oxide species and fine metallic Ni upon reduction. The small sized Ni metal particles enhanced the catalytic activity for the reforming reaction. Among all the catalysts studied, $LaNi_xAl_{1-x}O_3$ with $x=0.6$ exhibited remarkable efficiency in terms of CH_4 and CO_2 conversions. It is concluded that, the formation of trimetallic perovskite phase plays a key role in enhancing dispersion of Ni. This increases catalytic activity which is demonstrated in terms of conversion of reactants, production of syngas and resistance to coke formation during the DRM reaction.

4.2.6. Referencwes

1. https://www.co2.earth/
2. Lim, Y., Lee, C. J., Jeong, Y. S., Song, I. H., Lee, C. J., & Han, C. (2012). *Industrial & Engineering Chemistry Research, 51*, 4982-4989.
3. Wang, W., Su, C., Wu, Y., Ran, R., & Shao, Z. (2013). *Chemical Reviews, 113*, 8104-8151.
4. Upendar, K., Sagar, T. V., Raveendra, G., Lingaiah, N., Rao, B. V. S. K., Prasad, R. B. N., & Prasad, P. S. (2014). *RSC Advances, 4*, 7142-7147.
5. Shi, L., Yang, G., Tao, K., Yoneyama, Y., Tan, Y., & Tsubaki, N. (2013). *Accounts of Chemical Research, 46*, 1838-1847.
6. Daza, Y. A., Kent, R. A., Yung, M. M., & Kuhn, J. N. (2014). *Industrial & Engineering Chemistry Research, 53*, 5828-5837.
7. Hu, Y. H. (2010). *Advances in catalysts for CO_2 reforming of methane. In Advances in CO_2 Conversion and Utilization* (pp. 155-174). American Chemical Society.
8. Kumar, M. A., Venumadhav, C., Sagar, T. V., Surendar, M., Lingaiah, N., Rao, G. N., & Prasad, P. S. (2014). *Indian Journal of Chemistry – Section A, 53A*, 530-534.
9. Wang, S., & GQ (Max) Lu. (1999). *Industrial & Engineering Chemistry Research, 38*, 2615-2625.
10. Wang, S., & Lu, G. Q. (1998). *Energy & fuels, 12*, 248-256.
11. Tian, L., Zhao, X. H., Liu, B. S., & Zhang, W. D. (2009). *Energy & Fuels, 23*, 607-612.
12. Das, T., & Deo, G. (2012). *The Journal of Physical Chemistry C, 116,* 20812-20819.

13. Sierra Gallego, G., Batiot-Dupeyrat, C., Barrault, J., & Mondragón, F. (2008). *Industrial & Engineering Chemistry Research, 47*, 9272-9278.
14. Kathiraser, Y., Thitsartarn, W., Sutthiumporn, K., & Kawi, S. (2013). *Journal of Physical Chemistry C, 117*, 8120-8130.
15. Zhu, T., & Flytzani-Stephanopoulos, M. (2001). *Applied catalysis A: General, 208*, 403-417.
16. Wang, N., Shen, K., Huang, L., Yu, X., Qian, W., & Chu, W. (2013). *ACS Catalysis, 3*, 1638-1651.
17. Chen, H. W., Wang, C. Y., Yu, C. H., Tseng, L. T., & Liao, P. H. (2004). *Catalysis Today, 97*, 173-180.
18. Bradford, M. C. J., & Vannice, M. A. (1999). *Catalysis Reviews, 41*, 1-42.
19. Tomishige, K., Chen, Y. G., & Fujimoto, K. (1999). *Journal of Catalysis, 18*, 91-103.
20. Wang, J. B., Wu, Y. S., & Huang, T. J. (2004). *Applied Catalysis A: General, 272*, 289-298.
21. Gallego, J., Batiot-Dupeyrat, C., Barrault, J., & Mondragón, F. (2009). *Energy & Fuels, 23*, 4883-4886.
22. Mawdsley, J. R., & Krause, T. R. (2008). *Applied Catalysis A: General, 334,* 311-320.
23. Moradi, G. R., Khosravian, F., & Rahmanzadeh, M. (2012). *Chinese Journal of Catalysis, 33*, 797-801.
24. Qi, A., Wang, S., Fu, G., Ni, C., & Wu, D. (2005). *Applied Catalysis A: General, 281*, 233-246.
25. Moradi, P., & Parvari, M. (2006). *Iranian Journal of Chemical Engineering, 3*, 29-44.

26. Provendier, H., Petit, C., Schmitt, J. L., Kiennemann, A., & Chaumont, C. (1999). *Journal Of Materials Science, 34*, 4121-4127.

27. Li, J., Wang, D., Zhou, G., Xue, Y., Li, C., & Cheng, T. (2011). *Industrial & Engineering Chemistry Research, 50*, 10955-10961.

28. Nair, M. M., Kaliaguine, S., & Kleitz, F. (2014). *ACS Catalysis, 4,* 3837-3846.

29. Khalesi, A., Arandiyan, H. R., & Parvari, M. (2008). *Chinese Journal of Catalysis, 29*, 960-968.

30. Lima, S. M., Assaf, J. M., Pena, M. A., & Fierro, J. L. G. (2006). *Applied Catalysis A: General, 311*, 94-104.

31. Gallego, G. S., Marín, J. G., Batiot-Dupeyrat, C., Barrault, J., & Mondragón, F. (2009). *Applied Catalysis A: General, 369*, 97-103.

32. Rida, K., Peña, M. A., Sastre, E., & Martinez-Arias, A. (2012). *Journal of Rare Earths, 30*, 210-216.

33. Pereñiguez, R., Gonzalez-delaCruz, V. M., Caballero, A., & Holgado, J. P. (2012). *Applied Catalysis B: Environmental, 123*, 324-332.

34. Provendier, H., Petit, C., Estournes, C., Libs, S., & Kiennemann, A. (1999). *Applied Catalysis A: General, 180*, 163-173.

35. Moriga, T., Usaka, O., Imamura, T., Nakabayashi, I., Matsubara, I., Kinouchi, T., Kikkawa, S., & Kanamaru, F. (1994). *Bulletin of the Chemical Society of Japan, 67*, 687-693.

36. Zhou, D., Huang, G., Chen, X., Xu, J., & Gong, S. (2004). *Materials Chemistry And Physics, 84*, 33-36.

37. Hassanzadeh-Tabrizi, S. A., & Taheri-Nassaj, E. (2011). *Ceramics International, 37*, 1251-1257.

38. Couzi, M., & Huong, P. V. (1972). *Journal of Chemical Physics, 69*, 1339-1347.

39. Sudarsanam, P., Mallesham, B., Reddy, P. S., Großmann, D., Grünert, W., & Reddy, B. M. (2014). *Applied Catalysis B: Environmental, 144*, 900-908.

40. Sánchez-Sánchez, M. C., Navarro, R. M., & Fierro, J. L. G. (2007). *Catalysis Today, 129*, 336-345.

41. Cheng, C. K., Foo, S. Y., & Adesina, A. A. (2010). *Industrial & Engineering Chemistry Research, 49*, 10804-10817.

42. Bulusu, A., Kim, H., Samet, D., & Graham Jr, S. (2013). *Journal of Physics D: Applied Physics, 46*, 084014.

43. Asai, K., Takane, K., Nagayasu, Y., Iwamoto, S., Yagasaki, E., & Inoue, M. (2008). *Chemical Engineering Science, 63*, 5083-5088.

44. Valderrama, G., Goldwasser, M. R., de Navarro, C. U., Tatibouët, J. M., Barrault, J., Batiot-Dupeyrat, C., & Martínez, F. (2005). *Catalysis Today, 107,* 785-791.

45. Khalesi, A., Arandiyan, H. R., & Parvari, M. (2008). *Industrial & Engineering Chemistry Research, 47*, 5892-5898.

46. Provendier, H., Petit, C., & Kiennemann, A. (2001). *Comptes Rendus de l'Academie des Sciences-Series IIC-Chemistry*, *4*, 57-66.

47. Batiot-Dupeyrat, C., Valderrama, G., Meneses, A., Martinez, F., Barrault, J., & Tatibouët, J. M. (2003). *Applied Catalysis A: General, 248*, 143-151.

48. Rodriguez, G., Bedel, L., Roger, A. C., Udron, L., Carballo, L., & Kiennemann, A. (2003). *Dry Reforming of Ethane on Trimetallic Perovskites $LaCo_xFe_{1-x}O_3$: Characterizations and Reactivity.* ACS Symposium Series, Vol. 852, *Utilization of Greenhouse Gases Chapter 4*, pp 69–82 (DOI: 10.1021/bk-2003-0852.ch004).

49. http://scholarbank.nus.edu.sg/handle/10635/34725

50. Chen, X., Liu, Y., Niu, G., Yang, Z., Bian, M., & He, A. (2001). *Applied Catalysis A: General, 205*, 159-172.

51. Haack, L. P., Otto, K., & Chattha, M. S. (1992). *Applied Catalysis A: General, 82,* 199-214.

52. Fernández, R., Estelle, J., Cesteros, Y., Salagre, P., Medina, F., Sueiras, J. E., & Fierro, J. L. G. (1997). *Journal of Molecular Catalysis A: Chemical*, *119*, 77-85.

53. Djebaili, K., Mekhalif, Z., Boumaza, A., & Djelloul, A. X. P. S. (2015). *Journal of Spectroscopy*, Article ID 868109, 16 pages.

54. Mickevičius, S., Grebinskij, S., Bondarenka, V., Tvardauskas, H., Senulis, M., Lisauskas, V., Šliužienė, K., Vengalis, B., Orlowski, B. A., & Baškys, E. (2010). *Lithuanian Journal of Physics*, 50.

55. de la Cruz, R. G., Falcón, H., Pena, M. A., & Fierro, J. L. G. (2001). *Applied Catalysis B: Environmental*, *33*, 45-55.

56. Sutthiumporn, K., Maneerung, T., Kathiraser, Y., & Kawi, S. (2012). *International Journal of Hydrogen Energy*, *37*, 11195-11207.

57. Masiran, N., Vo, D. V. N., Salam, M. A., & Abdullah, B. (2016). *Procedia Engineering*, *148*, 1289-1294.

58. Kang, K. M., Kim, H. W., Shim, I. W., & Kwak, H. Y. (2011). *Fuel Processing Technology*, *92*, 1236-1243.

59. Kim, H. W., Kang, K. M., & Kwak, H. Y. (2009). *International Journal Of Hydrogen Energy*, *34*, 3351-3359.

60. Sadanandam, G., Ramya, K., Kishore, D. B., Durgakumari, V., Subrahmanyam, M., & Chary, K. V. (2014). *RSC Advances*, *4*, 32429-32437.

Chapter 5

Studies on Cerium modified $LaNiO_3$ catalysts for CO_2 reforming of methane

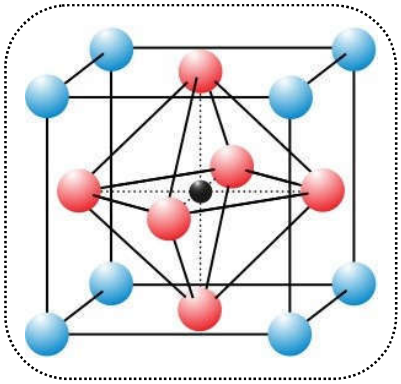

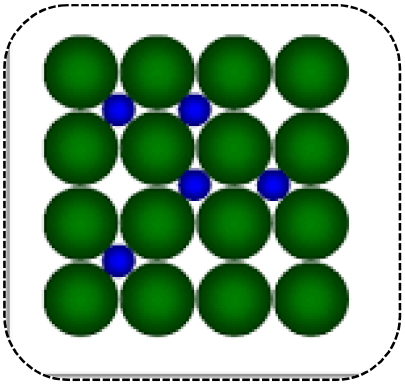

5.0. Introduction

The demand for syngas is increasing owing to its potential applications in diverse fields [1]. Syngas can be obtained through various catalytic and thermal processes from almost any carbon source such as oil, carbon, biomass or biodegradable waste. However, the natural gas which is available in abundance is currently the dominant feedstock for the production of syngas [2-4]. Nowadays researchers are keenly interested in studies on dry reforming of methane (DRM), because of its environmental and economic advantages. This reaction can produce syngas with ratio equal to unity. This ratio is preferable for the synthesis of higher hydrocarbons and the production of oxygenated derivatives [5-9]. As mentioned in the previous chapters, the DRM reaction is an endothermic reaction, operated at high temperature. In this process, the catalyst suffers with sintering and coking. Studies on developing suitable catalysts for this reaction are one of the focus areas of research groups working in catalysis field.

As mentioned in Chapter 1, noble metal catalysts were explored for the DRM but high cost and limited availability greatly restricted their use for commercial purposes [10,11]. In this aspect the nickel based catalysts are technically and economically viable in commercial reforming applications [12]. Deactivation of Ni catalysts due to coke formation during reaction is a major problem. It is observed that the coking problem can be minimized with the increase in mobile oxygen sites in the catalysts [13]. The formation of solid solution type catalysts results into high oxygen storage capacity (OSC) and helps to enhance the coke resistance [14]. The solid solution of NiO with CeO_2 or MgO as catalysts for DRM reaction are prominently studied [13-15]. The advantages of addition of Ce in the mixed oxide system have been studied extensively by many researchers. Enhancement in catalytic behaviour of mixed oxides by the presence of CeO_2 was attributed to its unique structural and redox properties [16]. In the methane reforming

reaction, the rate is usually controlled by the interaction of adsorbed carbon formed with lattice oxygen in CeO_2. This step is followed by a rapid gas solid reaction between the reactant CO_2 and the reduced Ce_2O_3 support to regenerate the lattice oxygen. CeO_2 is known to enhance the coke resistance of the catalysts, improve the Ni dispersion and hence cause increase in the catalytic activity [17-19].

In this chapter, the formation of Ni–Ce solid solution and its influence on catalytic activity is investigated. The synthesis of Ce modified $LaNiO_3$ oxide catalysts was carried out by adopting two different methods namely sol-gel method and hydrothermal method. The physico–chemical properties of these catalysts are determined by BET, XRD, TPR, FT–IR and XPS techniques and are correlated with the catalytic activity during the DRM reaction.

Section 5.1: Ce modified $LaNiO_3$ catalysts synthesized by sol-gel method

5.1.1. Introduction

Lima et al. [20] and Qi et al. [21] prepared $La_{1-x}Ce_xNiO_3$ mixed oxides by substitution of Ce in place of La by maintaining the Ni percentage constant. The Ni–Ce oxide solid solution exhibited excellent catalytic performance in partial oxidation of methane [22]. Xu et al. [23] also studied autothermal reforming of methane on Ce–Ni oxide catalysts. Although the above reports are quite interesting, a systematic study about the effect of the Ce/Ni ratio on $LaNi_xCe_{1-x}O_3$ is needed to determine the optimum composition for the CO_2 reforming of CH_4 reaction. In this section, results on characterization and catalytic activity of a series of $LaNi_xCe_{1-x}O_3$ mixed oxides synthesized by sol-gel method are presented. Studies are focused on the influence of formation of solid solution on the catalytic activity of the DRM reaction.

5.1.2. Results and Discussion

5.1.2a. Specific surface area measurements

Table 5.1.1 compiles the specific surface area values of $LaNi_xCe_{1-x}O_3$ catalysts synthesized by sol-gel method. The catalysts showed low specific surface areas values. These low values may be due to the high calcination temperature as explained in the previous chapter.

Table 5.1.1: Specific surface areas of $LaNi_xCe_{1-x}O_3$ catalysts synthesized by sol-gel method.

S. No.	Catalyst	Specific surface area (m^2/g)
1	$LaNi_{0.8}Ce_{0.2}O_3$	1.4
2	$LaNi_{0.6}Ce_{0.4}O_3$	9.3
3	$LaNi_{0.4}Ce_{0.6}O_3$	10.2
4	$LaNi_{0.3}Ce_{0.7}O_3$	11.7
5	$LaNi_{0.2}Ce_{0.8}O_3$	6.9

On the other hand, the formation of crystalline solid oxide in the catalysts may also lead to low surface area [20]. However, the surface areas of catalysts increased initially with increase in Ni content up to x = 0.3. Further, increase in Ni content showed a decreasing trend. The decrease in specific surface area is found to be more drastic beyond x = 0.6.

5.1.2b. Elemental analysis

The elemental analysis of the $LaNi_xCe_{1-x}O_3$ catalysts synthesized by sol-gel method was carried out by the ICP–OES technique. Table 5.1.2 shows values in wt% of each metal with experimental results compared with those of the theoretical values. It can be observed that these values are in close agreement indicating that there is no loss of mass during the preparation of catalysts.

Table 5.1.2: Elemental analysis of $LaNi_xCe_{1-x}O_3$ catalysts synthesized by sol-gel method.

Catalysts	Ni (wt%)		Ce (wt%)		La (wt%)	
	T	E	T	E	T	E
$LaNi_{0.8}Ce_{0.2}O_3$	17.9	17.6	10.7	10.7	53.0	53.8
$LaNi_{0.6}Ce_{0.4}O_3$	12.7	11.4	20.1	20.5	49.4	52.2
$LaNi_{0.4}Ce_{0.6}O_3$	7.9	8.1	28.6	28.1	47.2	48.8
$LaNi_{0.3}Ce_{0.7}O_3$	5.8	5.8	32.4	33.2	45.9	46.0
$LaNi_{0.2}Ce_{0.8}O_3$	3.8	3.7	36.1	35.3	44.7	45.3

*T=Theoretical; E=Experimental

5.1.2c. X–ray diffraction studies

The XRD patterns of the $LaNi_xCe_{1-x}O_3$ catalysts synthesized by sol-gel method are shown in Figure 5.1.1. At low x values, diffraction peaks are observed at 2θ = 27.5, 31.9, 45.6 and 54.08°, which are ascribed to La_2O_3. A coherent 2θ shift towards lower angle is observed with increase of x value in $LaNi_xCe_{1-x}O_3$ mixed oxides. This can be attributed to the dissolution of Ni^{2+} ions into La_2O_3 lattice to produce $LaNiO_3$ perovskite, as seen in catalysts with higher values of x.

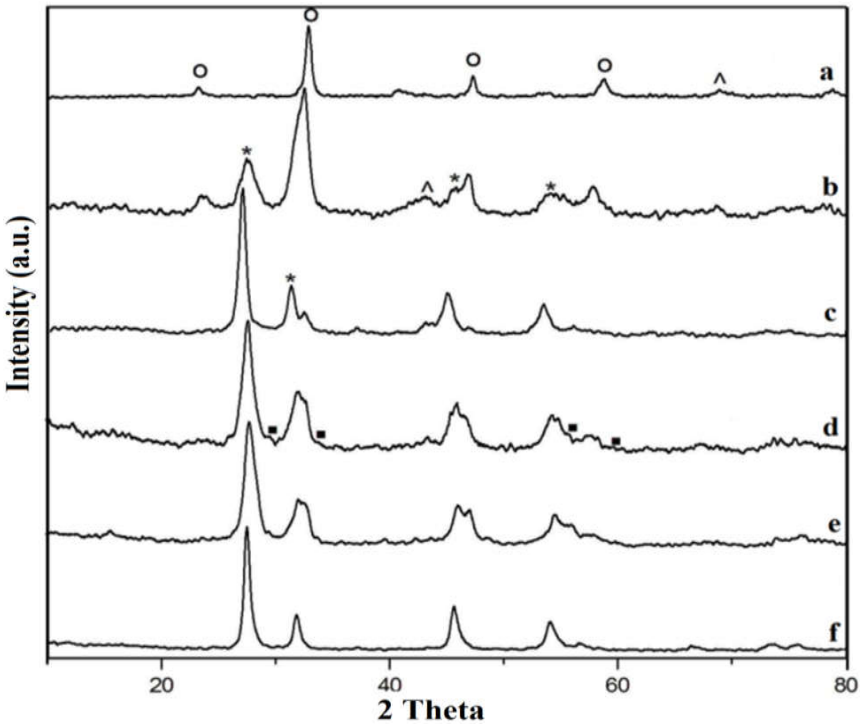

Figure 5.1.1: XRD patterns of $LaNi_xCe_{1-x}O_3$ catalysts synthesized by sol-gel method. a) x = 1; b) x = 0.8; c) x = 0.6; d) x= 0.4; e) x = 0.3; and f) x = 0.2. (*) La_2O_3,(O) $LaNiO_3$, (▪) CeO_2, (^) NiO.

Peaks at 2θ = 23.6, 32.9, 47.3 and 58.9° clearly reveals the presence of typical rhombohedral phase of $LaNiO_3$ (JCPDS 34–1028) with high intensity, particularly in catalysts with x = 0.8 and 1.0. A drastic decrease in the surface area (Table 5.1.1) in these samples also indicates the formation of crystalline perovskite. NiO showed very diffused peaks in samples with low Ni content probably due to the presence of smaller sized particles. Similarly, no peaks related to crystalline CeO_2 were observed, except its weak signals in catalysts with x = 0.3 and 0.4. The XRD data, when compared with those of the results of Lima et al. [20], revealed interesting observations. Lima et al., reported that, when La was substituted by Ce, $LaNiO_3$ was formed along with CeO_2 which existed in a discrete crystalline phase.

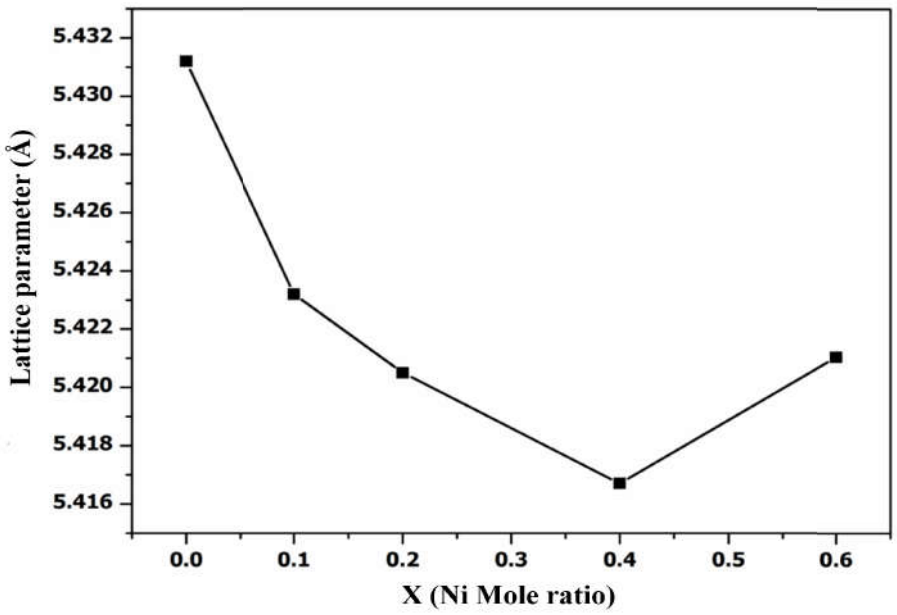

Figure 5.1.2: Lattice parameter of CeO_2 (111) plane in $Ni_xCe_{1-x}O_2$ mixed oxide catalysts synthesized by sol-gel method.

Interestingly, in the present work when Ce was substituted for Ni while maintaining lanthanum content constant, CeO_2 became amorphous and La_2O_3 crystallized out. The appearance of La_2O_3 as a separate phase indicated greater interaction between Ni and Ce. This increased the possibility of formation of Ni–Ce solid solution at low values of x [24], though it was not clearly visible in the XRD patterns of the present samples.

In order to verify the possibility of formation of the solid solution, samples containing Ce and Ni, mixed oxides of these metals with the same compositions were prepared separately (Section 5.3) and examined by XRD analysis. These samples evidenced the formation of Ni–Ce oxide solid solution as indicated by the decrease in the lattice parameter of CeO_2 111 plane from 5.430 to 5.416 Å (Figure 5.1.2). This gives credence to the hypothesis of the presence of Ni–Ce solid solution in the mixed oxide.

5.1.2d. H_2–temperature programmed reduction

TPR patterns of the $LaNi_xCe_{1-x}O_3$ catalysts synthesized by sol-gel method are shown in Figure 5.1.3. $LaNiO_3$ exhibited two peaks (inset in Figure 5.1.3) corresponding to $Ni^{3+} \rightarrow Ni^{2+}$ and $Ni^{2+} \rightarrow Ni^0$ reduction, with area ratio of second/first equaling 2. This observation is similar to the literature reports [25]. It is interesting to note from the TPR profiles of the catalysts that the peak shapes and their temperature maxima considerably vary with the Ni composition. At low values of x, the catalysts essentially contained La_2O_3 as a discrete phase, as this is a non reducible oxide. This catalyst showed Ni and Ce oxide reduction bands in their mixed oxide state.

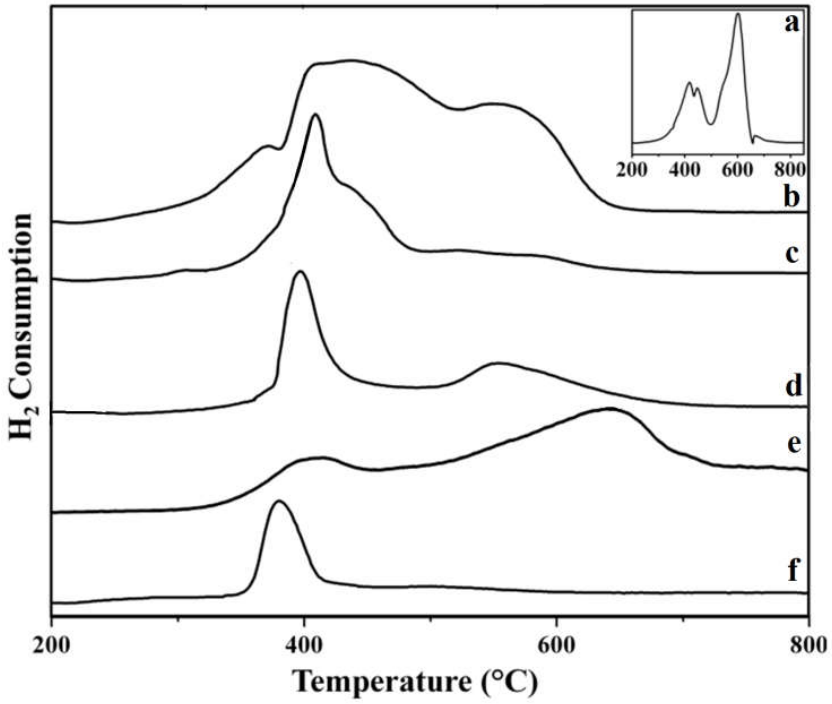

Figure 5.1.3: TPR Profiles of $LaNi_xCe_{1-x}O_3$ catalysts synthesized by sol-gel method. a) x = 1; b) x = 0.8; c) x = 0.6; d) x = 0.4; e) x = 0.3; and f) x = 0.2.

In the case of Ni containing CeO_2 catalysts, Yonggang et al. [25], assigned the TPR peaks into α, β, γ and δ types. The α peak noticed at around 330 °C was due to the reduction of the adsorbed oxygen on the Ni–Ce mixed oxide. The β peak appearing at 400 °C was specifically related to the reduction of NiO dispersed on ceria. The γ peak

normally observed at around 550 °C represented the reduction of NiO intimately in contact with CeO_2. The δ peak, on the other hand, was a result of the reduction of CeO_2 with its characteristic peak displayed beyond 800 °C (this peak is not seen in the present patterns).

In the case of the catalysts under study, the low temperature reduction peak (at temperature < 400 °C) was seen at higher Ni contents, whereas the β peak dominated in the catalysts indicating the availability of dispersed Ni species. The merging of γ peak with β could be due to agglomeration of NiO. The appearance of distinct peaks due to NiO in the XRD patterns of the catalysts with x = 0.8 and 0.6 also supported this phenomenon. It is also reported in the literature that the Ni species in Ni–Ce oxide solid solution are not easily reducible [24]. Therefore, the peaks representing the reduction of Ni in the solid solution appear at higher temperature regions. In the present work, this peak was distinguishable in catalysts with high Ni compositions. Thus, in support of the XRD results, the TPR information also confirmed the presence of the perovskite ($LaNiO_3$) in the catalysts with high Ni loading and the existence of NiO in two forms i.e, the agglomerated NiO and well dispersed NiO on support. It is interesting to see that, the catalyst with x = 0.4 displayed combined characteristics of both low and high Ni containing catalysts.

5.1.2e. X–ray photoelectron spectroscopy studies

The core–level XPS profiles of La 3d of $LaNi_xCe_{1-x}O_3$ catalysts synthesized by sol-gel method are shown in Figure 5.1.4. Distinguishing between Ni $2p_{3/2}$ and La $3d_{3/2}$ is a bit complicated due to close similarity of binding energies of these two species [26]. The binding energies recorded at 853.7 and 836.8 eV can be ascribed to La $3d_{3/2}$ and $3d_{5/2}$ energy levels, respectively. The most intense peak appearing at 853.7 eV overlapped with that of the Ni $2p_{3/2}$ peak. This band corresponds to Ni^{2+} in NiO (Figure 5.1.5) [22,27].

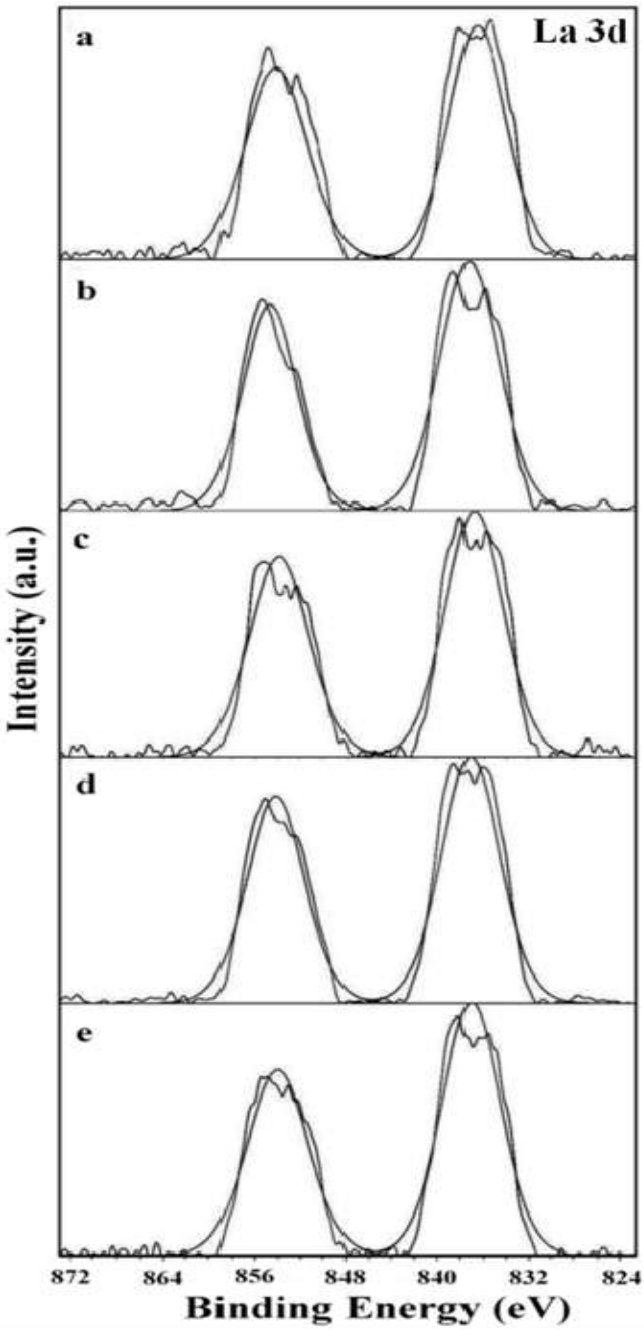

Figure 5.1.4: La 3d core level XP spectra of $LaNi_xCe_{1-x}O_3$ catalysts synthesized by sol-gel method. a) x = 1; b) x = 0.6; c) x = 0.4; d) x = 0.3; e) x = 0.2.

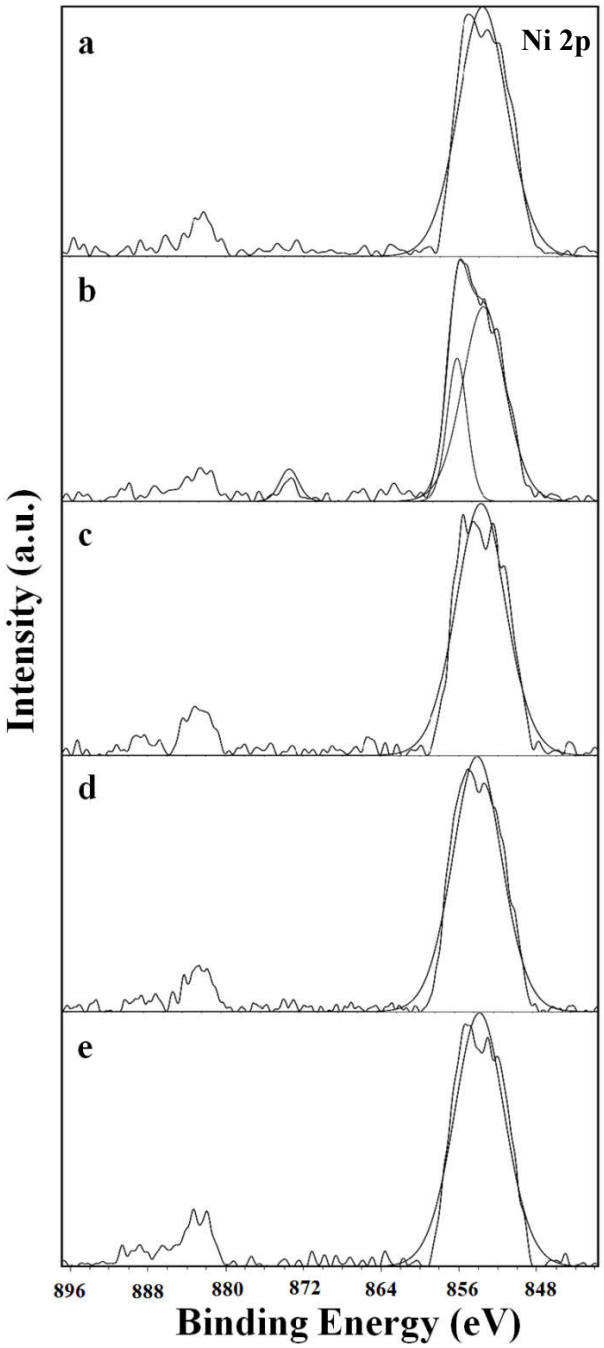

Figure 5.1.5: Ni 2p core level XP spectra of $LaNi_xCe_{1-x}O_3$ catalysts synthesized by sol-gel method. a) x = 1; b) x = 0.6; c) x = 0.4; d) x = 0.3; e) x = 0.2.

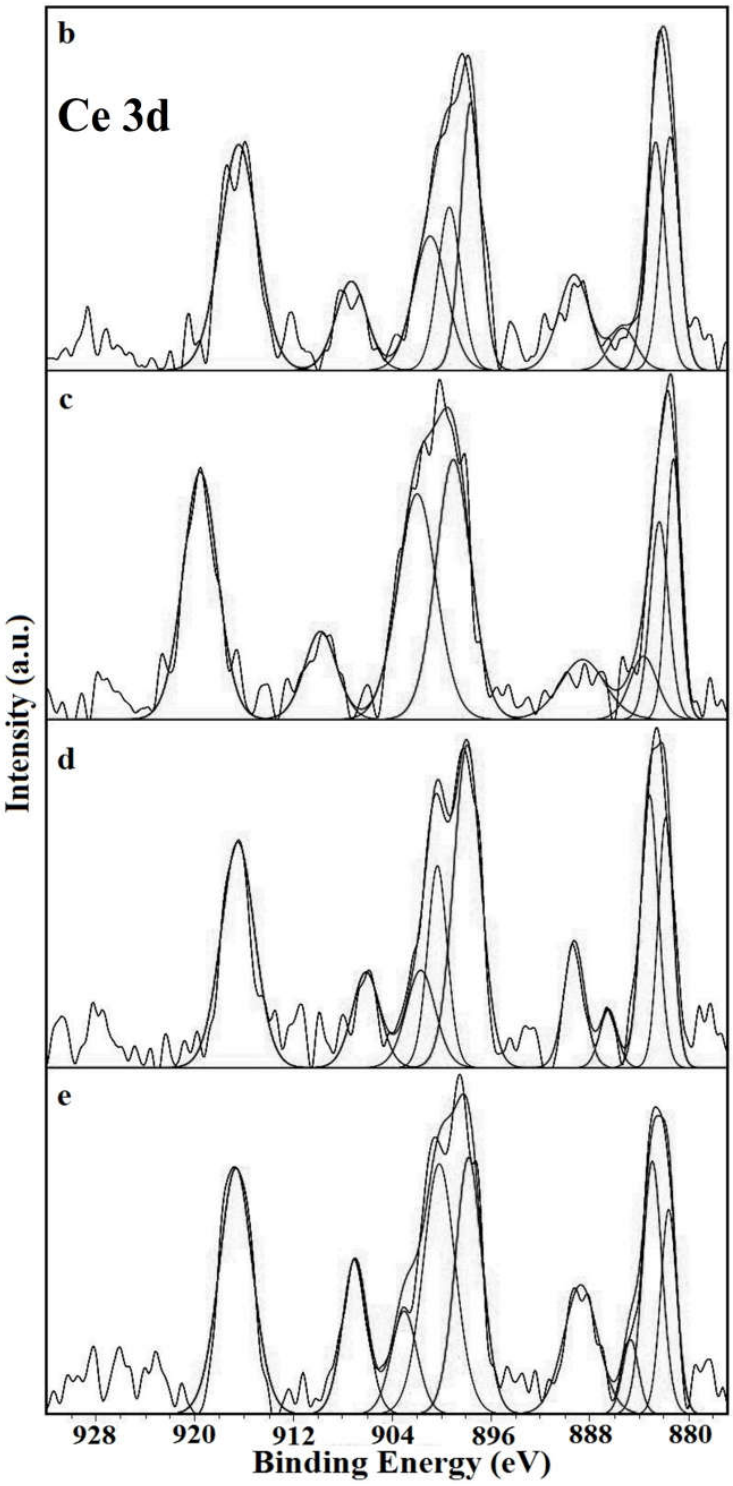

Figure 5.1.6: Ce 3d core level XP spectra of $LaNi_xCe_{1-x}O_3$ catalysts synthesized by sol-gel method. a) x = 0.6; b) x = 0.4; c) x = 0.3; and d) x = 0.2.

Ce 3d XP spectra of $LaNi_xCe_{1-x}O_3$ catalysts are shown in Figure 5.1.6. It can be observed that the spectra are complex and peaks appear in the range of 880–920 eV due to the hybridization of the O 2p valence band with the Ce 4f level in the final state of photoionization [28,29]. The Ce $3d_{5/2}$ peaks appeared to be more intense in comparison to Ce $3d_{3/2}$ peaks, suggesting that cerium existed mainly in Ce^{4+} oxidation state. On the other hand, the stabilization of certain amount of Ce^{3+} oxidation state was also observed in samples with low Ce–content, where the intensity of satellite peak around 916.6 eV (Ce^{4+}) decreased with simultaneous increase in the characteristic peaks of Ce^{3+} (885.7 and 903.9 eV). The observations suggest that at low concentrations of Ce (x = 0.8, 0.6 and 0.4), it exists as Ce^{3+} ion, whereas at higher concentrations, it exists as Ce^{4+}. These results evidently support the observations made from the TPR and XRD analysis, where the Ce–Ni interaction prevailed in low Ni containing catalysts.

Two O 1s peaks were noticed in the ranges 529.2–531.9 eV and 529.9–532.3 eV for all samples which can be attributed to the presence of hydroxyl and carbonate groups and adsorbed water (Figure 5.1.7) [30]. The obtained C 1s spectra showed two main peaks at ~284.6 and 285.9 eV which might be due to hydrocarbon contamination (C–C/C–H and C–O) (Figure 5.1.8). On the other hand, small peak observed in the region of 289 eV represents the carbonate species which reacts with La^{3+} when exposed to atmosphere [30,31].

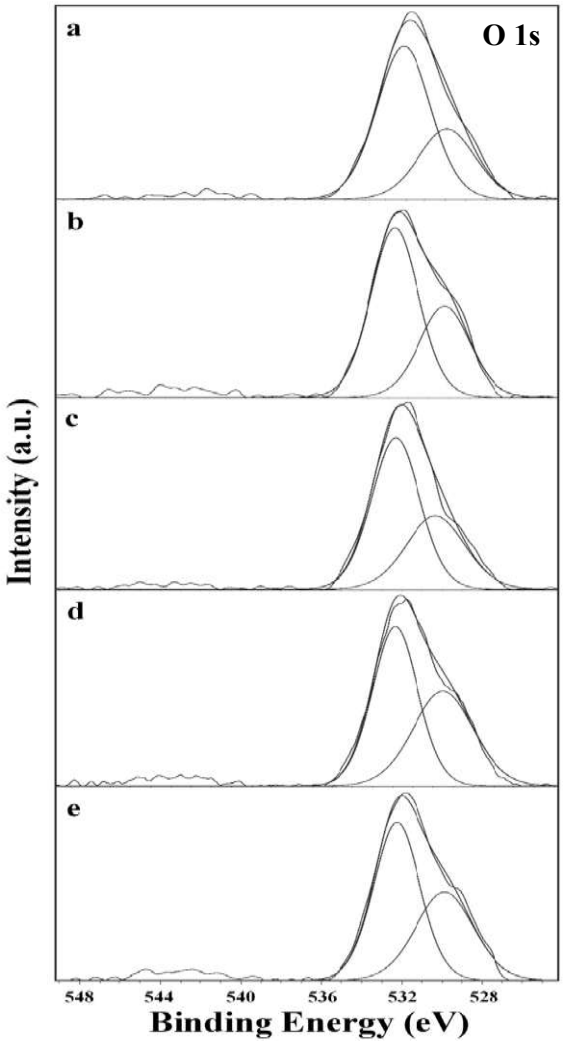

Figure 5.1.7: O 1s core level XP spectra of $LaNi_xCe_{1-x}O_3$ catalysts synthesized by sol-gel method. a) x = 1; b) x = 0.6; c) x = 0.4; d) x = 0.3; e) x = 0.2.

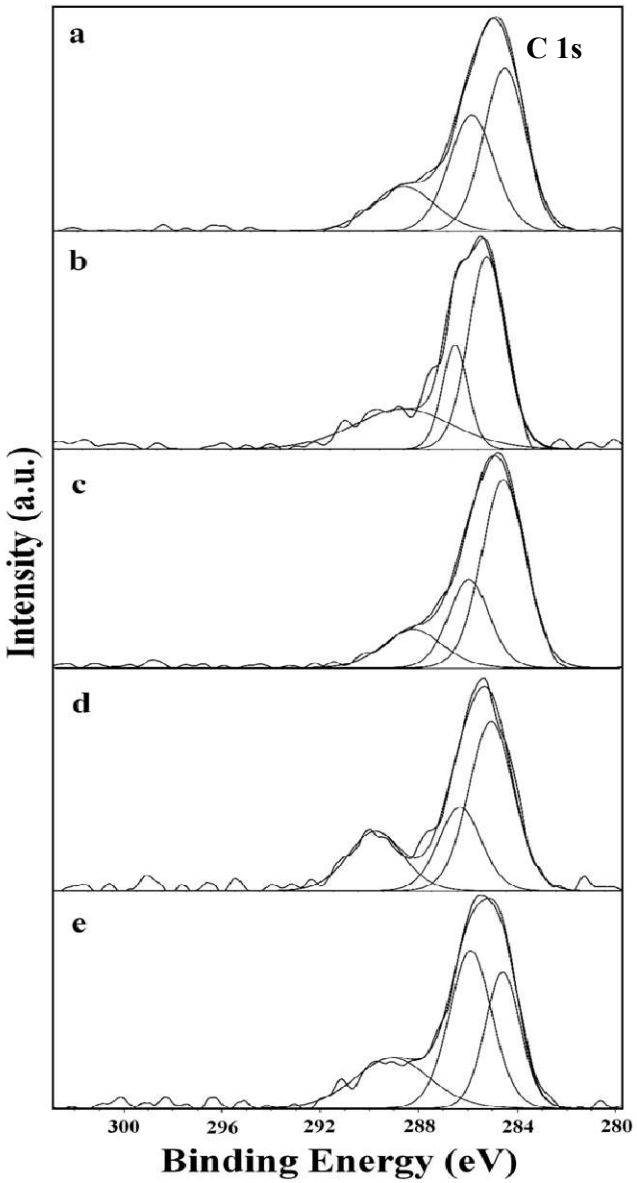

Figure 5.1.8: C 1s core level XP spectra of $LaNi_xCe_{1-x}O_3$ catalysts synthesized by sol-gel method. a) x = 1; b) x = 0.6; c) x = 0.4; d) x = 0.3; e) x = 0.2.

5.1.2f. Fourier transform infrared spectroscopy studies

The results of characterization studies on $LaNi_xCe_{1-x}O_3$ catalysts synthesized by sol-gel method using FT–IR spectroscopy are shown in Figure 5.1.9. Because of the usage of nitrate precursors in the preparation of catalysts, the residual nitrates can be present in the coordination sphere of corresponding metal cation, which in turn is surrounded by a propionic acid molecule (bands at ~853, 1379 and 1464–1471 cm^{-1}). The

observed IR band in the range of 3000–3600 cm^{-1} corresponds to –O–H stretching of structural hydroxyl groups and physisorbed and interlayer water [31]. The IR spectrum of $LaNiO_3$ catalyst did not show any characteristic peaks due to its low resistivity [32,33]. All the catalysts studied showed bands in the region of 546–489 cm^{-1}, in agreement with the vibrational stretching frequencies of the metal–oxygen bonds [34].

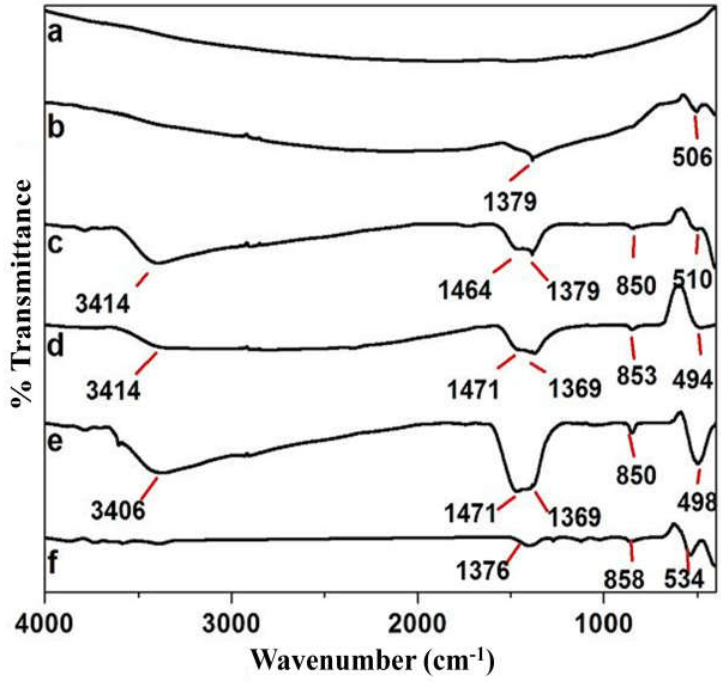

Figure 5.1.9: FT–IR patterns of $LaNi_xCe_{1-x}O_3$ catalysts synthesized by sol-gel method. a) x = 1; b) x = 0.8; c) x = 0.6; d) x = 0.4; e) x = 0.3; and f) x = 0.2.

5.1.3. Catalytic activity tests

The activities of the $LaNi_xCe_{1-x}O_3$ catalysts synthesized by sol-gel method were tested for methane dry reforming, at 800 °C and atmospheric pressure. It was observed that the activity of the $LaNi_xCe_{1-x}O_3$ catalysts increased up to x = 0.4 and then decreased continuously. $LaNi_{0.4}Ce_{0.6}O_3$ has exhibited the highest activity among all the catalysts reaching the conversion levels of more than 90%. The $LaNiO_3$ had shown low conversions (less than 20%) for both methane and carbon dioxide under the conditions of evaluation. This observation clearly suggests the significance of Ce in $LaNi_xCe_{1-x}O_3$

catalysts in dry reforming of methane. The initial increase in the conversions of methane and carbon dioxide can be attributed to the availability of well dispersed nickel. Figure 5.1.10 reveals the variation of dispersion and catalytic activity with the variation of Ni content. The dispersion and activity varied in a similar fashion, implying that activity is proportional to dispersion. Higher activity of catalysts even at low x values can be understood on the basis of higher dispersion of active metal (Ni). On the other hand, decrease in catalytic activity at higher values of x (i.e., $x > 0.4$) can be attributed to Ni agglomeration.

It is a well–established fact in the literature that Ni^0 is the active site for dry reforming of methane [35,36]. $LaNiO_3$ ultimately leads to the formation of well–dispersed Ni on La_2O_3. Lima et al. [20], reported the possibility of formation of Ni/La–Ce–O when Ce is substituted for La. Studies carried out on $LaNi_xCe_{1-x}O_3$ catalysts at varying x values, revealed that apart from the formation of the perovskite, the remaining nickel existed in a well dispersed form. At low values of x, the formation of Ni–Ce oxide solid solution appears to be feasible. As the x value increases the Ni–Ce oxide solid solution composition decreases. In the case of $LaNi_{0.4}Ce_{0.6}O_3$, the active Ni species might have reached its optimum level, making it the most efficient catalyst. The existence of CeO_2 in the proximity of Ni helped in further increase of activity [37,38]. It is reported that the formation of Ni–Ce solid solution improves the stability of the catalysts by modifying the chemical environment around Ni [23]. In the present reaction, CeO_2 was reduced either by the hydrogen formed during the reaction or by the carbon deposits formed during the decomposition of methane on Ni sites. CO_2 gets decomposed on reduced ceria (Ce_2O_3), in turn oxidizing it to CeO_2 and forming CO.

Thus, the variation of Ce/Ni ratio in $LaNi_xCe_{1-x}O_3$ mixed oxides (rather than La/Ce ratio) appears to have a positive effect in getting higher conversions (more than

90% for both CO_2 and CH_4). Therefore, superior catalytic performance of the $LaNi_{0.4}Ce_{0.6}O_3$ can be explained on the basis of formation of highly dispersed Ni on CeO_2 or La_2O_3 or their mixed oxide, as proposed by Lima et al. [20]. The formation of Ni–Ce solid solution phase is advantageous for stabilizing the dispersed Ni. Higher conversion of CO_2 might be due to the facile reverse water gas shift reaction, as reported previously [39].

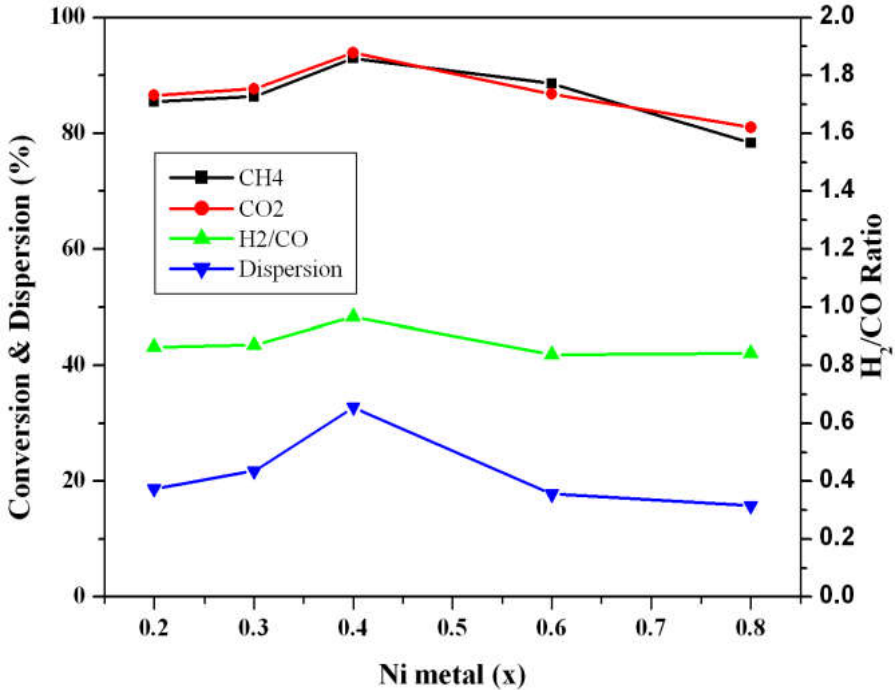

Figure 5.1.10: Variation of catalytic activity and Ni dispersion with Ni content in $LaNi_xCe_{1-x}O_3$ catalysis synthesized by sol-gel method.

The results of time on stream analysis performed on $LaNi_{0.4}Ce_{0.6}O_3$ (GC chromatograph has been given in Appendix section Figure 3) catalyst are shown in Figure 5.1.11. Promising conversions for both methane (91.6%) and carbon dioxide (93.5%) were observed. Similarly, the syngas ratio also attained a steady value in the region of 0.87–0.84. The catalyst also retained its activity to a large extent during the period of 9 h study, indicating reasonable stability of the catalyst. The catalyst showed sintering tendency, though not severe. This observation is based on the H_2 chemisorption studies of

the fresh and used catalysts where a slight increase in the particle size from 32.1 to 38.5 Å is noted.

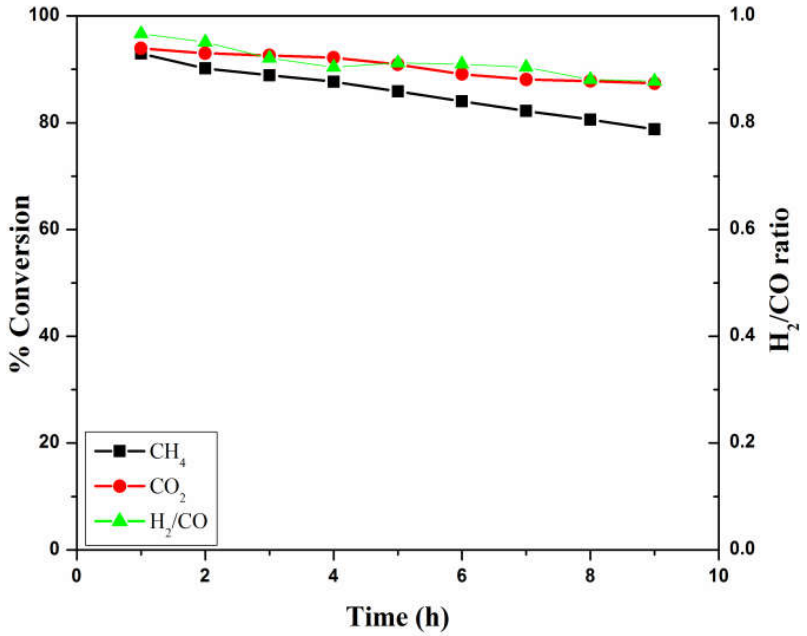

Figure 5.1.11: Time on stream study of $LaNi_{0.4}Ce_{0.6}O_3$ catalyst synthesized by sol-gel method during the DRM reaction at 800 ^{0}C.

5.1.4. Carbon analysis of used $LaNi_xCe_{1-x}O_3$ catalysts

Table 5.1.3: Coke content of the $LaNi_xCe_{1-x}O_3$ catalysts measured after 9 h of the DRM reaction.

S. No.	Catalyst	Carbon (%)
1	$LaNi_{0.8}Ce_{0.2}O_3$	0.34
2	$LaNi_{0.6}Ce_{0.4}O_3$	0.18
3	$LaNi_{0.4}Ce_{0.6}O_3$	0.15
4	$LaNi_{0.3}Ce_{0.7}O_3$	0.20
5	$LaNi_{0.2}Ce_{0.8}O_3$	0.25

The amount of carbon formed during the reforming reaction over $LaNi_xCe_{1-x}O_3$ catalyst is estimated by CHNS analysis and the results are reported in Table 5.1.3. Coking was reduced with increase in Ni content till x=0.4, then a sudden increase in the carbon formation was observed. This can be attributed to the formation of highly dispersed Ni and Ni–Ce solid solution possessing high resistivity towards coking.

5.1.5. Conclusions

Characterization studies carried out on $LaNi_xCe_{1-x}O_3$ catalysts synthesized by sol-gel method revealed that, their structural and redox properties are highly dependent on Ni/Ce composition. With the variation of Ni/Ce ratio in $LaNi_xCe_{1-x}O_3$ catalysts, it is observed that two types of active metallic phases are formed. The perovskite phase with bimetallic structural oxide and the Ni–Ce solid solution phase. These active species played a major role in the reducibility of catalysts. Further, they exhibited significant influence on the catalytic activity. Among the catalysts investigated in the present study, the $LaNi_{0.4}Ce_{0.6}O_3$ sample exhibited better catalytic performance towards conversions of both methane and carbon dioxide. Insignificant activity loss was observed for the $LaNi_{0.4}Ce_{0.6}O_3$ catalyst in the time on stream study after 9 h of reaction time which can be attributed to the formation of very small amount of coke on the catalyst surface.

Section 5.2: Ce modified $LaNiO_3$ catalysts synthesized by hydrothermal method

5.2.1. Introduction

In continuation of our earlier studies on $LaNi_xCe_{1-x}O_3$ catalysts synthesized by sol-gel method, in this section, studies on the same catalytic system synthesized under hydrothermal conditions are presented. The synthesized catalysts are characterized using several physico–chemical techniques and evaluated for the DRM reaction. The objective is to study the efficacy of $LaNi_xCe_{1-x}O_3$ catalysts synthesized by hydrothermal method on the DRM reaction, in terms of the influence of Ce substitution in $LaNiO_3$ perovskite, the optimum composition of Ce in $LaNi_xCe_{1-x}O_3$ for obtaining the best catalytic activity, ideal syngas ratio, better coke resistance and improved stability of the catalysts.

5.2.2. Results and Discussion

5.2.2a. Specific surface area measurements

Table 5.2.1 illustrates the specific surface areas of the $LaNi_xCe_{1-x}O_3$ catalysts synthesized by hydrothermal method, with varying x values. Specific surface areas of the catalysts are observed to be low. As discussed in the previous sections, the low surface areas of the catalysts may be due to high calcination temperature or high crystalline phases [20,35]. It can be seen from the table that the surface area gradually increases in $LaNi_xCe_{1-x}O_3$ catalysts with increase in nickel content from x = 0.2 – 0.8. This trend is in agreement with previously reported findings [40].

Table 5.2.1: Specific surface areas of $LaNi_xCe_{1-x}O_3$ catalysts synthesized by hydrothermal method.

S. No.	Catalyst	Specific surface area (m^2/g)
1	$LaNi_{0.8}Ce_{0.2}O_3$	4.1
2	$LaNi_{0.6}Ce_{0.4}O_3$	3.9
3	$LaNi_{0.4}Ce_{0.6}O_3$	3.5
4	$LaNi_{0.3}Ce_{0.7}O_3$	2.2
5	$LaNi_{0.2}Ce_{0.8}O_3$	0.4

5.2.2b. X–ray diffraction studies

The X–ray diffraction patterns of the $LaNi_xCe_{1-x}O_3$ catalysts synthesized by hydrothermal method are displayed in Figure 5.2.1. The peaks at 2θ = 23.6, 32.9, 47.3 and 58.9° are found to be in good agreement with the characteristic lines of the rhombohedral phase of $LaNiO_3$ (JCPDS 34–1028). The intensity of these peaks increased with increasing value of x in the range studied (x= 0.2 to 0.8).

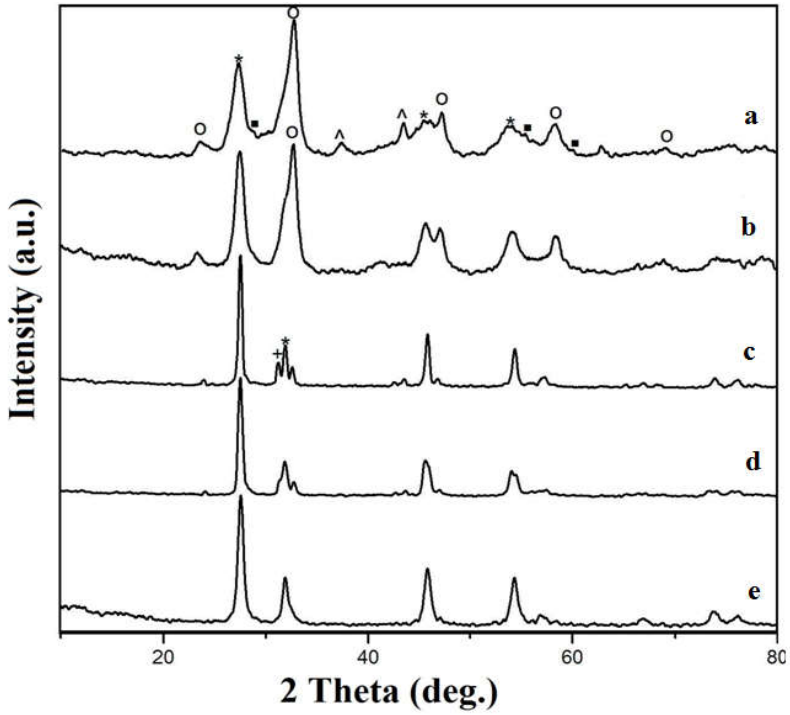

Figure 5.2.1: XRD patterns of $LaNi_xCe_{1-x}O_3$ catalysts synthesized by hydrothermal method. a) x = 0.8, b) x = 0.6, c) x = 0.4, d) x = 0.3 and e) x = 0.2. (*) La_2O_3, (O) $LaNiO_3$, (▪) CeO_2, (+) La_2NiO_4, (^) NiO.

Catalysts with low x values show peaks at 2θ = 27.5, 31.2, 45.8 and 54.3°. These are ascribed to La_2O_3 and are observed to be dominant over the perovskite. A shift in the 2θ values towards lower angles was observed with increasing x. This is due to the dissolution of Ni^{2+} ions in La_2O_3 lattice to form ABO_3 perovskite oxide i.e., $LaNiO_3$ perovskite. Low intense NiO diffraction peaks are observed in catalysts with low Ni content, probably due to the presence of smaller particles. However, their presence can be

clearly seen in catalysts with higher x values. Interestingly, peaks due to crystalline CeO_2 were not observed.

With the substitution of La by Ce, Lima et al. reported the formation of discrete crystalline phase of CeO_2, in addition to $LaNiO_3$ [20]. However, in the present work when Ce is substituted for Ni, CeO_2 became amorphous and La_2O_3 crystallized out. There was also the possibility of formation of Ce–Ni solid solution at low values of x, though it is not clearly visible in the XRD patterns of the synthesized catalysts [20]. It is also reported in the literature that nickel exists in two phases in the Ce–Ni solid solution, Ni^{2+} ions incorporated in the CeO_2 lattice and Ni as NiO on the surface of support [40,41].

5.2.2c. Temperature programmed reduction studies

Figure 5.2.2 provides the TPR patterns of the $LaNi_xCe_{1-x}O_3$ catalysts synthesized by hydrothermal method. The bimetallic perovskite phase $LaNiO_3$ (Figure 5.2.2a) exhibited two stage reduction of Ni i.e., $Ni^{3+} \rightarrow Ni^{2+}$ and $Ni^{2+} \rightarrow Ni^0$. The peak areas of these are found to be in the ratio of 2, this ratio indicates the perovskite phase as reported in the literature [20]. The peak shapes and their temperature maxima are found to vary with change in Ni composition. Since, La_2O_3 is not a reducible oxide, all the reduction bands are related to Ni and Ce oxides, either in the individual oxide phase or in the mixed oxide form. As discussed in the previous section, the reduction of adsorbed oxygen peak arose at 330 °C which is denoted as α. The reduction of NiO particles dispersed on ceria appeared at 400 °C which is indicated as β. The high temperature peak at 550 °C is due to the reduction of NiO intimately in contact with CeO_2 and it is designated as γ [25].

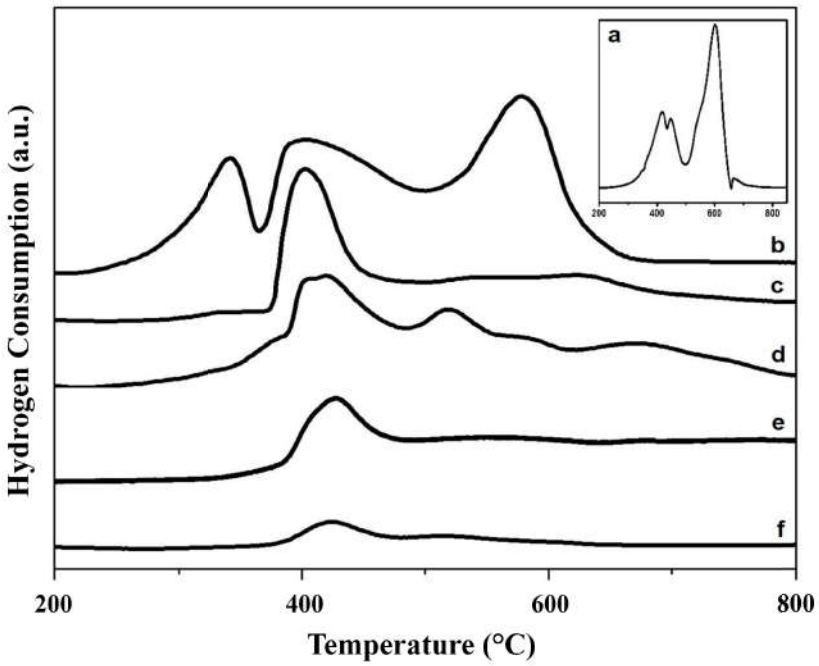

Figure 5.2.2: TPR patterns of $LaNi_xCe_{1-x}O_3$ catalysts synthesized by hydrothermal method. a) x =1, b) x = 0.8, c) x = 0.6, d) x = 0.4, e) x = 0.3 and f) x = 0.2.

It is evident from the TPR profiles that the areas of both β and γ peaks increase with increasing nickel content, particularly in the case of peak at higher temperature (γ). This is in agreement with the fact that CeO_2 influences the reduction of the NiO species to metallic nickel. On the other hand, the merging of γ with β peaks implies agglomeration of NiO. Appearance of distinct peaks due to NiO in the XRD patterns of the catalysts with x = 0.6 and 0.8 confirms this phenomenon. There is the possibility of the formation of a nickel–ceria solid solution at lower Ni composition. However, the reducibility of Ni species in the solid solution is difficult. The TPR peak with its maximum appearing in the range of 500–600 °C could be due to the Ni in solid solution. Thus, in support of the XRD results, the TPR information also confirmed the presence of the perovskite phase ($LaNiO_3$) in the catalysts with high Ni loading. Interestingly, TPR results revealed that the NiO exists in two forms, i.e., one with interaction of CeO_2 and

the other in perovskite ($LaNiO_3$). Particularly, the catalyst with x = 0.4 clearly exhibited the presence of both these forms.

5.2.2d. X–ray photoelectron spectroscopy studies

The core level binding energies of the La 3d and Ni 2p of $LaNi_xCe_{1-x}O_3$ catalysts synthesized by hydrothermal method are shown in Figure 5.2.3. Due to the closeness of the binding energies of Ni $2p_{3/2}$ and La $3d_{3/2}$, it is difficult to distinguish between these two species [26]. However, the binding energies recorded at 855.3 and 838.3 eV fitted well with La $3d_{3/2}$ and $3d_{5/2}$ energy levels, respectively. The most intense 855.3 eV peak overlapped with that of the Ni $2p_{3/2}$ peak.

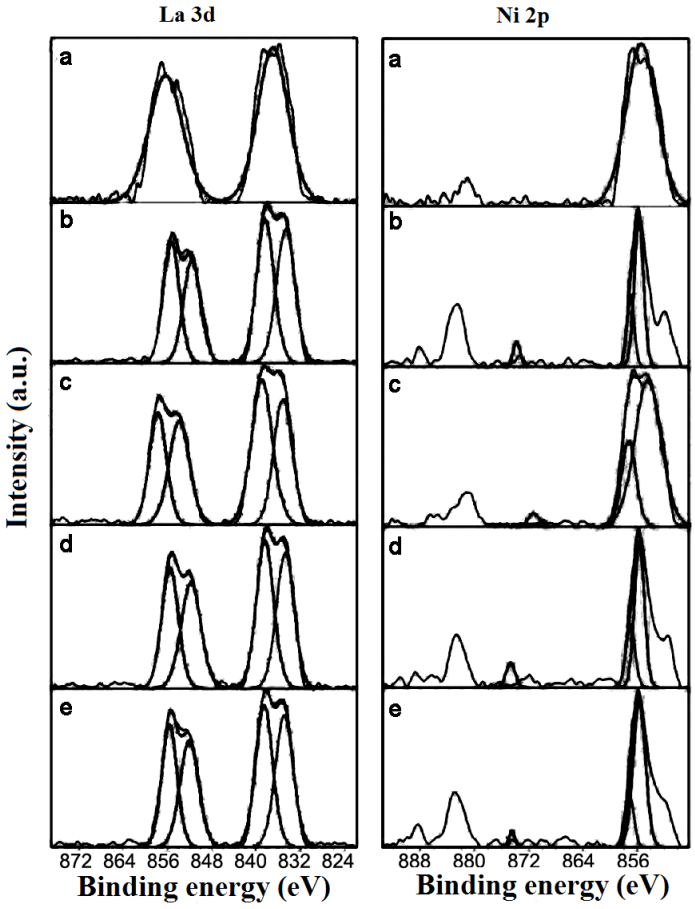

Figure 5.2.3: La 3d and Ni 2p core level XP–spectra of $LaNi_xCe_{1-x}O_3$ catalysts synthesized by hydrothermal method. a) x = 1, b) x = 0.6, c) x = 0.4, d) x = 0.3 and (e) x = 0.2.

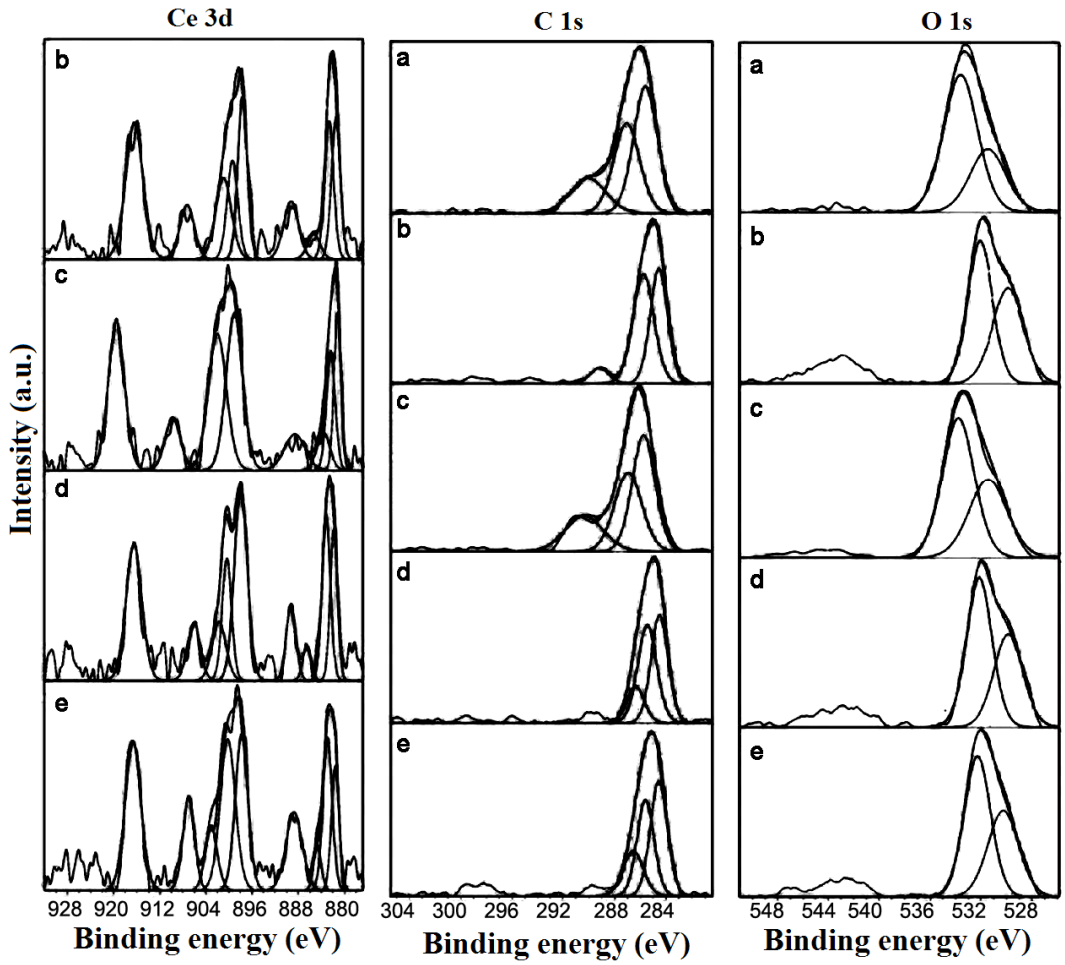

Figure 5.2.4: Ce 3d, C 1s and O 1s core level XP–spectra of $LaNi_xCe_{1-x}O_3$ catalysts synthesized by hydrothermal method. a) x = 1, b) x = 0.6, c) x = 0.4, d) x = 0.3 and (e) x = 0.2.

Figure 5.2.4 shows the Ce 3d, C 1s and O 1s profiles of the $LaNi_xCe_{1-x}O_3$ catalysts. The complex Ce 3d XP spectra are observed in the range of 880–920 eV. The binding energy peaks related to Ce $3d_{3/2}$ and Ce $3d_{5/2}$ are more intense suggesting that cerium exists in Ce^{3+} (885.3 and 903.4 eV) and Ce^{4+} oxidation state. These results support the observations from TPR and XRD characterization studies where the Ce–Ni interaction prevailed in the low Ni containing catalysts.

In the O 1s spectra, the peaks appearing between 529.2–531.9 eV and 529.9–532.3 eV arise from hydroxyl and carbonate groups and adsorbed water [30]. The

C 1s spectrum shows peaks at 284.6 and 285.9 eV which might be due to hydrocarbon contamination (C–C/C–H and C–O species). The small peak observed with binding energy in the region of 288.9–289.3 eV represents the carbonate species which is seen in lanthana materials due to the CO_2 reaction with La^{3+} when exposed to atmosphere [30,31].

5.2.2e. Fourier transform infrared spectroscopy studies

The FT–IR spectra of $LaNi_xCe_{1-x}O_3$ catalysts synthesized by hydrothermal method are shown in Figure 5.2.5. The vibrational bands around ~3000–3600 cm^{-1} correspond to –O–H stretching of structural hydroxyl groups and physisorbed and interlayer water [42]. The IR spectrum of $LaNiO_3$ catalyst did not show any characteristic peak due to its low resistivity [32,33]. The catalysts with x = 0.2, 0.3, 0.4, 0.6 and 0.8 showed bands in the region 546–489 cm^{-1}. These can be ascribed to the vibrational bending frequencies of the metal–oxygen bonds [34].

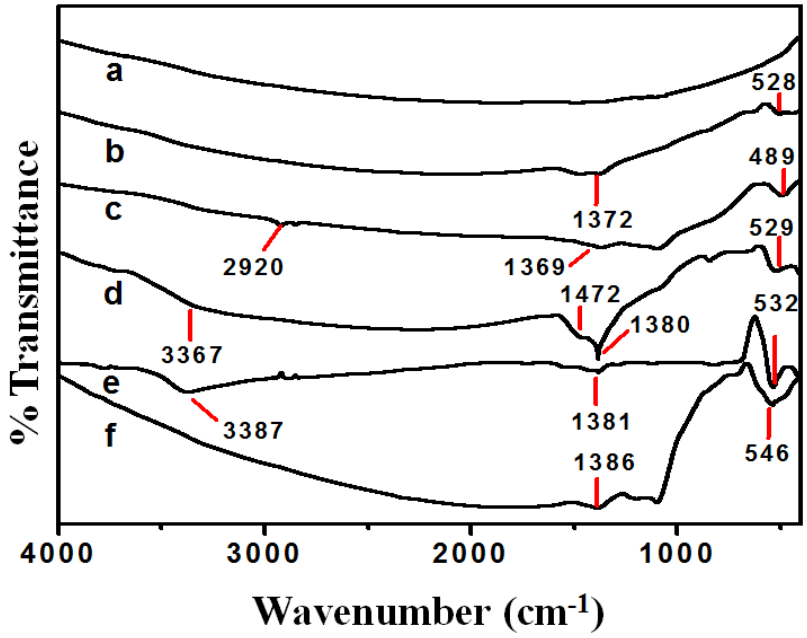

Figure 5.2.5: FT–IR patterns of $LaNi_xCe_{1-x}O_3$ catalysts synthesized by hydrothermal method. a) x = 1, b) x = 0.8, c) x =0.6, d) x = 0.4, e) x = 0.3 and f) x =0.2.

Nitrates of respective metals are used as precursors for the synthesis of these mixed oxide catalysts. It is highly probable that trace amounts of residual nitrates exist in the synthesized samples. These nitrate species may be situated on the coordination sphere of the corresponding metallic cation, which in turn is surrounded by a propionic acid moiety (bands ~1369 and ~1472 cm^{-1}), as observed in the previous section. The nitrate peak in the region of 830 cm^{-1} is often minimized in the hydrothermal treatment during the synthesis of perovskites.

5.2.3. Catalytic activity tests

The catalytic functionalities of the hydrothermally synthesized $LaNi_xCe_{1-x}O_3$ catalysts over the DRM reaction at 800 °C are presented in Figure 5.2.6. There is a near linear increase in the activity of the catalyst initially from x = 0.2 to 0.4. It remained steady up to x= 0.6 and then a sudden drop at x = 0.8 is observed. This behaviour can be explained as detailed below. With increasing composition of Ni initially, there is increase in the dispersion of Ni on La_2O_3 or on the Ce–Ni solid solution, thereby increasing the catalytic activity. CeO_2 promotes the activation of CO_2 due to its redox property (Ce_2O_3 + CO_2 → $2CeO_2$ + CO). La_2O_3, being basic, provides the necessary sites for the adsorption of CO_2. Higher composition of Ni primarily helps in $LaNiO_3$ formation, which is not as active as the dispersed Ni. The depletion of free La_2O_3 also decreases the CO_2 adsorption capacity. Hence, there is a sudden drop in the catalytic activity. Among all the synthesized catalysts screened for activity, $LaNi_{0.6}Ce_{0.4}O_3$ was found to exhibit the highest activity in terms of CH_4 (94%) and CO_2 (96%) conversions and H_2/CO ratio (0.94). These conversion percentages are very high compared to the activity of catalyst reported by Lima et al. [20], where the conversions of CH_4 and CO_2 were found to be 53% and 62% respectively.

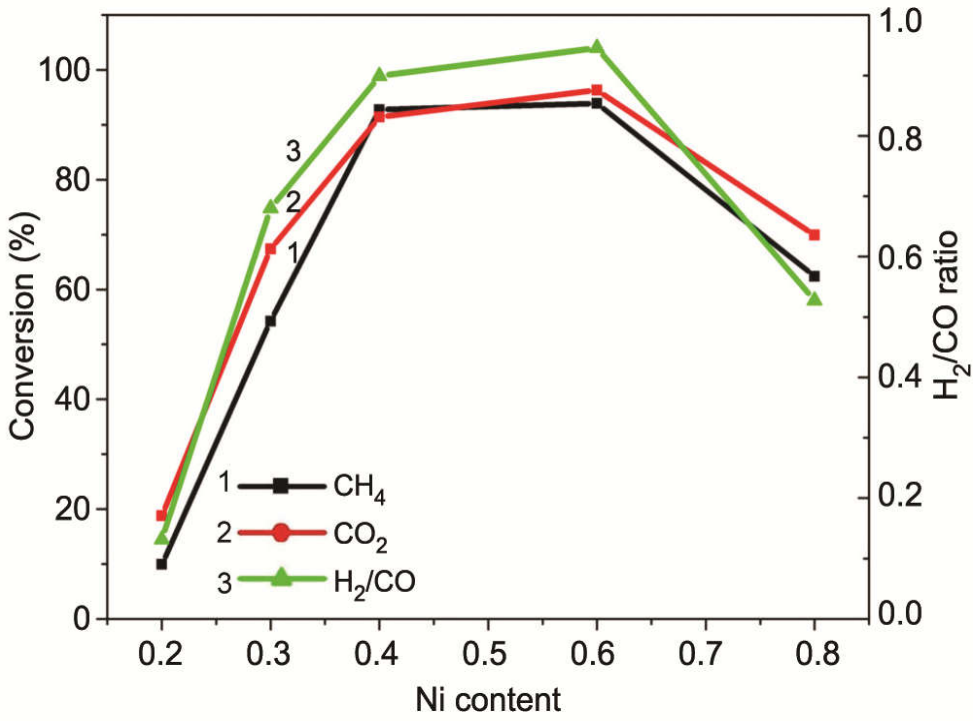

Figure 5.2.6: Catalytic Activity profiles during DRM reaction over $LaNi_xCe_{1-x}O_3$ catalysts synthesized by hydrothermal method (Temperature = 800 °C).

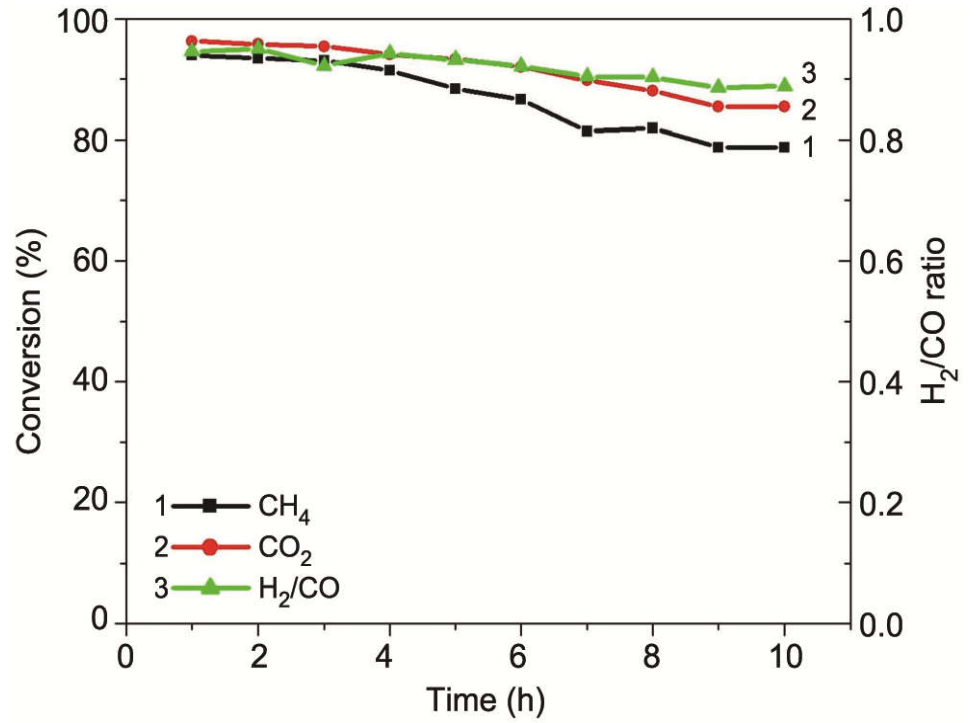

Figure 5.2.7: Time on stream analysis of $LaNi_{0.6}Ce_{0.4}O_3$ catalyst synthesized by hydrothermal method during DRM reaction at 800 °C.

The results of time on stream analysis performed on hydrothermally prepared $LaNi_{0.6}Ce_{0.4}O_3$ (GC chromatograph has been given in Appendix section Figure 4) catalyst at 800 °C are plotted in Figure 5.2.7. The catalyst could retain its activity to a larger extent during the 10 h period of evaluation showing a reasonable stability. The presence of strong interaction with Ni species and CeO_2 helps in resisting coke formation. Similarly, the syngas ratio was also retained in the region of 0.94 – 0.88. The H_2/CO ratio of the product gas in dry reforming is always less than the stoichiometric ratio of 1 as this reaction is always accompanied by the reverse water gas shift reaction.

5.2.4. H_2-TPR and XPS Correlation

The TPR patters were resolved and the composition of the first (β region) and second peak (γ region) are listed in Table 5.2.3. A continuous increase in the area of β region indicates that the active site belongs to this group. The actual dispersion of the active site can be identified by the H_2 Chemisorption analysis. As shown in Table 5.2.4 the dispersion correlated well with the activity. Though it is not possible with the available data to pin point the actual active site, it may be construed that the active site belongs to the β region of the solid solution. Table 5.2.5 also shows the increase in Ni^{2+}/Ni^{3+} ratio, giving credence to the observation that solid solution formation is predominant in these catalysts.

Table 5.2.3: H_2 uptake of $LaNi_xCe_{1-x}O_3$ catalysts synthesized by hydrothermal method.

S. No:	Catalyst	H_2 uptake (mmol/g)	
		β region	γ region
1	$LaNi_{0.2}Ce_{0.8}O_3$	0.000086939	0.000057661
2	$LaNi_{0.3}Ce_{0.7}O_3$	0.000392753	0.000062641
3	$LaNi_{0.4}Ce_{0.6}O_3$	0.000835732	0.000289297
4	$LaNi_{0.6}Ce_{0.4}O_3$	0.000461525	0.000405335
5	$LaNi_{0.8}Ce_{0.2}O_3$	0.000975095	0.000767613

Table 5.2.4: Ni Dispersion of $LaNi_xCe_{1-x}O_3$ catalysts synthesized by hydrothermal method.

S. No:	Catalyst	Ni Metal dispersion (%)	Ni Particle size (Å)
1	$LaNi_{0.2}Ce_{0.8}O_3$	10.3	47.8
2	$LaNi_{0.3}Ce_{0.7}O_3$	23.1	38.9
3	$LaNi_{0.4}Ce_{0.6}O_3$	31.1	32.5
4	$LaNi_{0.6}Ce_{0.4}O_3$	37.6	26.9
5	$LaNi_{0.8}Ce_{0.2}O_3$	17.4	58.1

Table 5.2.5: XPS data $LaNi_xCe_{1-x}O_3$ catalysts synthesized by hydrothermal method

S. No:	Catalyst	Peak Areas		Ratio Ni^{2+}/Ni^{3+}
		Ni^{2+}	Ni^{3+}	
1	$LaNi_{0.2}Ce_{0.8}O_3$	368	6634	0.055472
2	$LaNi_{0.3}Ce_{0.7}O_3$	591	5004	0.118106
3	$LaNi_{0.4}Ce_{0.6}O_3$	651	4867	0.133758
4	$LaNi_{0.6}Ce_{0.4}O_3$	781	4858	0.160766

5.2.5. Carbon analysis of the used $LaNi_xCe_{1-x}O_3$ catalysts

Table 5.2.6 comprises of the extent of carbon formation in samples collected after the DRM reaction which is carried out for 3 h. The carbon formation was found to be dependent on the amount of Ce present in the catalyst. Coking was reduced with increase in Ce. Ni–Ce solid solution formation might be the main reason to hinder the carbon formation and increase in the catalyst stability. Formation of Ni–Ce solid solution along with $LaNiO_3$ perovskite delivers highly dispersed Ni, as a result its agglomeration is prevented. Restriction of this ensemblement of Ni minimizes coking during DRM reaction.

Table 5.2.6: Carbon formed during the DRM reaction over $LaNi_xCe_{1-x}O_3$ catalysts synthesized by hydrothermal method.

S. No.	Catalyst	Carbon (%)
1	$LaNi_{0.8}Ce_{0.2}O_3$	0.55
2	$LaNi_{0.6}Ce_{0.4}O_3$	0.39
3	$LaNi_{0.4}Ce_{0.6}O_3$	0.34
4	$LaNi_{0.3}Ce_{0.7}O_3$	0.38
5	$LaNi_{0.2}Ce_{0.8}O_3$	0.32

5.2.6. Conclusions

Variation of Ni/Ce composition in $LaNi_xCe_{1-x}O_3$ catalysts results in two different types of active sites namely bimetallic perovskite with La i.e., $LaNiO_3$ and Ni–Ce solid solution. The characterization studies revealed that the structural and redox properties are highly dependent on the mole ratio of Ni used. The bimetallic perovskite phase ($LaNiO_3$) is observed in all the catalysts and it increased with the Ni molar ratio in catalysts. Ni–Ce solid solution phase is dominant in low Ni containing catalysts. These two active species play key role in the redox nature of Ni in $LaNi_xCe_{1-x}O_3$ catalysts and the catalytic activity over dry reforming of methane. Among the series of catalysts evaluated, the catalyst with $LaNi_{0.6}Ce_{0.4}O_3$ exhibited higher catalytic performance with conversions of methane and carbon dioxide as 94% and 96% respectively with syngas ratio equal to 0.94. This catalyst with x=0.6, when tested for its stability at 800 °C showed no considerable deactivation till 10 h of reaction time.

After a more quantitative analysis the following additional conclusions can be drawn. Ni^{2+}/Ni^{3+} ratio increases with increase in Ni content upto x=0.6. The solid solution formation is also predominant in these catalysts. The area of the TPR peak corresponding to the β region is higher than that of the γ region. A continuous increase in the area of β region indicates that the active site belongs to this group. The dispersion of the active site, as identified by the H_2 chemisorption analysis, correlated well with the activity. However, the exact nature of the active site cannot be established with the limited data available.

Section 5.3: $Ni_xCe_{1-x}O_2$ solid solution catalysts synthesized by sol-gel method

5.3.1. Introduction

Ni based catalysts which have been widely studied for the DRM reaction have strong thermodynamic potential for carbon deposition [43,44]. Therefore, influence of adding alkali, alkaline earth metals and rare earth metals to nickel has been investigated to improve the carbon resistance [45]. Ce showed good results among all the rare earth elements due to its red–ox properties derived from mobile oxygen vacancies. This material is also used to minimize the sintering of metal particles, thus, increasing the stability of the catalysts [16].

Work presented in this section deals with $Ni_xCe_{1-x}O_2$ solid solution catalysts synthesized by the sol-gel method. Synthesized catalysts are characterized by different techniques and evaluated for the DRM reaction. Incorporation of Ni into CeO_2 lattice increased the structural defects and helped to improve the reducibility of metal and resistance towards coking and sintering during the reaction. The results are discussed in detail below.

5.3.2. Results and Discussion

5.3.2a. Thermogravimetric analysis

The results of thermogravimetric analysis (TGA) performed on the $Ni_xCe_{1-x}O_2$ catalysts are presented in Figure 5.3.1. The decomposition of metal propionates was clearly observed. At first a small weight loss indicating a slow decomposition till 250 °C was observed. With the increase in the active metal ratio, the propionate decomposition moved towards lower temperatures. This may be due to the formation of Ni–Ce solid solution.

Possible decomposition pathway of metal propionate species is represented by the following equations [46].

$$M(O_4CCH_2CH_3)_2(OH)_2 \longrightarrow M(O_2CCH_2CH_3)(OH)_3 + CH_3CH = C = O \quad \text{-- 5.1}$$

$$M(O_2CCH_2CH_3)(OH)_3 \longrightarrow M(OH)_4 + CH_3CH = C = O \quad \text{-- 5.2}$$

$$M(OH)_4 \longrightarrow MO_2 + H_2O \quad \text{-- 5.3}$$

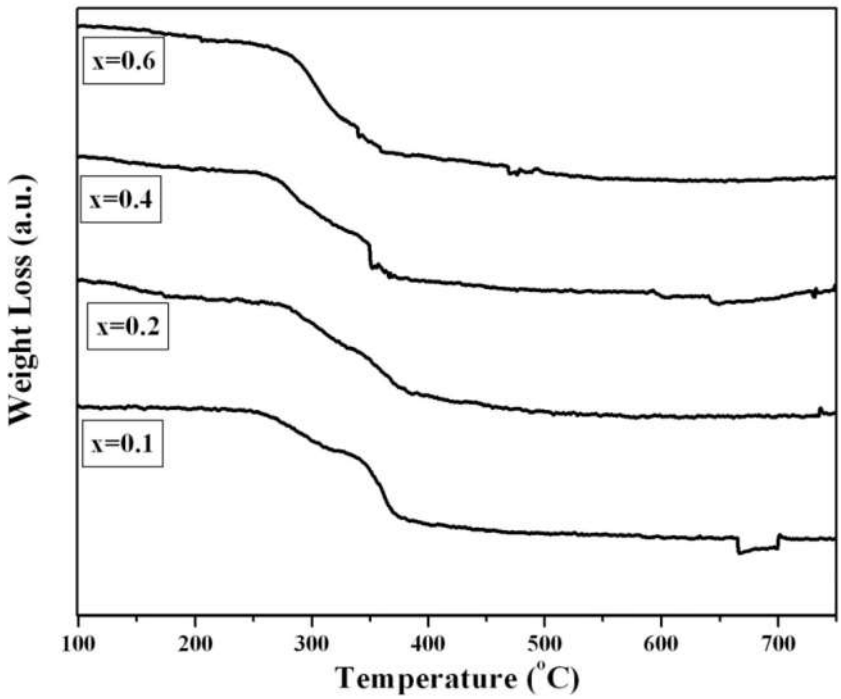

Figure 5.3.1: TGA patterns of $Ni_xCe_{1-x}O_2$ catalysts synthesized by sol-gel method.

5.3.2b. Specific surface area measurements

Specific surface areas of the calcined catalysts represented by general formula $Ni_xCe_{1-x}O_2$ were determined by BET method. The values are listed in Table 5.3.1. All the samples exhibited surface area under 20 m^2/g. The surface area increased with Ni content until x=0.4 and then a sudden drop was noticed. The surface areas of the catalysts are found to be dependent on the calcination temperature. In the present case, the high calcination temperature might be the reason for the low surface areas.

Table 5.3.1: Specific surface areas of $Ni_xCe_{1-x}O_2$ catalysts synthesized by sol-gel method.

S. No.	Catalyst	Specific surface area (m^2/g)
1	$Ni_{0.1}Ce_{0.9}O_2$	14.9
2	$Ni_{0.2}Cel_{0.8}O_2$	17.6
3	$Ni_{0.4}Cel_{0.6}O_2$	19.2
4	$Ni_{0.6}Cel_{0.4}O_2$	12.2

5.3.2c. X–ray diffraction studies

Figure 5.3.2 presents the diffraction patterns of $Ni_xCe_{1-x}O_2$ solid solution catalysts synthesized by sol-gel method. In all the synthesized catalysts, the high intense peaks at 2θ = 28.4, 33.2, 47.5, 56.3, 59.2, 69.7, 76.9 and 79.2° correspond to the cubic fluorite CeO_2 (JCPDS 81–0792). The low intense diffraction patterns appearing at 2θ = 37.2, 43.2, 63 and 75.5° can be ascribed to the presence of NiO (JCPDS 78–0643). These peaks were not observed in the low Ni containing samples. With the increase in Ni ratio, the intensity of the peaks related to NiO also increased, due to the formation of bulk NiO particles.

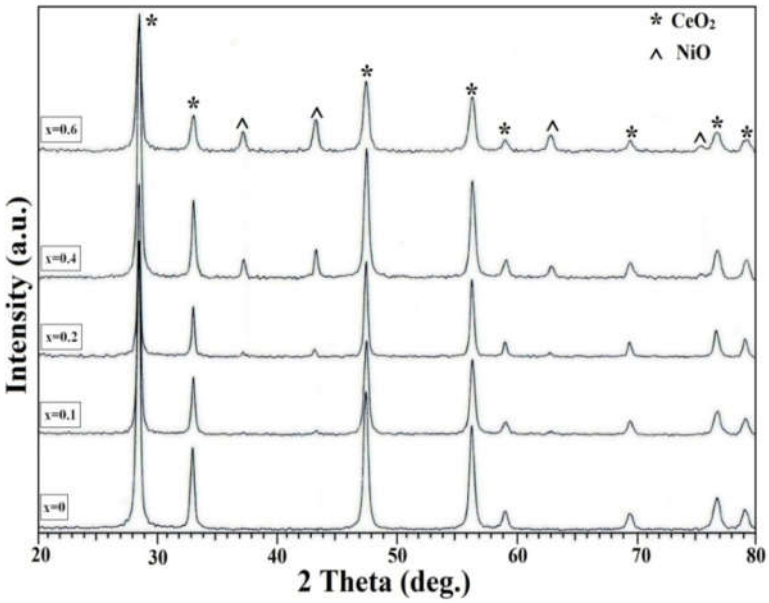

Figure 5.3.2: XRD patterns of $Ni_xCe_{1-x}O_2$ catalysts synthesized by sol-gel method.

Table 5.3.2: Variation of lattice parameter of Ce (111) plane in the $Ni_xCe_{1-x}O_2$ catalysts.

S. No.	Catalyst	Interplanar distance (d)	Lattice parameter (a) Å
1	CeO_2	3.13575	5.430
2	$Ni_{0.1}Ce_{0.9}O_2$	3.13185	5.422
3	$Ni_{0.2}Cel_{0.8}O_2$	3.13013	5.420
4	$Ni_{0.4}Cel_{0.6}O_2$	3.12735	5.416
5	$Ni_{0.6}Cel_{0.4}O_2$	3.12985	5.421

Change in lattice parameter of the cubic phase of CeO_2 111 plane is calculated with interplanar distance (d) in $Ni_xCe_{1-x}O_2$ catalysts and these values are displayed in Table 5.3.2. With increase in x value progressive decrease in the lattice parameter till x=0.4 is observed. Subsequently, slight increase in the lattice parameter is noticed. This deviation in lattice parameter is due to the exchange of Ni^{2+} ions with Ce^{4+} ions. Xu et al. [23] suggested the possibility of Ni^{2+} ion incorporation into CeO_2 lattice to form $Ni_xCe_{1-x}O_2$ solid solution. Under this condition two different types of active metal species can form in the higher Ni ratio catalysts. The first type is NiO dispersed on the surface layers of the CeO_2 and the second, Ni ion dissolved in the CeO_2 lattice to form the solid solution phase. This second type produces mobile lattice O^- species.

5.3.2d. Temperature programmed reduction studies

Figure 5.3.3 shows the temperature programmed reduction profiles of $Ni_xCe_{1-x}O_2$ catalysts. The high temperature (> 800 °C) peak can be ascribed to the reduction of CeO_2. The low temperature (< 300 °C) reduction band corresponds to the reduction of lattice oxygen generated after the formation of Ni–O–Ce solid solution, as observed by the lattice contraction (Table 5.3.1). The temperature maxima observed at 350–400 °C is due to the free NiO on CeO_2, and the one at 400–500 °C is ascribed to highly interacted NiO with CeO_2 support.

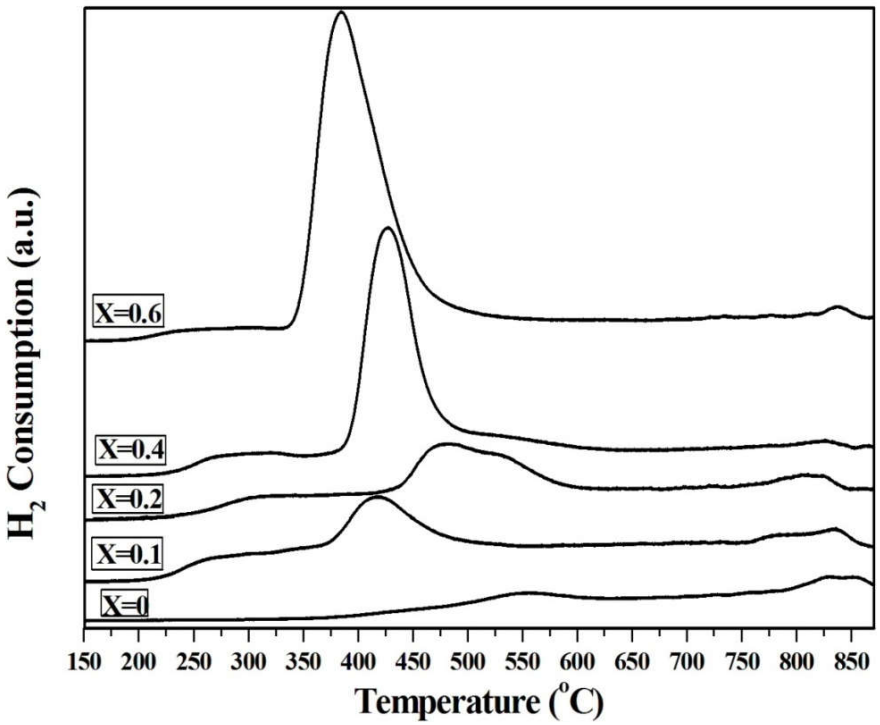

Figure 5.3.3: TPR profiles of $Ni_xCe_{1-x}O_2$ catalysts synthesized by sol-gel method.

The high intense peak in the case of catalyst with x=0.6 at ~400 °C is due the free NiO on the surface of the CeO_2. In the catalyst with x=0.4, there are two peak maxima corresponding to the reduction of free NiO and the NiO incorporated CeO_2. In the catalyst with x=0.2, the peak corresponding to the Ni–Ce oxide solid solution is mainly observed. These reduction profiles indicate the transformation of $Ni^{2+} \rightarrow Ni^0$ [23,25]. In the catalysts with x=0.1, the temperature maximum at 370 °C indicates the formation of free NiO on support CeO_2, along with the reduction of lattice oxygen.

As observed in XRD studies, the TPR studies on $Ni_xCe_{1-x}O_2$ catalysts also confirmed the formation of two types of active metal species in samples containing low Ni content (x= 0.1, 0.2 and 0.4) catalysts. Whereas, in high Ni content the catalysts showed bulkier NiO agglomerated on CeO_2 support.

5.3.2e. Raman Spectroscopy analysis

$Ni_xCe_{1-x}O_2$ catalysts were characterized by Raman spectroscopy. The results are depicted in Figure 5.3.4. The Raman band observed at 467 cm^{-1} corresponds to the F_{2g} pattern of CeO_2 fluorite structure [47]. The oxygen atoms around the Ce^{4+} ions were in symmetric mode. With the addition of Ni this F_{2g} band is shifted towards lower wavelength, also known as red Raman shift. This shift of Raman band is due to the change in lattice spacing and bond length as a consequence of incorporation of Ni in CeO_2 lattice [48].

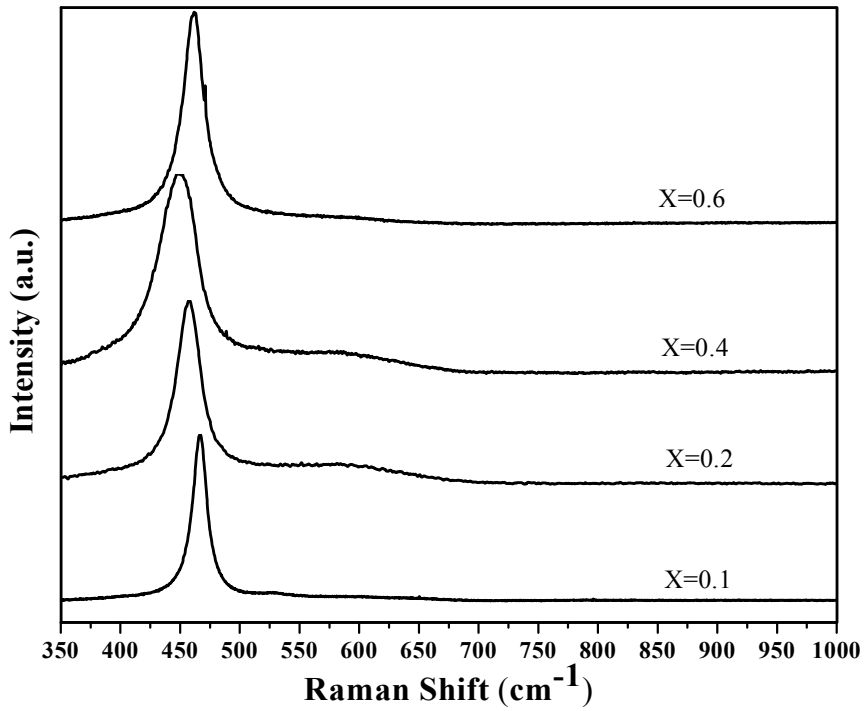

Figure 5.3.4: Raman spectra of $Ni_xCe_{1-x}O_2$ catalysts synthesized by sol-gel method.

The Raman spectroscopy results correlated well with the results of lattice parameter values presented in Table 5.3.2. It may be expected that either Ce^{4+} or Ce^{3+} was exchanged with Ni^{2+}. The Ni–O bond also shows some differences in vibration, polarizability and dipole moment [49]. With increase in the Ni ratio, the red shift increased for the catalysts with x = 0.2 - 0.4 and then returned to its original position.

This may be explained in terms of the estimated lattice parameter, which decreased till x=0.4 and then a sudden increase in catalyst with x=0.6 is observed. This confirms the dissolution of Ni ion in CeO_2, as clearly evidenced in X–ray diffraction studies.

A second band at 580 cm^{-1} was observed in the catalysts with x=0.2 and 0.4. In the literature, this band is ascribed to the defects induced in CeO_2 and it is denoted as D band, confirming the oxygen vacancies in CeO_2 [48]. The incorporation of Ni into CeO_2 leads to creation of oxygen vacancies, thereby increasing the redox nature of CeO_2.

5.3.2f. Fourier transform infrared spectroscopy studies

Figure 5.3.5 shows FT–IR spectra of the $Ni_xCe_{1-x}O_2$ catalysts scanned in the range of 2000–400 cm^{-1}.

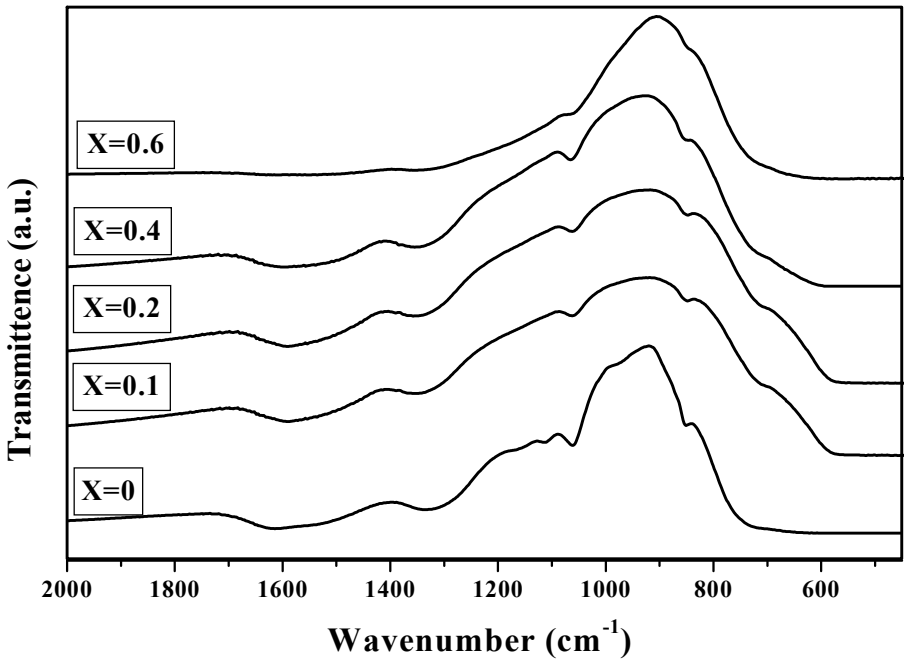

Figure 5.3.5: Fourier transform infrared spectra of $Ni_xCe_{1-x}O_2$ catalysts synthesized by sol-gel method.

The spectral data showed vibrational bands at ~1340 and ~1160 cm^{-1} which match with that of characteristic CeO_2 [50,51]. Transmittance band at ~974 cm^{-1} corresponds to the CeO_2 nano crystals [33]. With increasing Ni ratio in $Ni_xCe_{1-x}O_2$, the bands at 974,

1114 and 1160 cm^{-1} disappeared indicating the structural changes in the CeO_2. These observations are in conformity with those of XRD and Raman spectral studies.

5.3.2g. Scanning electron microscopy studies

Figure 5.3.6 shows SEM images of the $Ni_xCe_{1-x}O_2$ catalysts. The white spots in the images are attributed to the NiO species. Increase in the size of the white spots with increase in the Ni mole ratio is observed. This may be due to the formation of bulk crystalline NiO. These images support the evidence observed in the XRD studies, wherein it was noted that, the intensity of the peaks of NiO at 2θ = ~37°, 44° and 63° increases with increase in Ni ratio indicating the agglomeration NiO.

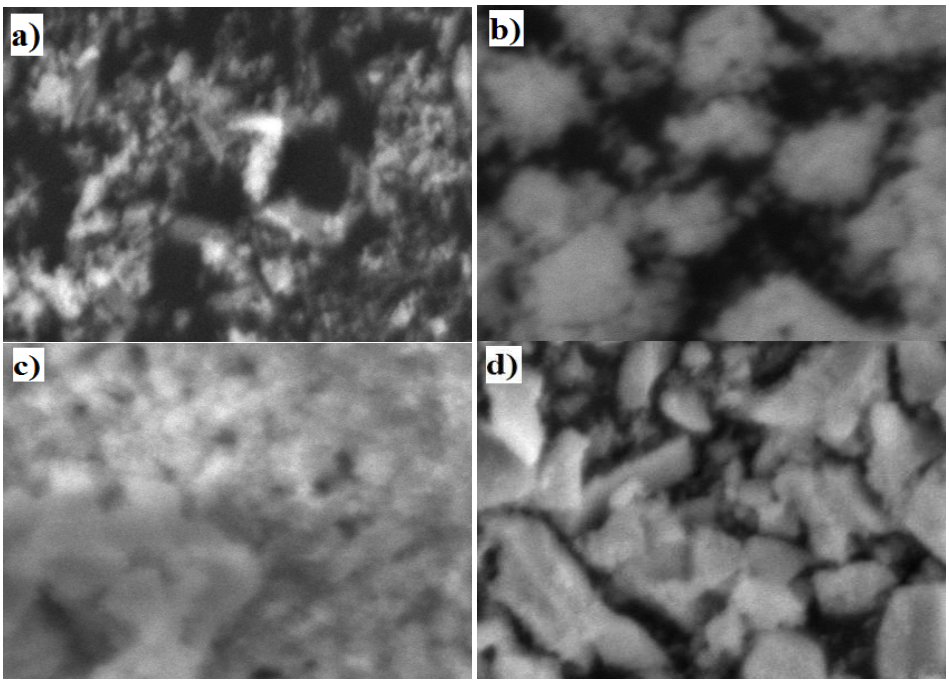

Figure 5.3.6: SEM Images of $Ni_xCe_{1-x}O_2$ catalysts synthesized by sol-gel method. a) x=0.1 b) x=0.2 c) x=0.4 and d) x=0.6.

5.3.3. Catalytic activity tests

Dry reforming of methane reaction was performed on the $Ni_xCe_{1-x}O_2$ catalysts in the temperature range of 650–800 °C with an increment of 50 °C. Figures 5.3.7 and 5.3.8 display the activity profiles of catalysts. It is observed that the activity of the catalysts

increased with the increase in Ni metal ratio till the value of x reaches to 0.4. This catalyst having $Ni_{0.4}Ce_{0.6}O_2$ (GC chromatograph has been given in Appendix section Figure 5) composition exhibited the highest activity showing methane conversion of 63% and carbon dioxide conversion of 68% with syngas ratio equal to 0.9. The XRD and TPR studies revealed that the catalyst with x=0.6 contains higher amount of free NiO on the surface than the others. However, free Ni can easily undergo sintering at high temperatures [12]. In the present work, the catalyst with x=0.6 showed higher activity (Figure 5.3.7) initially but got deactivated very fast due to plugging of coke.

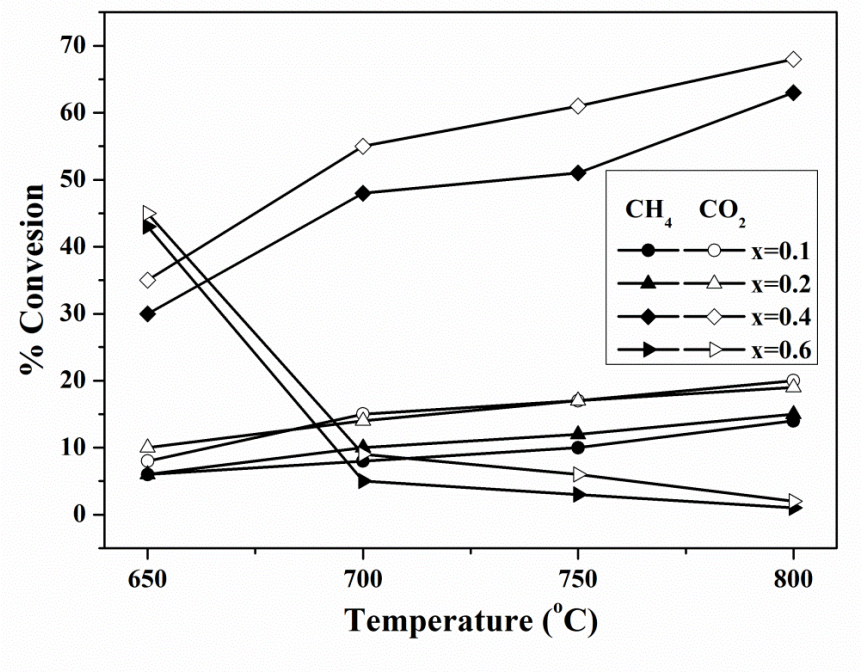

Figure 5.3.7: Variation of % of conversion of methane and carbon dioxide with temperature in the DRM reaction over $Ni_xCe_{1-x}O_2$ catalysts (Temperature = 800 °C).

The metal–support interaction plays a vital role during the reaction to inhibit the sintering of metal particles [35]. The NiO/Ni–CeO_2 phase formed in catalysts with x=0.4 showed the highest catalytic activity. Though catalyst with x=0.6 showed high reducibility due to the formation of NiO/CeO_2, the active site underwent heavy sintering

and coking. In this study, the carbon dioxide conversion was found to be higher than methane conversion due to favorable RWGS, as reported by Montoya et al. [37].

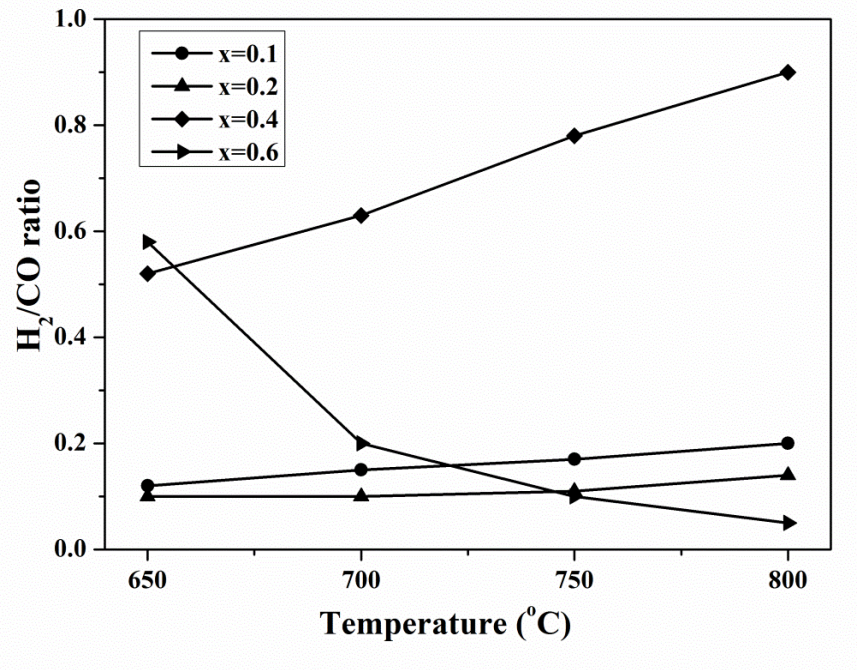

Figure 5.3.8: Variation of H_2/CO ratio with temperature during DRM reaction over $Ni_xCe_{1-x}O_2$ catalysts (Temperature = 800 °C).

5.3.4. Conclusions

Solid solution catalysts with general formula $Ni_xCe_{1-x}O_2$ (x = 0, 0.1, 0.2, 0.4 and 0.6) are prepared following the sol-gel method. These catalysts are characterized by TGA, BET, XRD, TPR, FT–IR and Raman techniques and are evaluated for carbon dioxide reforming of methane. The characterization studies illustrated that, successful incorporation of Ni into CeO_2 lattice results in the formation of Ni–Ce solid solution. Formation of the solid solution was confirmed by XRD, TPR, Raman and FT–IR studies. The $Ni_xCe_{1-x}O_2$ catalysts containing the solid solution phase along with highly dispersed NiO are found to be more active for the DRM reaction. The catalysts with x=0.4 showed the presence of both dispersed NiO and Ni–Ce solid solution and exhibited maximum catalytic activity. The carbon dioxide and methane conversions were found to be 68% and 65% respectively with a synthesis gas ratio of 0.9.

5.3.5. References

1. Yan, Z., Wang, Z., Bukur, D. B., & Goodman, D. W. (2009). *Journal Of Catalysis, 268*, 196-200.
2. Rostrup-Nielsen, J. R., Sehested, J., & Nørskov, J. K. (2002). *Advances In Catalysis, 47*, 65-139.
3. Riis. T., Hagen. E. F., Vie. P. J. S., & Ulleberg. Ø. (2005). International Energy Agency IEA Hydrogen production and storage. R&D priorities and gaps, 38pages
4. Ross, J. R. (2005). *Catalysis Today, 100*, 151-158.
5. Wang, S., Lu, G. Q., & Millar, G. J. (1996). *Energy & Fuels, 10*, 896-904.
6. Hu, Y. H., & Ruckenstein, E. (2004). *Advances in Catalysis, 48*, 297-345.
7. Fidalgo, B., Domínguez, A., Pis, J. J., & Menéndez, J. A. (2008). *International Journal of Hydrogen Energy, 33*, 4337-4344.
8. Domínguez, A., Fernández, Y., Fidalgo, B., Pis, J. J., & Menéndez, J. A. (2007). *Energy & Fuels, 21*, 2066-2071.
9. Fidalgo. B., & Menéndez. J. A., (2013). Syngas production by CO_2 reforming of CH_4 under microwave heating - Challenges and opportunity under Syngas: Production, Applications and Environmental Impact. ISBN: 978-1-62100-870-5, Eds: Indarto. A., Palguandi. J. Nova Science Publishers, Inc. pp: 121-149
10. Solymosi, F., Kutsan, G., & Erdöhelyi, A. (1991). *Catalysis Letters, 11*, 149-156.
11. Torniainen, P. M., Chu, X., & Schmidt, L. D. (1994). *Journal of Catalysis, 146*, 1-10.
12. Tsang, S. C., Claridge, J. B., & Green, M. L. H. (1995). *Catalysis Today, 23*, 3-15.
13. Kambolis, A., Matralis, H., Trovarelli, A., & Papadopoulou, C. (2010). *Applied Catalysis A: General, 377*, 16-26.

14. Roh, H. S., & Jun, K. W. (2008). *Catalysis surveys from Asia, 12*, 239-252.

15. Pakhare, D., & Spivey, J. (2014). *Chemical Society Reviews, 43*, 7813-7837.

16. Laosiripojana, N., & Assabumrungrat, S. (2005). *Applied Catalysis B: Environmental, 60*, 107-116.

17. Dong, W. S., Jun, K. W., Roh, H. S., Liu, Z. W., & Park, S. E. (2002). *Catalysis Letters, 78*, 215-222.

18. Pino, L., Recupero, V., Beninati, S., Shukla, A. K., Hegde, M. S., & Bera, P. (2002). *Applied Catalysis A: General, 225*, 63-75.

19. Nandini, A., Pant, K. K., & Dhingra, S. C. (2005). *Applied Catalysis A: General, 290*, 166-174.

20. Lima, S. M., Assaf, J. M., Pena, M. A., & Fierro, J. L. G. (2006). *Applied Catalysis A: General, 311*, 94-104.

21. Qi, A., Wang, S., Fu, G., Ni, C., & Wu, D. (2005). *Applied Catalysis A: General, 281*, 233-246.

22. Larimi, A. S., & Alavi, S. M. (2012). *International Journal of Chemical Engineering and Applications, 3*, 6-9.

23. Xu, S., Yan, X., & Wang, X. (2006). *Fuel, 85*, 2243-2247.

24. Pirez, C., Capron, M., Jobic, H., Dumeignil, F., & Jalowiecki-Duhamel, L. (2011). *Angewandte Chemie International Edition, 50*, 10193-10197.

25. Yonggang, W. E. I., Hua, W. A. N. G., Kongzhai, L. I., Xing, Z. H. U., & Yunpeng, D. U. (2010). *Journal of Rare Earths, 28*, 357-361.

26. Haack, L. P., Peters, C. R., & Otto, K. (1992). *Applied Catalysis A: General, 87*, 103-114.

27. Kumar, M. A., Venumadhav, C., Sagar, T. V., Surendar, M., Lingaiah, N., Rao, G. N., & Prasad, P. S. (2014). *Indian Journal of Chemistry -Section A, 53A*, 530-534.
28. Sudarsanam, P., Mallesham, B., Reddy, P. S., Großmann, D., Grünert, W., & Reddy, B. M. (2014). *Applied Catalysis B: Environmental, 144*, 900-908.
29. Kuntaiah, K., Sudarsanam, P., Reddy, B. M., & Vinu, A. (2013). *RSC Advances, 3*, 7953-7962.
30. Fierro, J. L. G. (1990). *Catalysis Today, 8*, 153-174.
31. Pena, M. A., & Fierro, J. L. G. (2001). *Chemical Reviews, 101*, 1981-2018.
32. Ganguly, P., & Vasanthacharya, N. Y. (1986). *Journal of Solid State Chemistry, 61*, 164-170.
33. Ying, J. Y., & Tschöpe, A. (1996). *The Chemical Engineering Journal and The Biochemical Engineering Journal, 64*, 225-237.
34. Nyquist. R. A., Putzig. C. L., & Leugers. M. A. (1997). in The Handbook of Infrared and Raman spectra of Inorganic Compounds and Organic Salts, ed. A. R. Nyquist, C. L. Putzig and M. A. Leugers, Academic Press Ltd., San Diego, CA, Vol. 4.
35. Khalesi, A., Arandiyan, H. R., & Parvari, M. (2008). *Chinese Journal of Catalysis, 29*, 960-968.
36. Moradi, P., & Parvari, M. (2006). *Iranian Journal of Chemical Engineering, 3*, 29-43.
37. Montoya, J. A., Romero-Pascual, E., Gimon, C., Del Angel, P., & Monzon, A. (2000). *Catalysis Today, 63*, 71-85.
38. Laosiripojana, N., Sutthisripok, W., & Assabumrungrat, S. (2005). *Chemical Engineering Journal, 112*, 13-22.

39. Taufiq-Yap, Y. H., Rashid, U., & Zainal, Z. (2013). *Applied Catalysis A: General, 468*, 359-369.

40. Sohier, M. P., Wrobel, G., Bonnelle, J. P., & Marcq, J. P. (1992). *Applied Catalysis A: General, 84*, 169-186.

41. Lamonier, C., Ponchel, A., D'huysser, A., & Jalowiecki-Duhamel, L. (1999). *Catalysis Today, 50*, 247-259.

42. Daza, C. E., Gallego, J., Moreno, J. A., Mondragón, F., Moreno, S., & Molina, R. (2008). *Catalysis Today, 133*, 357-366.

43. Chen, J., Wang, R., Zhang, J., He, F., & Han, S. (2005). *Journal of Molecular Catalysis A: Chemical, 235*, 302-310.

44. Ocsachoque, M., Pompeo, F., & Gonzalez, G. (2011). *Catalysis Today, 172*, 226-231.

45. Cheng, Z., Wu, Q., Li, J., & Zhu, Q. (1996). *Catalysis Today, 30*, 147-155.

46. Kim, M. (2008). Mixed-metal oxide nanopowders by Liquid-feed Flame Spray Pyrolysis (LF-FSP): Synthesis and processing of core-shell nanoparticles (Doctoral dissertation, The University of Michigan).

47. Reddy, B. M., Katta, L., & Thrimurthulu, G. (2009). *Chemistry of Materials, 22*, 467-475.

48. Mahammadunnisa, Sk., Reddy, P. M. K., Lingaiah, N., & Subrahmanyam, Ch. (2013). *Catalysis Science & Technology, 3*, 730-736.

49. Sun, S., Zhao, X., Lu, H., Zhang, Z., Wei, J., & Yang, Y. (2013). *CrystEngComm, 15*, 1370-1376.

50. Ketzial, J. J., & Nesaraj, A. S. (2011). *Journal of Ceramic Processing Research, 12*, 74-79.

51. Yan, B., & Zhu, H. (2008). *Journal of Nanoparticle Research, 10*, 1279-1285.

Chapter 6

Studies on Zirconium modified $LaNiO_3$ catalysts for CO_2 reforming of methane

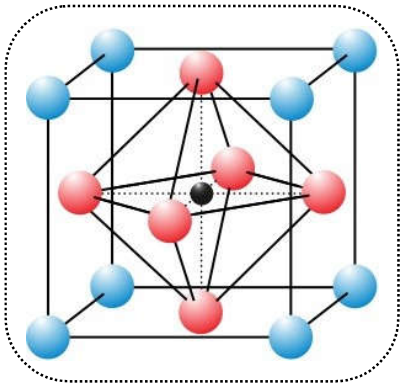

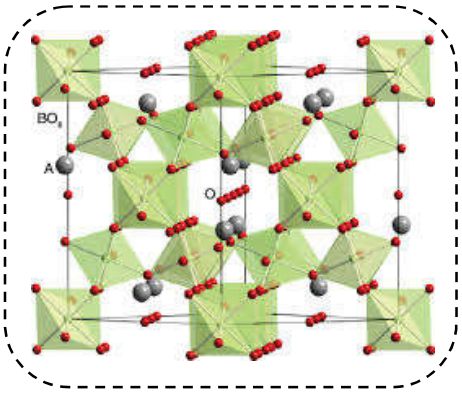

6.0. Introduction

As discussed in previous chapters, dry reforming of methane (DRM) is a process which converts potent greenhouse gases (CH_4 and CO_2) into useful syngas with H_2/CO ratio of 1 [1,2]. This ratio is the preferable feedstock for Fischer–Tropsch synthesis to produce higher hydrocarbons and the production of oxygenated derivatives. As DRM reaction operates at 600–800 °C, the catalyst suffers from sintering and coking. Because of these drawbacks no commercial catalyst has been developed so far for its industrial implementation [3]. Thus, the development of an efficient and suitable catalyst for DRM reaction is critical for future needs.

Several Ni catalysts supported on conventional oxides have been studied for DRM reaction, with limited success. The applications of Ni based structured oxides as catalysts for the reaction are many,the active metal can isomorphically substituted into various structures to enhance the catalytic activity [1]. The active metal in these materials is bound within the structure thereby increasing the thermal stability of the catalyst. The oxygen mobility in the catalyst can be enhanced by the substitution of active metals into the lattice, which helps to enhance the resistance towards carbon deposition [4-6]. The structural materials so far attempted include perovskite, pyrochlore, fluorite and hexaaluminate [6-10].Pyrochlores are highly crystalline mixed metal oxides having the general formula $A_2B_2O_7$. The A–site of these materials is usually occupied by the large rare–earth trivalent metal such as La and the B–site is occupied by a smaller tetravalent transition metal such as Zr. $Eu_2Ir_2O_7$pyrochlore materials were first used to study DRM reaction by Ashcroft et al. [12-14].

In this chapter, studies on Zr modified $LaNiO_3$catalysts ($LaNi_xZr_{1-x}O_3$) with varying x values synthesized by sol-gel method and hydrothermal method are presented. The structural properties of the catalysts are analyzed withBET, XRD, TPR, FT–IR, XPS

and CHNS (carbon analysis in used catalysts) techniques. The synthesized catalystsare evaluated for DRM reaction. The phase transformation with the modification of Zr inB–site is studied, to verify the advantages for the application of pyrochlore structure in syngas production by DRM reaction.

Section 6.1: Zr modified $LaNiO_3$ catalysts synthesized by sol-gelmethod

6.1.1. Introduction

The Zr modified mixed oxide catalysts $LaNi_xZr_{1-x}O_3$were synthesized by sol-gel method following the procedure outlined in Chapter 3 Section 3.1.2a.The structural properties of the catalysts have been determined by employing different analytical techniques. The synthesized catalysts have been evaluated for their efficacy towards DRM reaction. The transformation from perovskite structure to pyrochlore structure with the addition of Zr into the $LaNiO_3$ oxide frame work and its influence on catalytic performance of the material are discussed here.

6.1.2. Results and Discussion

6.1.2a. Specific surface area measurements

The specific surface areas of $LaNi_xZr_{1-x}O_3$ catalysts prepared by sol-gel method are determined by BET method and are reported in Table 6.1.1. Surface areas of $LaNi_xZr_{1-x}O_3$ catalysts decreased with increase in the Ni content.

Table 6.1.1: Specific surface areas of $LaNi_xZr_{1-x}O_3$ catalysts synthesized by sol-gel method.

S. No.	Catalysts	Specific surface area (m^2/g)
1	$LaNi_{0.2}Zr_{0.8}O_3$	13.61
2	$LaNi_{0.3}Zr_{0.7}O_3$	12.36
3	$LaNi_{0.4}Zr_{0.6}O_3$	6.87
4	$LaNi_{0.6}Zr_{0.4}O_3$	3.39
5	$LaNi_{0.8}Zr_{0.2}O_3$	5.16

This may be due to the change in surface properties of the catalysts with Ni content. As described in the previous chapters, the surface areas of the catalysts are dependent on the calcination temperature. This fact is also confirmed experimentally by Valderrama et al. [14,15].

With increase in Ni content the surface area dropped to 3.39 m^2/g when x=0.6. Decrease in the surface area indicates the bulk nature of the solids. Small increase in surface area at x=0.8 to 5.16 m^2/g is possibly due to the formation of free NiO.

6.1.2b. X–ray diffraction studies

Figure 6.1.1 shows XRD patterns of $LaNi_xZr_{1-x}O_3$ catalysts synthesized by sol-gel method. With change in Ni content, a variety of solid phases appeared in the catalysts. Low Ni–containing catalysts exhibited high intense diffraction peaks at 2θ = 28, 31, 47, and 55°. These peaks correspond to the compound of general formula $La_2Zr_2O_7$ having a crystalline cubic structure of typical pyrochlore compound. Along with this, a low intense $LaNiO_3$perovskite phase (JCPDS 34–1181) formation was also observed. On the other hand, the catalyst with high Ni loading (x=0.8) showed a completely different trend by the formation of $LaNiO_3$ bimetallic rhombohedral perovskite phase (JCPDS 34–1181). A low intensity peak was observed at 2θ = 43° in all the catalysts synthesized, which is ascribed to NiO (JCPDS 78–0643). With increase in Ni content, the intensity of perovskite peak increased indicating the formation of highly crystalline phase.

A study conducted by Bespalko et al. [17], on Ni–La–Zr oxide catalysts prepared by sol-gel method indicated the formation of $La_2Zr_2O_7$ along with NiO as a mono oxide phase. From their crystallographic studies, they concluded that the formation of bimetallic pyrochlore phase proceeded due to the formation of the biphasic system ($MeLaZr \rightarrow MeOx + La_2Zr_2O_7$) [17]. The same group (Bussi et al. [18]) opined that the amorphous oxide formed might be converted into the biphasic system. $(NiLaZr\ mixed\ oxides)_{amorphous} \rightarrow NiO + La_2Zr_2O_7$ [18]. Studies carried out by Gaur et al. [19], on doping Rh, Ni and Ca into La–Zr pyrochlore showed the formation of a discrete Ni oxide peak other than the pyrochlore structure in case of Ca due to the incorporation of Ca^{2+}cation in place of La^{3+}cation. The oxygen vacancies led to the structural defects and eventuallyto

the formation of $CaZrO_3$perovskite phase. They also concluded that the lowlevels of substitution at B–site did not have much of an effect on the pyrochlore structure [19].

According to the above studies the formation of pyrochlore with La–Zr catalysts are more favourable in the low B–site modification. Thesefindings are very much in agreement with the observations made in the present study, where the pyrochlore phase dominated in low Ni containing samples. On the other hand, with the increase in Ni loading, the formation of $LaNiO_3$perovskite became more favourable than La–Zr pyrochlore. These typical phase changes were observed with change in Ni metal content. It is clearly observed that at high Ni loading, the interaction between Ni and La was favourable for forming the pure perovskite phase, whereas at low Ni loading, the dominance of La–Zr interaction led to pyrochlore structure formation.

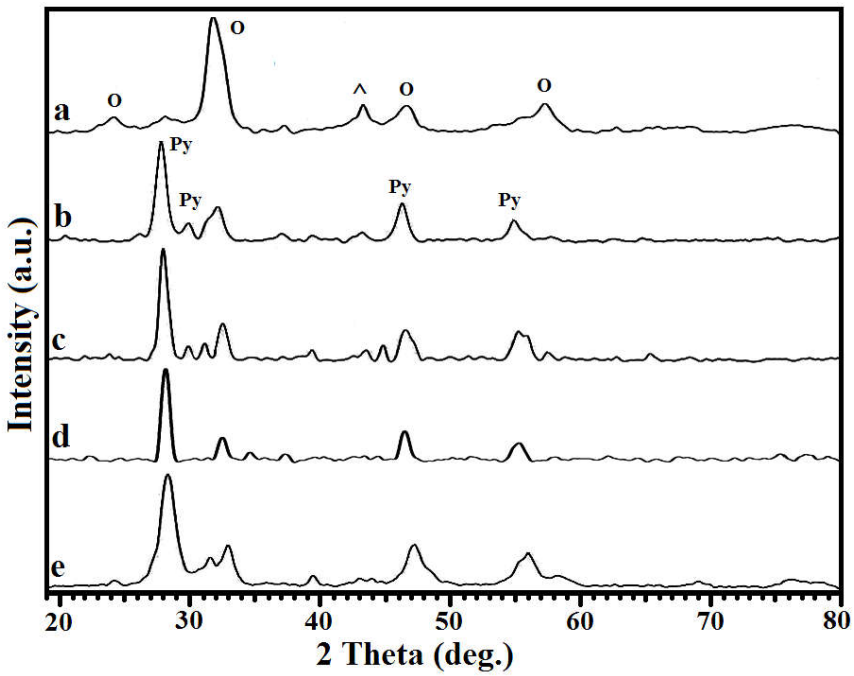

Figure 6.1.1:XRD patterns of $LaNi_xZr_{1-x}O_3$ catalysts synthesized by sol-gel method. a) x = 0.8, b) x = 0.6, c) x = 0.4,d) x = 0.3 and e) x = 0.2.(O) $LaNiO_3$,(Py) $La_2Zr_2O_7$, (^)NiO.

6.1.2c. Fourier transform infrared spectroscopy studies

Figure 6.1.2 shows FT–IR patterns of $LaNi_xZr_{1-x}O_3$ oxide catalysts synthesizedby sol-gel method. In catalysts with low Ni content, the –O–H stretching band of physisorbed inner layer water species appeared at 3200–3500 cm^{-1}. The bands at 1072–1180 and 1472–1424 cm^{-1} correspond to Zr–O and O–C=O of the carboxylate spices in the metal propionates, which suggest that traces of propionates still existed after calcination. Studies on La–Zr oxide thin films by Chen et al. [20], revealed the FT–IR transmittance bands at 3200–3500, 1039–1125 and 1403–1541 cm^{-1} related to –O–H, Zr–O–C and O–C=O species, respectively. In another study conducted by Koteswara Rao et al. [21], high intense bands of $La_2Zr_2O_7$pyrochlore phase were seen in the absorption region of 1120–1110 cm^{-1} and low intense bands in the region 2350–2360 cm^{-1} due to the Zr–O vibrations.

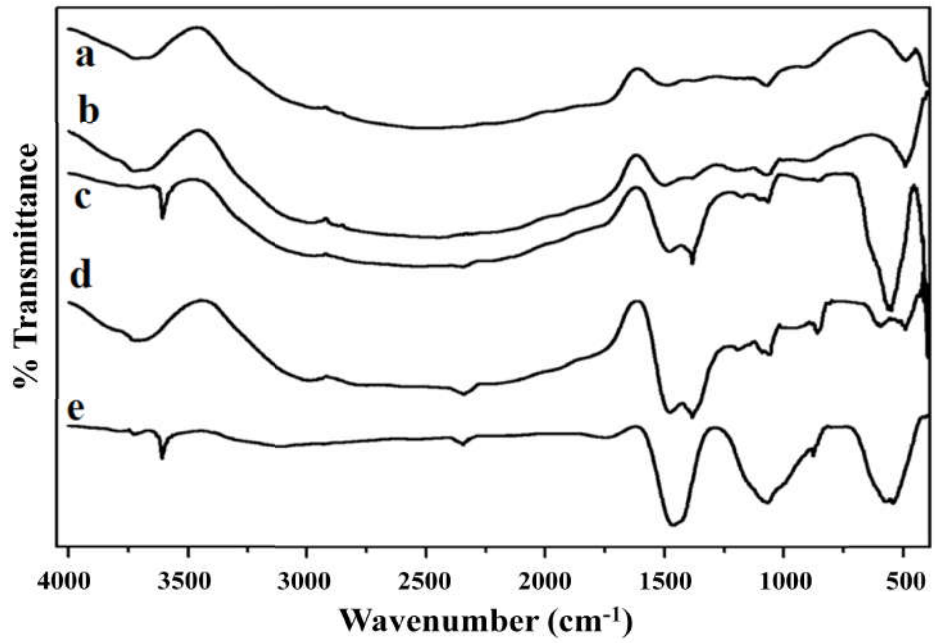

Figure 6.1.2:FT–IR patterns of $LaNi_xZr_{1-x}O_3$ catalysts synthesized by sol-gel method. a) $x = 0.8$, b) $x = 0.6$, c) $x = 0.4$, d) $x = 0.3$ and e) $x = 0.2$.

According to Tong et al. [22], in La–Zr pyrochlore, the ZrO_6 vibrational mode produces a transmittance band at 539 cm^{-1}. As Ni content increased, the intensities of the bands corresponding to Zr–O and ZrO_6 decreased and almost disappeared in higher Ni containing catalysts. When x=0.8, all the other bands were minimized and the peaks noticed were due to the metal oxygen stretching frequencies. The FT–IR spectra recorded in the present study are in good agreement with the previous observations [20-22].

The finding from FT–IR analysis is well corroboratedwith the results of X–ray diffraction studies.Where in all the low Ni containing catalysts showed La–Zr pyrochlore phase and with increase in Ni content, this pyrochlore phase disappeared, and $LaNiO_3$perovskite is formed.

6.1.2d. Temperature programmed reduction studies

TPR studies on $LaNi_xZr_{1-x}O_3$ catalysts synthesized by sol-gel method have been carried out by varying the Ni content in the range x = 0.2 to 0.8. The results are depicted in Figure 6.1.3. The reduction peaks appeared in two zones; the first falling in the temperature zone of 400–600 °C and the second falling in the temperature zone> 600 °C. Bussi et al. [23], in their studies on Ni/LaZr pyrochlore catalysts, demonstrated the difference in the properties of Ni catalysts prepared by co–precipitation method and impregnation method, particularly in the reduction behaviour. The catalysts prepared by co–precipitation method showed their reduction peaks at higher than 550 °C implying strong interaction of Ni with La–Zr pyrochlore. Whereas in the catalysts prepared by impregnation method, the major reduction peak appeared at <500 °C due to NiO available on the surface of La–Zr mixed oxide [23]. In the present investigation also the reduction patterns of $LaNi_xZr_{1-x}O_3$ catalysts prepared by sol-gel method followed the same trend.

At low concentrations of Ni, it has high interaction with support La–Zr pyrochlore leading to the domination of high temperature peak. As the Ni content increases, the NiO

exists in highly dispersed state on La–Zr pyrochlore. Consequently, the reduction temperature decreased. The dispersed NiO is easily reduced yielding Ni^0 species at lower temperature.

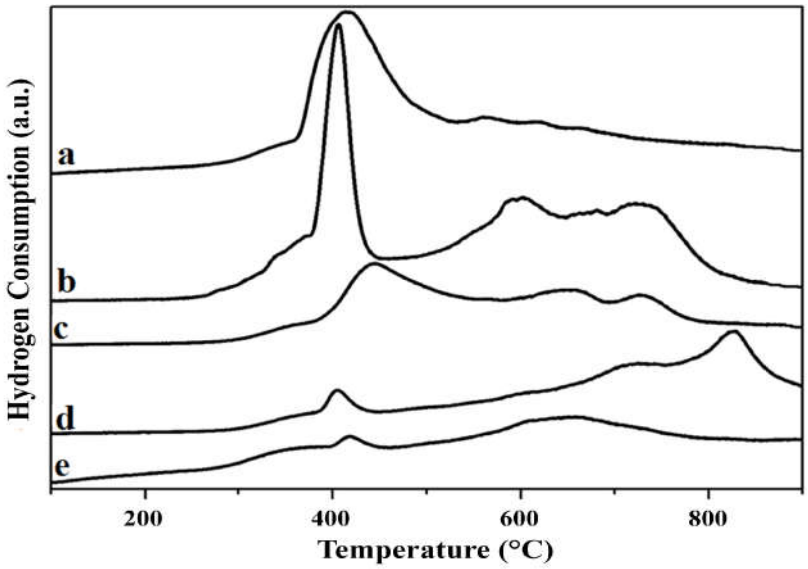

Figure 6.1.3:TPR Profiles of $LaNi_xZr_{1-x}O_3$ catalysts synthesized by sol-gel method. a) x = 0.8, b) x = 0.6, c) x = 0.4,d) x = 0.3, and e) x = 0.2.

6.1.2e. X–ray photoelectric spectroscopy studies

La 3d core level XP spectra of $LaNi_xZr_{1-x}O_3$ catalysts synthesized by sol-gel method are shown in Figure 6.1.4. The spectra showed two peaks corresponding to $3d_{5/2}$ with binding energies at 834 and 838 eV, as observed in the studies presented in previous chapters. Splitting of ~4 eV is due to the charge transfer from ligand (O 2p) to metal (La 4f). Similar observation was also made by Lima et al. [24], in their study on $La_xCe_{1-x}NiO_3$. In another study Xu et al. [25], noticed the doublet peak for $La3d_{5/2}$ appearing at 834.3 and 838.2 eV, they concluded that this binding energy valuesare higher than the simple La_2O_3. Hence, they predicted the possibility of La–Zr solid solution/pyrochlore formation [25]. In the present study, the binding energy peaks in the ranges of 834.3–838.5 and 851–852 eV correspond to $3d_{5/2}$ and $3d_{3/2}$, respectively [24]. These peaks confirm the presence ofLa^{3+} on the surface of the catalysts. The other peaks at 851–852

eV are due to La $3d_{3/2}$. However, due to overlapping of binding energies of La $3d_{3/2}$ and Ni $2p_{3/2}$, it is very difficult to interpret their peaks clearly.

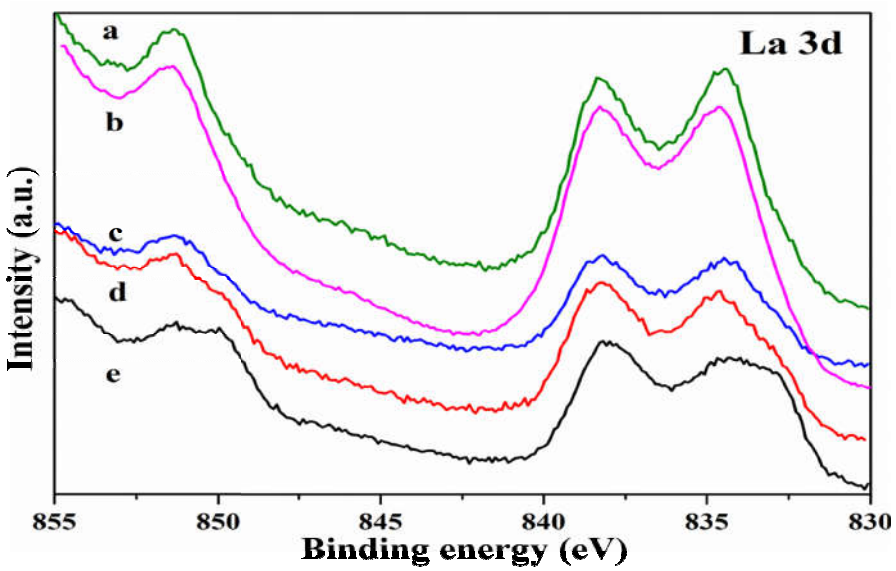

Figure 6.1.4: La 3d Core level spectra of $LaNi_xZr_{1-x}O_3$ catalysts synthesized by sol-gel method. a) $x = 1$, b) $x = 0.6$,c) $x = 0.4$, d) $x = 0.3$ and e) $x = 0.2$.

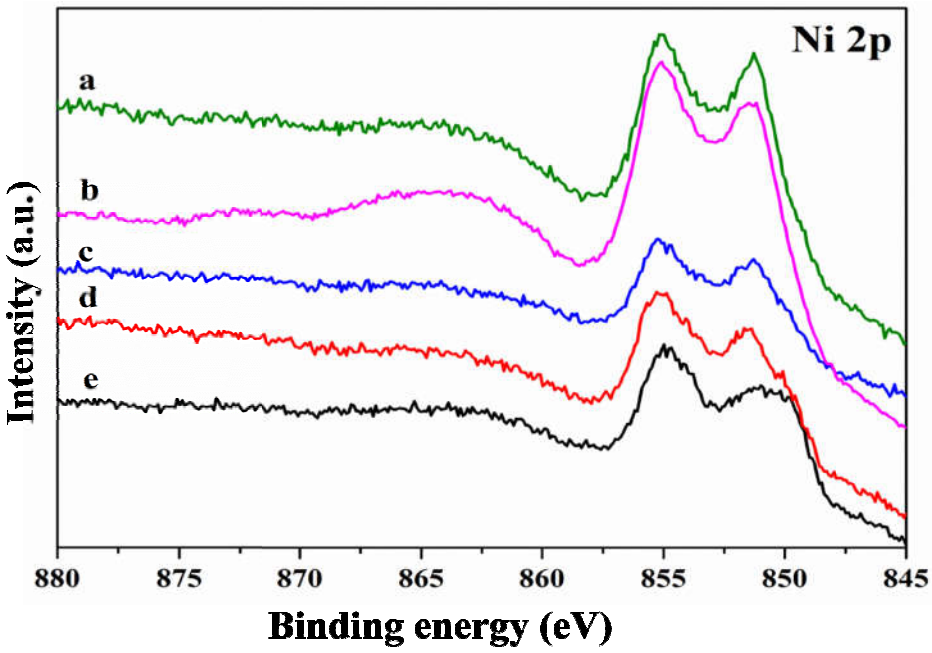

Figure 6.1.5: Ni 2p Core level spectra of $LaNi_xZr_{1-x}O_3$ catalysts synthesized by sol-gel method. a) $x = 1$, b) $x = 0.6$, c) $x = 0.4$, d) $x = 0.3$ and e) $x = 0.2$.

XP spectra of Ni 2p are presented in Figure 6.1.5.The peaks with binding energies

at 851 and 855 eV correspond to Ni $2p_{3/2}$. These binding energies of Ni are higher than the simple NiO signifying that Ni is stabilized in higher oxidation state, confirming the possible formation of perovskite in the catalyst samples with high Ni content. The same observation was also made by the Gaur et al. [19], in their studies on Rh, Ni, and Ca-substituted $La_2Zr_2O_7$ pyrochlore catalysts. They observed high binding energies for Ni $2p_{3/2}$ than the regular NiO (Ni^{2+}). They attributed this high binding energy shift due to the existence of Ni in Ni_2O_3 (Ni^{3+}). Other studies conducted on perovskite type oxide catalysts also showed high binding energy peaks than the regular NiO, indicating the presence of Ni^{3+} [24,26].This is due to the high oxygen environment around Ni. With increase in the Ni content in the catalysts, the peak is shifted towards higher binding energy value. This is also well corroborated with the results obtained from XRD studies which revealed that the formation of perovskite phase is dominant in higher Ni containing samples.

Figure 6.1.6 shows the Zr 3d XP spectra of the $LaNi_xZr_{1-x}O_3$ catalysts synthesized by sol-gel method. The bands corresponding to Zr^{4+} in Zirconium oxide appearing at 181.3 and 183.7 eV are attributed to Zr $3d_{5/2}$ and Zr $3d_{3/2}$, respectively [27]. However, in low Nicontainingcatalysts,the binding energy values recorded are little lower indicating that the Zr is in lower oxidation state due to the structural defects arising by strong interaction with other metals. With increase in Ni content in the catalysts, the binding energy bands got shifted to a higher value indicating that the Zr is stabilized in ZrO_2. This result is in accordance with XRD and FT–IR data of these samples. In the Zr 3d XP spectra reported by Xu et al. [25], the peaks corresponding tobinging energy 181.3 and 183.7 eV were of Zr 3d5/2 and Zr 3d3/2, respectively, the splitting of binding energies being 2.4 eV. This photoemission feature is well corroborated with previous literature studies [25].

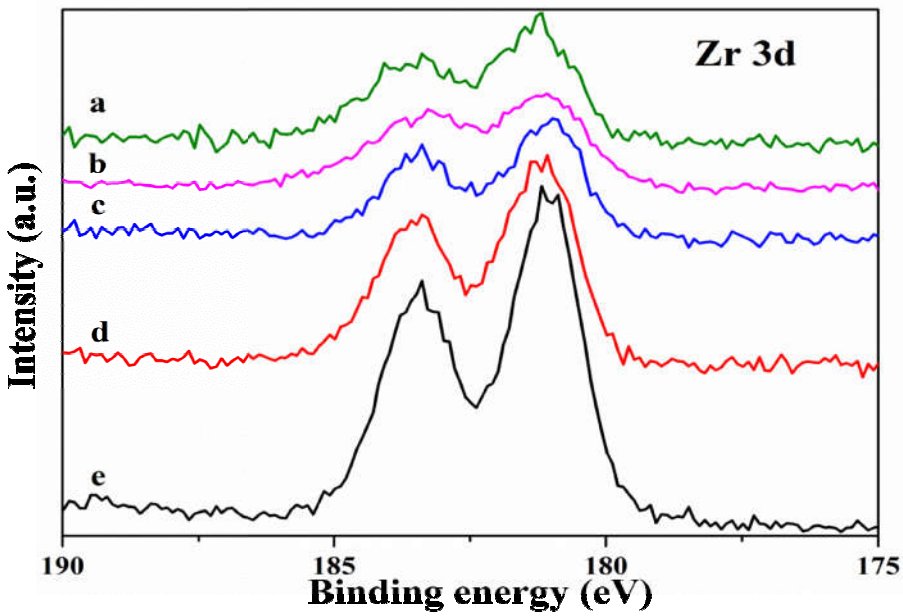

Figure 6.1.6: Zr 3d Core level spectra of $LaNi_xZr_{1-x}O_3$ catalysts synthesized by sol-gel method. a) $x = 1$, b) $x = 0.6$, c) $x = 0.4$, d) $x = 0.3$ and e) $x = 0.2$.

6.1.3. Catalytic activity tests

The DRM reaction was conducted over the synthesized $LaNi_xZr_{1-x}O_3$catalysts using the feed in the ratio of CH_4:CO_2:N_2=80:80:80 and a total gas flow rate of 240 ml/min in a fixed bed reactor. Figure 6.1.7 shows the activity profiles of $LaNi_xZr_{1-x}O_3$oxide catalysts observed at 800 °C. The conversion of both methane and carbon dioxide progressively increased with increase in the Ni content in the catalysts and attained their maximum values with catalysts having x value of 0.8. As discussed in the section on TPR studies (6.1.2d), the reducibility of the catalysts increased with the increase in Ni content. The catalytic activity also followed the same trend. As the Ni ratio increased, the formation of dispersed Ni on La–Zr support increased, leading to enhanced activity. On the other hand, catalysts with lower Ni ratio (x=0.2–0.4) showed greater interaction with the support lowering the reducibility. Among the series,x = 0.8 catalyst showed higher activity with 50% of CO_2 conversion and 37% of CH_4 conversion along with a syngas ratio of 0.76. This trend of higher conversion of CO_2 over methane was

also identified by other researchers [24,26,28]. Bachiller-Baeza et al. [28], observed that the DRM reaction is always accompanied by side reactions like reverse water gas shift reaction (RWGS). This reaction consumes H_2 produced in DRM reaction to form CO, thereby decreasing the syngas ratio.

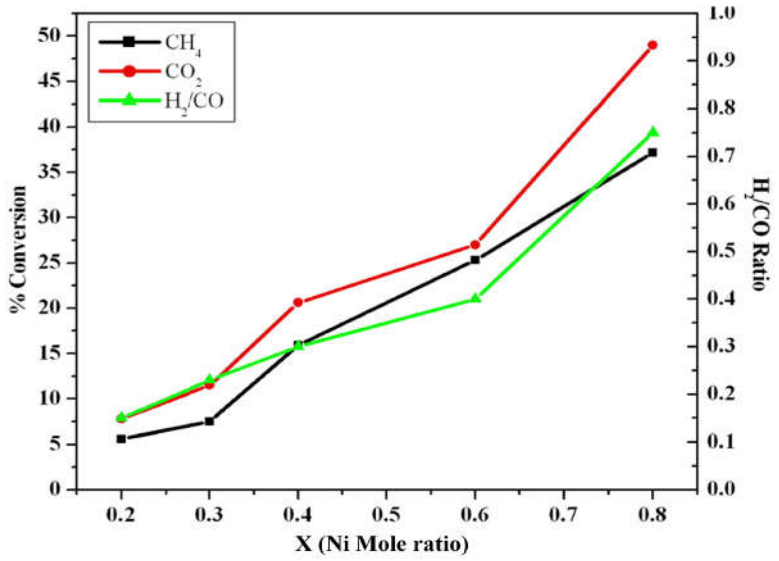

Figure 6.1.7: Catalytic activity study on DRM reactionover $LaNi_xZr_{1-x}O_3$ catalysts synthesized by sol-gel method (Temperature = 800°C).

In XRD studies the peaks due to free NiO were not observed clearly in low Ni containing catalysts probably due to its amorphous nature. Increase in Ni content in the catalysts changed the nature of phase from La–Zr pyrochlore to La–Ni perovskite. This phase transformation is also confirmed in the XPS studies. Catalysts with higher Ni content, after reduction could lead to the formation of Ni metal with its high dispersion on La_2O_3 and also free Ni in the bulk form. This may be the reason for higher activity of the catalysts having high Ni content.

Figure 6.1.8 shows the time on stream study of $LaNi_{0.8}Zr_{0.2}O_3$ (GC chromatograph has been give in Appendix section Figure 6) catalyst at 800 °C for 10 h for DRM reaction. The catalyst showed reasonable stability for 10 h. There was no decrease in the % of CH_4 conversion over the period of study (10h), but after 4 h of reaction, the % of

CO_2 conversion started to decline and concurrently syngas ratio also decreased. The high initial conversion of CO_2 could be due to the RWGS reaction. It is known that RWGS reaction is favourable when carried out on La–Zr pyrochlore catalysts [28].

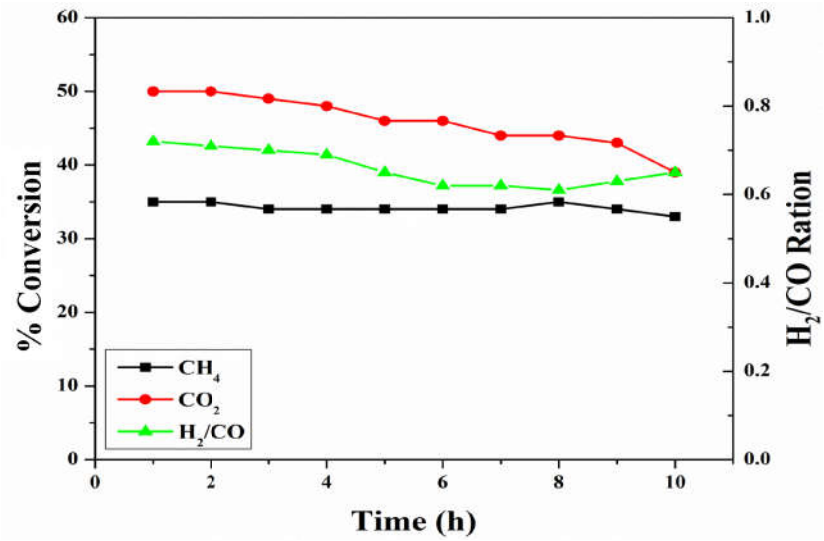

Figure 6.1.8: Time on stream study of $LaNi_{0.8}Zr_{0.2}O_3$ catalysts synthesized by sol-gel method during DRM reactionat 800°C.

6.1.4. Carbon analysis of the used $LaNi_xZr_{1-x}O_3$catalysts

Table 6.1.2: Carbon formation during the DRM reaction on $LaNi_xZr_{1-x}O_3$ catalysts synthesized by sol-gel method.

S. No.	Catalyst	Carbon (%)
1	$LaNi_{0.2}Zr_{0.8}O_3$	13.14
2	$LaNi_{0.3}Zr_{0.7}O_3$	7.89
3	$LaNi_{0.4}Zr_{0.6}O_3$	5.93
4	$LaNi_{0.6}Zr_{0.4}O_3$	3.56
5	$LaNi_{0.8}Zr_{0.2}O_3$	3.51

The amount of carbon formed on $LaNi_xZr_{1-x}O_3$ catalysts is estimated after the DRM reaction and the data obtained are reported in Table 6.1.2. The catalysts with low Ni loading showed high amount of carbon formation. Catalysts with high Ni content ≥ 0.6, originally existing in $LaNiO_3$ perovskite phase tend to produce highly dispersed Ni on La_2O_3–ZrO_2 during the reduction and enhance the coke resistance.

6.1.5. Conclusions

The results presented in this section deal with characterization and activity studies on $LaNi_xZr_{1-x}O_3$ catalysts synthesized by sol-gel method. The effect of Ni content on the performance of $LaNi_xZr_{1-x}O_3$ oxide catalysts ($0< x <1$) is studied for the dry reforming of methane reaction. At x=0.2, the formation of $La_2Zr_2O_7$ pyrochlore phase was observed. With the increase in Ni content, the pyrochlore phase disappeared at x=0.8 and the $LaNiO_3$perovskite oxide phase is formed. The catalyst with high x value (x=0.8) produced well dispersed Ni metal species supported on La_2O_3 upon reduction. Among the series of $LaNi_xZr_{1-x}O_3$ catalysts studied, the catalyst with x=0.8 showed highest efficiency in terms of CH_4 and CO_2 conversions. It is observed that the formation of perovskite phase plays a key role in the stability of catalyst by controlling coke formation during the DRM reaction.

Section 6.2: Zrmodified $LaNiO_3$catalystssynthesized by hydrothermal method.

6.2.1. Introduction

A series of $LaNi_xZr_{1-x}O_3$ catalysts were synthesized by the hydrothermal method. The details of the method of synthesis are explained in Chapter 3 Section 3.1.2b. The following paragraphs comprise the results and discussion on the characterization and evaluation of the synthesized $LaNi_xZr_{1-x}O_3$ catalysts for DRM reaction.

6.2.2. Results and Discussion

6.2.2a. Specific surface area measurements

Table 6.2.1 shows specific surface areas of $LaNi_xZr_{1-x}O_3$ perovskite oxides synthesized by hydrothermal method. As explained in the previous chapters,the high temperature calcination may lead to the low surface areas. The surface areas of these catalysts decreased till x=0.4 and then small increase is observed in the case of x=0.6 and 0.8. The Ni deposition on $La_2Zr_2O_7$ pyrochlore might have lead to the loss of surface area as described by the Bussi et al. [23].

Table 6.2.1: Specific surface areas of the $LaNi_xZr_{1-x}O_3$ catalysts synthesized by hydrothermal method.

S.No.	Catalysts	Specific Surface area (m^2/gm)
1	$LaNi_{0.2}Zr_{0.8}O_3$	13.7
2	$LaNi_{0.3}Zr_{0.7}O_3$	7.1
3	$LaNi_{0.4}Zr_{0.6}O_3$	6.56
4	$LaNi_{0.6}Zr_{0.4}O_3$	7.93
5	$LaNi_{0.8}Zr_{0.2}O_3$	7.65

6.2.2b. X–ray diffraction studies

Figure 6.2.1 shows XRD patterns of $LaNi_xZr_{1-x}O_3$catalysts synthesized by hydrothermal method and calcined at 800 °C. High intense peaks appeared at 2θ = 29, 33, 48, and 57° correspond to the well known cubic structure of pyrochlore compound with

formula of $La_2Zr_2O_7$. The pyrochlore peaks dominated the patterns in low Ni containing samples. Low intense diffraction peaks corresponding to $LaNiO_3$ perovskite phase (JCPDS 34–1181) were also observed. These catalysts exhibited another individual typical oxide phase with a peak at $2\theta = 43°$ related to NiO. Increase of Ni loading in $LaNi_xZr_{1-x}O_3$ catalysts showed deviations in all the peaks indicating differences in the extent of interaction of Ni with the pyrochlore support. On the other hand, the catalyst with high active metal (Ni) loading showed the dominance of bi–metallic rhombohedral perovskite phase of $LaNiO_3$ (JCPDS 34–1181), as observed in the previous section.

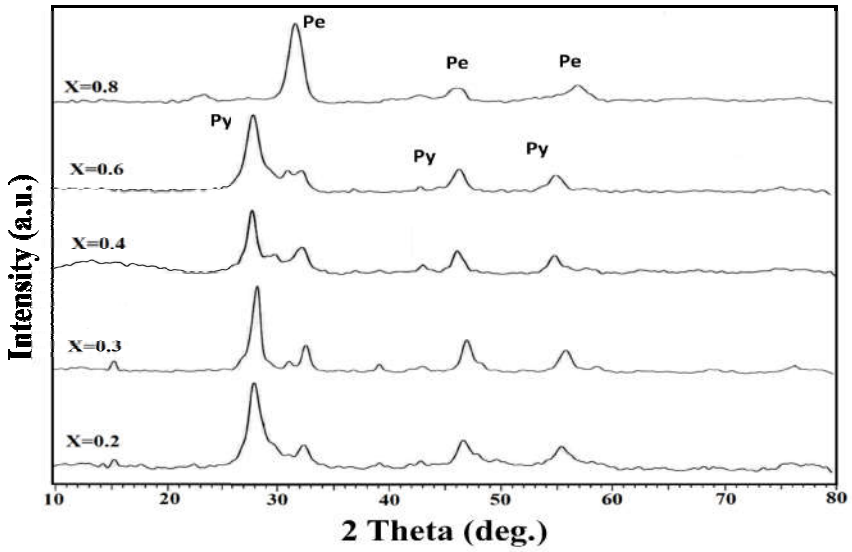

Figure 6.2.1: XRD patterns of $LaNi_xZr_{1-x}O_3$ catalysts synthesized by hydrothermal method. Pe = Perovskite phase and Py = Pyrochlore phase.

The X–ray diffraction data are in good agreement with the earlier literature reports [17,18]. The difference in phase transformation with the change in metal loading may be due to the difference in the extent of interaction of Ni and Zr with La. At high loading, Ni interacts with La to form the $LaNiO_3$ perovskite phase, whereas at lower Ni loading Zr interacts strongly with La to form the $La_2Zr_2O_7$ pyrochlore support, on which NiO agglomeration takes place.

6.2.2c. Fourier transform infrared spectroscopy studies

FT–IR spectra of $LaNi_xZr_{1-x}O_3$ catalysts synthesized by hydrothermal method are depicted in Figure 6.2.2. These spectra are similar to that of catalysts synthesized by sol-gel method (section 6.1).However, in the catalysts synthesized by hydrothermal process, the high wavelength–O–H stretching band appeared with low intensity indicating the difficulty in the formation of physisorbed inner layer water species.

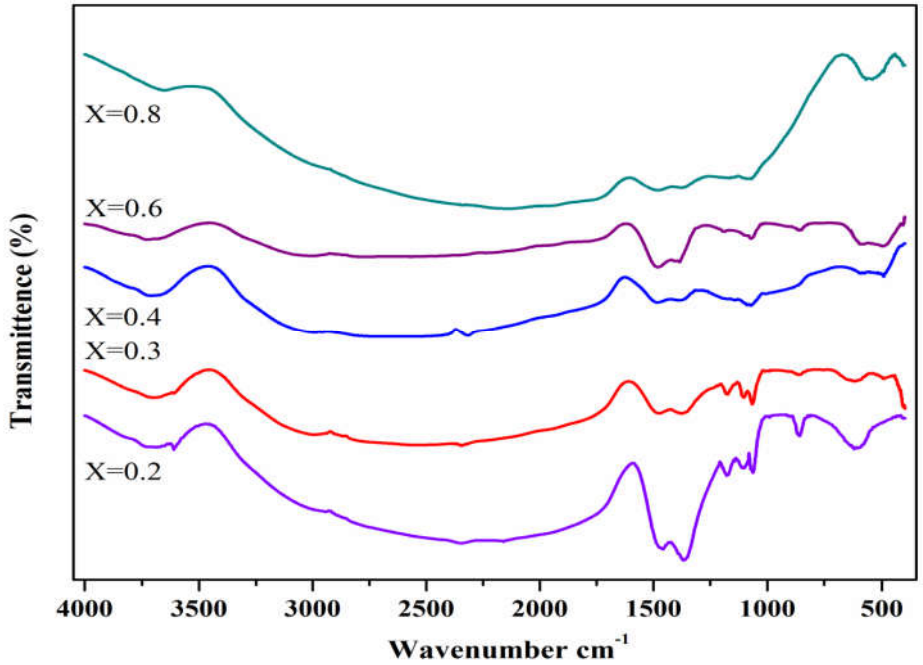

Figure 6.2.2: FT–IR patterns of $LaNi_xZr_{1-x}O_3$ catalysts synthesized by hydrothermal method.

The bands due to Zr–O (1072–1280 cm^{-1}) clearly appeared till x=0.4 and further increase in x made these peaks disappear. Bands due to O–C=O of the carboxylate spices of mono and bi–dentate ligandswere visible at 1472–1424 cm^{-1}, in all the catalysts except in the catalyst with x=0.8. Absorption bands in the region 546–489 cm^{-1}can be attributed to the nickel oxygen bonding [29]. The absence of bandsat 1072–1280 cm^{-1} corresponding to Zr–O indicate less probable formation of pyrochlore in catalyst with x=0.8. The formation of perovskite phase starts with catalysts having x=0.4 onwards. In the catalysts with x=0.8, all the other bands are minimized and the only peaks noticed are due to the nickel oxygen vibrational frequencies [20-22].

6.2.2d. Temperature programmed reduction studies

Temperature programmed reduction profiles of $LaNi_xZr_{1-x}O_3$catalysts synthesized by hydrothermal method are shown in Figure 6.2.3. Literature reveals that the La–Zr pyrochlore is not easily reducible. So, the reduction peaks that appeared in this study are ascribed to the reduction of NiO. As mentioned in the previous section, the peaks between 400 and 600 °C are due to the free NiO dispersed on La–Zr pyrochlore support. The high temperature peaks above 600 °C are due to the highly interacted Ni with La–Zr pyrochlore and/or $LaNiO_3$perovskite phase [23].

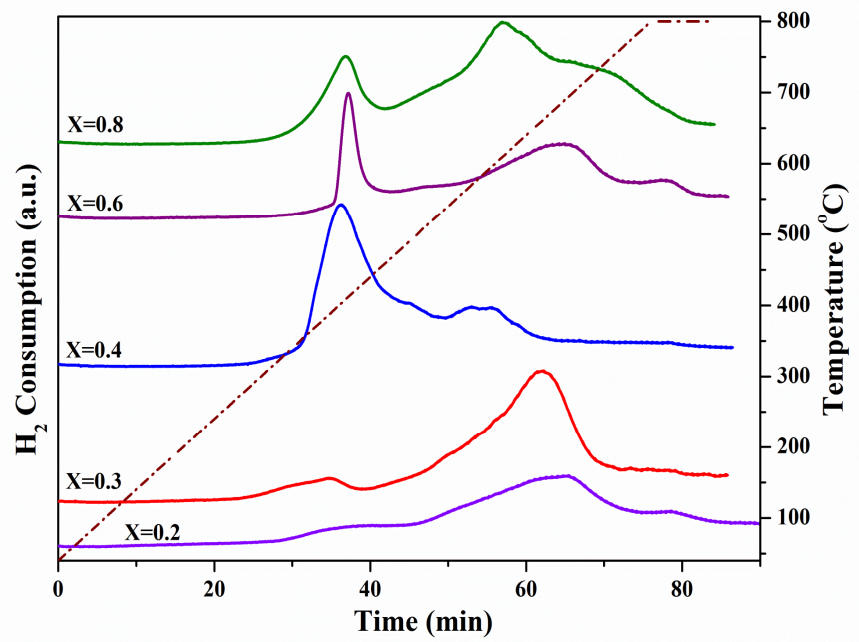

Figure 6.2.3: TPR patterns of $LaNi_xZr_{1-x}O_3$ catalysts synthesized by hydrothermal method.

The reduction profiles of low Ni containing catalysts showed peaks at high temperature due to strong interaction of Ni with support, $La_2Zr_2O_7$ pyrochlore. As the Ni content increased, the availability of dispersed NiO on $La_2Zr_2O_7$ pyrochlore is slowly increased. The formation of two different Ni species could be envisaged in the present study. The high temperature reduction band in the case of x=0.8 catalyst was broad. However, an important observation is that the ratio of area of the second peak to the first

peak is approximately 2, confirming the formation of $LaNiO_3$ perovskite as also evidenced in XRD.

6.2.2e. X–ray photoelectron spectroscopy studies

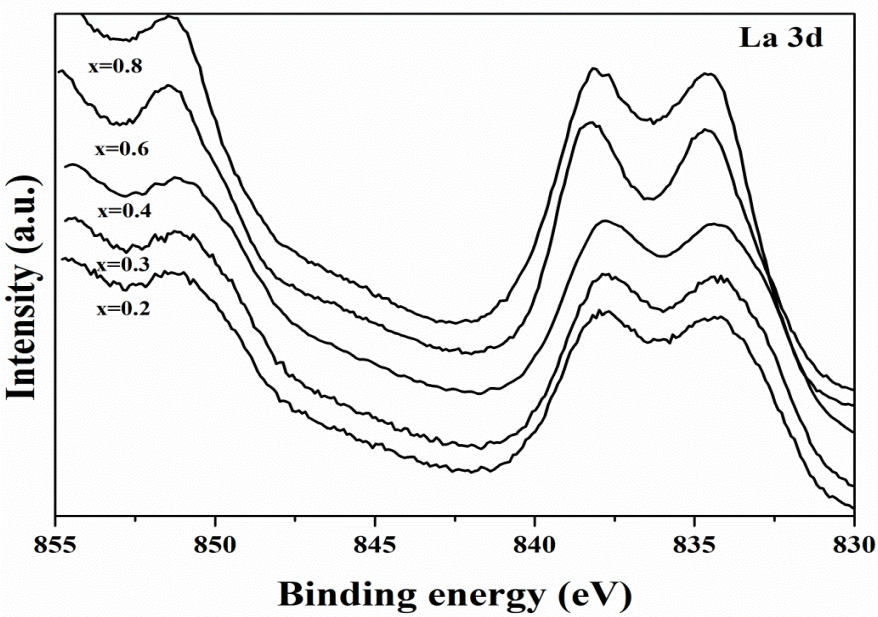

Figure 6.2.4: La 3d XP spectra of $LaNi_xZr_{1-x}O_3$ catalysts synthesized by hydrothermal method.

Figure 6.2.4 shows the La 3d core level XP spectra of $LaNi_xZr_{1-x}O_3$ catalysts. The bands with bonding energies at 834.4 and 839.1 eV correlates with La $3d_{5/2}$. These peaks confirmed the presence of Lain its3+ oxidation state on the surface of the catalysts. These bands showed higher values than in the case of catalysts synthesized by sol-gel method. Lima et al. [24], ascribed this phenomenon to the modification of La^{3+} ion with Ce^{4+} ions, in their case. The same phenomenon is also observed in the case of $LaNi_xZr_{1-x}O_3$ catalysts, where exchange of La^{3+} takes place with Zr^{4+} ions. The doublet bands are shifted continuously towards higher energy with increase of Ni content. The other band appearing at binding energy 852 eV is due to La $3d_{3/2}$. This peak overlaps with the binding energy peak of Ni $2p_{3/2,}$ thereby making their distinction difficult.

XP spectra of Ni 2p of $LaNi_xZr_{1-x}O_3$ catalysts are provided in Figure 6.2.5. The peaks with binding energies at 852 and 854–855 eV correspond to Ni $2p_{3/2}$. As observed

in the previous chapter, these bands of Ni 2p showed higher binding energy values than those reportedin the literature [19]. This signifies that Ni is stabilized in higher oxidation state, confirming the possible formation of perovskite. There is a coherent peak shift towards higher value, i.e, increasing binding energy with the increase in amount of Ni content. XP spectra are in good corroboration with the XRD study that the formation of perovskite phase dominated in high Ni containing samples.

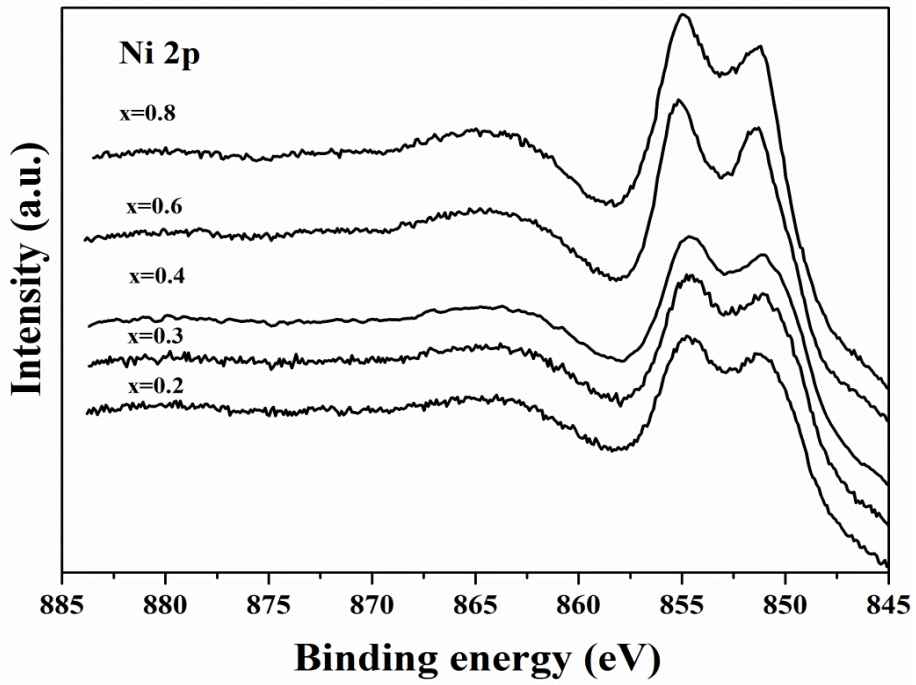

Figure 6.2.5: Ni 2p XP spectra of $LaNi_xZr_{1-x}O_3$ catalysts synthesized by hydrothermal method.

XP spectra of Zr 3d of $LaNi_xZr_{1-x}O_3$ catalysts are depicted in Figure 6.2.6. Binding energies at 181 and 183.5 eV are related to Zr $3d_{5/2}$ and Zr $3d_{3/2}$, respectively [27]. The bands signify the presence of Zr^{4+} ion on the catalyst surface as ZrO_2. These binding energy values are a little lower than reported in the literature indicating the existence of interactions with other metals. As explained in the La 3d spectra, the modification of La^{3+} with Zr^{4+} may result in change in binding energy. In catalysts with low Zr content, it is clearly observed that the binding energy bands are shifted to a higher

value. This shift to higher binding energy is in good agreement with that observed by Xu et al.[25]. In their results, they stated that this shift towards higherbinding energy is due to the dissolution of ZrO_2 ions into La_2O_3 lattices. The dissolution of ZrO_2 into La_2O_3 resulted in a pyrochlore phase. This phase is clearly observed in the lower Ni containing catalysts in XRD. These results are in good agreement with XRD data.

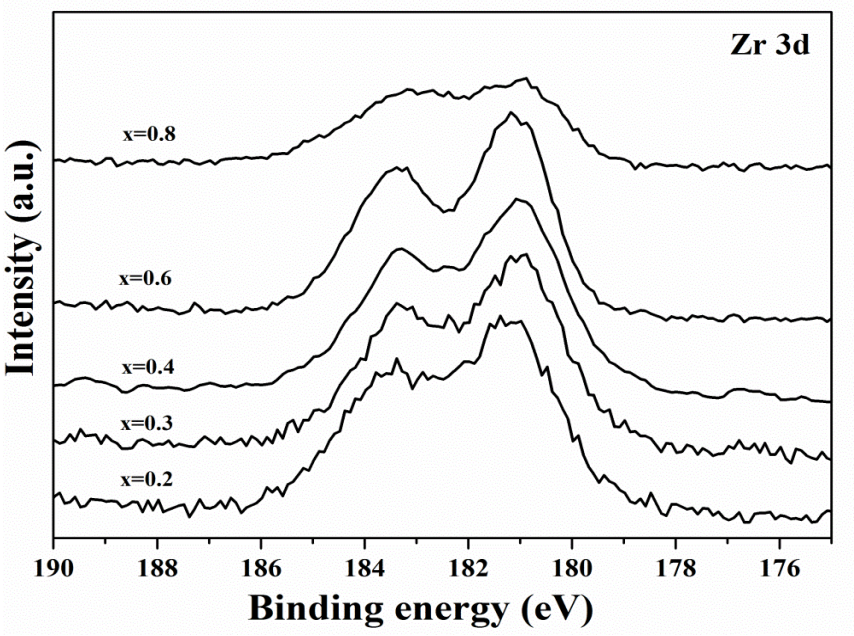

Figure 6.2.6: Zr 3d XP spectra of $LaNi_xZr_{1-x}O_3$ catalysts synthesized by hydrothermal method.

6.2.3. Catalytic activity tests

Figure 6.2.7 shows the activity profiles of DRM reaction over $LaNi_xZr_{1-x}O_3$ catalysts at 800 °C and atmosphere pressure. The conversionof CO_2 and CH_4as well as syngas ratio haveincreased with increase in Ni ratio and reached their maximum values at higher Ni loading. Methane conversion has risen from 15 to 61% with the increase in Ni content from x=0.2 to 0.8, the same trendwas observed in the case of CO_2 conversion, which increased from 22 to 65%. The syngas ratio also increased from 0.21 to 0.82 with the increase in Ni content. This higher CO_2 conversion was clearly observed in the case of catalysts with low Ni ratio (Zr rich) possibly due to RWGS reaction which is favoured

on Zirconium rich catalysts. The same observation was made by the Bachiller-Baeza et al. [28]. They stated that the non–promoted catalysts show high CO_2 conversion leading to increased formation of CO.

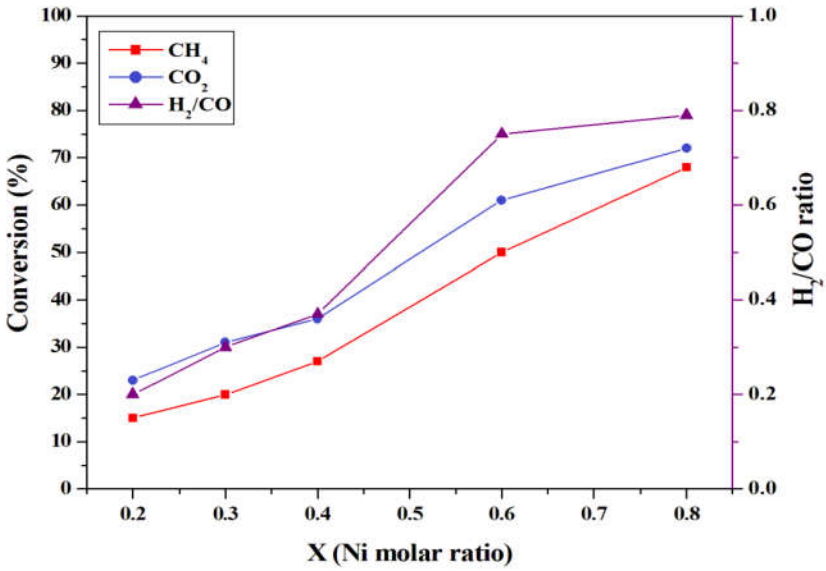

Figure 6.2.7: Catalytic activity study on DRM reaction over $LaNi_xZr_{1-x}O_3$ catalysts synthesized by hydrothermal method (Temperature = 800 °C).

X–ray studies revealed that the free NiO species is available in all the catalysts. However, its intensity is found to be small in low Ni containing catalysts. With the increase in Ni loading, phase transfer takes place from La–Zr pyrochlore to La–Ni perovskite. The presence of free NiO is also noticed. This phase transformation is also confirmed by the XPS studies. The incorporation of Zr^{4+} ions into La^{3+} might have led to the structural defects in catalysts with low x values. TPR studies on these samples, indirectly evidenced the formation of highly dispersed Ni on the La–Zr support. The available free NiO species enhanced the reducibility. On the other hand, catalysts with low Ni content (x=0.2 and 0.3) showed greater interaction with the support resulting in poor reducibility.

Figure 6.2.8 shows the results of the time on stream studies on DRM reaction over $LaNi_{0.8}Zr_{0.2}O_3$ (GC chromatograph has been given in Appendix section Figure 7) catalyst.

This catalyst showed stable activity till 9h of the reaction without any significant loss in the catalytic activity.

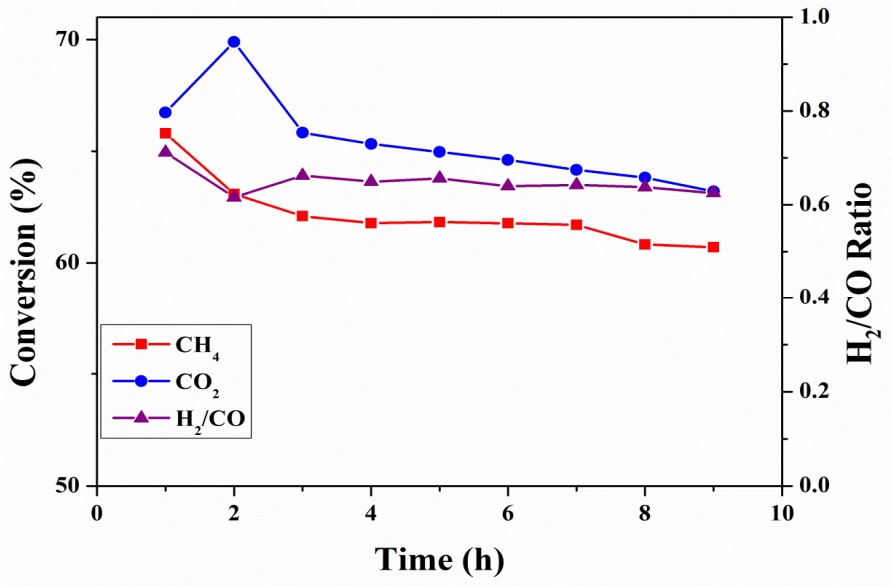

Figure 6.2.8: Time on stream study for DRM reaction over $LaNi_{0.8}Zr_{0.2}O_3$ catalyst synthesized by hydrothermal method (Temperature = 800 °C).

6.2.4. Carbon analysis of the used catalysts

Table 6.2.2 represents the carbon formed on the catalyst after 9 h of DRM reaction. The catalysts with low Ni content showed high amount of carbon formation. Whereas,high Ni ratio catalysts confirmed the formation of perovskite phase which tends to produce high dispersed Ni. This leads to increase in the carbon resistance.

Table 6.2.2: Analysis of carbon formation during the DRM reaction over $LaNi_xZr_{1-x}O_3$ catalysts synthesized by hydrothermal method.

S. No.	Catalyst	Carbon (%)
1	$LaNi_{0.2}Zr_{0.8}O_3$	11.12
2	$LaNi_{0.3}Zr_{0.7}O_3$	9.52
3	$LaNi_{0.4}Zr_{0.6}O_3$	7.81
4	$LaNi_{0.6}Zr_{0.4}O_3$	4.70
5	$LaNi_{0.8}Zr_{0.2}O_3$	4.49

6.2.5. Conclusions

A series of $LaNi_xZr_{1-x}O_3$catalysts with x values varying in the range of 0.2 to 0.8

were synthesized by the hydrothermal method. The characterization studies by XRD, FT–IR and XPS confirmed the formation of La–Zr pyrochlore phase predominantly in low Ni content samples. Whereas, withincrease in Ni content, the phase transformation from the pyrochlore phase to the $LaNiO_3$perovskite phase is clearly observed in XRD studies. Formation of perovskite phase results in producing highly dispersed active metal (Ni) species during reduction. Catalytic activity studies on all the synthesized catalysts revealed that $LaNi_{0.8}Zr_{0.2}O_3$ catalystis most efficient with 61% and 65% of CH_4 and CO_2 conversion, respectively and with a syngas ratio of 0.8. The formation of perovskite phase plays a key role in catalyst stability by restricting the coke formation.

6.2.6. References

1. Pakhare, D., & Spivey, J. (2014). *Chemical Society Reviews*, *43*, 7813-7837.
2. Yan, Z., Wang, Z., Bukur, D. B., & Goodman, D. W. (2009). *Journal of Catalysis*, *268*, 196-200.
3. Fidalgo. B.,& Menéndez. J. A., (2013). *Syngas production by CO_2 reforming of CH_4 under microwave heating - Challenges and opportunity under Syngas: Production, Applications and Environmental Impact*. ISBN: 978-1-62100-870-5, Eds: Indarto. A., Palguandi. J. Nova Science Publishers, Inc. pp: 121-149.
4. Pakhare, D., Haynes, D., Shekhawat, D., & Spivey, J. (2012). *Applied Petrochemical Research*, *2*, 27-35.
5. Gardner, T. H., Spivey, J. J., Campos, A., Hissam, J. C., Kugler, E. L., &Roy, A. D. (2010). *Catalysis Today*, *157*, 166-169.
6. Gardner, T. H., Spivey, J. J., Kugler, E. L., Campos, A., Hissam, J. C., &Roy, A. D. (2010). *The Journal of Physical Chemistry C*, *114*, 7888-7894.
7. Gardner, T. H., Spivey, J. J., Kugler, E. L., &Pakhare, D. (2013). *Applied Catalysis A: General*, *455*, 129-136.
8. Gurav, H. R., Bobade, R., Das, V. L., &Chilukuri, S. (2012). *Indian Journal of Chemistry -Section A,* 51A, 1339–1347.
9. Haynes, D. J., Berry, D. A., Shekhawat, D., & Spivey, J. J. (2008). *Catalysis Today*, *136*, 206-213.
10. Haynes, D. J., Berry, D. A., Shekhawat, D., & Spivey, J. J. (2009). *Catalysis Today*, *145*, 121-126.
11. Haynes, D. J., Campos, A., Berry, D. A., Shekhawat, D., Roy, A., & Spivey, J. J. (2010). *Catalysis Today*, *155*, 84-91.

12. Ashcroft, A. T., Cheetham, A. K., Foord, J. A., Green, M. L. H., & Grey, C. P. (1990). *Nature*, *344*, 319–321.
13. Ashcroft, A. T., Cheetham, A. K., & Green, M. (1991). *Nature*, *352*, 225-226.
14. Ashcroft, A. T., Cheetham, A. K., Jones, R. H., Natarajan, S., Thomas, J. M., Waller, D., & Clark, S. M. (1993). *Journal of Physical Chemistry, 97*, 3355–3358.
15. Valderrama, G., Goldwasser, M. R., de Navarro, C. U., Tatibouët, J. M., Barrault, J., Batiot-Dupeyrat, C., &Martínez, F. (2005). *Catalysis Today*, *107-108*, 785-791.
16. Valderrama, G., A. Kiennemann and M. R. Goldwasser. (2008).*Catalysis Today*, *133-135*, 142-148.
17. Bespalko, N., Roger, A. C., &Bussi, J. (2011). *Applied Catalysis A: General*, *407*, 204-210.
18. Bussi, J., Musso, M., Veiga, S., Bespalko, N., Faccio, R., & Roger, A. C. (2013). *Catalysis today*, *213*, 42-49.
19. Gaur, S., Haynes, D. J., & Spivey, J. J. (2011). *Applied Catalysis A: General*, *403*, 142-151.
20. Chen, H. S., Kumar, R. V., &Glowacki, B. A. (2010). *Materials Chemistry and Physics*, *122*, 305-310.
21. KoteswaraRao, K., Banu, T., Vithal, M., Swamy, G. Y. S. K., & Kumar, K. R. (2002). *Materials Letters*, *54*, 205-210.
22. Tong, Y., Zhu, J., Lu, L., Wang, X., & Yang, X. (2008). *Journal of Alloys and Compounds*, *465*, 280-284.
23. Bussi, J., Bespalko, N., Veiga, S., Amaya, A., Faccio, R., &Abello, M. C. (2008). *Catalysis Communications*, *10*, 33-38.

24. Lima, S. M., Assaf, J. M., Pena, M. A., &Fierro, J. L. G. (2006). *Applied Catalysis A: General*, *311*, 94-104.

25. Xu, Z., He, L., Zhao, Y., Mu, R., He, S., & Cao, X. (2010). *Journal of Alloys and Compounds*, *491*, 729-736.

26. Khalesi, A., Arandiyan, H. R., &Parvari, M. (2008). *Chinese Journal of Catalysis*, *29*, 960-968.

27. Duan, Y., Sun, F., Yang, Y., Chen, P., Yang, D., Duan, Y., & Wang, X. (2014). *ACS Applied Materials & Interfaces*, *6*, 3799-3804.

28. Bachiller-Baeza, B., Mateos-Pedrero, C., Soria, M. A., Guerrero-Ruiz, A., Rodemerck, U., & Rodríguez-Ramos, I. (2013). *Applied Catalysis B: Environmental*, *129*, 450-459.

29. Rahdar, A., Aliahmad, M., &Azizi, Y. (2015). *Journal of Nanostructures*, *5*, 145-151.

Chapter 7

Summary and Conclusions

7.1. Summary of the thesis

This thesis deals with the development of new, active and stable catalysts for the dry reforming of methane (DRM). The carbon dioxide reforming of methane to produce synthesis gas (H_2+CO) is not only an attractive route to produce value added chemicals and energy but also due to its importance in converting two major greenhouse gases.

Although, noble metal catalysts were extensively studied and showed good results for the DRM reaction, due to their low availability and high cost, their use in industry has not become practical. The alternative metal that holds promise is Ni. Previous studies on Ni supported catalysts revealed that the carbon deposition and metal sintering is high during the DRM reaction. In order to overcome these problems, researchers are working on structured oxides such as perovskites, pyrochlores and solid-solution type catalysts in place of supported Ni systems. The present work is undertaken to find suitable and efficient trimetallic catalysts for the DRM reaction.

In this study, $LaNi_xM_{1-x}O_3$ (M= Ce, Al and Zr) catalysts of varying composition are synthesized and investigated for the DRM reaction. The structure, reduction and dispersion of Ni in these catalysts are strongly influenced by the addition of a third metal.

The trimetallic perovskite phase is achieved by Al modified $LaNiO_3$. Optimization studies on $LaNi_xAl_{1-x}O_3$ catalysts revealed that, the best catalyst among those synthesized by sol-gel method is $LaNi_{0.3}Al_{0.7}O_3$ with 93% conversion of CH_4, 96% conversion of CO_2 and syngas ratio equal to 0.97. Among the catalysts synthesized by hydrothermal method, the most efficient one is found to be $LaNi_{0.6}Al_{0.4}O_3$ with 94% conversion of CH_4, 97% conversion of CO_2 and syngas ratio equal to 0.98.

The solid-solution along with the perovskite phase is achieved in Ce modified $LaNiO_3$ catalysts. The catalyst synthesized by sol-gel method having a composition of $LaNi_{0.4}Ce_{0.6}O_3$, with 92% of CH_4, 94% of CO_2 conversion and syngas ratio equal to 0.87

is observed to be the best in the series. Whereas, in the case of catalysts synthesized by hydrothermal method, the catalyst with the composition of $LaNi_{0.6}Ce_{0.4}O_3$ is found to be the best with 94% conversion of CH_4, 96% conversion of CO_2 and syngas ratio of 0.94.

Both pyrochlore and perovskite phases are achieved in the Zr modified catalysts. Among the catalysts investigated, samples with higher Ni content showed better results. The catalysts with a composition of $LaNi_{0.8}Zr_{0.2}O_3$ gave 37% of CH_4, 50% of CO_2 conversion and syngas ratio of 0.71 when catalysts are synthesized by sol-gel method. Whereas, the catalyst with composition $LaNi_{0.8}Zr_{0.2}O_3$ synthesized by hydrothermal method gave 61% conversion of CH_4, 65% conversion of CO_2 and syngas ratio of 0.81.

7.2. Conclusions

Conclusions drawn from the present thesis work are presented chapter-wise below.

7.2a. Studies on Al modified $LaNiO_3$ catalysts with general formula $LaNi_xAl_{1-x}O_3$

- The formation of trimetallic perovskite oxide phase was achieved in $LaNi_xAl_{1-x}O_3$ samples with $0.2 < x < 0.8$. This is indicated by shift in the high intense peak in XRD patterns.
- Trimetallic perovskite type oxide form in Al modified $LaNiO_3$ ($LaNi_xAl_{1-x}O_3$) catalysts produced well dispersed metal oxide species and fine Ni metal particles upon reduction. These small sized Ni^0 particles enhanced the catalytic activity.
- The trimetallic perovskite phase in $LaNi_xAl_{1-x}O_3$ catalyst played a key role in the stability of catalyst by offering high dispersion of Ni.
- High dispersion of Ni favored not only high conversions of CH_4 and CO_2 during the DRM reaction but also controlled the coke formation.

- Highly crystalline perovskite phase was observed in the $LaNi_xAl_{1-x}O_3$ catalysts synthesized by hydrothermal method as compared to the catalysts synthesized by sol-gel method.
- Ni^{3+}/Ni^{2+} cation pair surface environment was observed in $LaNi_xAl_{1-x}O_3$ catalysts synthesized by hydrothermal method.
- The surface species formed during Al modified $LaNiO_3$ ($LaNi_xAl_{1-x}O_3$) catalysts enhanced the reducibility of Ni.

7.2b. Studies on Ce modified $LaNiO_3$ catalysts with general formula $LaNi_xCe_{1-x}O_3$

- Variation of Ni/Ce ratio in $LaNi_xCe_{1-x}O_3$ catalysts yielded two types of active metal phases: 1) perovskite phase with bimetallic structural oxide $LaNiO_3$ and 2) Ni–Ce solid solution.
- In $LaNi_xCe_{1-x}O_3$ catalysts synthesized by hydrothermal method, existence of $LaNiO_3$ is noticed at low Ni composition (x=0.2 and 0.3). Whereas such species were clearly observed only at higher compositions in the catalysts synthesized by sol-gel method.
- Ce Modification of $LaNiO_3$ showed enhanced reducibility of catalysts.
- Highly dispersed Ni delivered from $LaNi_xCe_{1-x}O_3$ catalysts during *in situ* reduction increased the catalytic activity.
- Catalysts synthesized by sol-gel method showed relatively higher specific surface area than the catalysts synthesized by hydrothermal method.
- Ni exists in its 3+ state in the catalysts synthesized by hydrothermal method, whereas in the catalysts synthesized by sol-gel method, Ni^{3+}/Ni^{2+} cation surface environment is observed.
- Curves depicting variation of dispersion of Ni and catalytic activity with Ni mole ratio are found to be similar, implying that activity is proportional to dispersion.

7.2c. Studies on Zr modified $LaNiO_3$ catalysts with general formula $LaNi_xZr_{1-x}O_3$

- Studies on the effect of Ni content on the performance of $LaNi_xZr_{1-x}O_3$ catalysts prepared by both sol-gel method and hydrothermal method revealed that, at low Ni content the La–Zr pyrochlore phase ($La_2Zr_2O_7$) is formed.
- With increase in Ni content, the ratio of pyrochlore phase (La–Zr) in the $LaNi_xZr_{1-x}O_3$ catalysts decreased and that of perovskite phase ($LaNiO_3$) increased.
- Upon reduction, the catalysts with high x values produced well dispersed Ni^0 species supported on La_2O_3–ZrO_2.
- The $LaNi_xZr_{1-x}O_3$ catalysts synthesized by hydrothermal method showed perovskite type reduction behaviour, whereas the catalysts synthesized by sol-gel method showed supported oxide type reduction behaviour.
- Among all the $LaNi_xZr_{1-x}O_3$ catalysts synthesized, samples with x=0.8 showed the higher efficiency in terms of CH_4 and CO_2 conversions, syngas ratio and stability during the DRM reaction.

7.3. Overall conclusions

- Characterization studies of $LaNi_xM_{1-x}O_3$ (M= Al, Ce and Zr) catalysts revealed that their structural and redox properties are highly dependent on Ni/M composition.
- The formation of trimetallic perovskite phase in Al–modified $LaNiO_3$ catalysts offered higher conversions of CH_4 and CO_2 than the pyrochlore and solid-solution containing catalysts for the DRM reaction.
- Al modified $LaNiO_3$ catalysts synthesized by both hydrothermal and sol-gel methods have shown higher activity than Ce and Zr modified $LaNiO_3$ catalysts for the DRM reaction.

- Catalysts synthesized by hydrothermal method required higher Ni content in $LaNi_xM_{1-x}O_3$ (M= Al, Ce and Zr) than catalysts synthesized by sol-gel method for achieving higher conversions of CH_4 and CO_2 as well as syngas production.
- $LaNi_xM_{1-x}O_3$ (M= Al, Ce and Zr) catalysts having the perovskite phase have been found to be more efficient than catalysts having the pyrochlore phase or solid solution phase.

Appendix

Appendix

Carbon Balance for Best catalysts of each series:

Catalysts	Moles				Conversion		H_2/CO	Carbon balance
	CH_4	CO_2	H_2	CO	CH_4	CO_2		
Chapter 4								
$LaNi_{0.3}Al_{0.7}O_3$ Sol-gel method	0.000249	0.000142	0.006405	0.006603	93	96	0.97	98
$LaNi_{0.6}Al_{0.4}O_3$ Hydrothermal method	0.000214	0.000107	0.006541	0.006674	94	97	0.98	97
Chapter 5								
$LaNi_{0.4}Ce_{0.6}O_3$ (Sol-gel method)	0.0002876	0.000214	0.005527	0.006353	92	94	0.87	95
$LaNi_{0.6}Ce_{0.4}O_3$ (Hydrothermal method)	0.000214	0.000142	0.006173	0.006567	94	96	0.94	97
$Ni_{0.4}Ce_{0.6}O_3$ (Sol-gel method)	0.001320	0.001106	0.003838	0.004569	63	69	0.84	98
Chapter 6								
$LaNi_{0.8}Zr_{0.2}O_3$ (Sol-gel method)	0.002248	0.001784	0.002154	0.003034	37	50	0.71	99
$LaNi_{0.8}Zr_{0.2}O_3$ (Hydrothermal method)	0.001391	0.001249	0.003238	0.003998	61	65	0.81	93

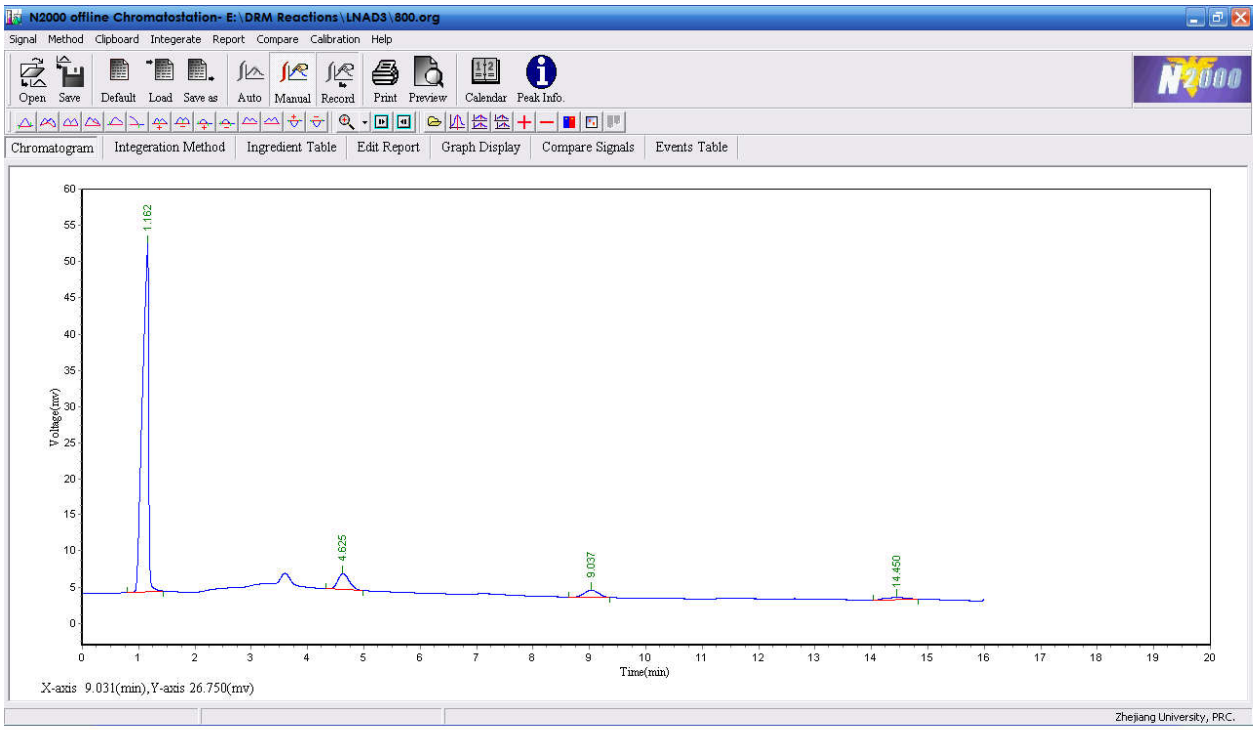

Results Data File - E:\DRM Reactions\LNAD3\800.org

Peak No.	Peak ID	Ret. Time	Peak Height	Peak Area	Peak Conc.
1	H_2	1.162	48154.098	3804058.101	86.8049
2	CO	4.652	2202.000	308509.893	7.3131
3	CH_4	9.037	998.780	93432.802	4.0504
4	CO_2	14.450	298.331	47334.225	1.8317
Total			51653.209	4253335.655	100.0000

Figure 1: Shows GC chromatographs of $LaNi_{0.3}Al_{0.7}O_3$ synthesized by sol-gel method.

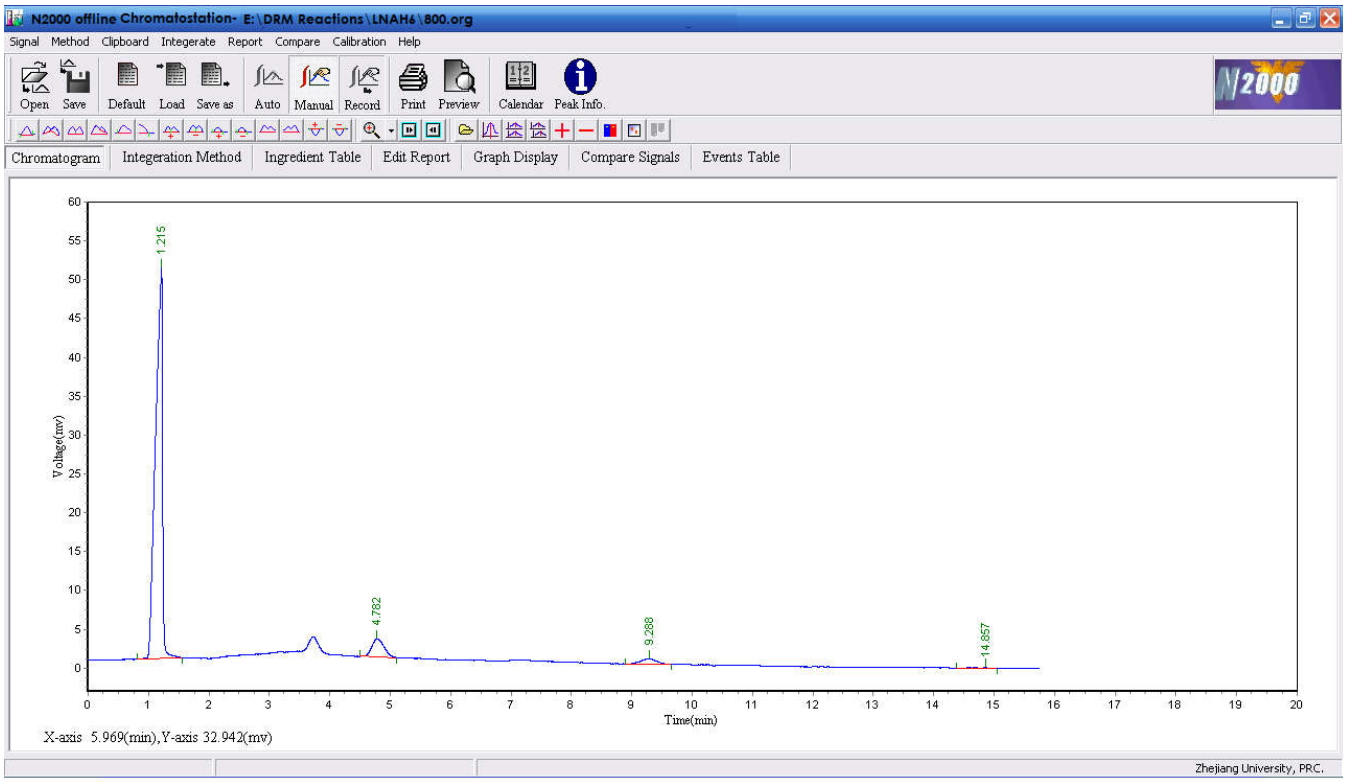

Results Data File - E:\DRM Reactions\LNAH6\800.org

Peak No.	Peak ID	Ret. Time	Peak Height	Peak Area	Peak Conc.
1	H_2	1.215	50212.867	4102678.237	89.7585
2	CO	4.782	2313.939	322211.378	7.4562
3	CH_4	9.288	673.672	46736.156	2.6016
4	CO_2	14.857	61.069	15878.095	0.1837
Total			53261.547	4487504.637	100.0000

Figure 2: Shows GC chromatographs of $LaNi_{0.6}Al_{0.4}O_3$ synthesized by hydrothermal method.

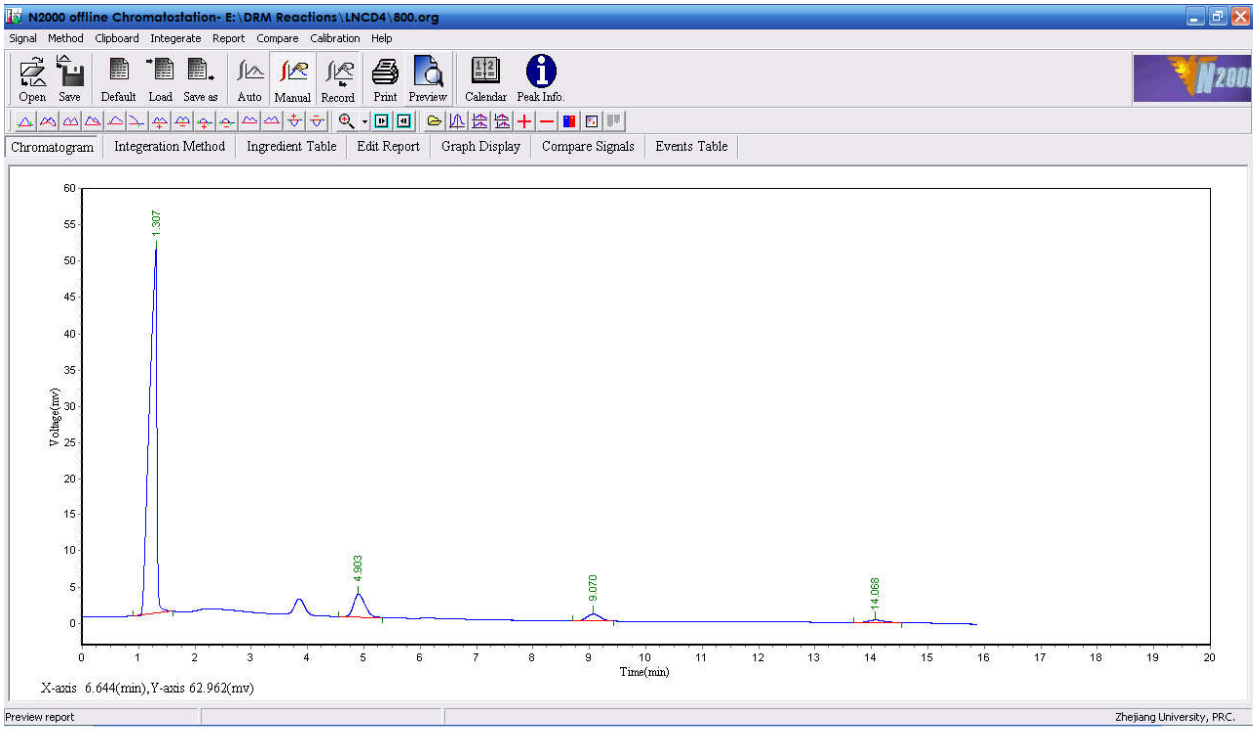

Results Data File - E:\DRM Reactions\LNCD4\800.org

Peak No.	Peak ID	Ret. Time	Peak Height	Peak Area	Peak Conc.
1	H_2	1.307	50234.391	3887652.842	89.6129
2	CO	4.903	3120.530	309289.936	7.1297
3	CH_4	9.070	952.114	93527.602	2.1562
4	CO_2	14.068	361.196	47609.275	1.0975
Total			54668.237	4338079.879	100.0000

Figure 3: Shows GC chromatographs of $LaNi_{0.4}Ce_{0.6}O_3$ synthesized by sol-gel method.

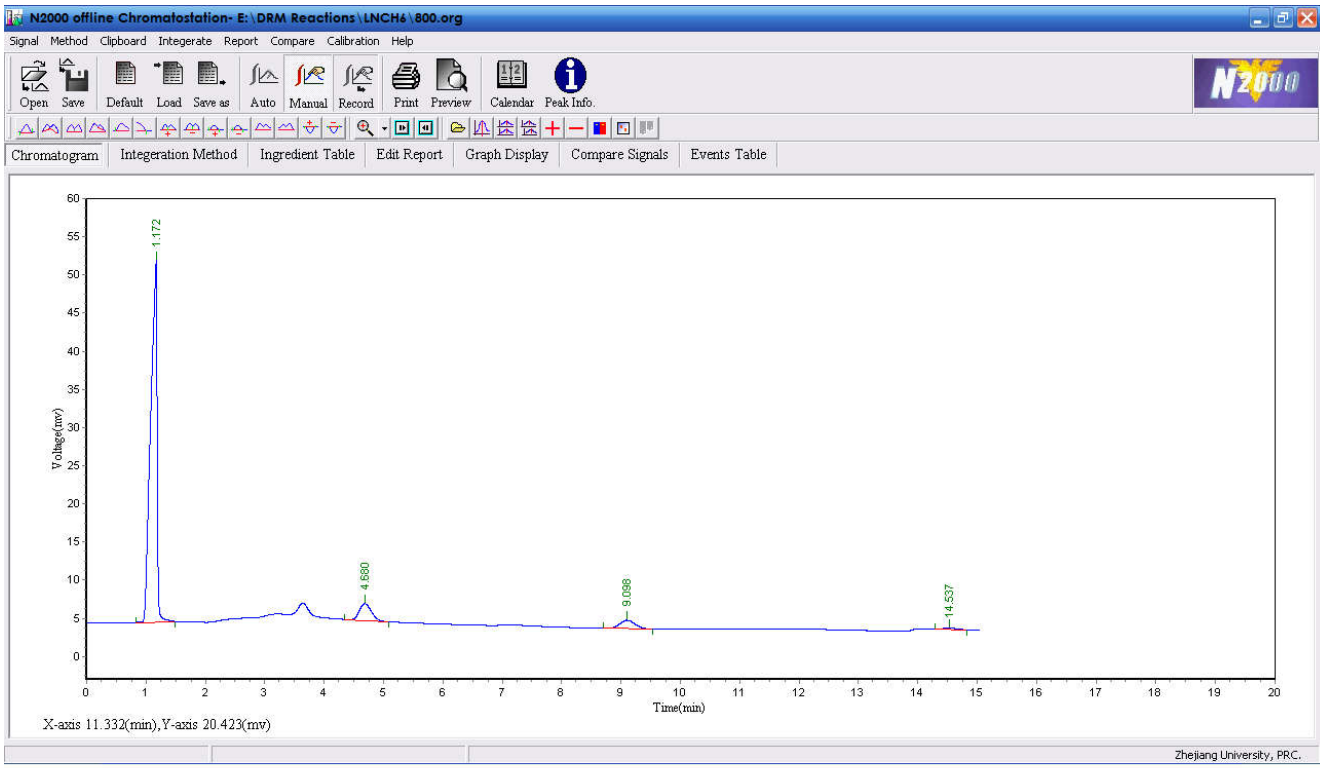

Results Data File - E:\DRM Reactions\LNCH6\800.org

Peak No.	Peak ID	Ret. Time	Peak Height	Peak Area	Peak Conc.
1	H_2	1.172	50374.844	3973022.905	90.5011
2	CO	4.680	3210.186	315355.446	7.1834
3	CH_4	9.098	1093.412	70075.327	1.5962
4	CO_2	14.537	161.904	31575.027	0.7192
Total			54840.346	4390029.611	100.000

Figure 4: Shows GC chromatographs of $LaNi_{0.6}Ce_{0.4}O_3$ synthesized by hydrothermal method.

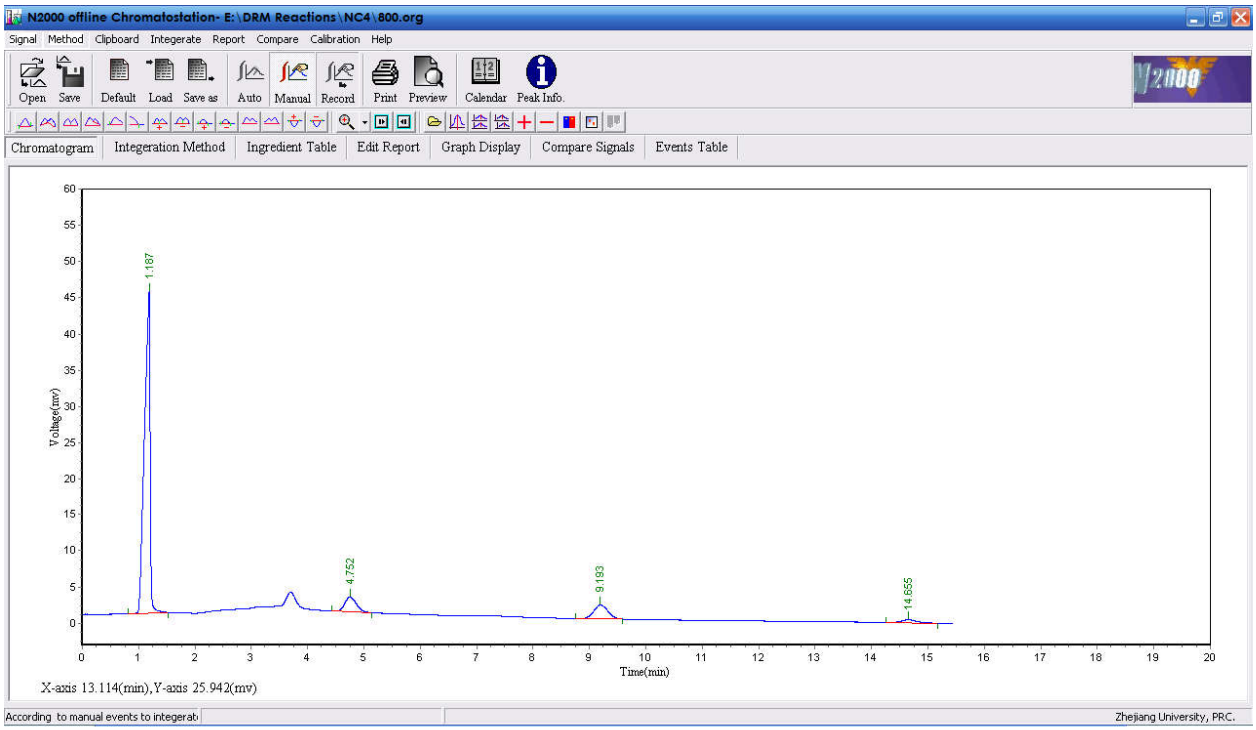

Results Data File - E:\DRM Reactions\NC4\800.org

Peak No.	Peak ID	Ret. Time	Peak Height	Peak Area	Peak Conc.
1	H_2	1.187	44408.828	2469816.27	73.3583
2	CO	4.752	2031.222	219377.702	6.5159
3	CH_4	9.193	2185.110	432132.95	12.8352
4	CO_2	14.655	1004.713	245459.297	7.2906
Total			49629.873	3366786.223	100.0000

Figure 5: Shows GC chromatographs of $Ni_{0.4}Ce_{0.6}O_2$ synthesized by sol-gel method.

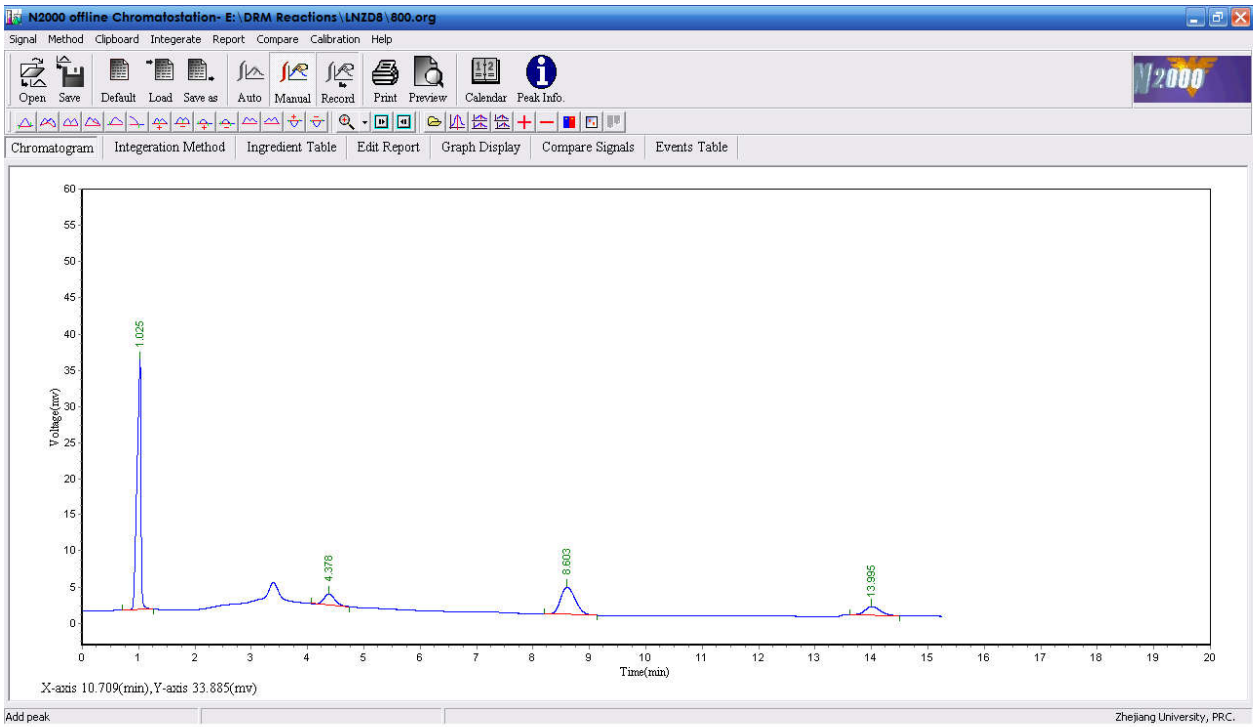

Results Data File - E:\DRM Reactions\LNZD8\800.org

Peak No.	Peak ID	Ret. Time	Peak Height	Peak Area	Peak Conc.
1	H_2	1.025	34566.891	1414080.077	52.7006
2	CO	4.378	1485.409	138824.952	5.1738
3	CH_4	8.603	3815.701	735777.296	27.4213
4	CO_2	13.995	1155.392	394550.173	14.7043
Total			41203.393	2683232.690	100.0000

Figure 6: Shows GC chromatographs of $LaNi_{0.8}Zr_{0.2}O_3$ synthesized by sol-gel method.

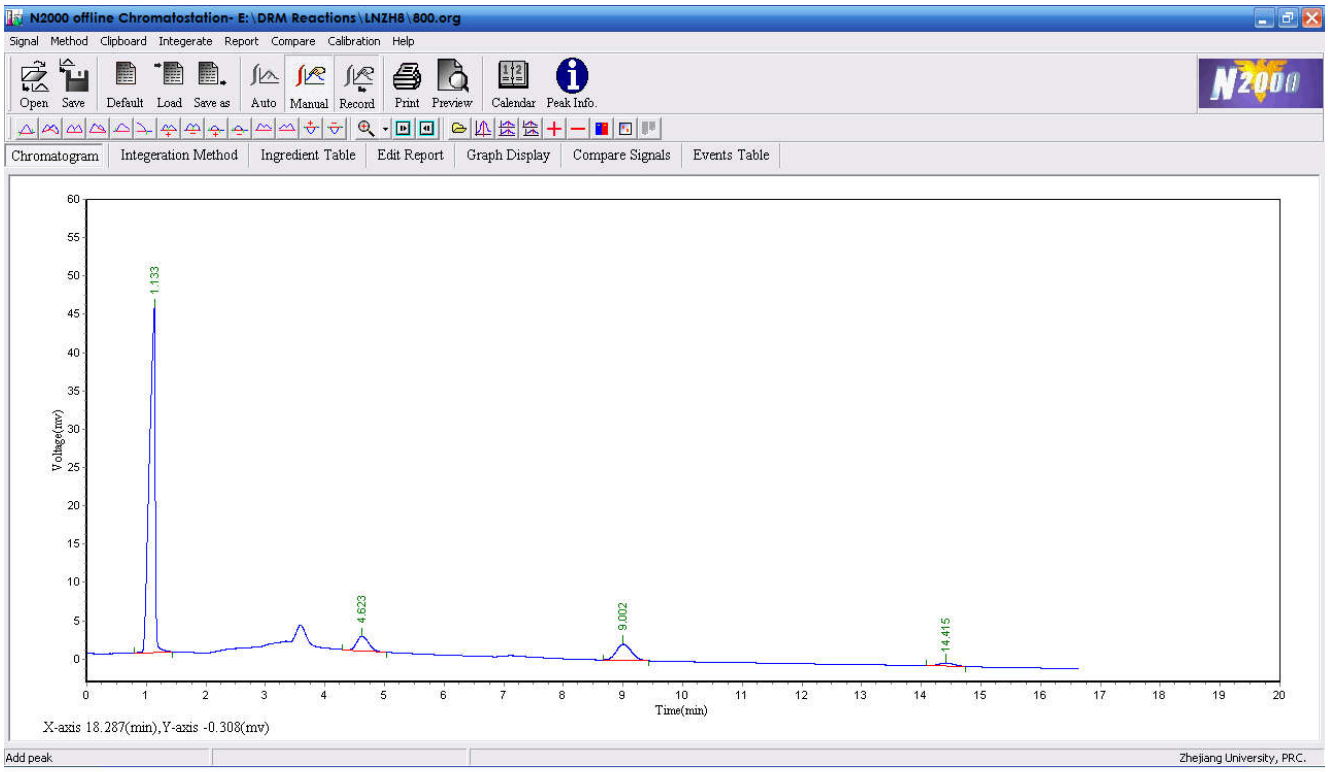

Results Data File - E:\DRM Reactions\LNZH8\800.org

Peak No.	Peak ID	Ret. Time	Peak Height	Peak Area	Peak Conc.
1	H_2	1.133	44959.871	2260322.929	70.6875
2	CO	4.623	1900.714	205666.595	6.4319
3	CH_4	9.002	2080.829	455481.049	14.2443
4	CO_2	14.415	911.372	276155.973	8.6369
Total			49852.786	3197627.226	100.0000

Figure 7: Shows GC chromatographs of $LaNi_{0.8}Zr_{0.2}O_3$ synthesized by hydrothermal method.

List of Publications

&

Papers Presented in Conferences

List of Publications from Thesis Work:

1. Influence of method of preparation on the activity of La–Ni–Ce mixed oxide catalysts for dry reforming of methane.**T. V. Sagar**, N. Sreelatha, G. Hanmant, M. Surendar, N. Lingaiah, K. S. Rama Rao, C. V. V. Satyanarayana, I. A. K. Reddy and P. S. Sai Prasad.***RSC Advances, 2014, 4,50226-50232.***
2. Methane reforming with carbon dioxide over La-Ni_x-Ce_{1-x} mixed oxide catalysts. **T. V. Sagar,**N. Sreelatha, G.Hanmant, K.Upendar, N. Lingaiah, K. S. Rama Rao, C. V. V. Satyanarayana, I. A. K. Reddy and P.S. Sai Prasad. ***Indian Journal of Chemistry, 2014, 53A, 478-483.***
3. Syngas production by CO_2 reforming of methane on $LaNi_xAl_{1-x}O_3$ perovskite catalysts: Influence of method of preparation. **T. V. Sagar**, D. Padmakar, N. Lingaiah, K. S. Rama Rao, I. A. K. Reddy and P. S. Sai Prasad. ***Journal of Chemical Sciences, 2017, DOI: 10.1007/s12039-017-1359-2.***
4. Dry reforming of methane on $LaNi_xZr_{1-x}O_3$ perovskite catalysts: Influence of pyrochlore formation. **T. V. Sagar**, D. Padmakar, N. Lingaiah, K. S. Rama Rao, I. A. K. Reddy and P. S. Sai Prasad. (manuscript under preparation)
5. CO_2 reforming of methane on $LaNi_{0.6}M_{0.4}O_3$ perovskite oxide catalysts: Effect of metal (M=Al, Ce, Zr) doping on catalyst performance. **T. V. Sagar**, D. Padmakar, N. Lingaiah, K. S. Rama Rao, I. A. K. Reddy and P. S. Sai Prasad. (manuscript under preparation)

Other Publications by the Author:

1. Selectivity Reversal in Oxidative Dehydrogenation of Ethane with CO_2 on CaO–NiO/Al_2O_3 Catalysts. **T. V. Sagar,** M. Surendar, D. Padmakar, G. Parameswaram, N. Lingaiah, K. S. Rama Rao, I. A. K. Reddy, C. Sumana and P. S. Sai Prasad. ***Catalysis Letters, 2017, 147, 82-89.***

2. Selective substitution of Ni by Ti in $LaNiO_3$ perovskites: A parameter governing the oxy-carbon dioxide reforming of methane. Nuvula Sreelatha, **T. V. Sagar**, ValluriDurgaKumari and P.S. Sai Prasad. ***International Journal of Hydrogen Energy (Accepted), 2017, DOI:*** *http://dx.doi.org/10.1016/j.ijhydene.2017.08.180***.**
3. Oxidative dehydrogenation of ethane with carbon dioxide over Cr_2O_3/SBA-15 catalysts: the influence of sulfate modification of the support. P. Thirumala Bai, S. Srinath, K. Upendar, T. V. Sagar, N. Lingaiah, K. S. Rama Rao, P. S. Sai Prasad published in ***Applied Petrochemical Research, 2017, DOI: 10.1007/s13203-017-0182-5.***
4. Pt doped $LaCoO_3$ perovskite: A precursor for a highly efficient catalyst for hydrogen production from glycerol. M. Surendar, **T. V. Sagar**, N. Lingaiah, K. S Rama Rao and P. S. Sai Prasad. ***International Journal of Hydrogen Energy, 2016,41, 2285–2297.***
5. Combating Global Warming due to Nitrous Oxide. Nayeem Pasha, P.S.ShankarReddy, **T. Vikram Sagar**, N. Lingaiah and P. S. Sai Prasad.***Science Spectrum, 2016, 4, 410-423 (ISSN 2455-5053).***
6. Influence of Co particle size on the glycerol steam reforming activity over $La_xCe_{1-x}CoO_3$ perovskite derived mixed oxide catalysts. M. Surendar, **T. V. Sagar**, B. Hari Babu, N. Lingaiah, K. S. Rama Rao and P. S. Sai Prasad ***RSC Advances, 2015, 5, 45184–45193.***
7. Development of a Low Temperature Adsorbent from Karanja Seed Cake for CO_2 Capture. K.Upendar, **T. V. Sagar**, G.Raveendra, N. Lingaiah, B. V. S. K. Rao, R. B. N. Prasad and P. S. Sai Prasad.***RSC Advances, 2014, 4, 7142-7147.***

8. Catalytic tri-reforming of glycerol for hydrogen generation. M. Ashwani Kumar, Ch.Venumadhav, **T. V. Sagar**, M. Surendar, N. Lingaiah, G.Nageswara Rao and P. S. Sai Prasad. ***Indian Journal of Chemistry, 2014, 53A, 530-534.***

List of Papers Presented in Conferences from Thesis Work:

1. Influence of Pd doping on the activity of Ni-Ce oxide catalyst during dry reforming of methane, **T.V.Sagar,** K. Upendar, K.S.Rama Rao, N.Lingaiah, I.A.K.Reddy, P.S.Sai Prasad, ***Oral presentation*** in 23rd National Symposium on Catalysis at Royal Orchid Convention Center, Bengaluru, in 17-19th January 2018, Bengaluru, Karnataka.
2. Dry reforming of methane on $LaNi_{0.6}M_{0.4}O_3$ perovskite oxide catalysts: The influence of metal (M=Al, Ce, Zr) doping on catalyst performance. **T.VikramSagar**, D. Padmakar, K. Upendar, N.Lingaiah, K.S.Rama Rao, I. A. K. Reddy and P.S.Sai Prasad, ***Poster presentation*** in "Recent Developments in Chemical Sciences and Allied Technologies (RDCST)" held during 29-30th June 2017 at NIT Warangal.
3. Synthesis gas production by a hydrothermally treated catalyst in CO_2 methane reforming.**T.V.Sagar,** M.Surendar, D.Padmakar, K.S.Rama Rao, N.Lingaiah, I.A.K.Reddy, P.S.Sai Prasad, ***Oral presentation*** in Asia-Pacific Congress on Catalysis (APCAT – 7) in Mumbai, India held during January 17-21, 2017.
4. An efficient coke resistant catalyst for dry reforming of methane.**T. Vikram Sagar**, M. Surendar, N. Lingaiah, K. S. Rama Rao, I. A. K. Reddy and P. S. Sai Prasad, ***Oral presentation*** in Chemcon-2015 during 27-30th December 2015, at IIT Guwahati, India.
5. Development of trimetallic oxidecatalysts by hydrothermal method for CO_2 reforming of methane. **T.V. Sagar**, K. Upendar, M. Surendar, M. Ashwani Kumar, N.Lingaiah, K.S.Rama Rao, I. A. K. Reddy and P.S.Sai Prasad, in APAS- Golden jubilee science congress, held in IICT-CCMB during November 13-15, 2014.

6. Ni-Ce solid solution catalyst prepared by sol-gel method for CO_2 reforming of methane.**T.VikramSagar**, M. Surendar, D. Padmakar, N.Lingaiah, K.S.Rama Rao, I. A. K. Reddy and P.S.Sai Prasad, ***Oral presentation*** in International Conference on New Dimension in Chemistry & Chemical Technologies -Applications in Pharma Industry (NDCT-2014) held during 23-25th June, 2014 at Jawaharlal Nehru Technological University, Hyderabad.
7. Development of Tri-metallic Oxides for CO_2 reforming of methane by sol-gel method.**T. Vikram Sagar**,B. Hari Babu, C.V. Pramod, N. Lingaiah, K.S. Rama Rao, P.S. Sai Prasad, ***Poster presentation*** in IASC-2013 Conference held during August 15-17th 2013, at International Center, Goa.
8. Catalytic reforming of methane on $LaNi_xCe_{1-x}O_3$ Oxides prepared by hydrothermal method.**T. Vikram Sagar**, G.Hanmant, N. Lingaiah, K.S. Rama Rao and P.S. Sai Prasad and C. V. V. Satyanarayana, ***Poster presentation*** in 21st National Symposium on Catalysis (CATSYMP-21) held during February 11-13, 2013, at Indian Institute of Chemical Technology (IICT), Hyderabad.

List of Papers Presented in Conferences by Author:

1. CO_2 utilization in Oxidative Dehydrogenation of Ethane to Ethylene over Sulphated Co_3O_4/SiO_2 catalysts, **T.V.Sagar,** M. Surendar, D. Padmakar , N.Lingaiah, K.S.Rama Rao, I.A.K. Reddy, P.S.Sai Prasad, ***Oral presentation*** in Chemcon-2016 in December 27 – 30th, 2016, in Chennai, India.
2. Production of Ethylene from Ethane in Presences of CO_2 Over Cr modified $Co/SO_4^{2-}/SiO_2$ Catalysts, **T.V.Sagar,** M.Surendar, D.Padmakar, N.Lingaiah, K.S.Rama Rao, I.A.K.Reddy and P.S.Sai Prasad, ***Oral presentation*** in Dr. NTR University of Health Sciences, Vijayawada, November 7 – 9th, 2016, Acharya Nagarjuna University, Guntur.

3. Catalytic CO_2 reforming of methane over palladium promoted nickel-cerium mixed oxide catalyst, **T.Vikram Sagar**, M. Surendar, D. Padmakar, N.Lingaiah, K.S.Rama Rao, I. A. K. Reddy and P.S.Sai Prasad, ***Poster presented*** in Frontiers in chemistry sciences and technologies, during 28-29th, January 2016 at NIT Warangal, India.
4. Oxidative Dehydrogenation of Ethane with CO_2 on Ca-Ni/Al_2O_3 Catalysts, **T.Vikram Sagar**, M. Surendar, G. Parameswaram, D. Padmakar, N.Lingaiah, K.S.Rama Rao and P.S.Sai Prasad, ***Oral presentation*** in Andhra Pradesh Akademi of Sciences Acharya Nagarjuna University Campus, Amaravathi held during 27-29 January, 2016.
5. Magnesium-Cerium Mixed Oxide Catalysts for the Synthesis of Glycerol carbonate by Transesterification of Glycerol, G. Parameswaram, **T. Vikram Sagar**, G. Nageswara Rao, N. Lingaiah, ***Poster presented*** in SusChemE 2015 at ICT Mumbai, Maharashtra.
6. Kinetic Studies on Oxidative Dehydrogenation of Ethane with CO_2 on Cr_2O_3/Nb_2O_5 Catalyst, P. Thirumala Bai, T. Vishnu Kiran, **T.Vikram Sagar**, S.Srinath, C.Sumana, P.S. Sai Prasad, ***Poster presentation*** in Chemcon-2015 in 27-30th December 2015, at IIT Guwahati, india.
7. Titania based nanomaterials as adsorbents for low temperature CO_2 capture, K. Upendar, J. Mahammad Rafi, **T.V. Sager**, G. Parameswaram, N. Lingaiah, P.S. Sai Prasad, ***Oral presentation*** in 22nd National Symposium on Catalysis at CSIR-CSMCRI in 7-9th January 2015, Bhavnagar, Gujarat.
8. Activated carbon supported cobalt catalysts for glycerol steam reforming, M. Surendar, M. Ashwani Kumar, **T. Vikram Sagar**,B. Hari Babu, N. Lingaiah, P. S. Sai Prasad, ***Oral presentation*** in 22nd National Symposium on Catalysis at CSIR-CSMCRI in 7-9th January 2015, Bhavnagar, Gujarat.

9. Glycerol steam reforming on Co/ZrO_2 catalysts, M. Surendar, K. Upendar, B.Haribabu **T.V. Sagar,** N. Lingaiah & P.S. Sai Prasad, ***Oral presetataion*** in Chemcon-2014 in 27-30th December 2014, at Panjab University, Chandigarh.
10. Hydrogen production from steam reforming of glycerol by La-Co-Ce mixed oxides, M. Surendar, **T. Vikram Sagar**, B. Hari Babu, N. Lingaiah, P.S. Sai Prasad, ***Oral presentation*** in International Conference on Emerging Frontiers and Challenges in Chemistry, ICEFCC-2014 on 17-18th February 2014 at All Saints' College, Thiruvananthapuram.
11. Ni-Substituted Lanthanum Zirconate for Oxy-carbon dioxide Reforming of Methane, N. Sreelatha, **T. Vikram Sagar,** V. Durga Kumari and P. S. Sai Prasad, ***Oral Presentation*** in ICONBMS-2014 on January 8-10th 2014, at Nizam College, Hyderabad.
12. Oxidative Dehydrogenation of Ethane with Carbon Dioxide as Oxidant over Cr_2O_3/Al_2O_3-ZrO_2 Catalysts, P. Thirumala Bai, B. Hari Babu, Y. Ramesh, **T. Vikram Sagar**, N. Lingaiah, P. S. Sai Prasad, ***Oral presetataion*** in Chemcon 2013 in 27-30th December 2013, at Institute of Chemical Technology (ICT), Mumbai.

Modifications carried out in the Thesis in compliance with the comments of the examiners.

Name : Tatiparthi Vikram Sagar
Roll No. : 701451
Title : Studies on Modified Lanthanum Nickel Oxide Perovskite Catalysts for Dry Reforming of Methane

Thesis Examiner 1:

S.No.	Comment	Action Taken/ Corrected version in compliance with the Examiners comment
Chapters 1-2:		
(i)	The thesis is missing an abstract, which should ideally support the main objectives and highlight the scope of this study. The novelty and impact, when contrasted with related systems in the literature must be clearly described, with a view to capturing the originality of this study.	As suggested by the examiner a three page abstract is included in the thesis before Chapter 1 with Page Numbers: i, ii, iii.
(ii)	In Chapter 1, please provide a detailed Table (Table 1) that summarizes and contrasts the performance of noble-metal and non-noble metal catalysts for CO_2 reforming of methane. In Chapter 2, rationalize how the progress summarized in Table 1 can be specifically related to analogous perovskite, pyrochlore and solid-solution catalysts. I would again suggest that this is summarized in Table (Table -2), which could serve as the basis for outlining the novelty of this work, as alluded in (i)	As suggested by the examiner, the details of catalytic activity performance of noble and Ni-based catalysts are included in Chapter 1 in the form of a Table (Table 1.1) at Page No. 17. The detailed literature survey of structural oxides like perovskite, pyrochlore and solid-solution catalysts and their catalytic activity are provided in Chapter 2 in the form of a Table (Table 2.1) at Page No. 44.
(iii)	On Page 42, The specific observations from the literature review (which is now captured in Table 1 and 2) need to be elaborated and discussions should be used to illustrate the novelty of this study on the basis of the structure-property correlations that can be derived from the results in chapters 4-6.	The detailed explanation for Table 1.1 is given in Chapter 1 at Page No. 11 and for Table 2.1 in Chapter 2 at Page No. 28 in the updated Thesis.

Chapter 3:		
(i)	Please provide sample GC chromatographs to show calibrations for the reactants and products with RF determination. How was the quantification done and provide details (and data) for mass-balance analysis.	As suggested by the examiner, the details of response factor evaluation are provided in the thesis and a sample gas chromatogram is also included in Chapter 3 at Page Nos. 72 and 73 respectively.
Chapter 4:		
(i)	Please provide details for indexing and Rietveld refinement of XRD data. Further to this, include lattice parameters and crystallite size information, in the basis of the Scherrer formula.	As suggested, the details for indexing of XRD data, lattice parameters and crystallite size information is provided in Chapter 4, Table 4.1.2 at Page No. 81 and in Chapter 4, Table 4.2.2 at Page No. 94
(ii)	It is mentioned that small metal particles enhance catalytic activity – please provide particle size distribution and correlate catalytic activity on the basis of site-isolation.	As suggested, particle size distribution has been included and catalytic activity is correlated with active sites in Chapter 4, Table 4.1.3 at Page No. 89.
(iii)	Quantify the fraction of Lewis and Brønsted sites, on the basis of the FTIR and TPD data, estimate acid site density and expand discussions to rationalize catalytic activity on the basis of nature and strength of acid sites (from above).	Quantification of total acidic sites have been included in Chapter 4, Table 4.2.3 at Page No. 104 and the expanding the discussion in Chapter 4 at Page No 110.
Chapter 5:		
(i)	On the basis of H_2-TPR and XPS results, quantify the fraction of individual redox sites and link this to catalytic results and associated discussions pertaining to the evolution of active metallic phases.	As suggested, the quantification of individual redox sites is linked with catalytic activity in Chapter 5, Table 5.2.3, Table 5.2.4 & Table 5.2.5. at Page Nos. 149 & 150.
(ii)	The conclusions from this chapter need a more quantitative analysis of results, to support the view that a wider set of catalytic descriptors can be deployed to vindicate site-isolation and dispersion of Ni active sites (this could be based on the suggested new tables in Introduction chapters).	As suggested, the quantitative analysis of results has been carried out and accordingly the conclusions are modified in Chapter 5 at Page No.152.

Chapters 4-6:		
(i)	Please provide GC chromatographs for the best set of results within each category of catalyst (perovskite, pyrochlore, etc) with details of how data was quantified with respect to the calibration in chapter 3 and provide mass-balance details for each set of results. This can be included in the Appendix section.	As suggested, an Appendix Section (Page No. I to VIII) has been added in the updated Thesis with GC chromatographs for the best catalysts and also their carbon balance details. Reference to these GC chromatographs has been cited in the text at appropriate places.

Thesis Examiner 2:

S. No.	Comment	**Action Taken/ Modified version in compliance with the Examiners comment**
1	In the first chapter, references are not in proper order, also recheck the references cited [6 &7]	As suggested, References have been cited in the proper order in Chapter 1 at Pages 4 & 5
2	Maintain uniformity in spacing while citing references in the text. Also the units have to be mentioned as S.I. units (Page. No.19 first paragraph)	Uniformity in spacing while citing references in the text has been maintained. S.I. Units have been mentioned in Chapter 1 at Page 20.
3	The font size for superscript in FT-IR section is different	The font size has been made uniform in Chapter 3 at Page 66.
4	Equations to be numbered in the thesis	All equations in the thesis have been numbered
5	In chapter 3, reference 12 is not cited in the text	In chapter 3, reference 12 is cited at Page 68.
6	In chapter 4, the conversion decreases with increase in Ni content, justification should be given	The discussion given justification has been included in the updated thesis in Chapter 4 at Page 88.
7	Figure caption should start with capital letter (Figure 4.2.14)	Figure caption is started with Capital in Chapter 4, Page 110 in Figure No. 4.2.14.
8	It is better to justify the conclusions as appropriate	As suggested, the conclusions are modified and justified appropriately in Chapter 5 at Page 152.

*****